



HAL
open science

Long-range Coulomb interactions and charge frustration in strongly correlated quantum matter

Katherine Driscoll

► **To cite this version:**

Katherine Driscoll. Long-range Coulomb interactions and charge frustration in strongly correlated quantum matter. Strongly Correlated Electrons [cond-mat.str-el]. Université Grenoble Alpes [2020-..], 2022. English. NNT : 2022GRALY003 . tel-03626120v2

HAL Id: tel-03626120

<https://hal.science/tel-03626120v2>

Submitted on 22 Jul 2022

HAL is a multi-disciplinary open access archive for the deposit and dissemination of scientific research documents, whether they are published or not. The documents may come from teaching and research institutions in France or abroad, or from public or private research centers.

L'archive ouverte pluridisciplinaire **HAL**, est destinée au dépôt et à la diffusion de documents scientifiques de niveau recherche, publiés ou non, émanant des établissements d'enseignement et de recherche français ou étrangers, des laboratoires publics ou privés.

THÈSE

Pour obtenir le grade de

DOCTEUR DE L'UNIVERSITÉ GRENOBLE ALPES

Spécialité : Physique Théorique

Arrêté ministériel : 25 mai 2016

Présentée par

Katherine DRISCOLL

Thèse dirigée par **Simone FRATINI**, Université Grenoble Alpes
et codirigée par **Arnaud RALKO**, Maître de conférences, Université
Grenoble Alpes

préparée au sein du **Laboratoire Institut Néel**
dans **l'École Doctorale Physique**

**Interactions coulombiennes à longue portée et
frustration de charge dans la matière quantique
fortement corrélée**

**Long-range Coulomb interactions and charge
frustration in strongly correlated quantum
matter**

Thèse soutenue publiquement le **21 janvier 2022**,
devant le jury composé de :

Monsieur SERGIO CIUCHI

Professeur associé, Università degli studi di L'Aquila, Rapporteur

Monsieur LUCA DE' MEDICI

Professeur, ESPCI PARIS, Rapporteur

Madame ANNA MINGUZZI

Directeur de recherche, CNRS DELEGATION ALPES, Présidente

Monsieur VINCENT RENARD

Maître de conférences HDR, UNIVERSITE GRENOBLE ALPES,
Examineur



Long-range Coulomb Interactions and Charge Frustration in Strongly Correlated Quantum Matter

Katherine Driscoll



Contents

Acknowledgments	5
Abstract	7
Résumé	11
1 Introduction	15
1.1 Historical perspectives	15
1.2 Theoretical studies of strongly correlated systems	16
1.3 Anomalous transport	18
1.3.1 Displaced Drude peak	20
1.4 Experimental candidates	22
1.4.1 Transition metal oxides	22
1.4.1.1 Cuprate superconductors	23
1.4.2 Layered organic salts	24
1.4.3 Transition metal dichalcogenide heterostructures	27
1.4.4 Atomic, molecular and optical systems	28
1.5 Summary and perspectives	30
2 Exact Diagonalization	33
2.1 Introduction	33
2.1.1 Basis representation	34
2.1.2 Diagonalization and limitations	35
2.2 Efficient implementation	37
2.2.1 Lanczos algorithm	38
2.3 Symmetries	42
2.3.1 Implementation	43
2.3.2 Calculating matrix elements	48
2.4 Twisted boundary conditions	50
2.4.1 Flux and Aharonov-Bohm effect	50
2.4.2 Implementation of twisted boundary conditions	51
2.5 Ewald summation	56
2.6 Summary	58
3 Pseudogap metal induced by long-range Coulomb interactions	61
3.1 Introduction	61
3.2 Model and method	63
3.3 Analytical estimates	66

3.4	Phase diagram	69
3.5	Correlated pseudogap metal	75
3.6	Self-induced disorder	79
3.7	Collective charge excitations	84
3.8	Conclusions and summary	87
4	Anomalous transport and interplay with Mott physics	91
4.1	Introduction	91
4.2	Hubbard-Wigner Model	93
4.3	Incoherent high- T transport	95
4.3.1	Nernst-Einstein description of transport	100
4.3.2	Self-generated disorder	106
4.4	Anomalous quantum transport: transient localization	110
4.4.1	Mixed quantum-classical treatment	111
4.4.2	Displaced Drude peaks	112
4.4.3	Beyond semi-classical transport	113
4.5	Conclusions and summary	117
5	Conclusions	121
	Appendix A Exact Diagonalization	131
A.1	Fermionic sign convention	131
A.2	Gram-Schmidt Orthogonalization	132
A.3	Orthonormalization of symmetry basis	132
A.4	Twisted boundary condition phase factor	134
	Appendix B Ewald Summation	137
B.1	Derivation of the Ewald Summation	137
	Appendix C Classical Monte Carlo	145
C.1	Classical Monte Carlo	145
	Appendix D Mott-Ioffe-Regel Limit	151
D.1	Mott-Ioffe-Regel limit	151
	Bibliography	153

Acknowledgments

This thesis would not have been possible without the constant support, guidance, and assistance of many people.

In addition to representing three years of my own hard work, this thesis also serves as a testimony to the many years of dedicated effort that Simone Fratini and Arnaud Ralko have undertaken in exploring the effects of long-range interactions in condensed matter systems. Frankly speaking, this thesis would have been impossible to complete without them and I am eternally grateful for their patience and direction over the past three years.

Simone, your endless excitement and broad vision of the field truly provided the inertia to drive this thesis forward. Thank you for always being available to explain countless concepts time and again. More importantly, thank you for acting as a calm and steadying force during the more trying moments of this thesis. Without a doubt, your steadfastness is responsible for the completion of this thesis.

Arnaud, your lighthearted and easygoing nature brought a lot of light to the darker days of this thesis. In addition to our many (surprisingly) fun debugging sessions, I would like to thank you for your numerous explanations of complicated technical points rooted in the physical context of our projects. And of course, I cannot forget to thank you for all of your delicious cookies that fueled many efforts.

I would like to sincerely thank Anna Minguzzi, Sergio Ciuchi, Luca de' Medici, and Vincent Renard for the time and effort that they have dedicated to serving as the committee for my thesis defense. I greatly appreciate their thorough feedback and the chance to discuss the finer points of my work, and its potential implications, with them.

I am also grateful for the hard work of Mathilde Binet and Ugo de Noyers in opening up new directions to be explored during their internships with our group. I would also like to extend my gratitude to

Patrick Belmain for his efficient technical support over the years.

I would like to acknowledge the European Union Horizon 2020 research and innovation program under the Marie Skłodowska-Curie grant agreement No. 754303 which made this work possible. I would also like to extend my gratitude to Román Orús at Donostia International Physics Center and Multiverse Computing for hosting me during my industrial secondment and for introducing me to the world of tensor networks.

I would also like to thank all of my colleagues at the Néel Institute for their warm welcomes and guidance throughout the past three years. Our interactions and exchanges can generally be classed into two categories. The first category involves scientific discussions and notably includes the personalized DFT course generously offered by Xavier Blase during the first year of my thesis. The second category consists of conversations about mountains and mountain-related sports and I am very grateful for the skiing advice of Gabriele D'Avino and the climbing advice of Serge Florens.

Although the pandemic scattered us to the winds, I would like to thank my officemates for the constant laughter and support that they brought to this thesis. Miguel Ángel, thank you for always being there when I needed to vent and for making me laugh countless times. Thank you for welcoming me in Murcia and for all of the wonderful times with your family. Y también gracias a tu madre por su constante apoyo.

Théo, thank you for your lively discussions of what constitutes a good figure, for your willingness to go to HONO, and for making me doubt my own understanding of the English language. I will miss our brunches and morning discussions immensely.

Massimiliano, thank you for your terrifying (but effective) ski lessons, for sharing delicious food, and for always being ready to have a good time. And perhaps most importantly, thank you for lending me your adapters to make my defense possible.

To Quentin, Sergueï, and Maxime, thank you for always making lunch and coffee breaks interesting and for your countless explanations of the French language.

There are many people beyond our working group in the lab to whom I must also extend my thanks. Kristin, thank you for your patience and for keeping me grounded. Richard, thank you for brightening my life with your many jokes and for the constant reminders that there is life beyond the thesis. Ángel and David, thank you for

exploring the mountains around Grenoble with me and for opening your homes for many delicious meals.

During my short time here in Grenoble, I have been fortunate to live with many wonderful roommates. Matteo, I am very grateful for all of the times we spent together, whether it was buying half of Ikea, enjoying a sunlit brunch on the balcony, or having movie night (which meant that I was sleeping on the couch while you actually watched the movie). Mónica and Ari, thank you for all of your support throughout the last year of my thesis, which included a lot of télétravail. Mónica, thank you for constantly reminding me that everything was going to turn out for the best, and Ari, thank you for always distracting me from the thesis with your mom's delicious food.

Although we were mostly unofficial roommates, I cannot forget to thank "The Coloc" for welcoming me into your home and for sharing many memorable times together. Daniel, thank you for always sharing your "famous" recipes. Laura, thank you for making me laugh by sharing your weird thoughts and for always being ready to vent about various frustrations from work. I am especially grateful to Léon and Antonia, for always listening and for always being ready to tackle complicated recipes together. I cannot thank you enough for taking care of me and especially for nourishing me throughout the writing process.

To my loving grandmother, Edie, thank you for your relentless support and for your weekly emails that always brought a smile to my face.

I cannot begin to express my thanks to my parents not only for their support throughout this process, but also for their many sacrifices over the years which made this thesis possible.

Y finalmente, mi amor, nunca podré agradecerle lo suficiente lo que has creído en mí y lo que me has apoyado en cada momento.

Abstract

This dissertation examines the impact of long-range interactions in lattice models of low-dimensional strongly correlated systems with a focus on their relevance to anomalous electronic transport. Traditionally, the Hubbard model forms the basis of theoretical and numerical investigations of strongly correlated quantum matter. This effective model constitutes the simplest model of electronic correlation and relies on an approximation that truncates electron-electron interactions to a local, on-site potential. While this approximation has proved valid in several instances, certain unexplained phenomena in correlated materials challenge us to develop new perspectives and approaches.

In the first part of this thesis, we discuss the historical motivation for our current work from both a theoretical and an experimental viewpoint. In particular, we cover the discovery of bad metallic transport and the associated breakdown of Boltzmann theory of electron transport. We further review examples of strongly correlated systems that exhibit bad metallic transport and other exotic phenomena that suggest the possibility of poorly screened electronic interactions acting as a common microscopic mechanism. This general feature justifies the development of a theoretical framework that is capable of examining long-range interactions in a controlled, systematic manner.

Motivated by this, we analyze a long-range interacting lattice model for spinless electrons in two dimensions via exact diagonalization on a finite cluster in real space. As this method is susceptible to finite-size errors, we discuss at length its implementation and technical details designed specifically to reduce these errors, namely the use of twisted boundary conditions and the Ewald summation. We determine the phase diagram at zero temperature and demonstrate that the long-range interactions act as a source of self-generated disorder that drives the development of a strongly correlated pseudogap phase, in a manner reminiscent of the classical Efros-Shklovskii Coulomb gap. Furthermore, we establish that this phenomenon is independent of lattice geometry, a fact that represents the broad potential of long-range interactions in giving rise to a novel form of strongly correlated behavior.

Following our zero-temperature study, we address the question of whether this self-generated disorder can survive in the presence of thermal fluctuations and local Coulomb repulsion (Hubbard terms) relevant in Mott systems, a situation closer to those in experimental systems. By means of classical Monte Carlo calculations, we show that not only does the self-generated disorder survive, but that it also acts as a microscopic mechanism that generates bad metallic transport. Upon further investigation, we determine that the long-range interactions, in combination with quantum fluctuations, cause a transient localization of the charge carriers, thereby suppressing the conductivity values below those predicted in conventional Boltzmann theory, as observed experimentally.

In conclusion, we have established that long-range interactions in electronic models act as a microscopic mechanism that is capable of causing exotic phenomena in numerous materials. We conclude that a proper treatment of both quantum fluctuations and long-range interactions should next be studied with the finite temperature Lanczos method, which will act as a bridge between our exact diagonalization and Monte Carlo studies. Overall, this dissertation emphasizes the capability of long-range interactions to produce novel phenomena and elicits further thought-provoking questions concerning the interplay with Mott-Hubbard physics and external disorder, crucial in metallic systems.

Résumé

Cette thèse examine l'impact des interactions à longue portée dans les modèles sur réseaux des systèmes fortement corrélés de basse dimension, en mettant l'accent sur leur pertinence pour le transport électronique anormal. Traditionnellement, le modèle de Hubbard constitue le modèle de base des études théoriques et numériques dans le domaine de la matière quantique fortement corrélée. Ce modèle effectif, le plus simple modèle électronique prenant en compte les interactions, repose sur l'approximation que les interactions sont écrantées et que seul un potentiel local, sur site, reste effectif. Cependant, bien que cette approximation se soit avérée valide dans de nombreux cas, certains phénomènes inexpliqués dans les matériaux corrélés nous mettent au défi de développer de nouvelles perspectives et approches allant au-delà des descriptions actuelles.

Dans la première partie, nous présentons l'état de l'art des systèmes dits mauvais métaux d'un point de vue théorique et expérimental. En particulier, nous présentons comment ces états électroniques ne sont plus correctement décrits par la théorie de Boltzmann du transport des électrons. Nous passons également en revue certains exemples de systèmes fortement corrélés présentant un mauvais transport métallique ainsi que d'autres phénomènes exotiques, suggérant la possibilité que des interactions électroniques soient faiblement écrantées et qu'elles seraient ainsi à l'origine du mécanisme microscopique produisant le comportement corrélé. Cette caractéristique générale justifie alors le développement d'un cadre théorique permettant d'examiner ces interactions à longue portée d'une manière contrôlée et systématique.

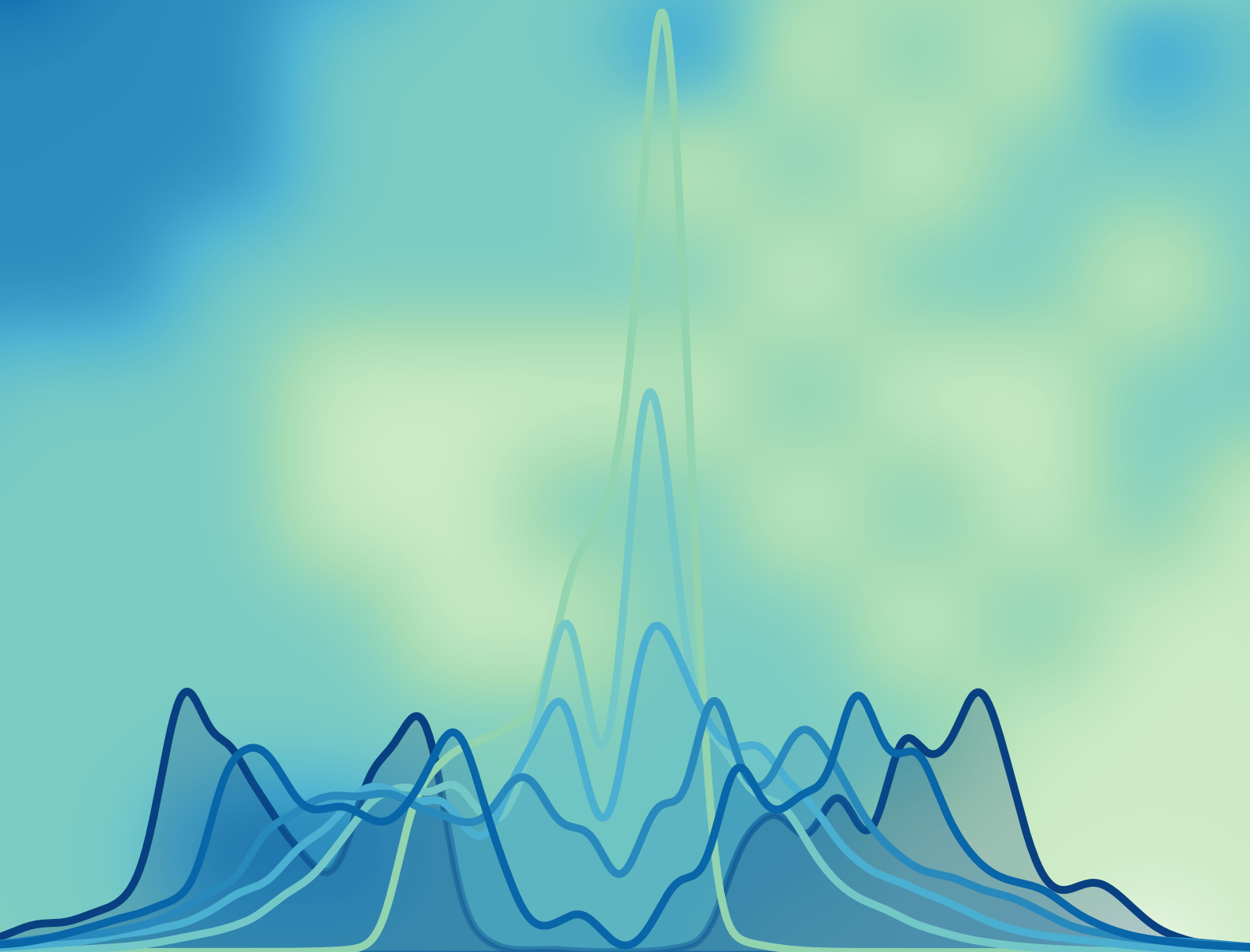
Dans cette optique, nous analysons un modèle de réseau d'interaction à longue portée pour des systèmes électroniques sans spin en deux dimensions, par diagonalisation exacte. Cette méthode étant sensible aux effets de taille, nous développons des approches techniques permettant d'en réduire les erreurs : conditions périodiques généralisées et sommation d'Ewald. Nous déterminons ainsi le diagramme de phases à température nulle et montrons comment les interactions à longue portée agissent comme une source de désordre auto-généré conduisant à l'apparition d'une phase pseudogap fortement corrélée,

rappelant le gap de Coulomb classique de type Efros-Shklovskii. De plus, nous établissons que ce phénomène est indépendant de la géométrie du réseau montrant ainsi son caractère générique et donc la possibilité de l'observer dans d'autres contextes.

Fort de ce résultat, nous adressons alors la question de savoir si ce désordre auto-généré peut survivre en présence de degrés de liberté de spin et aux fluctuations thermiques, une situation plus proche de l'expérience. Au moyen d'un Monte Carlo classique, nous montrons que non seulement ce désordre survit, mais il est également à l'origine microscopique d'un mauvais transport métallique. En rajoutant enfin le caractère quantique des électrons dans notre théorie, nous mettons en évidence que ces interactions à longues portées entraînent une localisation transitoire des porteurs de charge, supprimant ainsi les conductivités inférieure à celles prédites par la théorie Boltzmann, réconciliant certaines observations faites dans la littérature.

En conclusion, nous avons établi que les interactions à longue portée dans les modèles électroniques sont un mécanisme microscopique pouvant être à l'origine de phénomènes exotiques de nombreux matériaux. Il reste cependant des questions ouvertes, comme un traitement purement quantique à température finie. Ceci serait réalisable avec la méthode de Lanczos à température finie, qui comblerait nos études quantiques à température nulle et semi-classiques à température finie. Nous savons cependant d'ores et déjà que les interactions à longues portées sont à considérer si l'on veut s'intéresser aux questions du rôle des spins et du désordre externe, cruciales dans les systèmes métalliques.

Chapter 1: Introduction



Chapter 1

Introduction

1.1 Historical perspectives

The birth of condensed matter is rooted in the development of the Drude model, at a time when condensed matter research was still referred to as solid state physics [1, 2]. This classical description of electron transport in metals enjoyed much success as the first microscopic model to describe experimentally observed trends of physical observables, such as the Wiedemann-Franz law [3]. However, this simple model failed to describe other key phenomena, such as the specific heat and low temperature behavior of the resistivity. As condensed matter evolved with the incorporation of quantum mechanics, contributions from Pauli and Sommerfeld were crucial to the improvement of the Drude model, eventually leading to a correct description of the specific heat [4–6]. Furthermore, Bloch’s description of electronic motion through a periodic lattice led to the development of band structure calculations which contributed to a number of breakthrough discoveries in condensed matter systems in the mid-twentieth century [7, 8].

In particular, these early band structure calculations, which were based on non-interacting electrons, and other mean field theory treatments (such as Hartree-Fock) were successfully employed to characterize metallic and insulating phases and to determine metal-insulator transitions in terms of external parameters, such as temperature or pressure. However, these techniques failed to accurately predict the insulating nature of certain materials. The first instance of this failure was pointed out by Verwey and de Boer for transition metal oxides in 1937 [9]. Subsequently Peierls and Mott called the community’s attention to the importance of electronic correlations arising from interactions, thereby ushering in a new era in condensed matter physics—the study of strongly correlated systems [10–14].

The two main research directions in this field can be summarized as:

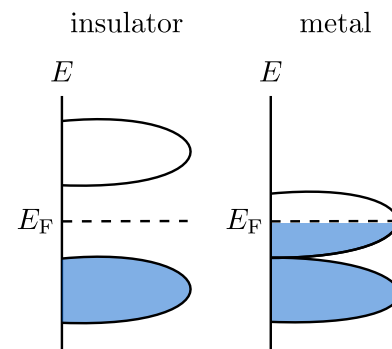


Figure 1.1: Illustration of band theory prediction of an insulator versus a metal.

understanding the correlation-based mechanisms driving the metal-insulator transitions in various strongly correlated systems (transition metal oxides, layered organics, etc.); and characterizing the anomalous metallic phases often found in the vicinity of the correlated insulators. At first glance, investigating these phenomena in a systematic, controlled manner across a variety of electronic systems may appear to be a daunting, even unthinkable, challenge.

1.2 Theoretical studies of strongly correlated systems

A common theoretical approach to unraveling the mysteries of strongly correlated systems has been to utilize effective fermionic lattice models, which reduce the numerous degrees of freedom to a minimal number that is relevant to the problem at hand [8]. The logic behind this reduction scheme is that typically only a few degrees of freedom dominate the physics, which can be justified upon a comparison of energy scales. Perhaps the most famous example of an effective fermionic lattice model is the Hubbard model. Described by the following Hamiltonian,

$$H = -t \sum_{\langle ij \rangle, \sigma} \left(\hat{c}_{i\sigma}^\dagger \hat{c}_{j\sigma} + \hat{c}_{j\sigma}^\dagger \hat{c}_{i\sigma} \right) + U \sum_i \hat{n}_{i\uparrow} \hat{n}_{i\downarrow} \quad (1.1)$$

this model simplifies the many-electron problem to a study of only the conduction band of electrons [15–17].

The first term in the Hamiltonian is typically referred to as the hopping, or kinetic, term. In this term, $\langle ij \rangle$ indicates a summation over nearest neighbor sites, i and j , with the particle spin indexed by σ . The prevalence of nearest-neighbor hopping processes for a fixed spin sector are controlled by the value of the hopping integral, t , which describes the overlap between atomic wavefunctions localized to sites i and j in the tight binding approximation. The second term in Eq. 1.1 reflects the on-site (local) Coulomb potential experienced by two electrons on the same lattice site. As the Coulomb interaction decays rapidly with distance and most materials exhibit efficient screening of charges, this on-site term is typically the only source of electron-electron interaction treated in effective lattice models. In summary, this model of conduction band electrons assumes that the electronic motion happens via nearest-neighbor hops (first term) and that interaction effects are only considerable for doubly occupied sites (second term).

Already at this minimal level (in terms of parameters), this model is capable of producing correlated behavior, such as the famed Mott metal-insulator transition [17, 18] in half-filled systems, that previously failed to be described by non-interacting band theory. Unfortunately, even this relatively simple model only has an exact solution in one-dimension via the use of the Bethe ansatz [19] and infinite dimensions [20]. These limiting cases have been the focus of much research over the past several decades and a wealth of results, including in-

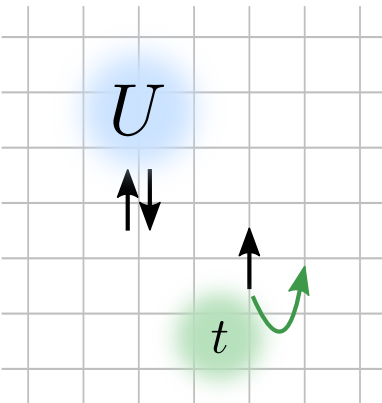


Figure 1.2: Illustration of Hubbard model terms on a square lattice.

depth analyses of ground state and excited state properties at zero and finite temperatures, has been accrued [21,22]. This knowledge has been useful in the understanding of quasi-one-dimensional systems which display strongly correlated physics, such as quantum wires, Bechgaard organic salts, and Fabre organic salts [23,24].

However, most strongly correlated systems in condensed matter correspond to higher dimensions ($d = 2, 3$) which is exactly where the deceptively simple Hubbard model fails to yield an exact solution. Throughout the past few decades, this limitation has spurred a massive development of numerical methods and approximations to extend the use of the Hubbard model (and its related variants). One well-known example is the invention of dynamical mean field theory (DMFT) which maps lattice models to quantum impurity models [20]. Another notable example is the extension of the density matrix renormalization group (DMRG) method (arguably the best numerical method for $d = 1$) to two-dimensional systems [25–28]. Other state-of-the-art numerical methods include quantum Monte Carlo [29–31], exact diagonalization [32,33], diagrammatic Monte Carlo [34–36], tensor network methods [37–39], and, more recently, machine learning techniques [40–42]. Recent works have focused on collaborations of these state-of-the-art numerical techniques to benchmark basic quantities related to the two-dimensional Hubbard model, such as the ground-state energy and double occupation fraction (see Fig. 1.3).

The growth in numerical methods used to study strongly correlated systems also coincides with recent progress in experimental techniques [44]. In particular, heterostructure systems give rise to emergent moiré lattices with strong interaction effects, thereby providing us with an experimental platform to perform carefully controlled studies into the interaction-driven physics [45,46]. These systems include heterostructures composed of transition metal dichalcogenides, which will be discussed in more detail later. Additionally, advances in cold atoms have produced systems capable of acting as Hamiltonian model solvers [47].

Together, these theoretical and experimental advances have been greatly successful in improving our understanding of strongly correlated materials. For example, we have acquired a qualitative understanding of the phase diagram and superconductivity observed in the famous high-temperature cuprate superconductors [48]. Obviously, a comprehensive review and analysis of the myriad theoretical, numerical and experimental advances (and their shortcomings) related to strongly correlated matter lies outside the scope of this thesis. We invite the interested reader to refer to Refs. [44,49,50] which are graduate-level textbooks that provide a technical overview of recent theoretical, numerical and experimental advances.

Despite the immense progress made, we are still far from a complete understanding of strong electronic correlations and the exotic phases to which they give rise. Moreover, explaining the anomalous

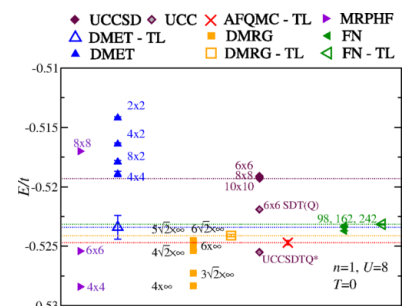


Figure 1.3: Thermodynamic-limit ground-state energy of the Hubbard model at $n = 1$ with $U/t = 8$ as obtained by various algorithms (open symbols). Ground state estimates for finite-size systems (closed symbols) are also provided. Reproduced from Ref. [43].

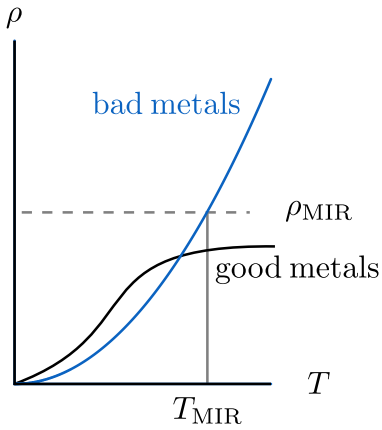


Figure 1.4: Illustration of bad metallic transport where the resistivity climbs past the Mott-Ioffe-Regel limit.

transport observed in multiple strongly correlated systems remains one of the main challenges in the field today. These systems include the high-temperature cuprate superconductors [51], pnictides [52–54], fullerenes [55], vanadium dioxide [56], ruthenates [57], layered organic salts [58, 59], and nickelates [60]. Their transport is deemed *bad* or anomalous because the experimental measurements of the electrical resistivity have shown that it grows with temperature beyond a point known as the Mott-Ioffe-Regel limit in these systems. This limit will be discussed in more detail in the following section, but for now it suffices to say that this behavior signals the breakdown of the conventional Boltzmann theory of transport. The remarkable fact that such vastly different systems (in terms of chemical composition, structure, etc) display similar anomalous behavior suggests that the underlying mechanism must be not only quite general, but could also be lacking from the typical microscopic models used to study strongly correlated systems. While conventional microscopic models are capable of giving rise to resistivity growth beyond the MIR limit, they are unable to describe other signatures of anomalous transport which will be discussed in the following section. One proposed mechanism in particular constitutes the main focus of this thesis—the effect of long-range (non-local) interactions in strongly correlated matter. As such, we will concentrate the remainder of this discussion on selected developments that we deem as relevant to understanding this mechanism.

1.3 Anomalous transport

The conventional understanding of electron transport in solids relies on the use of Boltzmann theory, a semi-classical treatment that describes electron transport in terms of quasiparticle scattering processes with other electrons, lattice vibrations or other sources of disorder (see Fig. 1.5). Typically at low temperatures in Fermi liquids, the resistivity scales with the temperature as T^2 due to electron-electron scattering and Umklapp processes. With increasing temperature, electron-phonon scattering processes dominate, leading to a T^5 scaling behavior before reducing to a linear rate at high temperatures. The average distance that a charge carrier, or quasiparticle, travels between scattering processes is called the *mean free path* and is denoted by ℓ .

As the temperature increases, this quantity decreases as the rate of scattering events increases with increasing thermal fluctuations. In conventional metals, such as copper, the mean free path is typically much larger than the lattice spacing, a , all the way up to the melting temperature, T_m . Therefore, Boltzmann theory accurately describes the transport properties in these materials, such as the fact that the resistivity typically scales linearly with temperatures beyond the energy scale of lattice vibrations [61]. The fact that the mean free path should be much larger than the lattice spacing ($\ell \gg a$) turns out to be a non-trivial criterion in determining the relevance of the Boltzmann picture

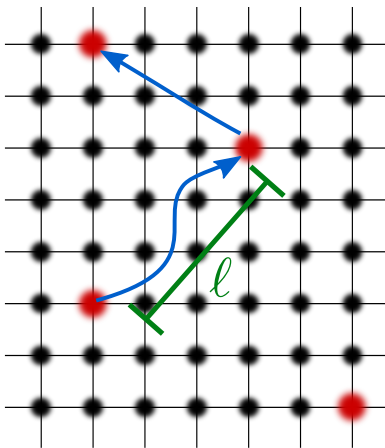


Figure 1.5: Illustration of an electron scattering process with disorder (red). The average distance traveled between scattering events is labeled by ℓ (green).

of transport.

Indeed, in 1960 Ioffe and Regel identified that Boltzmann transport is no longer valid when the mean free path falls below a limiting, minimum value [62]. This limitation on the mean free path came to be known as the Mott-Ioffe-Regel (MIR) limit as Mott similarly proposed a minimal metallic conductivity in 1972 [63]. Although conflicting definitions exist in the literature, we work with the definition $\ell_{\min} = a$ throughout this manuscript. The physical interpretation of this limit is that the semi-classical description of electron scattering processes only works when the scattering events occur at least one lattice spacing apart.

This limit was confirmed by the experimental observation of resistivity saturation in a number of materials, even those who displayed resistivity values higher than those predicted by Boltzmann theory. In other words, as the temperature approached the value T_{sat} at which $\ell \approx a$, the growth of the resistivity would slow down and would display saturated behavior until the melting transition at T_m . Typically this saturation is well-described by a parallel-resistor formula developed by Wiesmann in the late 1970s [64]. This formula states that the resistivity can be described as

$$\frac{1}{\rho(T)} = \frac{1}{\rho_{\text{ideal}}(T)} + \frac{1}{\rho_{\text{sat}}} \quad (1.2)$$

where $\rho_{\text{ideal}}(T)$ is the value predicted by Boltzmann theory if saturation did not occur, and ρ_{sat} is the resistivity value predicted from Boltzmann theory at $\ell_{\min} = a$. This simple formula performed so well that resistivity saturation was commonly accepted as a universal property of all metals [65].

However, one of the first instances of non-saturating behavior was reported in two different cuprate systems in 1987 [51], suggesting that phonons were not the dominant scattering force at high temperature and that the MIR limit was violated according to parameters from band structure calculations. This discovery, coupled with other findings of non-saturating behavior in vastly different materials [57,66,67], has motivated the search for a theoretical framework of transport that extends beyond the typical semi-classical approach. The observed anomalous behavior not only violates the MIR limit without any crossover indication, but also typically shows no sign of saturating at higher temperatures in these so-called *bad metals*.

This term was first coined by Emery and Kivelson in 1995 in an early attempt to describe the non-saturating metallic systems where the calculated mean free path at high temperature implies that the quasiparticle picture can no longer be valid [68]. Furthermore, they postulated that the non-quasiparticle mechanism driving transport at high temperature could also control the low temperature transport ($T < T_{\text{MIR}}$) because these systems do not display any crossover in temperature dependence [68]. The existence of such an exotic phase (non-Fermi

Alternative definitions include $\ell_{\min} = k_F^{-1}$, and $\ell_{\min} = 2\pi k_F^{-1}$, where k_F is the Fermi wave vector [61].

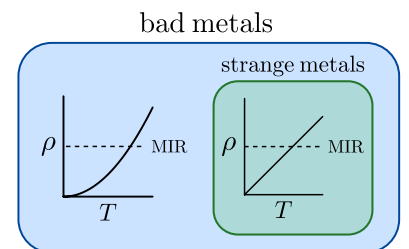


Figure 1.6: A note on terminology: bad metallic resistivity violates the MIR limit while strange metallic resistivity additionally exhibits linear behavior below the MIR limit.



Figure 1.7: Illustration of the regime of resilient quasiparticles.

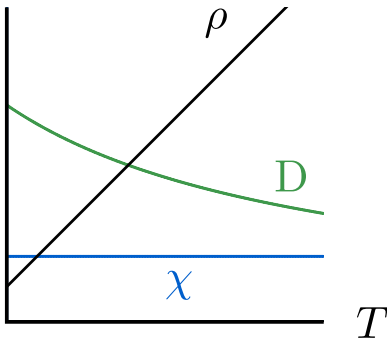
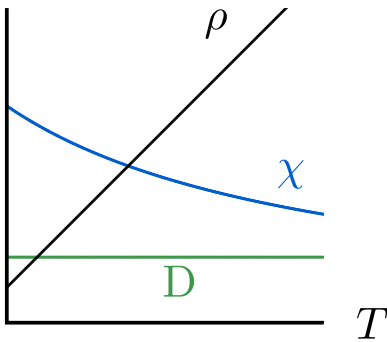


Figure 1.8: Illustration of two possibilities of strange metallic behavior emerging from the charge diffusion description.

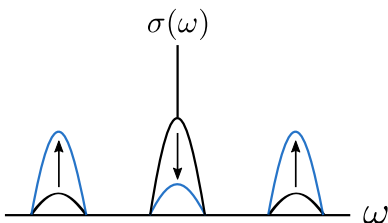


Figure 1.9: Transfer of spectral weight to higher frequencies, with no DDP observed.

liquid) has spurred several theoretical attempts at an explanation, but no widely accepted conclusion has been reached [69,70]. DMFT works by Deng et al. [71] have analyzed the behavior of the spectral function and determined that the quasiparticle picture is valid below the Fermi temperature, T_F . As this temperature can be much lower than T_{MIR} , they also examined the intermediate temperature regime and discovered signatures of *resilient quasiparticles* which eventually disappear at T_{MIR} (Fig. 1.7). Overall, the extent to which quasiparticles contribute to bad metallic transport remains a topic of much debate and there is no generally accepted theoretical description of an exotic, quasiparticle-free mechanism.

A lack of understanding also exists for the anomalous scaling behavior associated with strange metals. In this subgroup of bad metallic systems, the resistivity scales (with respect to the temperature) with a power law that is not consistent with that dictated by the Fermi liquid picture. In the high temperature limit, it has been proposed that charge transport is best understood from the simple Einstein diffusion relation [69,72,73] that connects the electrical conductivity, σ , to the charge compressibility, χ , by means of the diffusion constant, D ,

$$\sigma = \chi D. \quad (1.3)$$

Two possible pictures of universal behavior of strange metallic systems immediately emerge. One consists of a constant value for the compressibility while the diffusion constant scales with $1/T$, overall leading to a resistivity that scales linearly with temperature [73]. This concept is often referred to as the *Planckian regime* and arguments extracted from experimental data suggest that a wide range of materials (including strongly correlated systems and conventional metals) display a universal Planckian scattering rate [74]. However, these extracted scattering rates actually differ a lot across materials and the lack of a universally accepted definition for a transport scattering rate suggests that perhaps the charge diffusion picture is the safest route to developing a unified theoretical framework for bad metallic behavior [69]. The other picture of universal behavior emerging from the simple diffusion relation in Eq. (1.3) is that of a constant value of the diffusion constant while the compressibility instead scales as $1/T$, thereby controlling the high-temperature behavior of the resistivity (see Fig. 1.8).

1.3.1 Displaced Drude peak

While much theoretical discussion has been directed towards efforts of a unifying theory describing bad metallic (and potentially non-Fermi liquid) behavior, relatively little focus has been directed towards explaining another experimental signature of bad metallic systems. This signature is the appearance of a *displaced Drude peak* (DDP) in the optical conductivity spectrum as temperature increases beyond the MIR

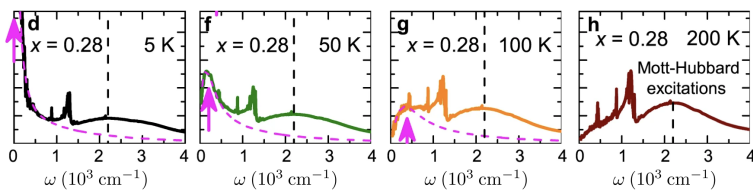


Figure 1.10: Evolution of the displaced Drude peak (pink arrows) in the optical conductivity spectra of $\kappa\text{-ET}_2\text{Cu}_2(\text{CN})_3$ with increasing temperature (from left panel to right panel) for fixed doping, $x = 0.28$. The dashed line indicates the location of Mott-Hubbard type excitations. Adapted from Ref. [75].

limit [75]. However, these DDPs only appear in some bad metallic systems, which could explain the scarcity of theoretical investigations into their origins. In the bad metallic systems without DDPs, the low-frequency spectral weight contained in the Drude peak is transferred to incoherent excitations with high energy scales, such as the upper and lower Hubbard bands [61,76] (see Fig. 1.9).

However, in bad metallic systems that host DDPs, the spectral weight in the zero-frequency Drude peak is shifted to finite frequency values, thereby forming a DDP. Two general mechanisms have been identified that are capable of producing DDPs:

1. An additive mechanism that relies on non-quasiparticle collective modes from pinned charge density waves [70] creating an additional conduction channel at finite frequencies.
2. A subtractive mechanism in which the build-up of transient localization suppresses the weight at zero-frequency [77].

An illustration of these mechanisms can be seen in Fig. 1.11. The transient localization scheme that comprises the second mechanism was originally developed in the context of organic semi-conductors [78], where large molecular weights create very slow lattice vibrations that act as strong electron scatterers. Essentially the electrons explore a disordered landscape and localize within it. Eventually the disordered landscape changes and the electronic motion resumes before an ultimate relocation. This transient localization description of organic semi-conductors has been incorporated into a unifying theoretical framework that smoothly connects the limit of strong disorder with the limit of weak disorder, or the semi-classical limit [79]. Recently this framework was applied to a many-body electronic lattice model with electron-phonon interactions that reduced the carrier diffusion, leading to the development of a displaced Drude peak in the conductivity spectra [77].

Another possible mechanism for localization originates in the self-generated disorder caused by long-range interactions, which is the focus of this thesis. Typically, effective models assume that charges are effectively screened and therefore only treat local interactions, such as the U term in the Hubbard Hamiltonian (Eq. (1.1)). The Hubbard model is capable of producing some anomalous transport properties as

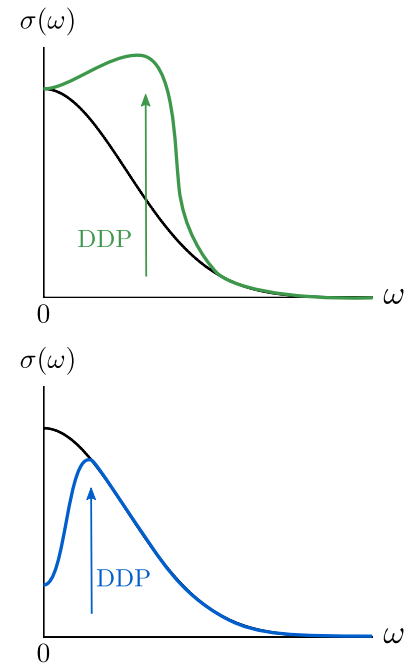


Figure 1.11: Illustration of two possible mechanisms leading to the development of a displaced Drude peak.

the resistivity calculated from it grows beyond the MIR limit without showing any sign of changing slope at high temperatures [72]. However, the DDP phenomenon is not captured in the optical conductivity spectra, with the growth of the resistivity as temperatures increase being linked to a transfer of spectral weight to higher values [72,80].

In this thesis, we demonstrate that the inclusion of non-local (long-range) interactions provides a microscopic mechanism for bad metallic transport in the form of a resistivity that greatly exceeds the MIR limit and the development of a DDP. Furthermore, we show that long-range interactions give rise to a novel correlated pseudogap phase at zero temperature. The anomalous behavior driven by such a general mechanism provides novel insight into explanations of bad metallic trends ($\rho > \rho_{\text{MIR}}$, DDP) across a wide variety of materials. In the following section, we discuss a non-exhaustive selection of strongly correlated materials that display unconventional phenomena and that we deem pertinent in the context of long-range interactions.

1.4 Experimental candidates

In this section, we aim to provide the reader with a brief introduction to strongly correlated systems in which long-range interactions either play, or are suspected to play, an important role in the experimentally-observed behavior. The systems covered here do not constitute an exhaustive list, but our hope is that the reader can develop a general appreciation for the widespread impact of long-range interactions in strongly correlated materials, and potentially apply that appreciation to their preferred system of interest. We begin our discussion with the transition metal oxides, specifically focusing on the famous cuprate family of high-temperature superconductors. Following this, we turn our attention to the broad class of layered organic salts, several of which also display influences from a charge frustration phenomena. Finally, we conclude with an analysis of recent experiments in transition metal dichalcogenide heterostructures and a brief word on the unique position of cold atom systems in realizing a complete understanding of complicated correlation effects in lattice models.

1.4.1 Transition metal oxides

The group of transition metal oxides is a broad association of materials comprised of oxygen and transition elements in various structures and stoichiometries. The identity of the transition element can be used to further classify the materials into subgroups, such as the cuprates, nickelates, manganates, and ruthenates. An example of the structure of a representative cuprate member is shown in Fig. 1.12. While individual properties of different transition metal oxides can vary drastically, they all share a few common features that justify their overall importance in strongly correlated materials. The valence electrons of

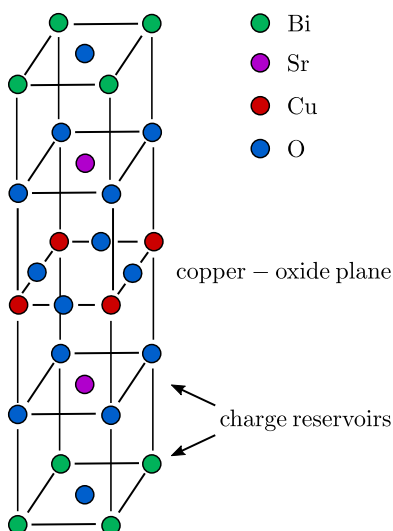


Figure 1.12: Example of the perovskite crystal structure for $\text{Bi}_2\text{Sr}_2\text{CuO}_6$.

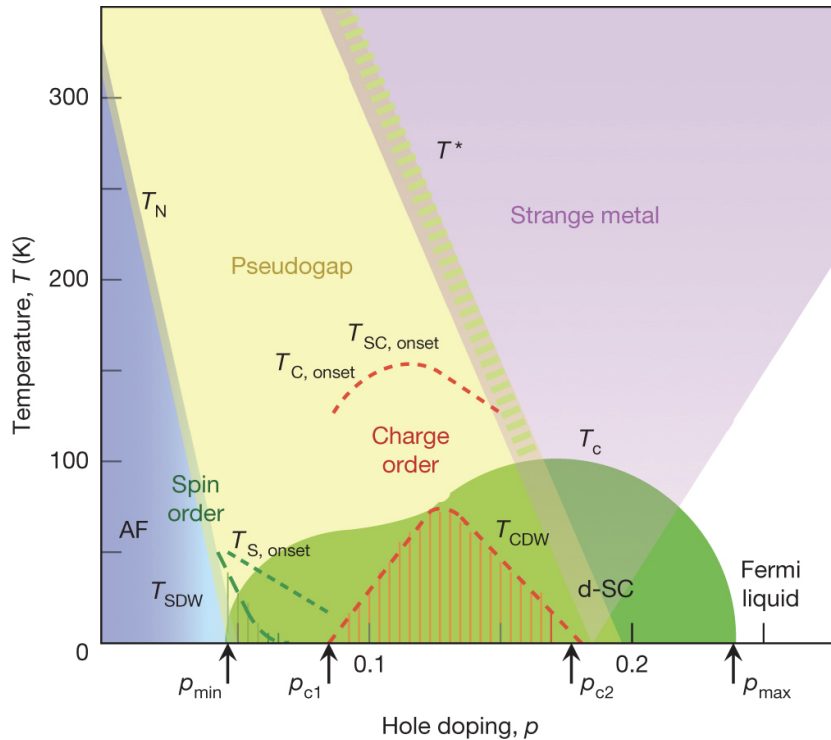


Figure 1.13: Phase diagram of the cuprates in terms of temperature T and hole doping p , with antiferromagnetic order (AF, blue), pseudogap (yellow), superconductor (SC, green), Fermi liquid (white), and strange metal (purple) shown. Reproduced from Ref. [48].

the transition elements correspond to electrons in narrow d orbitals, causing the electrons to localize at atomic sites due to strong Coulomb repulsion effects. This interaction-driven localization competes with orbital hybridization that forms with the p orbitals of the oxygen elements and promotes electron delocalization [81]. The typically narrow bandwidth of transition metal oxides signifies the presence of strong electron correlation effects which produces a rich variety of phases when combined with the various charge, spin and orbital degrees of freedom in individual materials [13, 81, 82]. Additionally, many of these systems can be considered as low-dimensional due to their specific crystal structure and chemistry [82], thereby inviting studies with low-dimensional effective lattice models, such as the Hubbard model on the square lattice.

1.4.1.1 Cuprate superconductors

The cuprate oxides are arguably the most famous family of transition metal oxides due to the discovery of high-temperature superconductivity in these systems in 1986 [83–85]. However, we will not focus on their superconducting properties in this thesis and merely mention it for the sake of completeness in this discussion. These systems are composed of superconducting copper-oxide planes that are intercalated with charge reservoir layers with the entire complex resembling a perovskite (see Fig. 1.12). Exotic phases, such as the unconventional superconductor, typically emerge as these materials are doped away

from half-filling in which they have one electron per copper atom. At this filling, the system is a Mott insulator due to the strong Coulomb repulsion that effectively suppresses any double occupation inside the narrow d orbitals [86].

Over the past few decades, an immense amount of research has been conducted on the cuprates and the general phase diagram is by now well-established (see Fig. 1.13). Despite this intense effort, many questions remain, including a microscopic understanding of the observed pseudogap phase and the bad metallic behavior. The resistivity-temperature curves for a representative member of the cuprate family is shown in Fig. 1.14. Typically, theoretical studies of the cuprates employ the Hubbard model on the square lattice as a minimal model of strong electron correlation. The cuprates are also frequently studied with more realistic models, such as multi-band models that highlight the importance of the oxygen atoms [87]. As there is no analytical solution to the Hubbard model in two dimensions, recent efforts have centered on analyzing the numerous competing orders through application of state-of-the-art numerical techniques, including DMRG and QMC [88, 89].

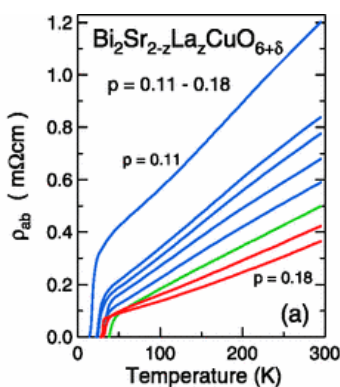


Figure 1.14: The resistivity as a function of temperature for various doping levels p for $\text{Bi}_2\text{Sr}_{2-2x}\text{La}_2\text{CuO}_{6+\delta}$. Adapted from Ref. [90].

In particular, these studies addressed the seemingly simple question of the characterization of stripe order in the underdoped region (left side of the superconducting dome in Fig. 1.13), a phenomenon that was first discovered in 1995 [91]. Ref. [88] could not successfully recover the experimentally predicted stripe wavelength with the conventional Hubbard model (Eq. (1.1)) and concluded that this simplistic model of electron correlation was missing a key ingredient. One proposed ingredient was the inclusion of non-local Coulomb interactions, the contribution of which is expected to be of the order of the energy scales among the various competing ground states.

Despite the fact that strong correlation effects were discovered in transition metal oxides almost 80 years ago, we are still very far from arriving at a commonly accepted, microscopic understanding of their various exotic phenomena. This shortcoming is particularly glaring in the case of the cuprates, which have received a tremendous amount of interest in the recent decades. However, systematic numerical studies have recently demonstrated that we might be reaching the limits of knowledge contained within the confines of the Hubbard model, thereby stimulating the urgent need for effective lattice models that treat non-local effects. As will be discussed in the following sections, the development of such models will improve our collective knowledge of not only the cuprates, but also other strongly correlated systems.

1.4.2 Layered organic salts

Another example of a strongly correlated system that would be well-described by a non-local (long-range) interacting model is the group

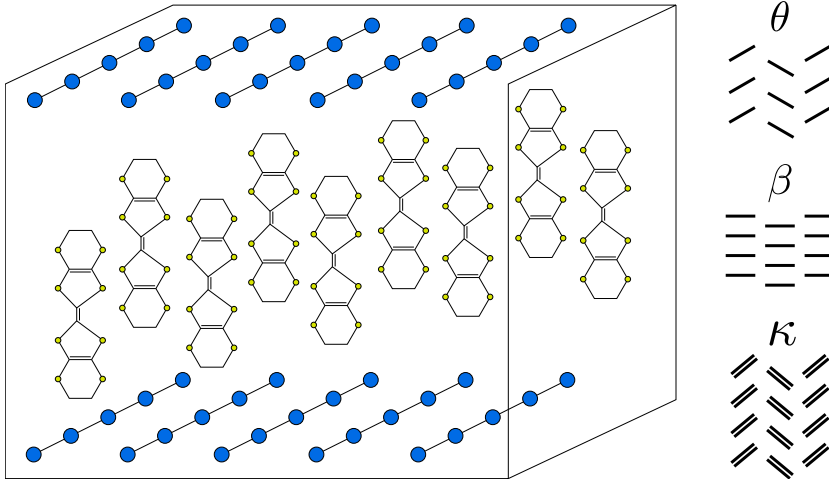


Figure 1.15: Illustration of the crystal structure of BEDT-TTF [93,96]. The layers of the large ET molecules are separated by layers of poorly conducting anions (blue). The ET molecules pack together in different patterns, which are labeled by different Greek letters. Examples of packing structures are shown on the right.

of layered organic salts. An early prediction that room-temperature superconductivity should be accessible in synthetic organic materials incited a wave of research into the electronic properties of low-dimensional organic salts [92,93]. While the discovery of superconductivity in quasi-one-dimensional salts (known as the Bechgaard salts) and its theoretical description are interesting in their own right [94], we choose to focus on quasi-two-dimensional systems constructed from bisethylenedithio-tetrathiafulvalene (BEDT-TTF). This molecule is commonly referred to as ET and its skeletal structure is shown in Fig. 1.16. These large molecules are typically combined with a monovalent anion in the stoichiometric ratio A_2B where A is the ET molecule and B is an anion [93,95]. These remarkably clean organic crystals are grown via electrocrystallization and the crystallographic structure consists of anionic layers interspersed between layers of ET laid out in various packing configurations (see Fig. 1.15) [93].

This class of materials hosts a plethora of phases, including charge density waves, superconductor, and anti-ferromagnetic insulators [98], all of which are readily accessible via controllable tuning of various external parameters, such as temperature, pressure, and magnetic field. The clean nature of the crystals coupled with this accessible control renders these systems a playground for testing various effective lattice models. While the microscopic specifics underlying each packing structure might differ, the standard tight-binding model employed is the extended Hubbard model (or some variation thereof). The Hamiltonian for the most general case is given as

$$H_{\text{EHM}} = - \sum_{\langle ij \rangle, \sigma} t_{ij} \left(\hat{c}_{i\sigma}^\dagger \hat{c}_{j\sigma} + \hat{c}_{j\sigma}^\dagger \hat{c}_{i\sigma} \right) + U \sum_i \hat{n}_{i\uparrow} \hat{n}_{i\downarrow} + \sum_{\langle ij \rangle, \sigma} V_{ij} \hat{n}_i \hat{n}_j \quad (1.4)$$

where the last term includes a non-local interaction, V , between nearest-neighbor sites, $\langle ij \rangle$. The inclusion of this term is a departure from the conventional Mott-Hubbard physics and can be justified by the ob-

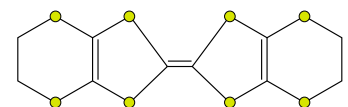


Figure 1.16: Structure of BEDT-TTF [97]. Sulfur atoms are shown in yellow.

For a comprehensive review with the phase diagrams in terms of temperature, pressure and geometrical structure, the reader is referred to Ref. [98].

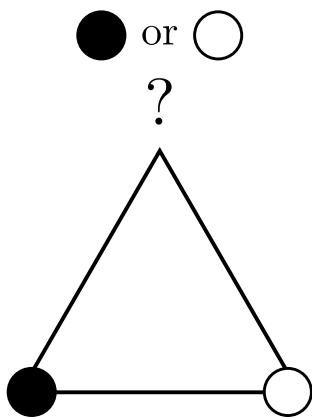


Figure 1.17: Illustration of charge frustration on a triangular lattice. One site is occupied (black circle), one is unoccupied (white circle) and the system is frustrated in the sense that it does not know whether to have the last site be occupied or unoccupied.

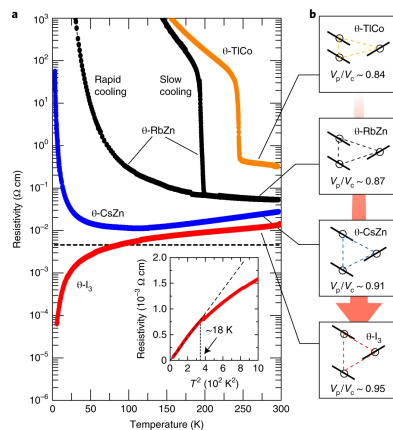


Figure 1.18: Left: The resistivity as a function of temperature for θ -TlCo (orange), θ -RbZn (black), θ -CsZn (blue) and θ -I₃ (red). The dashed line in the main panel indicates the level of the Mott–Ioffe–Regel limit estimated for these materials. The inset displays resistivity against T^2 for θ -I₃. Right: Systematic variation in the degree of charge frustration for the series of materials studied here. Reproduced from Ref. [59]

servation that only local potentials (Hubbard U terms) are not sufficient to explain the charge-ordered phases observed in these mostly quarter-filled materials. Quantum chemistry studies suggest that U , which is approximately 1eV, is the dominant energy scale (as to be expected). However, the ratio of intersite interaction to on-site interaction, V/U , has been estimated as 0.2-0.7, suggesting that long-range interactions are important [99–102]. Furthermore, the extended Hückel method places estimates for kinetic effects, t_{ij} , to be around 0.1-0.25 eV [95, 99, 102–105]. Overall, these energy scales qualify quasi-two-dimensional organics as strongly correlated materials with significant non-local interactions and we can conclude that proper treatment of these effects is necessary for understanding their exotic phases.

One particular phase of interest is the charge-ordered (CO) insulator observed at low temperatures in the $\theta - \text{ET}_2\text{X}$ family. This phase and its accompanying melting transition have attracted much theoretical interest over the past several decades. The CO transition is understood to be driven by charge frustration, which can be explained in the context of the filling and lattice geometry. These A_2B salts are typically three-quarters filled in terms of electrons (quarter-filled in terms of holes). If we consider a quarter-filled system, then we expect to find one particle per two sites on average. As a triangle has three sites, this filling translates to 1.5 particles every three sites. Therefore, the system must decide whether to have a particle or not on the third site of the triangular unit and is said to be frustrated. This geometrical charge frustration and the strong, long-range electronic correlation are responsible for the experimental observation of competing charge orders that eventually freeze into a CO insulating phase [59, 106]. This transition cannot be captured in theoretical models that do not account for the correlations and the intersite Coulomb interaction [99, 107–109]. Fig. 1.18 shows the temperature-resistivity profiles for four members of the θ - ET_2X family. Two materials (θ -CsZn, and θ -RbZn with rapid cooling) evolve into CO insulators at low temperatures. Interestingly, θ -TlCo, and θ -RbZn (with slow cooling) exhibit charge glass behavior at low temperatures, a direct consequence of the frustration arising from the non-local interactions and the lattice geometry [110].

More recently, attention has turned to understanding the bad metallic phases found near charge ordering in layered organics, specifically in the quarter-filled, non-dimerized $\theta - \text{ET}_2\text{X}$ systems [59]. The phase diagram for these materials includes charge-ordered insulators and novel charge glass states, which are the charge analogue of spin glass states. Interestingly, the degree of geometric frustration depends on the identity of the X anion, with the most frustrated case occurring for $\text{X}=\text{I}_3$. This system lacks a transition to a charge-ordered insulating state and instead exhibits bad metallic behavior with the resistivity exceeding the expected value at the MIR limit [59]. It is unclear the degree to which charge fluctuations from the charge glass play a role in this anomalous transport. Overall, the clean nature of these materi-

als hints at the importance of non-local interactions in the observed exotic phenomena and renders these materials an ideal foundation upon which to study strongly interacting physics beyond the Hubbard model.

1.4.3 Transition metal dichalcogenide heterostructures

Over the course of the last decade, twisted bilayer electronic systems have been the center of attention in many research groups. Strong correlation effects are also extremely important in these clean systems, which host a plethora of exotic phases. For example, the phase diagram of magic-angle twisted bilayer graphene presents regions of correlated insulating phases and unconventional superconducting phases [111]. While twisted bilayer graphene is arguably the most famous example of bilayer structures, more recently attention has shifted to understanding the strong correlation physics at play in transition metal dichalcogenide heterostructures [46].

Typically semi-conductors, transition metal dichalcogenides (TMDs) are two-dimensional materials that hold a lot of promise for various technological applications, such as solar cells, bio-sensors, and ultra small transistors [112]. The chemical formula for TMDs is of the form MX_2 , where M corresponds to a transition metal and X to a chalcogen, such as oxygen, sulfur, selenium, tellerium or polonium. The transition metal layer is sandwiched between two layers of chalcogen atoms in the crystal structure for monolayer TMD. The most commonly studied TMDs are molybdenum disulfide (MoS_2), molybdenum diselenide (MoSe_2), tungsten disulfide (WS_2), and tungsten diselenide (WSe_2) [112]. The two-dimensional TMD layers can be stacked upon each other, where the layers are held together with weak van der Waals forces. This structure is known as a van der Waals heterostructure and can provide unique function that is not otherwise observed in monolayer TMDs (see Fig. 1.19).

In particular, these materials can be combined and stacked to form Moiré superlattices. These systems have large unit cells and very narrow bandwidths which produce particularly strong correlation effects that in turn give rise to exotic phases. In particular, a recent study announced the discovery of a Mott insulating phase and generalized Wigner crystal phases at fractional filling in a van der Waals heterostructure constructed from WSe_2 and WS_2 [46]. The Mott insulating phase was discovered at a filling that corresponds to one hole per superlattice site ($n = 1$), while the proposed Wigner crystal phases were discovered at filling fractions $n = 1/3, 2/3$. A later study confirmed the presence of these correlated insulator phases and also provided evidence for more correlated insulating phases at different fractional fillings [45].

Wigner crystals are perhaps the most familiar phenomena arising from long-range interactions. These phases, originally predicted in

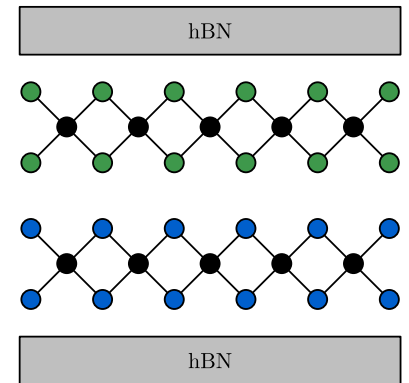


Figure 1.19: Diagram of a transition metal dichalcogenide heterostructure. The different colors indicate that the atomic identity can be different. The sandwiching substrate (gray) is typically hexagonal boron nitride.

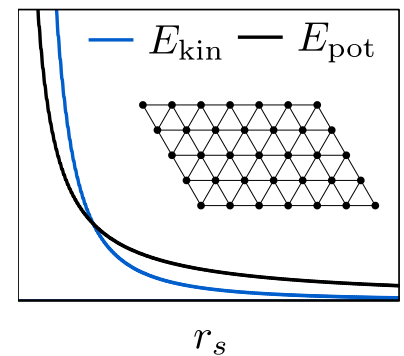
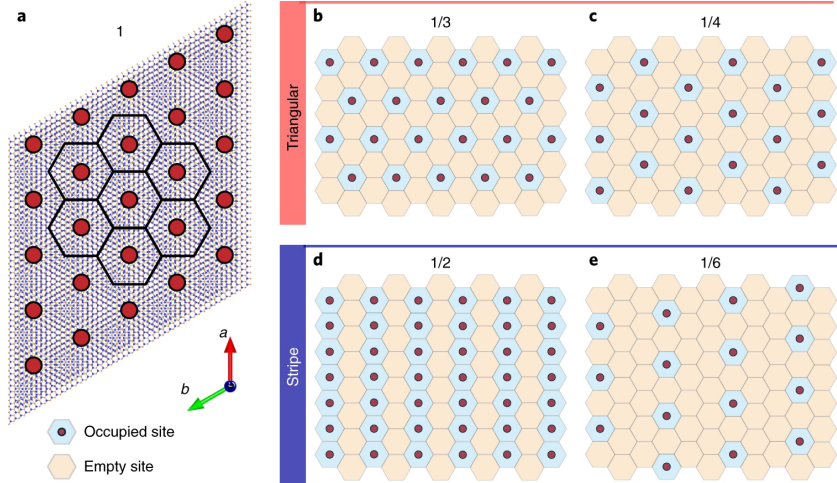


Figure 1.20: The Coulombic potential energy dominates at large r_s (low density), leading to an ordered phase. Calculations have predicted that the hexagonal phase has the minimal energy configuration in two-dimensions [113].

Figure 1.21: Left: Illustration of the moiré superlattice for the the WS_2/WSe_2 heterostructure with one carrier per moiré unit cell ($n = 1$). Top row: Patterns for the triangular Wigner crystal formed at fractional fillings of $n = 1/3$ and $1/4$. Bottom row: Patterns for the striped Wigner phase formed at fractional fillings of $n = 1/2$ and $1/6$. Reproduced from Ref. [120].



1934 [114] and discovered in liquid helium in 1979 [115], are formed by the domination of the Coulomb repulsion among electrons in comparison to their kinetic energy. Wigner argued that the potential energy scales as $1/r_s$ whereas the kinetic energy scales as $1/r_s^2$ in a low-density homogeneous electron gas where r_s is defined as the average interparticle spacing in units of the Bohr radius [116]. At sufficiently low densities, the Coulomb repulsion would therefore dominate and cause the electrons to crystallize into a minimum energy configuration (see Fig. 1.20). Originally predicted to occur in three-dimensional solids, experiments have thus far only observed Wigner crystal phases in lower-dimensional systems [115, 117], which is already a remarkable feat due to its fragile character. Additionally, there has been much theoretical discussion concerning the nature of the melting transition [118, 119].

Overall, the clean nature of TMD heterostructures (and potentially other bilayer systems [121, 122]) provides an ideal playground on which to explore these unanswered questions concerning long-range (Wigner) physics. A thorough investigation into the impact of long-range interactions on transport properties would be particularly of interest. The novel insulating phases discovered in Refs. [45, 46] point to the need for theoretical approaches capable of providing a controlled analysis of the impact of long-range interactions in correlated electronic systems.

1.4.4 Atomic, molecular and optical systems

Before concluding, we would like to briefly discuss the use of atomic, molecular, and optical (AMO) systems for simulating lattice Hamiltonians and how these systems could play a crucial role in unraveling the complicated correlation effects of long-range interactions. The AMO field has its foundations in the successful creation of a Bose-Einstein condensate in dilute atomic gases in 1995 [123]. Since then the field

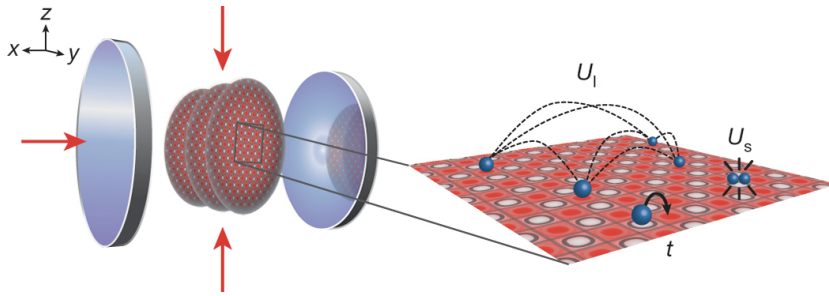


Figure 1.22: Illustration of the experimental scheme that realizes a lattice model with on-site and infinite-range interactions. A stack of two-dimensional systems along the y axis is exposed to a two-dimensional optical lattice in the $x - z$ plane (red arrows). Reproduced from Ref. [130].

has exploded and presently many experimental setups can be used to simulate quantum lattice models, including cold atomic gases, trapped ion arrays, Rydberg atom arrays, and optical lattices [124, 125]. These systems are highly tunable and as such can be tuned in a controllable manner from a regime with well-understood physics to a regime that remains a challenge for theoretical and numerical approaches. For example, the interaction strength, U/t , in optical lattices is controlled by the depth of the lattice potential and has been used to study the transition from a superfluid to a Mott insulator in the Bose-Hubbard model [126].

Bad metallic transport in the Hubbard model (i.e. without long-range interactions) has also recently been studied in optical lattice systems [127–129]. These studies have shown that the high-temperature behavior of the Hubbard model gives rise to a resistivity that grows linearly with temperature, crossing the MIR limit without any changes in slope or scaling behavior. However, studies of the optical conductivity are unable to explain the displaced Drude peak phenomenon previously discussed [80, 128].

Recently, experimental platforms have been constructed that can be used to study quantum systems with long-range interactions: Rydberg atoms, dipolar quantum gases, polar molecules, quantum gases coupled to optical cavities, and trapped ions. Trapped ion setups use lasers to confine ions into equilibrium configurations and have been used to study effective spin models with power-law type interactions, $|i - j|^{-\alpha}$, where the range can be tuned from $\alpha = 0$ to 3 [125]. For several years now, the Hubbard model has been studied by means of ultracold atomic gases [124, 131], but recently coupling to a cavity has emerged as a promising avenue with which to add long-range interactions into the systems under study [47, 130] (see Fig. 1.22). We hope that this provides the reader with a sampling of AMO methods uniquely situated to study long-range interacting lattice models. More details can be found in the recent review of Ref. [47].

Overall, the abundance of AMO platforms provides us with direct access to well-controlled studies of quantum lattice models. Not only are a number of setups capable of hosting long-range interactions, but the interaction strength and range can be tuned in these systems,

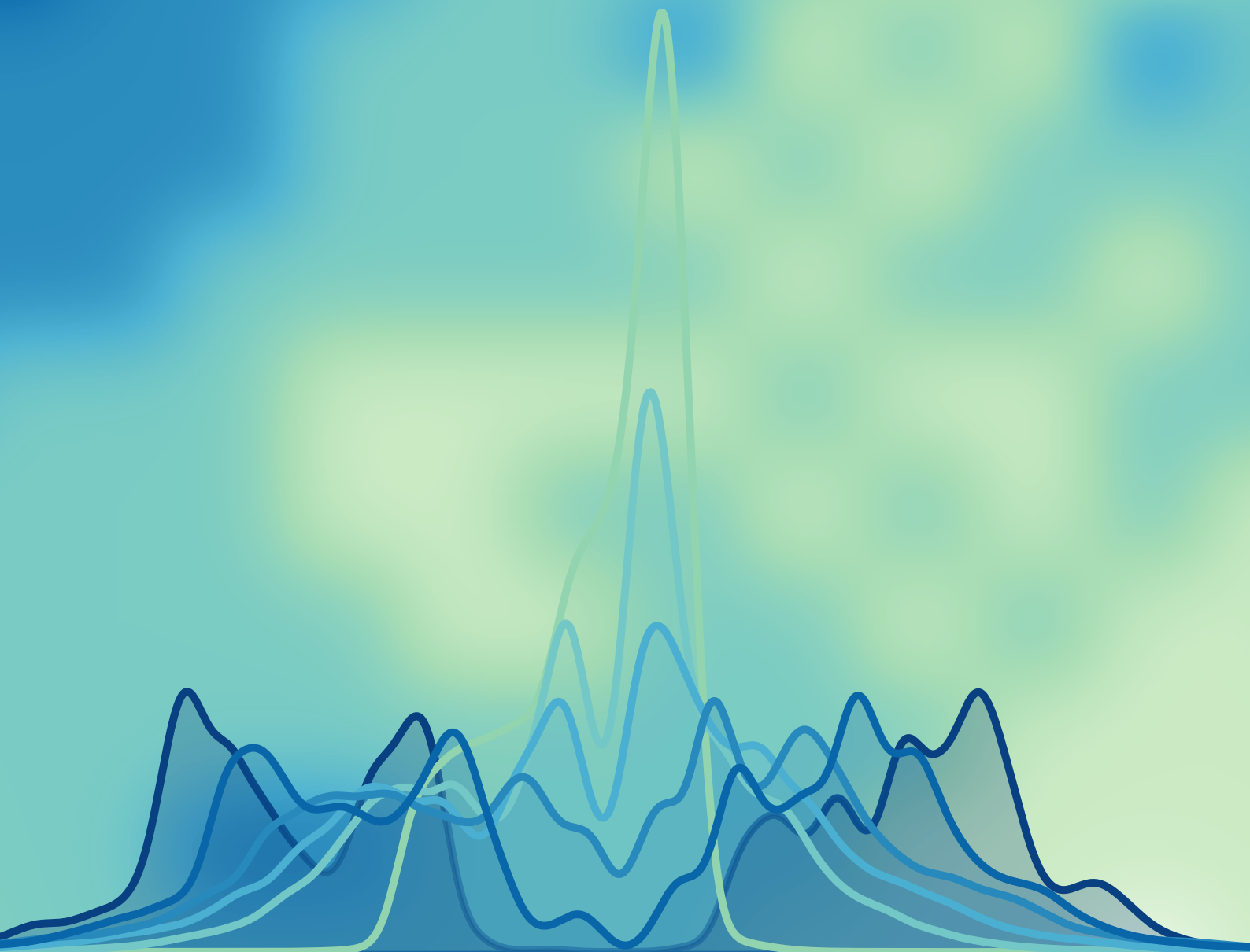
thereby opening the door to investigations focused on extricating the effect of these interactions in many-body physics [47]. This holds a lot of promise for many future studies, particularly those targeting the role of long-range interactions in bad metallic transport.

1.5 *Summary and perspectives*

In this chapter, we have presented a broad picture of the state-of-the-art in strongly correlated electronic materials. In particular, we have discussed the immense progress made in the theoretical description of these systems, which undoubtedly would not have been possible without the simultaneous development of cutting edge numerical techniques. Despite these advances, experimental observations of unexplained phenomena continue to challenge our perspectives and drive us to develop new theoretical ideas. A microscopic explanation for bad metallic behavior observed in numerous systems notably stands out as one such challenge.

This unconventional electronic transport manifests itself in materials with strikingly different characteristics, such as their chemical components and crystalline structure. Notwithstanding these physical differences, experimental observations for each system suggest that long-range electron interactions could play an important role in their expressions of strongly correlated behavior. However, effective lattice models typically neglect the effects of long-range interactions by implementing screening-based approximations that truncate the range of interactions. The fact that long-range interactions are consequential in terms of producing exotic correlated behavior *and* that they are often overlooked therefore sets the stage for the examination of the effect of long-range interactions in effective lattice models of strongly correlated materials in this dissertation. The following chapter will address technical details regarding the implementation of long-range interactions in numerical studies of quantum studies. Following this, we will discuss our results from an exact diagonalization study at zero temperature of a model of spinless electrons before proceeding to our finite-temperature results that examine their role in generating bad metallic transport.

Chapter 2: Exact Diagonalization



Chapter 2

Exact Diagonalization

2.1 Introduction

Over the course of the past century, effective lattice models and their underlying approximations have greatly advanced our understanding of a variety of electronic systems in condensed matter and solid-state physics. However, modern condensed matter focuses on the understanding of strongly correlated matter which cannot be solved analytically in many cases. This limitation has therefore spurred the development of advanced numerical techniques designed specifically to study these correlated systems, such as density matrix renormalization group [25–28], exact diagonalization [32, 33, 132], and quantum Monte Carlo [29–31].

As each numerical technique incurs its own set of limitations, one must appropriately choose which technique (or set of techniques) to apply to each individual problem. For example, quantum Monte Carlo excels in extracting finite-temperature properties of quantum systems in the thermodynamic limit but can be plagued by the so-called *sign problem* in which Hamiltonian matrix elements can be negative, rendering them incompatible with a probabilistic approach [133]. In our case, we are interested in understanding the effects of long-range interactions in low-dimensional quantum systems, which requires a versatile numerical technique to assess the interplay of these interactions with other parameters of the system, such as the presence of spin or geometrical structure of the lattice.

Exact diagonalization satisfies this requirement by granting complete control over the various microscopic degrees of freedom present in our models including (but not limited to) the lattice geometry, the form of interactions, the range of interactions, the presence of spin, and the temperature. First pioneered in Ref. [132] for numerical studies of correlated Hamiltonians, this approach also provides access to

a wide range of static and dynamical observables necessary to characterize the physics of long-range interacting systems, such as the Drude weight, D , and the single-particle spectral function, $A(\omega)$, which will both be discussed in greater detail in Chapter 3. With this extremely versatile technique, we can choose an appropriate basis in which to write the Hamiltonian as a matrix to be diagonalized. The eigenvalues and eigenvectors obtained from the diagonalization procedure can then be manipulated to provide relevant information about the system. The following sections shall address the theoretical and developmental/technical background of exact diagonalization and some specific details necessary for studies of strongly correlated systems, with a special focus on techniques that are useful in studies of long-range interacting models.

2.1.1 Basis representation

Let us begin by assuming that we have an arbitrary Hamiltonian, H , that defines the energetics of our system of interest with N sites. Before we can write H in the form of a matrix, we must first choose an appropriate basis of states, $\{|\phi\rangle\}$. The choice of basis is problem-dependent and as we are interested in studying a fermionic lattice model, we choose to define our basis in terms of the occupation number of sites in real space. The occupation number operator is defined as $\hat{n}_{i,\sigma}$ where $i \in 0, 1, \dots, N-1$ indexes the sites and σ indexes the spin sector (\uparrow or \downarrow) under consideration.

For example, let us suppose that we are interested in a model of spinless particles on a one-dimensional chain with $N = 10$ sites. As the particles are spinless, we can neglect the spin index, σ , and consider states $|\phi\rangle = |n_0 n_1 \dots n_{N-1}\rangle$. A generic state in this basis could then be numerically represented as a binary string:

$$|\phi\rangle = 0111010111 \quad (2.1)$$

where the i -th element of the string tells us whether or not site i is occupied (see Fig 2.1).

This binary string representation can also be readily adapted for spinful systems. Assuming that we are interested in spin-1/2 particles ($\sigma = \uparrow, \downarrow$), we can increase the length of the string from N to $2N$. The first N values in the bitstring are then defined as the occupation number representation of a fixed spin sector, $\sigma = \uparrow$ for example. Consequently, the second N values describe the occupation number representation of the other spin sector, $\sigma = \downarrow$. For example, the state $|\phi\rangle = |\uparrow, \downarrow, \uparrow, \downarrow, 0, \downarrow\rangle$ could be represented by

$$|\phi\rangle = \underbrace{101100}_{n_{i,\uparrow}} \underbrace{010101}_{n_{i,\downarrow}} \quad (2.2)$$

on a chain with $N = 6$ sites (see Fig. 2.2).

This particular representation is advantageous because each component of the binary string is a bit (0 or 1), which is the smallest unit

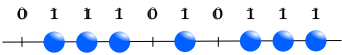


Figure 2.1: Example configuration of spinless particles, $|\phi\rangle$.

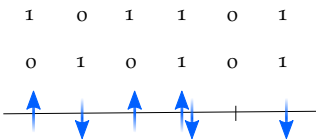


Figure 2.2: Example configuration of spinful particles, $|\phi\rangle$.

of information in computing. For convenient storage and access, we can furthermore think of each binary string as a representation of an integer. We can represent 2^N integers (from 0 to $2^N - 1$) by binary strings of a fixed length N . For example, for a spinless chain of $N = 3$, we can represent 8 integers with strings of length 3:

$$\begin{array}{ll} 000 = 0 & 100 = 4 \\ 001 = 1 & 101 = 5 \\ 010 = 2 & 110 = 6 \\ 011 = 3 & 111 = 7 \end{array}$$

where the integer value can be read off from the bit string as

$$I = \sum_{l=1}^N n_l 2^{l-1}. \quad (2.3)$$

The states and their respective integer representations are depicted in Fig. 2.3. Representing each state, or configuration, with a unique integer is extremely convenient for organization and storage purposes. Furthermore, being able to convert between integer representations and bit string representations is opportune because we can easily translate an integer into a configuration of bits, upon which we can perform certain manipulations (such as flips) in order to represent the actions of our operators on the states.

Armed with an appropriately-selected and advantageous basis representation, we may now proceed to constructing a Hamiltonian matrix. This matrix will have dimensions $N_{\mathcal{H}} \times N_{\mathcal{H}}$ where $N_{\mathcal{H}}$ is the size of the Hilbert space, or in other words, the number of states. The matrix elements will correspond to the values obtained from the various operations involved in the Hamiltonian. These values are model-dependent and we will only refer to them in an abstract sense so that the reader can develop a general understanding of the Hamiltonian matrix and its treatment during the diagonalization procedure. In particular, we would like to emphasize that operations that do not change the identity of a basis state will yield diagonal elements, while operations that transform one basis state into another will yield off-diagonal elements. Once the Hamiltonian matrix has been established, we may turn our attention to the numerical task of diagonalization, which is covered in the following sections.

2.1.2 Diagonalization and limitations

Linear algebra defines a square matrix, \mathbf{A} , to be diagonalizable if it is similar to a diagonal matrix. In other words, \mathbf{A} is diagonalizable if there exists an invertible square matrix, \mathbf{C} , and diagonal square matrix, \mathbf{D} , such that

$$\mathbf{A} = \mathbf{C}\mathbf{D}\mathbf{C}^{-1} \quad (2.4)$$

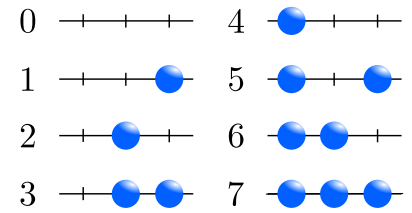


Figure 2.3: Example of integer representation of spinless particles.

A note on convention: the value n_l is the value of the l -th bit, where the bits are ordered from right to left.

$$\begin{pmatrix} A & B & & B \\ & A & B & \\ B & & A & B \\ & B & & A & B \\ B & & B & A & A \end{pmatrix} \begin{array}{l} \text{diagonal :} \\ \hat{A}|\phi\rangle \rightarrow A|\phi\rangle \\ \text{off - diagonal :} \\ \hat{B}|\phi\rangle \rightarrow B|\phi'\rangle \end{array}$$

Figure 2.4: Illustration of Hamiltonian matrix. Diagonal elements (blue) do not change the state $|\phi\rangle$, while off-diagonal elements (green) do.

where all matrices have dimension $n \times n$. Diagonalizable matrices can be written in terms of their eigenvalues, $\{\lambda_i\}$, and eigenvectors, $\{\mathbf{v}\}$, as

$$\mathbf{A}\mathbf{v} = \lambda\mathbf{v}.$$

A Hermitian matrix is a complex, square matrix that is equal to its conjugate transpose, $A = A^\dagger$.

As the Hamiltonian is Hermitian, we are interested in the special case of the eigendecomposition of complex, Hermitian matrices. The spectral theorem states that

- (a) all Hermitian matrices are diagonalizable,
- (b) all eigenvalues are real,
- (c) and the eigenvectors corresponding to different eigenvalues are orthogonal.

For more information about numerical methods of linear algebra, please refer to Refs. [134, 135].

We are generally interested in solving for the eigenvalues and eigenvectors of a Hamiltonian matrix,

$$\mathbf{H}\mathbf{v} = \lambda\mathbf{v}, \tag{2.5}$$

because the eigenvectors constitute an orthogonal basis of the Hilbert space and can be used to easily extract relevant information about the system of interest. If we rearrange the eigendecomposition of the Hamiltonian matrix, we obtain

$$(\mathbf{H} - \lambda\mathbb{1})\mathbf{v} = 0, \tag{2.6}$$

The expression $P(\lambda) = \det(\mathbf{H} - \lambda\mathbb{1})$ is called the characteristic polynomial.

where $\mathbb{1}$ is the identity matrix of the same dimensions as \mathbf{H} . This implies that $\det(\mathbf{H} - \lambda\mathbb{1}) = 0$ and provides us with a method to obtain all of the eigenvalues of \mathbf{H} : solving for the roots of the characteristic equation. The roots (eigenvalues) can then be re-inserted into the characteristic equation to solve for the eigenvectors. Unfortunately, solving for the roots of this highly non-linear equation is only practical for extremely small system sizes.

The Hilbert space of a quantum lattice model scales with the number of sites, typically as n_{dof}^N where n_{dof} is the number of degrees of freedom on a given site and N is the total number of sites in the lattice. For example, spinless particle systems scale as 2^N and spinful systems scale as 4^N . This exponential growth of the Hilbert space with the number of sites is demonstrated in the left panel of Fig. 2.5. Not only does a large Hilbert space result in a progressively more complicated non-linear characteristic equation, but it also guarantees that one will very quickly hit the memory limits of modern computers.

This concept is also illustrated in the right panel of Fig. 2.5, where a rough estimate for the memory requirements for the Hamiltonian are plotted as a function of N . These estimations for the memory have assumed that the Hamiltonian is stored as a dense matrix using a complex data type with 128 bits where the real and imaginary parts are each represented by a double-precision float. The gray line indicates a reasonable amount of memory (256GB) available on modern

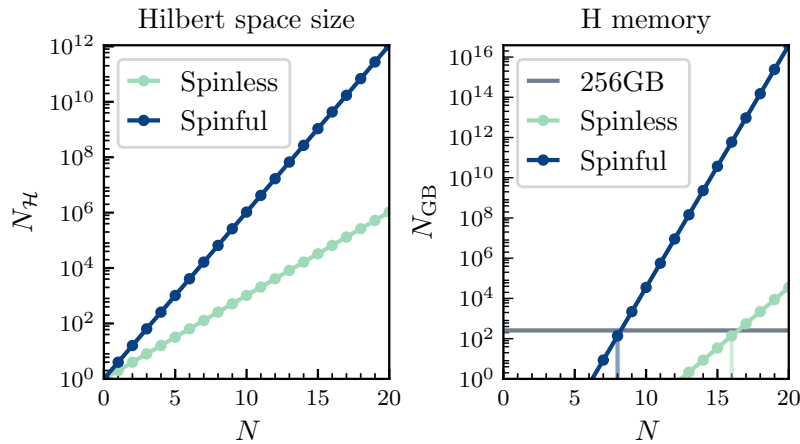


Figure 2.5: *Left*: Exponential growth of the Hilbert space size, $N_{\mathcal{H}}$, with the number of sites, N . *Right*: Memory required (in gigabytes) to store the Hamiltonian corresponding to the number of sites, N . Both plots display results for spinless (light green lines) and spinful (dark blue lines) systems.

computing clusters. We quickly realize that naïve implementations of an exact diagonalization code will restrict calculations to systems of $N \lesssim 16$ for spinless systems and $N \lesssim 8$ for spinful systems. These sizes are typically too small to justify that one has reached the thermodynamic limit and different approaches must be explored to overcome these limitations of exact diagonalization.

The next two sections include a discussion on the two main avenues for lightening the computational workload:

1. Efficient implementation of variables and algorithms (sparse matrix format, Lanczos diagonalization).
2. Reduction of the Hilbert space motivated by physical intuition (restriction to fixed particle or spin sector, use of translational and point-group symmetries).

The first section will highlight relevant technical points in the development of an exact diagonalization code, while the second will focus on using physical understanding to maximize our success on these finite-sized systems. Following these two sections, we will proceed to discuss two more techniques (twisted boundary conditions and Ewald summation) that are crucial to obtaining model-specific accurate results from finite-size calculations, particularly for our long-ranged interacting model of interest which will be discussed in detail in Chapter 3.

2.2 *Efficient implementation*

For the sake of simplicity, let us assume that we are interested in studying a spinless lattice system with N sites that is described by a Hamiltonian with an off-diagonal (kinetic) term that scales with N and the lattice coordination (z), and with a diagonal (interaction) term that

For reference, the standard complex data type in Python, `numpy.complex128`, occupies 128 bits of memory.

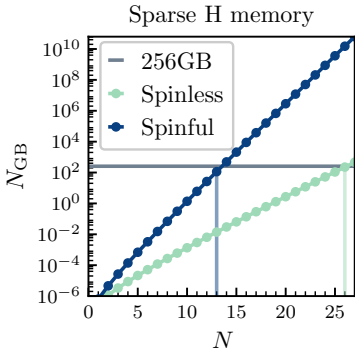


Figure 2.6: Memory requirements for storage of sparse Hamiltonian.

The QR algorithm returns all eigenpairs (eigenvalues and eigenvectors) of a general dense matrix, A , by performing a so-called QR decomposition, $A = QR$, into an orthogonal matrix, Q , and an upper triangular matrix, R , [134].

scales with N . The Hilbert space is described by a basis of $N_{\mathcal{H}}$ orthonormal states; therefore, the Hamiltonian matrix will have dimensions $N_{\mathcal{H}} \times N_{\mathcal{H}}$. We shall work under the assumption that the operators are complex and Hermitian, which requires us to store the Hamiltonian matrix elements as memory-intensive, complex data types.

In order to reduce the memory load, we are obliged to find a resourceful method to store the Hamiltonian. Upon inspection of the terms of the Hamiltonian, we observe that the matrix is sparse which means that most of its components are zero. In other words, a state in the Hilbert space is only connected to a finite number of other states via the operators present in the Hamiltonian. The diagonal term leaves a state unchanged,

$$\langle \phi_j | \hat{O}_{\text{diag}} | \phi_i \rangle = O_{ij} \delta_{ij}, \quad \text{where } \delta_{ij} = 0 \text{ if } i \neq j$$

where \hat{O}_{diag} is the operator and O_{ij} is the expectation value of \hat{O}_{diag} on $|\phi\rangle$. Therefore, we cannot improve the storage of the $N_{\mathcal{H}}$ diagonal matrix elements.

However, the operators in the off-diagonal term act on a state, $|\phi\rangle$, and transform it into another state,

$$\langle \phi_j | \hat{O}_{\text{off-diag}} | \phi_i \rangle = O_{ij} \delta_{ij}, \quad \text{where } \delta_{ij} = 0 \text{ if } |\phi_j\rangle \neq \hat{O}_{\text{off-diag}} | \phi_i \rangle$$

From the scaling information of the off-diagonal operators, we realize that the number of non-zero off-diagonal elements is $N_{\text{off-diag}} \sim N_{\mathcal{H}} \times N \times z$. As a result, the Hamiltonian matrix can be stored in sparse matrix format, with a reduction of stored components from $N_{\mathcal{H}} \times N_{\mathcal{H}}$ to $N_{\mathcal{H}}(1 + zN)$.

As we see from Fig. 2.6, utilizing a sparse storage implementation of the Hamiltonian increases the limiting size from $N = 16$ to $N = 26$ for spinless systems and from $N = 8$ to $N = 13$ for spinful systems. The limiting size can further be increased by computing matrix elements *on the fly* or by using distributed memory architectures. However, these approaches will not be discussed here as we chose to focus our efforts on the implementation of twisted boundary conditions and the Ewald summation, which will both be discussed in the later half of this chapter. Instead, we will move to a discussion of the Lanczos algorithm, an efficient diagonalization routines for Hermitian matrices.

2.2.1 Lanczos algorithm

While certain algorithms can solve for all eigenpairs (eigenvalues and eigenvectors) of a matrix, such as the QR algorithm, we are typically not interested in *all* of the eigenpairs of a system in condensed matter physics [134]. Instead, we are usually only interested in solving for the ground state wave vector and its associated (ground state) energy. Already with one eigenpair we will be able to extract valuable information about the ground state of a system at zero temperature. If we are interested in understanding excitations or finite temperature

properties, then we will need to solve for more eigenpairs but for the moment we shall only focus on solving for the lowest extremal eigenpair (the ground state).

In particular, we shall focus on the Lanczos algorithm, named after Cornelius Lanczos who developed it in 1950 [136]. The following discussion and derivation of the Lanczos algorithm is based in a large part upon summer school notes found in Refs. [137, 138] and is intended as a gentle introduction for the Lanczos novice. This algorithm is derived from another family of numerical diagonalization algorithms, known as power methods [134]. The main idea of the Lanczos algorithm is to construct an effective basis, the *Krylov basis*, from which we can build a tri-diagonal matrix whose low-lying eigenvalues approach those of the full Hamiltonian matrix. This entire algorithm relies on a series of various linear algebra operations, such as matrix multiplication and addition. To handle these operations easily and efficiently, we will make use of external linear algebra libraries: *Armadillo* for C++ codes, and *NumPy* and *SciPy* for Python codes.

The first step of the algorithm involves building an initial vector, $|\tilde{x}_0\rangle$, whose components are selected from a random distribution. The length of $|\tilde{x}_0\rangle$ should be equal to the number of states in our basis, $N_{\mathcal{H}}$, which is also the dimension of our Hamiltonian matrix, $N_{\mathcal{H}} \times N_{\mathcal{H}}$. This vector is normalized as

$$|x_0\rangle = \frac{|\tilde{x}_0\rangle}{\|x_0\|} \quad (2.7)$$

and we may proceed the next steps, which add new vectors to the Krylov basis. The following step is to compute the expected energy of the normalized, initial vector, $|x_0\rangle$, as

$$\varepsilon_0 = \langle x_0 | \hat{H} | x_0 \rangle. \quad (2.8)$$

where \hat{H} is the Hamiltonian describing our system of interest. The computation of the energy is a process that will be repeated throughout the algorithm and the energy, ε_i , must be stored at each step. Now we can turn our attention to adding the next vector to the basis \mathcal{K} :

$$|\tilde{x}_1\rangle = \hat{H} |x_0\rangle - \varepsilon_0 |x_0\rangle. \quad (2.9)$$

This particular definition is chosen to ensure that an orthogonal basis is being constructed. However, it is recommended to continue to use the Gram-Schmidt orthogonalization procedure at every step to prevent numerical errors and improve the stability of the algorithm. This vector should also be normalized accordingly,

$$|x_1\rangle = \frac{|\tilde{x}_1\rangle}{\|\tilde{x}_1\|}. \quad (2.10)$$

From Eq. (2.8), we can see that $|x_1\rangle$ should be orthogonal to $|x_0\rangle$. We can again define the expected energy for this new vector as $\varepsilon_1 = \langle x_1 | \hat{H} | x_1 \rangle$ and store its value for use in future steps. At this point, we

We will denote the Krylov basis with the symbol \mathcal{K} .

[Armadillo documentation](#)

[NumPy documentation](#)

[SciPy documentation](#)

The notation $|\tilde{x}_i\rangle$ signifies that a vector is not normalized.

The interested reader can find a more details on the Gram-Schmidt orthogonalization in Appendix A.

Orthogonality of $|x_0\rangle, |\tilde{x}_1\rangle$:

$$\begin{aligned} \langle x_0 | \tilde{x}_1 \rangle &= \langle x_0 | \hat{H} | x_0 \rangle - \varepsilon_0 \langle x_0 | x_0 \rangle \\ &= \varepsilon_0 - \varepsilon_0 = 0 \end{aligned}$$

have two vectors, $\mathcal{K} = \{|x_0\rangle, |x_1\rangle\}$. These can be used to build the next vector in the basis, $|\tilde{x}_2\rangle$, which is defined as

$$|\tilde{x}_2\rangle = \hat{H}|x_1\rangle - \varepsilon_1|x_1\rangle - k_1|x_0\rangle, \quad (2.11)$$

where k_1 is chosen to be

$$k_1 = \langle x_0|\hat{H}|x_1\rangle \quad (2.12)$$

Orthogonality of $|x_0\rangle, |x_1\rangle, |\tilde{x}_2\rangle$:

$$\begin{aligned} \langle x_1|\tilde{x}_2\rangle &= \langle x_1|\hat{H}|x_1\rangle - \langle x_1|\varepsilon_1|x_1\rangle \\ &\quad - \langle x_1|k_1|x_0\rangle \\ &= \varepsilon_1 - \varepsilon_1 - k_1 \langle x_1|x_0\rangle \\ &= 0 \end{aligned}$$

$$\begin{aligned} \langle x_0|x_2\rangle &= \langle x_0|\hat{H}|x_1\rangle - \langle x_0|\varepsilon_1|x_1\rangle \\ &\quad - \langle x_0|k_1|x_0\rangle \\ &= k_1 - \varepsilon_1 \langle x_0|x_1\rangle - k_1 \langle x_0|x_0\rangle \\ &= 0 \end{aligned}$$

in order to guarantee that $|\tilde{x}_2\rangle$ is orthogonal to $|x_1\rangle$ and $|x_0\rangle$. We can also see that k_1 is simply the norm of $|\tilde{x}_1\rangle$ by recalling from Eq. (2.9) that $|\tilde{x}_1\rangle = \hat{H}|x_0\rangle - \varepsilon_0|x_0\rangle$. If we rearrange for $\hat{H}|x_0\rangle$ and then take the complex conjugate, then we obtain $\langle \tilde{x}_1| + \varepsilon_0 \langle x_0|$, which we can insert into the expression for k_1 ,

$$\begin{aligned} k_1 &= \langle x_0|\hat{H}|x_1\rangle \quad (2.13) \\ &= \langle \tilde{x}_1|x_1\rangle + \langle x_0|\varepsilon_0|x_1\rangle \\ &= \|\tilde{x}_1\| \end{aligned}$$

where we have used Eq. (2.10) and the orthogonality of $|x_0\rangle$ and $|x_1\rangle$. In addition to ε_i , we will also need to keep track of these normalization values, k_i , at each step. Now with the ε_i and k_i computed in the previous steps, we can build the vector $|\tilde{x}_2\rangle$, defined in Eq. (2.11), and its associated energy expectation value, ε_2 , and normalization constant, k_2 . From this point forward, the iterative structure of the Lanczos algorithm becomes apparent and we can continue iterating to form an orthonormal basis of our Krylov vectors. The scheme is as follows:

$$|\tilde{x}_{n+1}\rangle = \hat{H}|x_n\rangle - \varepsilon_n|x_n\rangle - k_n|x_{n-1}\rangle \quad (2.14)$$

$$\varepsilon_n = \langle x_n|\hat{H}|x_n\rangle \quad (2.15)$$

$$k_n = \langle x_{n-1}|\hat{H}|x_n\rangle = \|\tilde{x}_n\| \quad (2.16)$$

$$|x_{n+1}\rangle = \frac{|\tilde{x}_{n+1}\rangle}{\|\tilde{x}_{n+1}\|} \quad (2.17)$$

In a manner similar to the orthogonality condition proved above, we can demonstrate that each new vector, $|\tilde{x}_{n+1}\rangle$, is orthogonal to all the others in the Krylov basis.

$$\begin{aligned} \langle x_n|\tilde{x}_{n+1}\rangle &= \langle x_n|\hat{H}|x_n\rangle - \varepsilon_n \langle x_n|x_n\rangle - k_n \langle x_n|x_{n-1}\rangle \quad (2.18) \\ &= \varepsilon_n - \varepsilon_n - 0 = 0. \end{aligned}$$

$$\begin{aligned} \langle x_{n-1}|\tilde{x}_{n+1}\rangle &= \langle x_{n-1}|\hat{H}|x_n\rangle - \varepsilon_n \langle x_{n-1}|x_n\rangle - k_n \langle x_{n-1}|x_{n-1}\rangle \quad (2.19) \\ &= k_n - 0 - k_n = 0. \end{aligned}$$

Thus, for any $i = 1, \dots, n-2$ we realize that the overlap between $|x_i\rangle$ and any vector $|\tilde{x}_{n+1}\rangle$ is

$$\langle x_i|\tilde{x}_{n+1}\rangle = \langle x_i|\hat{H}|x_n\rangle - \varepsilon_n \langle x_i|x_n\rangle - k_n \langle x_i|x_{n-1}\rangle = \langle x_i|\hat{H}|x_n\rangle. \quad (2.20)$$

Because of the Hermitian nature of \hat{H} , we see that

$$\begin{aligned} \langle x_i | \hat{H} | x_n \rangle &= \left(\langle x_n | \hat{H} | x_i \rangle \right)^* \\ &= \left(\langle x_n | (|\tilde{x}_{i+1}\rangle + \varepsilon_i |x_i\rangle + k_i |x_{i-1}\rangle) \right)^* \\ &= 0. \end{aligned} \quad (2.21)$$

In other words, the matrix elements of the Hamiltonian computed in the Krylov basis, \mathcal{K} , are zero if the difference in indices (iteration numbers) is greater than 2:

$$H_{n,i}^{\mathcal{K}} = H_{i,n}^{\mathcal{K}} = 0 \quad \text{if } |i - n| > 2. \quad (2.22)$$

Therefore, $H^{\mathcal{K}}$ possesses a tridiagonal structure, populated with the energy expectation value for each vector $|x_i\rangle$ and the overlap between neighboring vectors, $k_i = \langle x_{i-1} | \hat{H} | x_i \rangle$ and $k_{i+1} = \langle x_i | \hat{H} | x_{i+1} \rangle$. Here is an example of the structure after $n = 4$ iterations:

$$H_{n=4}^{\mathcal{K}} = \begin{pmatrix} \varepsilon_0 & k_1 & 0 & \cdot & \cdot \\ k_1 & \varepsilon_1 & k_2 & 0 & \cdot \\ 0 & k_2 & \varepsilon_2 & k_3 & 0 \\ \cdot & 0 & k_3 & \varepsilon_3 & k_4 \\ \cdot & \cdot & 0 & k_4 & \varepsilon_4 \end{pmatrix}.$$

As the algorithm proceeds, $H^{\mathcal{K}}$ will have dimensions that correspond to the number of Lanczos iterations, L , which is typically much smaller than the number of states in the basis. At each step n , we can diagonalize $H^{\mathcal{K}}$ to obtain its ground state eigenvalue, E_0^n , and check its convergence with respect to the eigenvalue obtained from the previous iteration, E_0^{n-1} .

Once the desired convergence has been reached, the eigenvalues returned from the diagonalization of the tri-diagonal matrix in the last iteration are a very good approximation to the true eigenvalues of the large Hamiltonian matrix that we are unable to fully diagonalize via brute-force methods. The iterative Lanczos scheme converges to the extremal (maximal or minimal) eigenpairs quickly. Figure 2.7 illustrates how the low-lying eigenvalues converge quickly with the number of iterations. As the number of iterations increases and approaches the size of the Hilbert space, $N_{\mathcal{H}}$, the spectrum converges to that of the exact, full spectrum.

Obtaining the lowest-lying eigenvalues is already quite an achievement and we can learn a lot of information about the system simply in terms of these eigenvalues. For instance, we can study how the value of the energy per particle changes as a function of a given parameter, such as the strength of electronic interactions. Similarly, we can examine the degeneracy of the ground state(s) and determine the internal energy gap, $\Delta = E_0 - E_1$, where E_0 is the energy of the ground state(s) and E_1 is the energy of the lowest-lying excited state. This quantity can be used to characterize the ground state as metallic or insulating.

We will denote the Hamiltonian projected onto the Krylov basis as $H_n^{\mathcal{K}}$, where n indicates the iteration number.

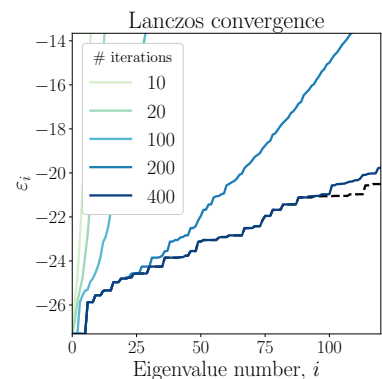


Figure 2.7: Convergence of eigenvalue spectrum to exact (dashed, black) with increasing number of iterations for long-range interacting model of spinless electrons, the specific details of which will be discussed in Chapter 3.

In addition to extracting information from the eigenvalues, we will also want to extract information from the eigenvectors returned from diagonalizing the tri-diagonal matrix in the last iteration. We can use these eigenvectors as a good approximation to the eigenvectors of the original Hamiltonian matrix, $|\Psi_v\rangle$, via the following construction

$$|\Psi_v\rangle = \sum_{i=1}^L c_i^v |x_i\rangle, \quad (2.23)$$

where $\{|x_i\rangle\}$ are the Krylov vectors created at each iteration and the number of iterations reached is L . The c_i^v are the components of the eigenvectors obtained from the diagonalization of the tri-diagonal matrix. If we are interested in accessing eigenpairs corresponding to excited states, then the convergence criterion will need to be modified appropriately.

For more information about computing specific observables, especially dynamic quantities, please refer to Refs. [137,139].

In this section we have discussed many technical details regarding the diagonalization of large, Hermitian matrices. By recognizing that our Hamiltonian matrix is sparse, we can immediately identify more efficient storage methods. Furthermore, we can turn to specialized algorithms that are capable of efficiently diagonalizing sparse, Hermitian matrices. In our work in particular, we have implemented the Lanczos algorithm in order to increase the sizes of systems accessible via the exact diagonalization technique. In addition to the application of the Lanczos algorithm, we also employ symmetries in order to increase the finite-size limits. This topic will be covered in the following section and then we will conclude with a discussion of other numerical methods designed to improve treatment of strongly correlated systems.

2.3 Symmetries

At the end of Sec. 2.1.2, we stated that we can use two main approaches to lighten the computational workload of an exact diagonalization code and to increase the size of systems to be studied. The first approach, discussed in Sec. 2.2, relies on optimizing various choices involved in the numerics, including the storage representations and the diagonalization algorithm. This present section will discuss the second approach, which relies on the use of symmetries to reduce the size of the Hilbert space in an effort to further streamline calculations [140–142].

The interested reader is invited to learn more about the applications of group theory to modern condensed matter physics in Ref. [143].

The Hamiltonians that describe most, if not all, modern condensed matter physics systems possess inherent symmetries. Formally, we can define a symmetry transformation as the effect of a unitary operator, U , and we say that the Hamiltonian is invariant under that action if U commutes with the Hamiltonian,

A unitary operator satisfies $UU^\dagger = U^\dagger U = \mathbf{1}$.

$$[H, U] = HU - UH = 0. \quad (2.24)$$

The operators that leave the Hamiltonian invariant under their operations give rise to good quantum numbers. A simple example of this is the total particle number operator, \hat{N} , which can be used to define the average filling of the system. For example, if one considers the Hubbard model (introduced in Chapter 1), it is straightforward to see that \hat{N} should commute with the Hamiltonian.

We can use these symmetry transformations to our advantage to write a symmetrized basis such that the Hamiltonian matrix is transformed to a block diagonal structure. The dimensions of each block will necessarily be smaller than those of the untransformed matrix by a factor approximately equal to the number of symmetries present, \mathcal{N}_s . The diagonalization of each smaller block will be much easier and faster than the diagonalization of the original, non-symmetrized matrix. Furthermore, each block will provide insight into the physics of that particular symmetry sector, which might not have otherwise been evident from diagonalization of the entire (non-reduced) Hamiltonian.

In the simple case of reduction based on fixed particle number, we can restrict our calculation to a specific particle number sector that is of interest. To better understand the benefits of this simple reduction, let us assume that we are interested in studying a spinful electronic system and calculate the necessary basis size. For L sites in a given lattice, the size of the Hilbert space grows exponentially as 4^L and diagonalization of matrices of this size quickly becomes intractable. However, if we introduce a simple assumption, such as a restriction of the density to the half-filled case, $n = 1.0$, then we can reduce the number of states in our computational basis. This specific example would reduce the size of the Hilbert space to $2L!/(L!)^2$.

L sites	Full basis	Reduced basis
4	256	70
6	4096	924
8	65,536	12,870
10	1,048,576	184,756
12	16,777,216	2,704,156

Block diagonalizing the Hamiltonian by fixing the particle number (or density) sector already yields a useful reduction of dimensions. However, one can typically reduce further by utilizing the inherent symmetries of the underlying lattice. In the following discussion, we shall develop more formally the use of translation and point group symmetries to build a symmetrized basis for the Hamiltonian of interest.

2.3.1 Implementation

We begin with a few useful definitions from group theory. In our case, we will consider a group composed of various symmetry operations, such as rotations, reflections and inversions. For example, if we

The total particle number \hat{N} is defined as $\sum_{i\sigma} \hat{c}_{i\sigma}^\dagger \hat{c}_{i\sigma}$ for spinful systems and as $\sum_i \hat{c}_i^\dagger \hat{c}_i$ for spinless systems.

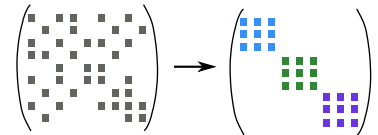


Figure 2.8: Illustration of transformation of a sparse matrix to a sparse, block-diagonal matrix where colors distinguish different symmetry sectors. For example, blue corresponds to states with $N = 1$, green to $N = 2$, and purple to $N = 3$, where N is the number of particles.

We define the filling as the number of particles per site, $n = N/L$.

Table 2.1: Dimensions of the Hamiltonian matrix for systems of L sites. The restriction to half-filling reduces the dimension of the matrix to be diagonalized by a factor $\sim L$.

A mathematical group is a collection of elements that:

1. contains an identity element, E
2. contains an inverse for each element
3. obeys the associative law, $(AB)C = A(BC)$
4. returns another element of the group if two elements are multiplied together.

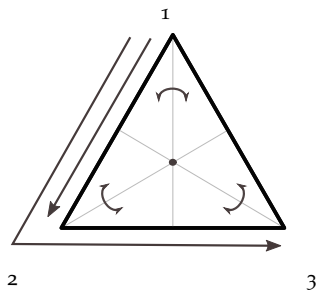


Figure 2.9: The 6 different symmetry operations are: E (identity), two rotations by $\pi/3$ and $2\pi/3$, and three reflections about the gray lines stemming from each vertex.

The representations are not unique because they can undergo a similarity transformation, $UM(A)U^{-1}$, which changes the matrices but not the trace (sum of the diagonal elements).

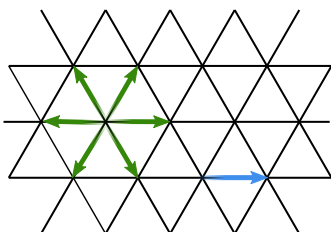


Figure 2.10: Illustration of point group and translation symmetries in isotropic triangular lattice. Rotations by $\theta = \pi/3$ are illustrated by green arrows and a translation by one lattice spacing is represented by a blue arrow.

consider the group of symmetry operations possible on an equilateral triangle (Fig. 2.9), then it is straightforward to see that this group has 6 elements. While visualizing one individual operation is simple, visualizing repeated operations rapidly becomes cumbersome. Furthermore, the visual consideration of composite symmetry operations on more complicated geometrical objects (such as two-dimensional lattices) is extremely inconvenient. However, this inconvenience can instead be overcome with the use of matrix representations for symmetry operations.

Matrix representations represent each symmetry operation by a matrix such that the products of the matrices behaves as the product of the operations does:

$$M(AB) = M(A)M(B). \tag{2.25}$$

Here, $M(A)$ signifies the matrix representation of the symmetry operation A . These matrix representations (and their ensuing linear algebra operations) are much easier to work with in terms of analytical and numerical calculations. For example, the matrix representation of the rotation of a triangle by $2\pi/3$ (see Fig. 2.9) in terms of Cartesian coordinates is:

$$\begin{pmatrix} -1/2 & -\sqrt{3}/2 & 0 \\ \sqrt{3}/2 & -1/2 & 0 \\ 0 & 0 & 1 \end{pmatrix}. \tag{2.26}$$

However, these matrix representations are typically not unique. Therefore, in order to effectively work with the matrix representations of the symmetries in our system, we will need to use the characters, or the traces of the matrices, as these will remain invariant under transformation. We can also overcome the ambiguity of the matrix representations by working with irreducible representations of the symmetry elements. An irreducible representation signifies that a given matrix representation of a symmetry group cannot be written in terms of a matrix with lower dimensionality. Irreducible representations are important from a physical point of view because they describe the transformation properties of a set of eigenfunctions and correspond to distinct energy eigenvalue [143].

For the sake of clarity in the subsequent discussion, let us establish that we are interested in taking advantage of the translation and point group symmetries of two-dimensional lattices to build a symmetrized basis for a general Hamiltonian. We shall also assume that the system has periodic boundary conditions. The following ideas can be generalized for systems of different dimensionality. We shall use the terms *representation of a symmetry group* and *symmetry sector* interchangeably. Let us assume that we have a symmetry group,

$$G = G_T \otimes G_{PG}, \tag{2.27}$$

which is composed of the groups of translation and point group symmetry operations, respectively. G has $N_s = N_T + N_{PG}$ unique ele-

ments, where N_T and N_{PG} are the number of translation and point group symmetries, respectively.

Each symmetry sector, ℓ , corresponds to an irreducible representation of the symmetry group and can be labeled with a quantum number, n_ℓ . If we only consider $G = G_T$, then this quantum number would simply be the momentum,

$$\mathbf{k} = n_0 \mathbf{k}_0 + n_1 \mathbf{k}_1, \quad (2.28)$$

where \mathbf{k}_i are the two-dimensional reciprocal lattice vectors and n_i are integers. In the general case $G = G_T \cup G_{PG}$, we must restrict ourselves to the subgroup $G_{PG}^{\mathbf{k}} \subset G_{PG}$ containing symmetry operations that leave the momentum invariant,

$$g_{PG}(\mathbf{k}) = \mathbf{k}. \quad (2.29)$$

This concept is illustrated in Fig. 2.11. We can proceed to write the quantum number labeling a particular symmetry sector in the general form as $n_\ell = (\mathbf{k}, \tau_{\mathbf{k}})$, where $\tau_{\mathbf{k}}$ is one of the irreducible representations of the constrained point group, $G_{PG}^{\mathbf{k}}$.

The central idea of using symmetries to ease the computational burden is not to find the matrix representing the unitary transformation of the Hamiltonian into a symmetrized, block-diagonal matrix. Rather, we want to use the symmetry group G to construct a compact, symmetrized basis of states in which each smaller, block-diagonal matrix can be written. In the case of the particle number operator earlier, the choice of states was straightforward as each block contained only states with a fixed number of particles (recall Fig. 2.8).

In the present case, we divide the full basis into subsets of states that are equivalent under repeated application of the same symmetry operation in G . In other words, a state $|r_i\rangle$ in a given subset, \mathcal{R}_i , can be used to create all the other states $\{|r'\rangle\} \in \mathcal{R}_i$ via repeated applications of the same symmetry operation, \hat{g}_i . This original state, $|r_i\rangle$, is referred to as the *parent* or *representative* (see Fig. 2.12). Consequently, each subset can be represented by a representative (parent) state, which implies that the number of subsets is equal to the number of parents, $N_{\mathcal{R}}$. The choice of parent among the configurations of a given subset is arbitrary, but we utilize the convention that the configuration represented by the smallest integer (when converted from a bit string) is the parent.

We no longer need to retain the entire basis as the set of representatives, \mathcal{R} , can be used in conjunction with G to represent the other configurations. We can construct general states from linear combinations of the parents,

$$|\phi\rangle = \sum_{i=1}^{N_{\mathcal{R}}} c_i |r_i\rangle, \quad (2.30)$$

but we will need to properly symmetrize them in order to represent wave functions of the system.

The momentum operator, $\hat{\mathbf{p}}$, is the generator of translation, $\hat{T}(\mathbf{r}) = e^{-i\mathbf{r}\hat{\mathbf{p}}/\hbar}$.

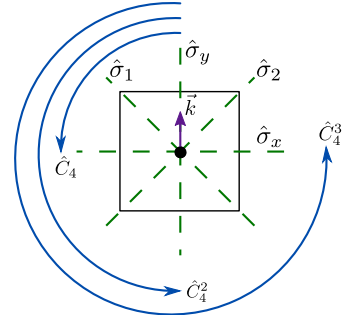


Figure 2.11: The square lattice has D_4 symmetry with the identity (E), three rotations (C_4, C_4^2, C_4^3) and four reflections ($\sigma_x, \sigma_y, \sigma_{AC}, \sigma_{BD}$). If we consider a momentum vector $\mathbf{k} = (0, k_y)$ with $k_y < k_{BZ}$ where k_{BZ} is the value at the edge of the Brillouin zone, then only E and σ_y leave this vector invariant.

We will use \mathcal{R} to refer to the set of parents (representatives) instead of P to avoid confusion with the group of point group symmetries.

Note: The generative symmetry operation for a given subset, \hat{g}_i , cannot be used to transform the states in \mathcal{R}_i into a state contained in another subset, \mathcal{R}_j . This ensures that the parents remain disconnected from each other.

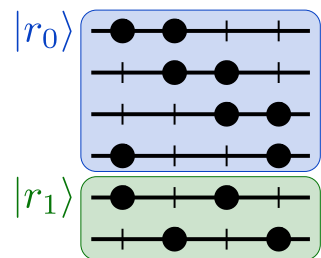


Figure 2.12: Basis for the one-dimensional spinless chain ($L=4, N=2$, periodic boundary conditions) divided into $N_{\mathcal{R}}=2$ subsets. In a given subset, $|r_i\rangle$ can generate the other states via repeated application of the translation operator ($i=0, 1$).

In order to build properly symmetrized states from \mathcal{R} , we will also need to use the characters, χ_s which detail how a configuration $|r\rangle$ transforms under the application of a general symmetry operation, \hat{s} ,

$$\hat{s}|r\rangle = \chi_s |s(r)\rangle. \quad (2.31)$$

The subspace of symmetrized states can now be built from \mathcal{R} with the symmetrized states defined as

$$|\tilde{\psi}\rangle = \frac{1}{\sqrt{N_s}} \sum_{s=1}^{N_s} \hat{s}|\phi\rangle = \frac{1}{\sqrt{N_s}} \sum_{s=1}^{N_s} \hat{s} \left(\sum_{i=1}^{N_{\mathcal{R}}} c_i |r_i\rangle \right) \quad (2.32)$$

where the first sum is over all symmetry operations and the second sum is over all parents. Here the general symmetry operation, \hat{s} , contains both the translation and point group operations, $\{\hat{s} \in G|G = G_T \cup G_{PG}\}$. This yields a general character of the form

$$\chi_s = \chi_{\tau_{\mathbf{k},g}} e^{i\mathbf{k}\cdot\mathbf{r}_t} \quad (2.33)$$

where $\chi_{\tau_{\mathbf{k},g}}$ is the character of \hat{g} in the irreducible representation, $\tau_{\mathbf{k}}$, of the constrained point group, $G_{PG}^{\mathbf{k}}$, and \mathbf{r}_t is the vector of translation along the lattice. For a symmetry sector (labeled by ℓ), the symmetrized states in Eq. (2.32) typically do not require all $N_{\mathcal{R}}$ parent configurations as will be explained next. This will enable us to reduce the dimensions of the block diagonal matrix from $N_{\mathcal{R}} \times N_{\mathcal{R}}$ to $N_{\ell} \times N_{\ell}$.

Let us now explore how this simplification of the symmetrized states works in detail. We can exchange the order of the summations

$$|\tilde{\psi}\rangle = \frac{1}{\sqrt{N_s}} \sum_{i=1}^{N_{\mathcal{R}}} \sum_{s=1}^{N_s} c_i \hat{s} |r_i\rangle \quad (2.34)$$

such that the summation over the parents (indexed by i) comes first, followed by the summation over the various symmetry operations (indexed by s). We can now break Eq. (2.34) into two terms,

In other words, the summation splits as:
 $\sum_{s=1}^{N_s} \rightarrow \sum_{s \in \epsilon_i} + \sum_{s \in \bar{\epsilon}_i}$

$$|\tilde{\psi}\rangle = \frac{1}{\sqrt{N_s}} \sum_{i=1}^{N_{\mathcal{R}}} c_i \left[\sum_{s \in \epsilon_i} \chi_s |r_i\rangle + \sum_{s \in \bar{\epsilon}_i} \chi_s |s(r_i)\rangle \right], \quad (2.35)$$

where ϵ_i is the set of symmetries that leave r_i unchanged and $\bar{\epsilon}_i$ is the set of symmetries that change r_i ,

Combining these two sets gives us the original, complete set of symmetries of the system: $N_s = |\epsilon_i| + |\bar{\epsilon}_i|$.

$$\epsilon_i = \{s | \hat{s}(r_i) = r_i\} \quad \text{and} \quad \bar{\epsilon}_i = \{s | s \notin \epsilon_i\}. \quad (2.36)$$

We introduce another set Q_{ℓ} which is the set of the parent indices such that the sum of the characters for the symmetries $s \in \epsilon_i$ is zero.

$$Q_{\ell} = \left\{ i \left| \sum_{s \in \epsilon_i} \chi_s |r_i\rangle = 0 \right. \right\} \quad (2.37)$$

In other words, this is the subset of the parents where the symmetries either have no effect or the effects completely cancel each other out.

It is straightforward to see that the parents belonging to Q_ℓ will not contribute to the first term of Eq. (2.35).

This set of parents will also not contribute to the second term, but this is not immediately straightforward to see. We shall call the second term B and write it here without the constant in the front:

$$B = \sum_{i=1}^{N_{\mathcal{R}}} \sum_{s \in \bar{\epsilon}_i} c_i \chi_s |s(r_i)\rangle \quad (2.38)$$

This can be rewritten as

$$B = \sum_{i=1}^{N_{\mathcal{R}}} \sum_{s \in \bar{\epsilon}_i} c_i \hat{s} |r_i\rangle \quad (2.39)$$

$$= \sum_{i=1}^{N_{\mathcal{R}}} \sum_{s \in \bar{\epsilon}_i} c_i \chi_p^* \hat{p} \hat{s} |r_i\rangle \quad (2.40)$$

where the last step utilizes the fact that $\chi_p^* \hat{p} = 1$ when $p \in \epsilon_i$. We apply $\frac{1}{|\epsilon_i|} \sum_{p \in \epsilon_i}$ so that we now have

$$B = \frac{1}{|\epsilon_i|} \sum_{i=1}^{N_{\mathcal{R}}} \sum_{p \in \epsilon_i} \sum_{s \in \bar{\epsilon}_i} c_i \chi_p^* \hat{p} \hat{s} |r_i\rangle \quad (2.41)$$

$$= \frac{1}{|\epsilon_i|} \sum_{i=1}^{N_{\mathcal{R}}} \sum_{p \in \epsilon_i} \sum_{s \in \bar{\epsilon}_i} c_i \hat{s} \chi_p^* \hat{p} |r_i\rangle. \quad (2.42)$$

The sum over the parent indices can be split into two components, $\sum_{i=1}^{N_{\mathcal{R}}} = \sum_{i \in Q_\ell} + \sum_{i \notin Q_\ell}$, and we see that the first term does not contribute, due to the sum over $p \in \epsilon_i$. We are therefore left with

$$B = \frac{1}{|\epsilon_i|} \sum_{i \notin Q_\ell} \sum_{p \in \epsilon_i} \sum_{s \in \bar{\epsilon}_i} c_i \hat{s} \chi_p^* \hat{p} |r_i\rangle \quad (2.43)$$

and upon removal of the factor of 1 inserted in the form of $1 = \frac{1}{|\epsilon_i|} \sum_{p \in \epsilon_i} \chi_p^* \hat{p}$, we are finally left with

$$B = \sum_{i \notin Q_\ell} \sum_{s \in \bar{\epsilon}_i} c_i \hat{s} |r_i\rangle. \quad (2.44)$$

Finally, we can conclude that a general symmetrized state can be rewritten from Eq. (2.35) as

$$|\tilde{\psi}\rangle = \frac{1}{\sqrt{N_s}} \sum_{i=1}^{N_\ell} c_i \left[\sum_{s \in \epsilon_i} \chi_s |r_i\rangle + \sum_{s \in \bar{\epsilon}_i} \chi_s |\hat{s}(r_i)\rangle \right] \quad (2.45)$$

$$= \frac{1}{\sqrt{N_s}} \sum_{i=1}^{N_\ell} \sum_{s=1}^{N_s} c_i \hat{s} |r_i\rangle \quad (2.46)$$

where the summation over all parents, $\sum_{i=1}^{N_{\mathcal{R}}}$ has now been reduced to $\sum_{i=1}^{N_\ell}$, with $N_\ell = N_{\mathcal{R}} - |Q_\ell|$. Therefore, we observe that in a given symmetry sector, ℓ , we only need to work with N_ℓ number of configurations. For the sake of simplicity, we assume that the set of parents and the ensuing symmetrized states are properly orthonormalized and we proceed to the discussion on the calculation of matrix elements in the symmetrized basis for a fixed symmetry sector.

If $p \in \epsilon_i$, then $\hat{p} |r_i\rangle = |r_i\rangle$. Therefore,

$$\begin{aligned} \hat{p} |r_i\rangle &= \chi_p |r_i\rangle \\ \chi_p^* \hat{p} |r_i\rangle &= |r_i\rangle \\ \implies \chi_p^* \hat{p} &= 1. \end{aligned}$$

We rewrite $\sum_{i \notin Q_\ell}$ as $\sum_{i=1}^{N_\ell}$ where N_ℓ is the number of parents that contribute to our symmetrized state, $|\tilde{\psi}\rangle$.

The interested reader can find more information about the orthonormalization procedure Appendix A

2.3.2 Calculating matrix elements

Naturally we are interested in the ground-state expectation value of various operators,

$$\langle \tilde{l} | \hat{O} | \tilde{m} \rangle, \quad (2.47)$$

where we assume that the operator commutes with the Hamiltonian, $[\hat{O}, \hat{H}] = 0$. We must consider how a general operator \hat{O} acts on our symmetrized states. Recall that the parents form the basis for these symmetrized states which are defined as

$$|\tilde{l}\rangle = \sum_{s=1}^{N_s} \hat{s} \left(\sum_{j=1}^{N_\ell} \mu_{lj}^\ell |r_j\rangle \right) \quad (2.48)$$

where μ_{lj}^ℓ is a matrix that arises from the orthonormalization of the states (see Appendix A) and ℓ indicates the symmetry sector. In order to compute the matrix elements, we establish that every parent is connected via the operator, \hat{O} , to a set of configurations with an associated weight that depends on the form of the given operator,

$$\left\{ |c_k\rangle \right\}_{k=1, \dots, N_c} \text{ with weights } \left\{ \alpha_k \right\}_{k=1, \dots, N_c}. \quad (2.49)$$

The states generated from the parent configurations via symmetry operations are referred to as *children*. Therefore, each configuration, $|c_k^i\rangle$, that arises from the action of \hat{O} on a parent is then either a parent itself or it is connected to its own respective parent

$$|r_i\rangle \xrightarrow{\hat{s}} |c_k^i\rangle \quad (2.50)$$

via a symmetry operation, \hat{s} . Here the superscript i labels which configuration $|r_i\rangle$ is the parent of $|c_k^i\rangle$. We begin by writing out the full expression for the matrix elements,

$$\langle \tilde{l} | \hat{O} | \tilde{m} \rangle = \sum_{i,j=1}^{N_\ell} \sum_{p,s=1}^{N_s} \mu_{jl}^{\ell*} \mu_{mi}^\ell \langle r_j | \hat{p}^\dagger \hat{O} \hat{s} | r_i \rangle. \quad (2.51)$$

We shall assume that $\mathcal{R} = \{|r_i\rangle\}$ forms an orthogonal basis, which allows us to rewrite Eq. (2.51) with the expressions for the mixing matrix elements as

$$\langle \tilde{l} | \hat{O} | \tilde{m} \rangle = \sum_{i,j=1}^{N_\ell} \sum_{p,s=1}^{N_s} \frac{\delta_{jl}}{\sqrt{\deg(r_l)}} \frac{\delta_{mi}}{\sqrt{\deg(r_m)}} \langle r_j | \hat{p}^\dagger \hat{O} \hat{s} | r_i \rangle \quad (2.52)$$

where $\deg(r_l)$ is the degeneracy of the parent $|r_l\rangle$, defined as

$$\deg(r_l) = \sum_{s \in \epsilon_l} \chi_s(r_l). \quad (2.53)$$

Via the delta functions, we reduce the two summations over all of the parents to obtain:

$$\langle \tilde{l} | \hat{O} | \tilde{m} \rangle = \sum_{p,s=1}^{N_s} \frac{1}{\sqrt{\deg(r_l)}} \frac{1}{\sqrt{\deg(r_m)}} \langle r_l | \hat{p}^\dagger \hat{O} \hat{s} | r_m \rangle. \quad (2.54)$$

We use $|l\rangle$ to indicate an unsymmetrized state and $|\tilde{l}\rangle$ a symmetrized state.

We assume that the factors of $\frac{1}{\sqrt{N_s}}$ are included in the mixing matrix.

The derivation of the mixing matrix, μ_{ij}^ℓ , is provided in Appendix A.

We proceed by combining the two symmetry elements \hat{p}^\dagger and \hat{s} into one element \hat{q} by the group multiplication property,

$$\langle \tilde{l} | \hat{O} | \tilde{m} \rangle = \sum_{q=1}^{N_s} \frac{1}{\sqrt{\deg(r_l)}} \frac{1}{\sqrt{\deg(r_m)}} \langle r_l | \hat{q} \hat{O} | r_m \rangle. \quad (2.55)$$

Finally we act the observable of interest on $|r_m\rangle$ to arrive at the following expression:

$$\langle \tilde{l} | \hat{O} | \tilde{m} \rangle = \sum_{k=1}^{N_c} \sum_{q=1}^{N_s} \frac{\alpha_k}{\sqrt{\deg(r_l)\deg(r_m)}} \langle r_l | \hat{q} | c_k^i \rangle. \quad (2.56)$$

We recall the connection between children and parents from Eq. (2.50), which allows us to rewrite Eq. (2.56) as

$$\langle \tilde{l} | \hat{O} | \tilde{m} \rangle = \sum_{k=1}^{N_c} \sum_{i=1}^{N_\ell} \sum_{r,\hat{q}=1}^{N_s} \frac{\alpha_k}{\sqrt{\deg(r_l)\deg(r_m)}} \chi_r^{-1} \langle r_l | \hat{q} \hat{r} | r_i \rangle \quad (2.57)$$

$$= \sum_{k=1}^{N_c} \sum_{i=1}^{N_\ell} \sum_{s=1}^{N_s} \frac{\alpha_k}{\sqrt{\deg(r_l)\deg(r_m)}} \chi_r^{-1} \langle r_l | \hat{s} | r_i \rangle. \quad (2.58)$$

Here we use again the multiplicative property of the symmetry group, $\hat{r} \hat{q} = \hat{s}$ with $\hat{s} \in G$.

As the parents should not be connected to one another via a symmetry operation, we realize that we will only have non-zero contributions when $|r_i\rangle = |r_l\rangle$. This requires a restriction of our summations to a sum over the children whose parents are $|r_l\rangle$ (Σ_{k^*}) and a sum over the symmetries, $s \in \epsilon_l$, which leave $|r_l\rangle$ unchanged.

$$\langle \tilde{l} | \hat{O} | \tilde{m} \rangle = \sum_{k^*}^{N_c} \sum_{s \in \epsilon_l} \frac{\alpha_k}{\sqrt{\deg(r_l)\deg(r_m)}} \chi_r^{-1} \langle r_l | \hat{s} | r_i \rangle \quad (2.59)$$

$$= \sum_{k^*}^{N_c} \sum_{s \in \epsilon_l} \frac{\alpha_k}{\sqrt{\deg(r_l)\deg(r_m)}} \chi_r^{-1} \chi_s \quad (2.60)$$

$$= \sum_{k^*}^{N_c} \alpha_k \chi_r^{-1} \sqrt{\frac{\deg(r_l)}{\deg(r_m)}} \quad (2.61)$$

We finally arrive at an expression for the calculation of generic matrix elements given an orthonormal basis of parent configurations by use of Eq. 2.53. This expression is relatively straightforward and simply requires knowledge of the degeneracies, characters and naturally the weights of the observable. More details are presented in Appendix A.

Overall, incorporating the use of translation and point group symmetries into our exact diagonalization code enables us to further reduce the size of the matrices that need to be diagonalized. However, this implementation is highly tedious and requires careful attention to detail. This general method can be employed for any Hamiltonians containing discrete translation and/or point group symmetries. We have employed the discrete lattice symmetries to perform finite size checks between systems with $N_s = 12, 18,$ and 24 sites to verify that our results do not change drastically with size and hence, are representative of the thermodynamic limit. For the remainder of the

chapter, we shall focus on numerical techniques that are more specific to our models of interest. In particular, we shall discuss twisted boundary conditions which serve to minimize finite-size errors in the kinetic terms of a Hamiltonian. Following this, we will cover briefly the Ewald summation which allows us to perform controlled calculations of long-ranged potentials.

2.4 Twisted boundary conditions

In the following section we will detail the use of twisted boundary conditions (TBCs) in finite-size ED calculations to minimize finite-size errors arising from the kinetic portion of the Hamiltonian [144, 145]. The kinetic terms in all of the models studied as part of this Hamiltonian are of the form

$$-t \sum_{\langle ij \rangle, \sigma} (c_{i\sigma}^\dagger c_{j\sigma} + h.c.) \quad (2.62)$$

where the hopping matrix amplitude t is assumed to be the same along all nearest-neighbor links in a lattice unless explicitly stated otherwise. We assume that the electrons are localized to the ionic sites i that comprise the lattice and that the overlap between electronic wave functions on different sites falls off exponentially with distance. Therefore, we restrict the possible hopping processes to occur between nearest neighbors, as denoted by the summation over $\langle ij \rangle$.

As the name implies, twisted boundary conditions amount to including a twist in the boundary conditions, as depicted in Fig. 2.13. The use of TBCs was initially more common in particle physics and eventually gained traction in condensed matter physics through the quantum Monte Carlo community. There are two different, but equivalent, manners in which to visualize TBCs:

1. as a twist included on the periodic link between the two end sites of the lattice, or
2. as a twist included on each nearest-neighbor link.

After briefly introducing TBCs and their connection to the well-known Aharonov-Bohm effect, we shall discuss the various prescriptions used to implement TBCs in ED calculations and the sensitivity of different observables to the boundary conditions.

2.4.1 Flux and Aharonov-Bohm effect

Formally speaking, TBCs amount to a modification of the hopping terms of the Hamiltonian by a Peierls phase,

$$t \hat{c}_i^\dagger \hat{c}_j \rightarrow e^{i\delta \cdot \mathbf{k}} t \hat{c}_i^\dagger \hat{c}_j, \quad (2.63)$$

where δ is the distance between sites i and j , which are typically restricted to nearest-neighbor sites. The other component of the phase,

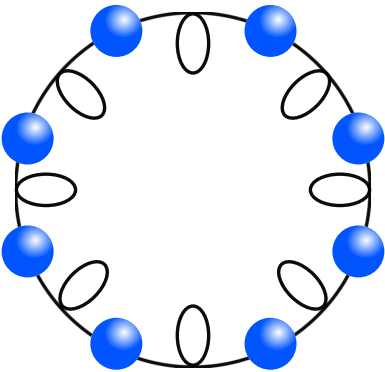


Figure 2.13: Illustration of twist introduced in the periodic boundary conditions of a one-dimensional chain.

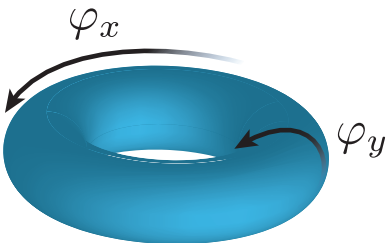


Figure 2.14: Illustration of insertion of flux along two directions of a torus.

κ , can be thought of as a flux inserted along the unit directions of the finite cluster under consideration (see Appendix A for more details). In the case of a two-dimensional periodic lattice, which is geometrically equivalent to a torus, the flux can be inserted along the two unit directions as

$$\kappa = 2\pi \left[\frac{\varphi_x}{L_x} \hat{x} + \frac{\varphi_y}{L_y} \hat{y} \right], \quad (2.64)$$

which can be seen in Fig. 2.14. Periodic boundary conditions correspond to $\kappa = 0$, or equivalently $(\varphi_x, \varphi_y) = (0, 0)$, whereas anti-periodic boundary conditions correspond to $(\varphi_x, \varphi_y) = (0.5, 0.5)$. From this flux κ , we can define a vector potential, $\mathbf{A} = \kappa/2\pi$ such that the phase factors can be expressed as

$$e^{i\delta \cdot \kappa} = e^{2\pi i \int_i^{i+\delta} \mathbf{A} \cdot d\ell} \quad (2.65)$$

in the hopping term of the Hamiltonian of interest. It is important to note that the presence of a vector potential ($\mathbf{A} \neq 0$) does not signify that we have modified our original Hamiltonian by introducing a magnetic field, \mathbf{B} . In fact, as we know from the Aharonov-Bohm effect, quantum mechanical particles can acquire a phase difference as they travel along different paths in a region with $\mathbf{B} = 0$. The acquisition of the phase factor is then due solely to the vector potential, and not to any underlying magnetic interaction terms. Therefore, we are free to employ TBCs in numerical calculations of finite-size systems to improve our estimates of the system's behavior in the thermodynamic limit. However, the implementation of TBCs in such calculations is not straightforward and requires some care as will be discussed in the following section.

2.4.2 Implementation of twisted boundary conditions

In this section, we shall discuss both the benefits and the caveats of using TBCs in numerical calculations of strongly correlated systems. For the sake of simplicity, we will use the one-dimensional Hubbard model,

$$H = -t \sum_{\langle ij \rangle, \sigma} (c_{i\sigma}^\dagger c_{j\sigma} + h.c.) + U \sum_{i=1}^{N_s} n_{i\uparrow} n_{i\downarrow}, \quad (2.66)$$

with fixed filling (canonical) where necessary to demonstrate various concepts. The flux introduced above is appropriately reduced to

$$\kappa = 2\pi \frac{\varphi_x}{L_x} \hat{x} \quad (2.67)$$

along the one-dimensional chain, where L_x is the length of the chain. In most cases, the ground state is highly sensitive to the choice of boundary condition, as shown in Fig. 2.15. With such strong dependence of the results upon the boundary condition, we cannot safely argue that periodic boundary conditions are necessarily a better choice

For details on the calculation of the phase factor for a finite size cluster with a fixed lattice geometry, see Appendix A.

The Aharonov-Bohm effect was actually discovered a decade before Aharonov and Bohm by Ref. [146].

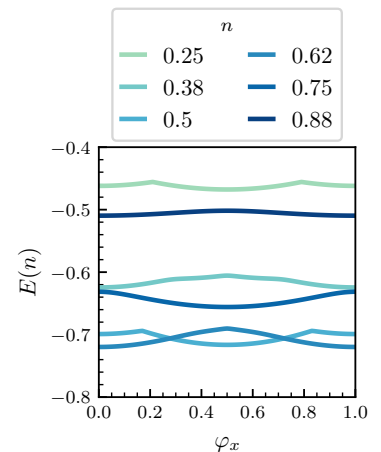
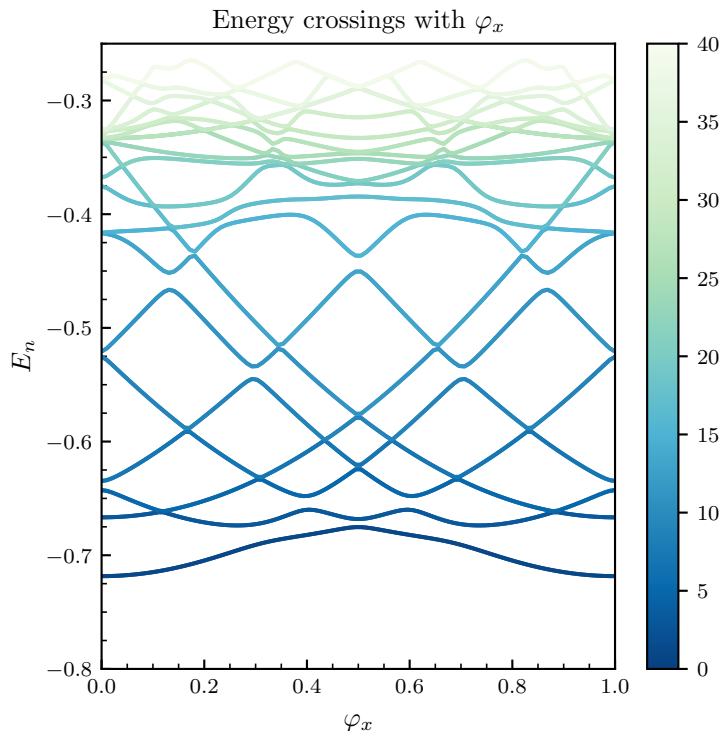


Figure 2.15: Effect of twisted boundary conditions on the energy per site, $\epsilon(n)$, for various fillings n of the 1d Hubbard chain with $N_s = 8$ sites and $U/t = 8$.

Figure 2.16: Flux energy level crossings as the flux is applied to the Hubbard model on the one-dimensional chain with $N_s = 6$ sites, $U/t = 8$ and $n = 0.25$. The lowest 40 eigenvalues are plotted as a function of φ_x . The energies of the ground state *and* excited states are all impacted by the choice of boundary condition.



than any other single boundary choice, such as anti-periodic boundary conditions.

As can be seen in Fig. 2.15, the flux dependence of the ground state energy is periodic in φ_x , leading to what resembles energy bands in flux space (instead of momentum space). In numerical calculations of strongly correlated systems, TBCs serve to minimize degeneracy effects because the application of flux along the unit directions of the lattice can split the multiply degenerate ground states that are frequently found at periodic boundary conditions [147]. The splitting of the various energy levels via application of φ_x is shown in Fig. 2.16. We emphasize that the application of a flux impacts *all* energy levels, and not merely the ground state level.

With our finite-size calculations, we are interested in computing quantities that can accurately be used to predict behavior in the thermodynamic limit. As such, we must determine a prescription for the boundary conditions that will yield consistent and accurate results. As a simplistic, first attempt, we could choose to impose one, fixed boundary condition for all calculations. This is typically done in finite-size calculations that work exclusively in periodic or anti-periodic boundary conditions, for example. However, as Fig. 2.15 and Fig. 2.16 demonstrate, fixing one choice of boundary condition does not yield consistent results and can potentially miss information contained in degenerate states that are accessible instead at other boundary conditions.

Another straightforward choice would be to run the ED calculations over a grid of flux points, $\{\varphi_i \in [0,1]\}$, and to select the φ_i corresponding to the absolute minimal energy as the boundary condition of choice [148]. These two different prescriptions are presented in Fig. 2.17, where we can observe that the choice of prescription changes the results in an unpredictable manner as a function of the filling, n . While these two prescriptions (fixed and absolute minimum) are straightforward to implement, there is no guarantee that either should consistently yield an accurate result across all parameters being considered (filling, disorder, interaction strength, etc.). Furthermore, for higher dimensions, there are more arbitrary choices of boundary condition, such as $(\varphi_x, \varphi_y) = (0,0.5)$ or $(\varphi_x, \varphi_y) = (0.5,0.5)$, that again are not guaranteed to consistently yield an accurate result.

However, it has been shown that averaging instead over a grid of boundary conditions yields an accurate and consistent result [145]. More specifically, this procedure recovers the non-interacting, thermodynamic limit of the Hubbard model through grand canonical calculations on a finite lattice and an average over boundary conditions. In this approach, the basis of states is not reduced by a restriction on the number of particles. Instead, the grand canonical ground state energy on the chain is computed as

$$E_{GC}(\mu) = \frac{1}{L} \int_0^1 d\varphi_x \sum_{m_x}^{N_x} \left(\varepsilon(\mathbf{k} - \mu) \theta(\mu - \varepsilon(\mathbf{k})) \right) \quad (2.68)$$

where $\varepsilon(\mathbf{k} - \mu)$ is the energy dispersion, μ is the chemical potential, and $\theta(\varepsilon)$ is the Heavyside step function. The discrete momenta are those obtained from the discrete lattice sites that have been shifted by the boundary conditions,

$$k_x = \frac{2\pi(m_x + \varphi_x)}{L_x} \quad \text{with } m_x = 0, \dots, L_x - 1. \quad (2.69)$$

The total number of flux points is defined as N_φ . The canonical ground state energy is determined by the Legendre transform,

$$E_C = \sup_{\mu} (E_{GC}(\mu) - \mu) \quad (2.70)$$

and converges quickly with N_φ , as shown in Fig. 2.18 for the non-interacting limit.

Fig. 2.19 demonstrates that the boundary condition averaging in the grand canonical ensemble recovers the parabolic dependence of the ground state energy upon the filling for a reasonable N_φ . The numerical cost is linear in N_φ . Thus far, the grand canonical integration (or averaging) technique from Ref. [145] appears to be a promising avenue for the implementation of TBCs in finite-size ED calculations. In particular, this method ensures that gap-dependent quantities (or observables not computed in a fixed particle sector) are rigorously defined. However, the use of the full grand canonical ensemble is less than ideal

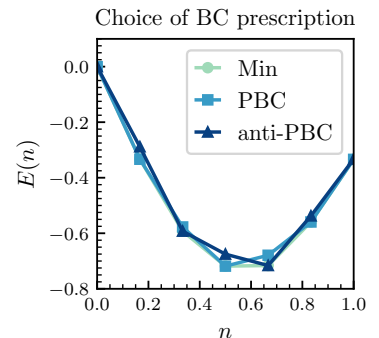


Figure 2.17: Different prescriptions of boundary condition on the energy per site, $\varepsilon(n)$, for 1d Hubbard model on chain with $N_s = 6$ sites. Calculations with a fixed boundary condition are shown for the periodic case (blue squares) and anti-periodic case (dark blue triangles). Calculations using the absolute minimum prescription are shown in green.

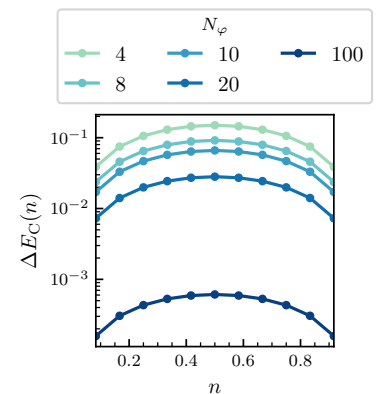


Figure 2.18: Convergence of the canonical ground state energy with the number of flux points, N_φ , for the non-interacting tight-binding model of spinless particles on the 1d chain ($N_s = 12$).

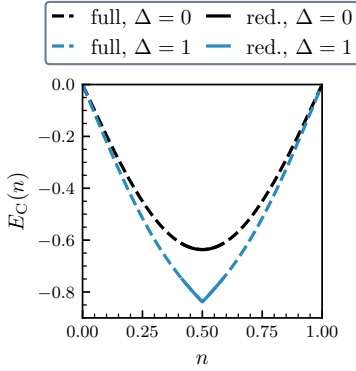


Figure 2.19: Canonical ground state energy, $E_C(n)$, for the free electron in $d = 1$ (black). The parabolic energy dependence on filling is recovered from calculations with the full, grand canonical scheme, as well as for the reduced scheme with the number of particles restricted to $\frac{N_s}{2} - 1 \leq N_p \leq \frac{N_s}{2} + 1$. The reduced scheme similarly recovers the energy from the full scheme for the nearly free electron model with a gap $\Delta = 1$. Here $N_s = 8$ and $N_\varphi = 10$.

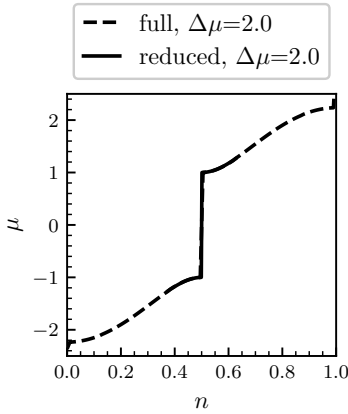


Figure 2.20: Determination of the charge gap from the nearly free electron model on the $1d$ chain with $N_s = 8$ and $N_\varphi = 100$. Results are displayed for the full, grand canonical scheme and the reduced scheme.

because it requires that we store the number of states corresponding to *all* particle number sectors.

In Chapter 3, we shall be interested in computing the single-particle spectral function, $A(\omega)$, which depends on an accurate determination of the chemical potential, μ , in order to identify gaps and pseudogaps in its spectral structure. If we restrict our calculations to the two neighboring sectors to the filling of interest, then we observe in Fig. 2.19 that the reduced approach also reproduces the correct energy dependence of the free electron model. This reproduction upon reduction of the computed fillings is also observed for the case when a gap, Δ , has been introduced into the energy dispersion in the nearly free electron model. In fact, this reductive approach corresponds with the prescription detailed in Ref. [149], where the charge gap is defined as

$$\Delta_{\text{ch}} = \max(\mu^+ - \mu^-, 0) \quad (2.71)$$

where

$$\mu^+ = \frac{1}{2} \min_{\varphi} (E_0^{N+1}(\varphi) - E_0^N(\varphi)) \quad (2.72)$$

$$\mu^- = \frac{1}{2} \max_{\varphi} (E_0^N(\varphi) - E_0^{N-1}(\varphi)) \quad (2.73)$$

The estimation of the charge gap for the full, grand canonical scheme and the reduced scheme around $n = 0.5$ are shown in Fig. 2.20. This use of TBCs to determine gaps and gap-dependent quantities intuitively makes sense as a gap is defined from extremal points along an energy band, as opposed to an average value in the band [149]. While the grand canonical (or reduced grand canonical) averaging procedure is necessary for gap-dependent quantities, Ref. [144] demonstrated that averaging over boundary conditions in the canonical ensemble is sufficient to obtain accurate results with a sufficiently fine grid of flux points. In summary, for the quantities computed via ED calculations in this thesis, we apply TBCs either via the canonical averaging technique (for non-gap dependent quantities) or via the reduced grand canonical procedure (for gap-dependent quantities).

TBCs additionally provide us with access to denser, or more continuous, spectra when we are interested in computing dynamic quantities. One such example is the optical conductivity, defined as

$$\sigma(\omega) = \frac{\pi}{\text{vol}} \sum_{n=1} \frac{|\langle \psi_n | \hat{J} | \psi_0 \rangle|^2}{\omega} \delta(\omega - (E_n - E_0)) \quad (2.74)$$

where vol is the volume of the system, ψ_n is the n -th excited state, ψ_0 is the ground state, and \hat{J} is the current operator. As Fig. 2.21, increasing the number of sampled flux points increases the density of the spectrum. The spectral density rapidly increases with N_φ (raw data, left panel) and the filtered results (right panel) appear essentially identical with $N_\varphi \geq 4$. We note that the results presented in Fig. 2.21 were obtained from a one-dimensional model with long-range interactions

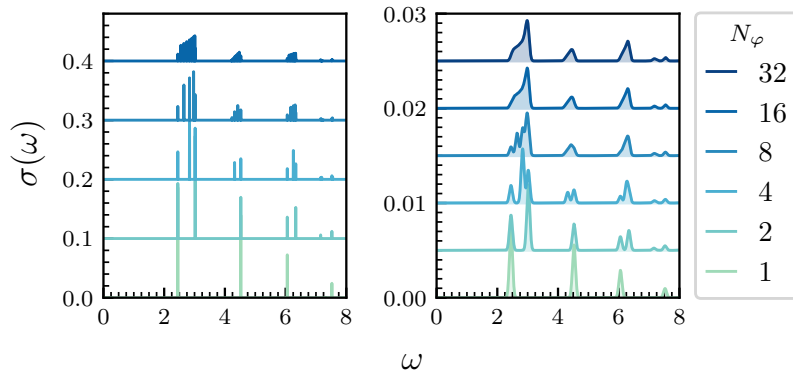


Figure 2.21: Optical conductivity for a $d = 1$ chain of spinless particles with long-range interactions (model to be discussed in Chapter 3) with $V/t = 10$ as a function of N_ϕ . Left panel (histogram with bin width $\delta\omega = 0.005$) shows that increasing N_ϕ (green to blue color gradient) enables sampling of more values of ω , leading to a more continuous spectrum. Right panel (Gaussian filtered with broadening $\delta = 0.05t$) demonstrates the convergence of $\sigma(\omega)$ with N_ϕ .

(similar to that in Chapter 3). The purpose of this figure is merely to demonstrate the capability of TBCs to sample more energy values than are accessible with periodic boundary conditions.

While the exact diagonalization study in this thesis was conducted at $T = 0\text{K}$, these methods can be further extended to analyze systems at finite temperature. Notably, the finite temperature Lanczos method (FTLM), developed by Ref. [150], computes both static and dynamical quantities through an averaging over randomly sampled states,

$$\langle A \rangle = \frac{N_{\text{st}}}{ZR} \sum_{r=1}^R \sum_{j=0}^M e^{-\beta\epsilon_j^r} \langle r | \psi_j^r \rangle \langle \psi_j^r | A | r \rangle, \quad (2.75)$$

where $|r\rangle$ are the randomly sampled states that are used as initial vectors in the Lanczos algorithm. N_{st} is the number of states in the Hilbert space and $\epsilon_j^r, |\psi_j^r\rangle$ are the eigenvalues and eigenvectors obtained from each Lanczos run (of which there are M). The partition function is defined as

$$Z = \frac{N_{\text{st}}}{R} \sum_{r=1}^R \sum_{j=0}^M e^{-\beta\epsilon_j^r} \left| \langle r | \psi_j^r \rangle \right|^2. \quad (2.76)$$

This sampling scheme over random states is only employed at high temperatures and the $T = 0\text{K}$ result can be recovered upon generalization of Eq. (2.76).

Thus far, we have seen that the application of TBCs can lift degeneracies and that the averaging technique provides a controlled method for obtaining well-converged results for (gap-independent) observables. We have also discussed how to accurately define gaps within the framework of TBCs. Additionally, TBCs improve the smoothness of spectral quantities by enabling access to a denser (more continuous) measurement, thereby mimicking larger cluster sizes (see Fig 2.21). Finally, we can also use TBCs to access momentum vectors throughout the Brillouin zone, as was hinted at in Eq. (2.69). For instance, this will allow us to compute the momentum distribution function, $n_{\mathbf{k}} = \langle \psi_0 | \hat{n}_{\mathbf{k}} | \psi_0 \rangle$, along paths in momentum space in a quasi-continuous manner where

the precision of the path is directly linked to the number of flux points. This gives access in particular to the quasiparticle weight, Z , which is defined as the jump in $n_{\mathbf{k}}$ at the Fermi wave vector. On the other hand, observables such as the density correlation in reciprocal space, $C(\mathbf{q}) = \langle \psi_0 | \hat{\rho}_{\mathbf{q}} \hat{\rho}_{-\mathbf{q}} | \psi_0 \rangle$, cannot be extended to the entire Brillouin zone, but we can still employ TBCs to obtain decent averages over a fine grid of flux points. Overall, TBCs can greatly improve the accuracy of finite-size ED calculations by providing a controlled, rigorous manner in which to minimize errors resulting from the kinetic term of the Hamiltonian under study.

2.5 Ewald summation

The use of TBCs is intended to cure errors stemming solely from the kinetic portion of the Hamiltonian as it amounts to a modification of the hopping terms by a phase factor. However, they do not reduce errors arising from the interaction, or potential, part of the Hamiltonian. In particular, the work conducted in this thesis focuses on long-range interacting models which can be generally written as

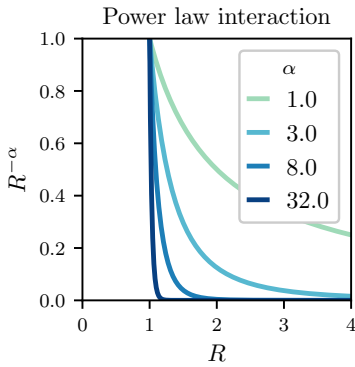


Figure 2.22: Illustration of power law interactions for $\alpha = 1, 3, 8, 32$.

$$H = - \sum_{\langle ij \rangle} t (\hat{c}_i^\dagger \hat{c}_j + \hat{c}_j^\dagger \hat{c}_i) + \frac{V}{2} \sum_{\substack{ij, \\ i \neq j}} \frac{(\hat{n}_i - \bar{n})(\hat{n}_j - \bar{n})}{|\vec{R}_i - \vec{R}_j|^\alpha} \quad (2.77)$$

where t is the hopping amplitude, and c_i^\dagger and c_i are creation and annihilation operators, respectively. This particular Hamiltonian is written for spinless particles, but it can easily be generalized to include spin.

The second term describes the electrostatic interactions between the particles and consists of a double summation over all pairs of sites, i and j , excluding the pairs forbidden by the Pauli exclusion principle ($i = j$). The electrostatic interaction between two sites depends on the product of the electric charge on each site, which is equivalent to $(\hat{n}_i - \bar{n})(\hat{n}_j - \bar{n})$ in Eq. (2.77). The average density, \bar{n} , is subtracted to ensure charge neutrality in our finite-size calculations. The interaction also depends on the inverse distance between the two sites, $|\vec{R}_{ij}|^{-\alpha}$, and the range of the interaction is controlled by the parameter α (illustrated in Fig. 2.22). The case of pure Coulomb interactions occurs for $\alpha = 1$, whereas the case of dipolar interactions occurs at $\alpha = 3$. The larger the value of α , the shorter the range of the interactions. Finally, the prefactor, $V/2$, contains the interaction strength at one lattice spacing, V , and a factor of $1/2$ to account for double counting of pairs in the summation.

As we are restricted to finite-sized systems for our calculations, we must find a method to accurately represent the thermodynamic limit of this electrostatic interaction. To begin, we consider that our finite cluster is infinitely repeated (via periodic boundary conditions) in order to mimic the thermodynamic limit (see Fig. 2.24). Now we can

$$\rho_{\text{ch}}(\mathbf{r}) = \rho_{\text{ch}}(\mathbf{r}) + \rho_{\epsilon}(\mathbf{r}) - \rho_{\epsilon}(\mathbf{k})$$

Figure 2.23: Illustration of the splitting of charge distributions in the Ewald summation technique.

consider the electrostatic potential to be

$$U_{\alpha} = \frac{1}{2} \sum_{\mathbf{R}}' \sum_{ij} \frac{V(\hat{n}_i - \bar{n})(\hat{n}_j - \bar{n})}{|\mathbf{r}_{ij} + \mathbf{R}|^{\alpha}} \quad (2.78)$$

where \mathbf{R} is the vector that translates a site j to its image in one of the replicas. However, this summation is conditionally convergent and the final result depends upon the order in which one sums over the replicas [151]. Furthermore, even when the correct order is chosen, the convergence is very slow. Thankfully this problem was resolved with the development of the Ewald summation technique, which rewrites the potential into two terms—one that converges rapidly in real space, and the other that converges rapidly in momentum space. The general idea of the Ewald summation is to rewrite the original point charge distribution as a summation of said distribution plus two Gaussian-smearred charge distributions that cancel each other out,

$$\rho_{\text{ch}}(\mathbf{r}) = \rho_{\text{ch}}(\mathbf{r}) + \rho_{\epsilon}(\mathbf{r}) - \rho_{\epsilon}^{\mathbf{k}}(\mathbf{r}), \quad (2.79)$$

where ϵ is a smearing (cutoff) parameter associated with the Gaussian distributions. The \mathbf{k} superscript on the last term indicates that this term undergoes a Fourier transform to reciprocal (momentum) space. This idea is schematically represented in Fig. 2.23. The two terms in real space are combined into one, rapidly converging term and the sum in reciprocal space also converges rapidly. Included in the calculation is also a correction term that accounts for the inclusion of self-energy from the replicated clusters.

The complete derivation for the Ewald summation in arbitrary dimension and for arbitrary interaction range α is provided in Appendix B. The final result is provided here:

$$\begin{aligned} U_{\alpha} = & \frac{1}{2\Gamma(\alpha/2)} \sum_{\mathbf{R}}' \sum_{ij} \frac{V_{ij}}{|\mathbf{r}_{ij} + \mathbf{R}|^{\alpha}} \Gamma\left(\alpha/2, \epsilon^2 |\mathbf{r}_{ij} + \mathbf{R}|^2\right) \\ & + \frac{\pi^{d/2} \text{vol}^{-1}}{2^{\alpha-d+1} \Gamma(\alpha/2)} \sum_{\mathbf{k} \neq 0} \sum_{ij} |\mathbf{k}|^{\alpha-d} \Gamma\left(\frac{d-\alpha}{2}, \frac{|\mathbf{k}|^2}{4\epsilon^2}\right) \cos(\mathbf{k} \cdot \mathbf{r}_{ij}) \\ & + \frac{\pi^{d/2} \text{vol}^{-1}}{\Gamma(\alpha/2)} \frac{\epsilon^{\alpha-d}}{(\alpha-d)} \sum_{ij} V_{ij} - \sum_i \frac{V_{ii} \epsilon^{\alpha}}{\alpha}. \end{aligned}$$

where we have defined $V_{ij} = V(\hat{n}_i - \bar{n})(\hat{n}_j - \bar{n})$ for the sake of simplicity. This technique can be implemented in a straightforward manner

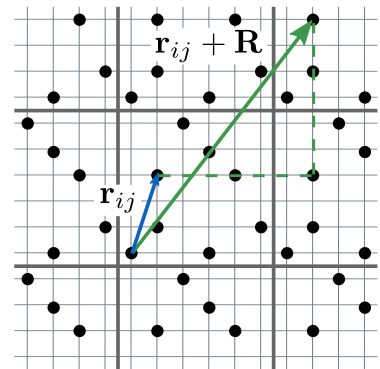


Figure 2.24: Illustration of replicas of the finite cluster to mimic the thermodynamic limit. Although only the nearest-neighbor clusters are shown for illustrative purposes, we consider many more replicas when computing the Ewald summation.

for general lattice geometries and dimensions and converges rapidly with the number of replicas. Typically only a few replicas ($N_R \sim 5 - 10$) are required to reach well-converged results. In conclusion, the Ewald summation enables us to compute electrostatic potentials that are representative of the thermodynamic limit for the finite-size configurations used in ED calculations.

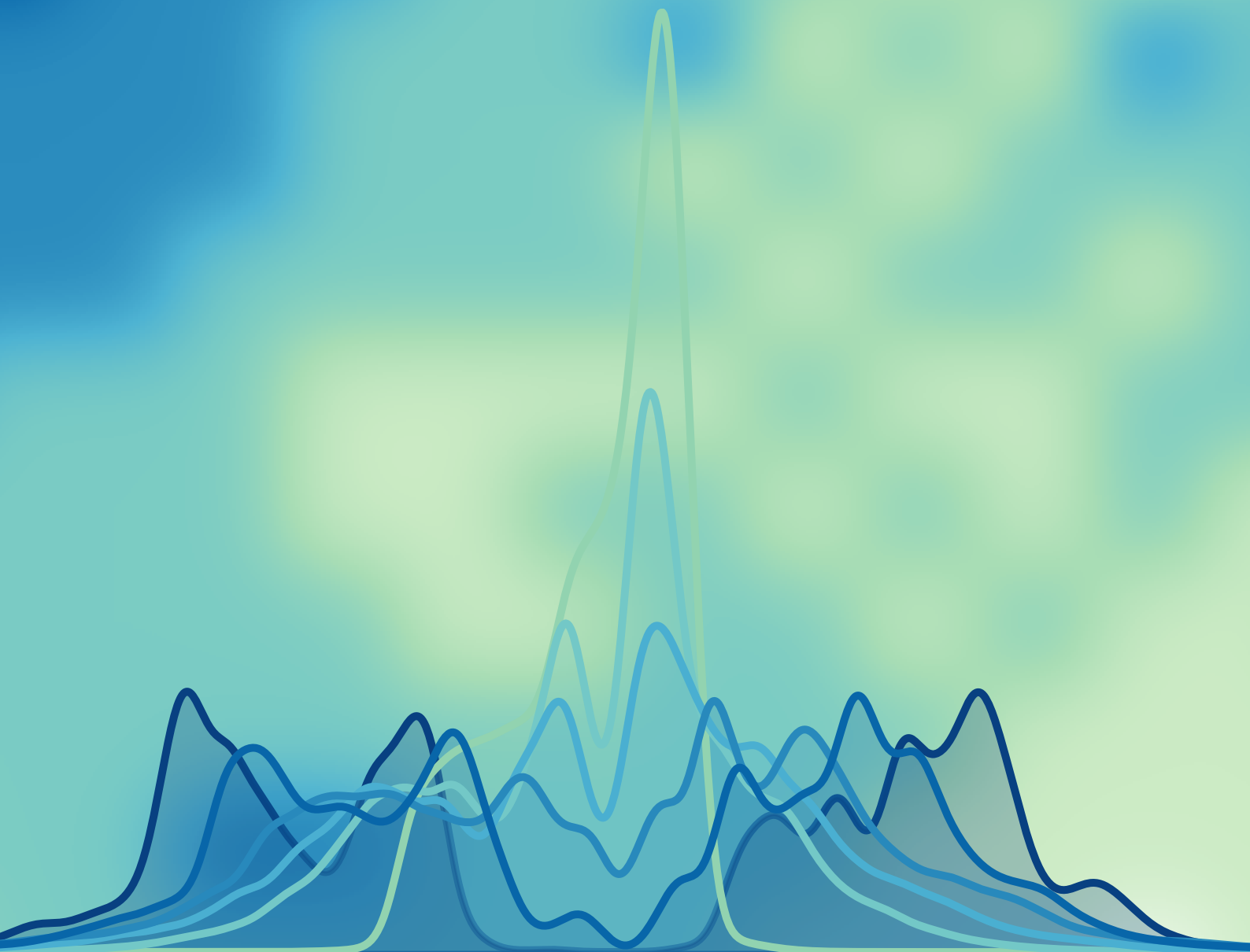
2.6 Summary

The current chapter has served as a technical introduction and has introduced exact diagonalization as a versatile numerical technique with which to study strongly correlated systems, a necessary quality for our investigations. We have explained a sampling of the technical details of this method that we have deemed relevant. Among these details, we have reviewed the framework for representations of a general Hamiltonian and its efficient implementation in a diagonalization code, while providing estimates for finite sizes accessible. Furthermore, we have discussed at length the Lanczos algorithm which is utilized to diagonalize large, sparse Hermitian matrices such that the extremal eigenpairs are rapidly obtained. We have also reviewed the use of symmetries in diagonalization codes as an effort to increase the accessible sizes.

Finally, we discussed strategies to reduce finite-size errors in both the kinetic and the interacting portions of the Hamiltonian. The errors stemming from the kinetic terms can be minimized by the implementation of twisted boundary conditions. This implementation contains many subtleties and we have summarized the various approaches and laid out an optimal strategy for our future work. The errors arising from the computation of a long-ranged potential are handled with the Ewald summation. In conclusion, this wealth of technical knowledge places us in an ideal position from which to investigate the effects of long-range interactions at zero temperature which will be examined in the following chapter by means of exact diagonalization.

Chapter 3:

Pseudogap metal induced by long-range Coulomb interactions



Pseudogap metal induced by long-range Coulomb interactions

3.1 Introduction

Sir Nevill Mott changed the landscape of condensed matter physics in 1949 by explaining that strong interaction effects would split conduction bands into one empty band and one filled band at half-filling ($n = 1$) [11]. This observation correctly explained the insulating nature of narrow band systems, such as transition metal oxides, where simple band theory erroneously predicted these materials to be metallic. An interaction-centered treatment of electrons came to be understood as the critical mechanism behind the Mott metal-insulator transition (MIT) and enabled condensed matter physicists to begin to understand interaction effects in other correlated materials.

Shortly thereafter, John Hubbard derived the simple Hubbard model to study the Mott MIT [17]. This model assumes that only an on-site energy term, U , is sufficient to explain the physics of the electron-electron interactions in narrow band systems,

$$H = - \sum_{ij,\sigma} t_{ij} (\hat{c}_{i\sigma}^\dagger \hat{c}_{j\sigma} + h.c.) + U \sum_{i=1}^N \hat{n}_{i\uparrow} \hat{n}_{i\downarrow} - \mu \sum_{i=1}^{N_s} \hat{n}_i. \quad (3.1)$$

but exact, analytical solutions are limited [19]. This dearth therefore drove the development of several sophisticated numerical techniques over the course of the past fifty years, including dynamical mean field theory [20], quantum Monte Carlo [29, 30], and exact diagonalization [32, 33, 132]. The discovery of the high-temperature cuprate superconductors [83] and attempts to explain the exotic correlated phases

in their phase diagrams also helped to fuel the explosion of numerical and theoretical works on the Hubbard model [48]. This model on the square lattice serves as the preferred model for electronic correlation in these systems [43,88].

However, despite the rigorous application of state-of-the-art techniques to the Hubbard model, several phenomena remain unexplained, including the nature of ordering patterns in the cuprates and the source of bad metallic transport observed across a broad class of materials [74,88]. Indeed, these shortcomings suggest that the Hubbard model lacks certain ingredients to properly describe strongly correlated materials. Furthermore, the wide variety of materials that display these novel phenomena indicates that the missing ingredient(s) should be general in nature. As many of these systems host exotic phases in the vicinity of Mott insulators, a potential candidate could be linked to the incipient breakdown of screening of electric charges. With reduced screening, the impact of long-range interactions would play an important role in determining the resulting physics.

In classical systems, long-range interactions have been shown to produce strong frustration effects which lead to unusual charge states, including charge glasses [110] and pseudogap phases with strong short-range order [152]. Experimentally, manifestations of strong non-local interactions have been discovered in the θ -(BEDT-TTF)₂X family of organic conductors [59], which host charge glass and strange metal phases in geometrically frustrated lattices, as previously discussed in Sec. 1.4.2. These materials consist of layers of organic molecules laid out in a triangular lattice structure, intercalated with insulating, anionic layers that enable the organic layers to be studied as quasi-two-dimensional systems. These clean materials could act as an ideal experimental platform to investigate anomalous phenomena beyond the conventional Mott-Hubbard physics.

Overall, the need to understand if extensions to the Hubbard model can adequately address the open questions in strongly correlated materials motivates us to study the effect of long-range interactions on the zero-temperature ground state of a two-dimensional lattice. Our particular choice of lattice is motivated by the experimental findings in the θ -(BEDT-TTF)₂X salts. In this chapter, we first introduce our long-range model and discuss relevant technical details. We then proceed to an explanation of the phase diagram and a characterization of each of the phases contained therewithin. We discover that the long-range interactions act as a novel mechanism for producing strongly correlated behavior and provide an understanding for this mechanism in the context of disordered insulators. Finally, we conclude with an analysis of the role of charge fluctuations in the correlated metallic phase and consider the impact of these fluctuations on transport at finite temperatures. Many of these results have been published in Ref. [153].

3.2 Model and method

The family of organic materials mentioned in the previous section are considered quasi-two-dimensional materials because of their insulating anionic layers. As such, we consider a two-dimensional triangular lattice model with non-local interactions that will reasonably describe the physics present in these materials. Furthermore, the layer of organic molecules is quarter-filled ($n = 0.5$) in terms of holes. By the use of particle-hole symmetry, we choose to study a model that is quarter-filled in terms of electrons. Moreover, as discussed in Chapter 1, we would not reasonably expect any doubly occupied sites at low temperatures based upon estimates of the ratio between the on-site energy, U , and the non-local potential, V . This expectation that the magnetic channel will not play a significant role in the physics, coupled with the fact that we are mostly interested in the charge degrees of freedom, permits us to focus our efforts on a spinless model. This model has an average density of one particle every two sites, respecting the original density of the holes.

While these justifications might appear to be highly material-dependent, we would like to emphasize that the general understanding of long-range interactions in a spinless model at $T = 0\text{K}$ remains the main focus of our study. The family of organic materials acts as the physical justification for investigating such a model and provides us with a starting point in terms of lattice type and filling. However, our model can easily be adapted to apply to studies of the various systems discussed in Chapter 1. We study spinless electrons interacting through a long-range repulsive potential on an isotropic triangular lattice as described by the following Hamiltonian [152],

$$H = -t \sum_{\langle ij \rangle}^{N_s} (\hat{c}_i^\dagger \hat{c}_j + h.c.) + \frac{1}{2} \sum_{ij}^{N_s} V_{ee}(R_{ij}, \alpha) (\hat{n}_i - \bar{n})(\hat{n}_j - \bar{n}). \quad (3.2)$$

Here \hat{c}_i^\dagger and \hat{c}_i are creation and annihilation operators for electrons in local atomic orbitals, $h.c.$ is the Hermitian conjugate, \hat{n}_i is the local density operator, t is the hopping matrix element between nearest neighbor sites, and $\bar{n} = 0.5$ is the average electron density which is subtracted in the second term to enforce charge neutrality. The potential, $V_{ee}(R_{ij}, \alpha)$, describes the interaction between two electrons at a distance R_{ij} from each other,

$$V_{ee}(R_{ij}, \alpha) = V \cdot \left(\frac{a}{R_{ij}} \right)^\alpha, \quad (3.3)$$

where the power-law exponent α controls the range of interactions. The strength of the interactions is controlled by V , the value of the potential at one lattice spacing a (which we set as the unit length). This particular form of $V_{ee}(R_{ij}, \alpha)$ includes:

- the pure Coulomb potential, $V_{ee}(R) \sim 1/R$ with $\alpha = 1$,

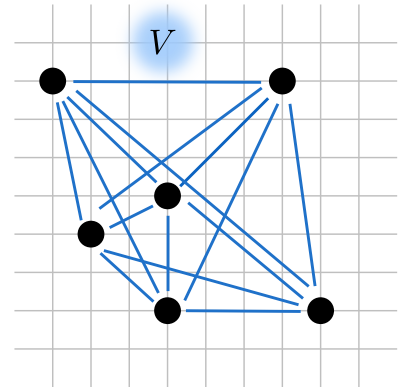
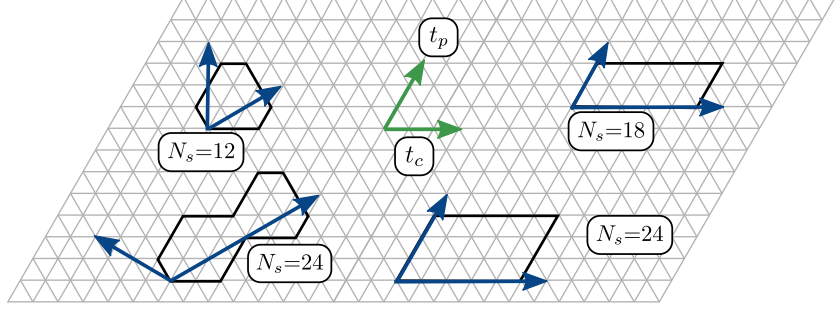


Figure 3.1: Illustration of the long-range model of spinless particles.

Figure 3.2: Sketch of cluster definitions for $N_s = 12, 18$ and 24 sites complete with the cluster translation vectors (blue arrows) and the hopping lattice directions (green arrows) with respect to those of the organic salts, θ -(BEDT-TTF) $_2$ X. The hopping processes occur between nearest-neighbor sites, but the green arrows indicating them have been enlarged for ease of reading.



- the nearest-neighbor interaction, $V_{ee}(R) \sim \sum_{\langle ij \rangle} \hat{n}_i \hat{n}_j$ with $\alpha = \infty$, which has been previously been studied in the extended Hubbard model [154],
- and the dipolar form $V_{ee}(R) \sim 1/R^3$ of the two-dimensional electron gas near a metallic gate ($\alpha = 3$) [155, 156].

Eq. (3.2) is solved numerically via both brute-force and Lanczos exact diagonalization at zero temperature on finite-size clusters with $N_s = 12, 18, 24$ sites. When the Hilbert space of the system is sufficiently small, the Hamiltonian is diagonalized via brute-force exact diagonalization. Otherwise, the Lanczos algorithm is employed as discussed in Chapter 2.

The finite size clusters are shown in Fig. 3.2. The hopping and interaction terms along the different bond directions are taken to be isotropic (i.e., $t_c = t_p = t$ and $V_c = V_p = V$). The linear size is defined as L and the translation vectors, \mathbf{T}_1 and \mathbf{T}_2 , for each cluster are given as follows:

- $N_s = 12$: $\mathbf{T}_1 = (L, L)$, $\mathbf{T}_2 = (-L, 2L)$ with $L = 2$
- $N_s = 18$: $\mathbf{T}_1 = (L, 0)$, $\mathbf{T}_2 = (0, L/2)$ with $L = 6$
- $N_s = 24$: $\mathbf{T}_1 = (L, 0)$, $\mathbf{T}_2 = (0, 2L/3)$ with $L = 6$
- $N_s = 24$: $\mathbf{T}_1 = (L, L)$, $\mathbf{T}_2 = (-L, L/2)$ with $L = 4$.

The hexagonal Brillouin zone corresponding to the isotropic triangular lattice is shown in Fig. 3.3. The N_s sites in each real space cluster correspond to N_s discrete momenta in the Brillouin zone. The specific geometries of the clusters in real space are chosen such that we do not bias the ED calculations to exclude certain charge-ordering patterns, namely stripe order (M point) and three-fold order (K point). The locations of these high-symmetry points are highlighted in Fig. 3.3. The only exception is that of the parallelogram cluster with $N_s = 24$ sites as the set of momenta from this cluster does not include the K point. However, this does not impact our results and will be discussed in more detail later, along with the relevance of the wave vector to charge order (see Sec. 3.4).

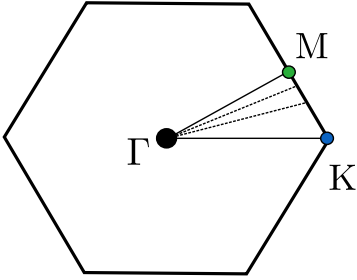


Figure 3.3: Brillouin zone corresponding to the triangular lattice. The dotted lines are the paths along which the occupation number $\langle \hat{n}_{\mathbf{k}} \rangle$ is calculated for the determination of the quasiparticle renormalization Z .

As described in Chapter 2, we applied translation symmetries to reduce the computational cost and to minimize any spurious effects of degenerate ground states [140]. The use of these symmetries reduces the size of the Hilbert space in a given symmetry sector by a factor approximately equal to the number of symmetries, $N_{\mathcal{H}} \rightarrow N_{\mathcal{H}}/N_{\text{sym}}$. We also applied twisted boundary conditions (TBCs) to improve discretization errors arising from the kinetic term in the Hamiltonian (Eq. 3.2) and to lift the degeneracy of the ground state. We averaged over TBCs at fixed particle number for non-gap-dependent quantities [144], and we averaged over the (reduced) grand canonical scheme for gap-dependent quantities [145]. This restores the exact thermodynamic limit ($N_s \rightarrow \infty$) result in the non-interacting limit, $V/t \rightarrow 0$, and lets us reasonably expect a better approximation when $V/t \neq 0$. TBCs essentially modify the hopping terms of our Hamiltonian such that when a particle hops between nearest-neighbor sites, it picks up a phase from the flux (boundary condition) applied. We can define the phase acquired along a given direction by an angle θ_i that is written in terms of a vector potential, \mathbf{A} , as

$$\theta_i = 2\pi\xi_i = \frac{2\pi}{\phi_0} \oint (A_1\hat{u}_1 + A_2\hat{u}_2) \cdot d\vec{l}, \quad (3.4)$$

where \hat{u}_i corresponds to the unit lattice translation vector along the i -th direction of the torus. The prefactor, $2\pi/\phi_0$, corresponds to a constant factor $2\pi q/hc$, where we set $\phi_0 = hc/q = 1$. We introduced a small, random shift to the TBCs, designated by η , in order to lift the degeneracy in the vicinity of the periodic boundary (and other highly degenerate) condition(s) such that diagonalization via the Lanczos algorithm could be employed. More details on TBCs can be found in Chapter 2 and details on the calculation of this phase factor, θ_i , can be found in Appendix A.

For the non-local electrostatic interaction term, we extended the finite size cluster to the thermodynamic limit by considering infinitely repeated simulation cells and then performing the electrostatic lattice sums using the Ewald summation method [152]. This ensures that the electrostatic (Madelung) energy of periodic configurations is exactly recovered in the classical limit, $t/V \rightarrow 0$. A full derivation of the Ewald summation for general dimension d and interaction range α can be found in Appendix B. We performed all calculations with a sufficient number of cluster replicas to guarantee the convergence of the non-local potential. The Ewald summation typically only requires a few replicas to reach convergence ($N_{\text{replicas}} \sim 5$). For our codes written in C++, we used $N_{\text{replicas}} = 200$. However, for our codes written in Python, we reduced this number to $N_{\text{replicas}} = 5$ due to Python's slow treatment of loop structures. We benchmarked the results from the Python codes against those of the C++ codes to ensure that no errors were introduced by reduction of the number of replicas.

With the specifics of the model and the method established, we now

For more information on the implementation and benefits of TBCs, please refer to Chapter 2 and Appendix A.

The vector potential is related to the flux inserted along the torus by $\mathbf{A} = \kappa/2\pi$ with $\kappa = 2\pi\left(\frac{\phi_x}{L_x}\mathbf{x} + \frac{\phi_y}{L_y}\mathbf{y}\right)$.

The prefactor arises from the expression of the Lorenz force in c.g.s. units

$$\mathbf{F} = q\left(\mathbf{E} + \frac{\mathbf{v}}{c} \times \mathbf{B}\right) \quad (3.5)$$

where q is the charge of the particle, c is the speed of light, \mathbf{v} is the speed of the particle, and \mathbf{E} and \mathbf{B} are the electric and magnetic fields, respectively.

This shift was typically taken to be $\eta = (1.07654 \times 10^{-4}, -1.98673 \times 10^{-4})$.

proceed to the results for our long-range interacting model of spinless particles. First, we shall provide analytical estimates of phase transitions for our model before proceeding to a presentation of the phase diagram, complete with a description of all phases in it. Finally, we will analyze the correlated pseudogap phase that we discover for long-range interactions and we discuss its relation to the classical Coulomb gap caused by self-generated disorder.

3.3 Analytical estimates

Before diving into the details of the phase diagram in the following section, we would like to paint a general picture of what one should expect based on previous studies and physical intuition. We remind the reader that the Hamiltonian of our system is of the form

$$H_{\text{LR}} = -t \sum_{\langle ij \rangle}^{N_s} (\hat{c}_i^\dagger \hat{c}_j + h.c.) + \frac{V}{2} \sum_{ij}^{N_s} \frac{\hat{n}_i \hat{n}_j}{|R_{ij}|^\alpha} \quad (3.6)$$

where α controls the range of the interactions. Naturally, we want to understand where to expect phase transitions (if any) in terms of the energy scale, V/t . We begin by examining the classical limit ($t = 0$) where the ground state is determined by the configuration with the minimum electrostatic (Madelung) energy. As the interaction between particles is repulsive, we intuitively expect that the charges in this ground state would arrange themselves in an ordered fashion. In other words, we expect them to form a generalized Wigner crystal at zero temperature to minimize the electrostatic interactions [157, 158]. We note that as we are considering a lattice model (as opposed to the continuum in the original proposition of the Wigner crystal), then the ordered electrostatic configuration must minimize the repulsive interactions with respect to the geometric constraints of the lattice.

We take the nearest-neighbor limit ($\alpha \rightarrow \infty$) of interactions, which corresponds to

$$H_{\text{classical}}^{\text{NN}} = \frac{V}{2} \sum_{\langle ij \rangle}^{N_s} \frac{\hat{n}_i \hat{n}_j}{R_1^\alpha}, \quad (3.7)$$

where $\langle ij \rangle$ indicates that the summation is restricted to nearest neighbors. The distance between nearest-neighbor sites, R_1 , is trivially equal to one lattice spacing, but we retain its expression in the Hamiltonian for the sake of completeness. Spinless particles on triangular lattice at half-filling (one particle every two sites) display a macroscopic number of degenerate configurations that minimize the electrostatic energy. Two such configurations are shown in Fig. 3.4 for a typical finite cluster ($N_s = 12$ sites) with periodic boundary conditions. The boundary conditions are depicted by the repeated images of the central cluster.

The panel on the left shows a threefold order of a fraction of the electron density (black sites), while the remaining charges (blue sites) occupy the honeycomb lattice excluded by the threefold sites. The

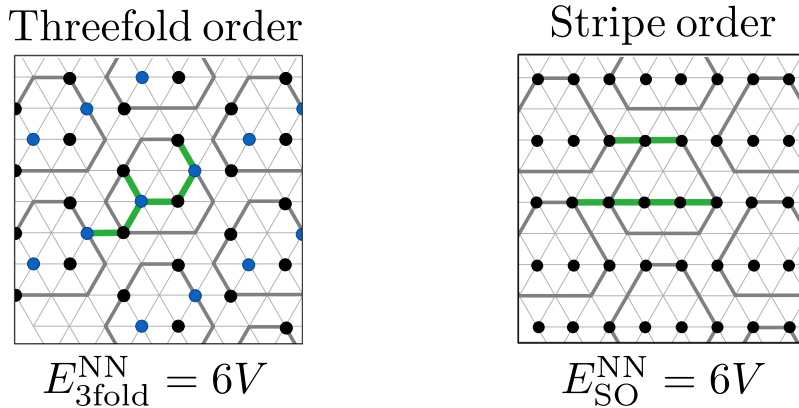


Figure 3.4: Energetic cost of the threefold-ordered (left) and stripe-ordered (right) phases. The nearest-neighbor interactions (green) sum up for a total energy of $E_{3\text{fold}}^{\text{NN}} = E_{\text{SO}}^{\text{NN}} = 6V$.

Madelung energy of this configuration, computed as a summation over all of the lattice legs in the finite cluster that connect two occupied sites (highlighted in green), is $E_{3\text{fold}}^{\text{NN}} = 6VR_1^{-\alpha} = 6V$. This value is the same as the Madelung energy of the stripe order configuration (right panel of Fig. 3.4) where the lattice legs connecting two occupied sites are again highlighted in green.

We would like to understand how the respective energies of these configurations changes with the inclusion of longer-ranged interactions. As such, we extend the range to include next-nearest-neighbor interactions,

$$H_{\text{classical}}^{\text{NNN}} = \frac{V}{2} \sum_{\langle\langle ij \rangle\rangle} \frac{\hat{n}_i \hat{n}_j}{R_{ij}^\alpha}, \quad (3.8)$$

where $\langle\langle ij \rangle\rangle$ indicates the summation over next-nearest neighbor sites. The Madelung energies with next-nearest-neighbor interactions now differ between the two configurations as shown in Fig. 3.5. The nearest-neighbor interactions are still highlighted in green and the next-nearest-neighbor interactions are highlighted in purple. We observe that the energy difference between the two configurations is

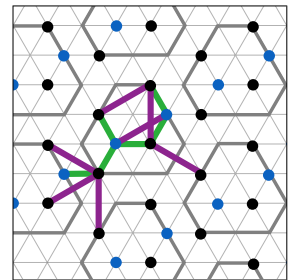
$$\Delta E^{\text{NNN}} = E_{3\text{fold}}^{\text{NNN}} - E_{\text{SO}}^{\text{NNN}} = 4VR_2^{-\alpha} \quad (3.9)$$

which indicates that the stripe-ordered (SO) configuration becomes more favorable with the inclusion of longer-ranged interactions. We now have a basic understanding of the impact of the long-range interactions on the competing charge orders due to electrostatic repulsion in the classical limit.

Next we proceed to examine what happens when we include quantum fluctuations. If we start again from the nearest-neighbor limit ($\alpha \rightarrow \infty$), this corresponds to the $t - V$ model,

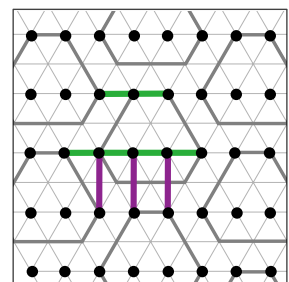
$$H_{t-V} = -t \sum_{\langle ij \rangle} (\hat{c}_i^\dagger \hat{c}_j + h.c.) + \frac{V}{2} \sum_{\langle ij \rangle} \hat{n}_i \hat{n}_j, \quad (3.10)$$

Threefold order



$$E_{3\text{fold}}^{\text{NNN}} = 6V + 7VR_2^{-\alpha}$$

Stripe order



$$E_{\text{SO}}^{\text{NNN}} = 6V + 3VR_2^{-\alpha}$$

Figure 3.5: Energetic cost of the threefold-ordered (left) and stripe-ordered (right) phases. The next-nearest-neighbor interactions (green) sum up for a total energy of $E_{3\text{fold}}^{\text{NNN}} = 6V + 7VR_2^{-\alpha}$ and $E_{\text{SO}}^{\text{NNN}} = 6V + 3VR_2^{-\alpha}$.

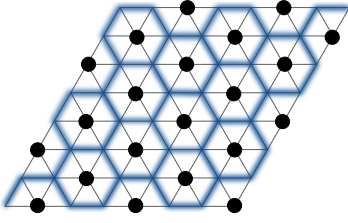


Figure 3.6: Illustration of the pinball liquid phase.

E

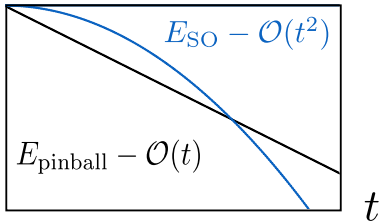


Figure 3.7: Illustration of the evolution of energy for the pinball (black) and stripe order (blue) states as a function of quantum fluctuations, t .

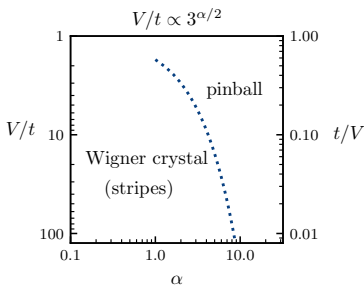


Figure 3.8: Preliminary estimate of the phase diagram in $(V/t, \alpha)$ space for our long-range interacting Hamiltonian.

which has previously been studied via exact diagonalization in Refs. [159, 160]. This model hosts a *pinball liquid*, which will be discussed in greater detail in the following section. For the time being, it suffices to describe this phase as the quantum analogue of the threefold-ordered classical phase presented in Fig. 3.4 where a fraction of the charge density remains localized (black sites) while the remaining charge density (blue sites) delocalize and flow around the honeycomb lattice excluded by the black sites. A sketch of this phase is shown in Fig. 3.6.

For the moment, we are only concerned with determining the melting transition from the pinball liquid phase to the Wigner crystal phase, in terms of the energy scale, V/t , and the range of interactions, α . In order to do this, we compare the energies of the two phases to the lowest order of the kinetic term, t . These values have been computed in Ref. [159] as $\sim t$ for the pinball phase and $\sim t^2$ for the stripe-ordered phase. We observe that the pinball liquid gains more kinetic energy than the stripe-ordered phase when the quantum fluctuations are weak (small t). This concept is illustrated in Fig. 3.7.

Finally, we predict the melting transition from the pinball liquid phase to the (striped) Wigner crystal phase at large α by comparing the difference in electrostatic energy of the two phases to the lowest order in the kinetic term,

$$\Delta E^{\text{LR}} \propto t \quad \longrightarrow \quad VR_2^{-\alpha} \propto t \quad \longrightarrow \quad (V/t)_c \propto 3^{\alpha/2} \quad (3.11)$$

Here we have used the fact that the next-nearest-neighbor distance, R_2 , on the triangular lattice is $\sqrt{3}$. We additionally emphasize that the factor of 4 in the difference in Madelung energies calculated previously arises from the simple case of comparing nearest-neighbor to next-nearest-neighbor interactions, ΔE^{NNN} . Therefore, we chose to write the difference in Madelung energies in a more general form, $\Delta E^{\text{LR}} \propto VR_2^{-\alpha}$, to emphasize the fact that this prefactor can change depending on the lattice geometry and range of interactions. This estimated transition is plotted in a preliminary phase diagram in Fig. 3.8.

At smaller values of α , we anticipate that the stripe-ordered (Wigner crystal) melts into another phase as the existence of the pinball is pushed to weaker values of t/V with increasing range of interactions (see Fig. 3.8). Furthermore, classical studies of long-range interacting systems provide us with the insight that the Wigner crystal becomes increasingly unstable with increasing interaction range [152]. These two insights lead us to expect that a new phase will be obtained upon the melting of the stripe ordered (Wigner crystal) phase. This new phase will likely retain strong electronic correlations reminiscent of the stripe-ordered phase, a topic that will be discussed at length in the remainder of this chapter. Furthermore, the melting transition will occur when defects around stripe order become energetically favorable as they gain kinetic energy by their proliferation [161].

To understand this transition, we focus on the charge-ordered phase, previously shown in Fig. 3.4, in the strong coupling limit, $t/V \rightarrow 0$.

The stripe-ordered configuration minimizes the electrostatic interactions and any modification of the placement of the charges will necessarily result in a higher Madelung energy. It is straightforward to determine that the lowest excited state is obtained by creating a defect that consists of displacing a particle by one lattice spacing from the occupied stripe to the unoccupied stripe [162] (see Fig. 3.9). The creation of this defect will necessarily cost a certain amount of potential energy, E_d , due to the electrostatic interactions. The exact value of E_d will depend on the range of interactions, α .

As quantum fluctuations are turned on ($t/V > 0$), these charge defect excitations will become more accessible with longer-ranged interactions. We can estimate the quantum melting transition as it should occur via the proliferation of these low-lying defects. In other words, we anticipate that the quantum melting transition takes place when the energetic cost of creating a defect is overcome by their gain in kinetic energy, $t \sim E_d$ [161–163]. In the small α limit, we can determine an expression for E_d by computing the differences in Madelung energy of a stripe-ordered configuration and a defect configuration. These energies are readily obtained as a function of α by the Ewald summation method (top panel, Fig. 3.10). The energies are fit to a linear model, $E_d = a_0 + a_1\alpha$, the slope of which is plotted against the inverse system size in the bottom panel of Fig. 3.10. The intercept of this finite-size scaling analysis yields the asymptotic value expression $E_d \simeq 0.469V\alpha$, which we use to obtain an estimate for the critical interaction strength for the quantum melting transition at small α ,

$$E_d \sim t \quad \longrightarrow \quad (V/t)_c \propto 1/\alpha. \quad (3.12)$$

We combine this with our earlier estimate of the transition from the pinball phase to the stripe-order phase for a preliminary phase diagram shown in Fig. 3.11. At this point, we have established a preliminary understanding of the effects of long-range interactions in quantum lattice models based upon our knowledge of nearest-neighbor models and long-range interactions in the classical limit. However, this is the limit of analytical estimates that we can obtain and we must proceed to analyzing our long-range Hamiltonian (Eq. (3.2)) numerically. This is done via exact diagonalization (discussed in Chapter 2) and we present our numerical results in the remainder of the chapter. First, we establish a comprehensive phase diagram in terms of interaction strength, V/t , and range, α . The discussion on the phase diagram is followed by an in-depth analysis of the novel correlated phase discovered and its connection to the Coulomb gap observed in classically disordered systems.

3.4 Phase diagram

In this chapter we study a quantum lattice model with generic interactions of the form $R^{-\alpha}$. Our model essentially serves as a hybrid be-

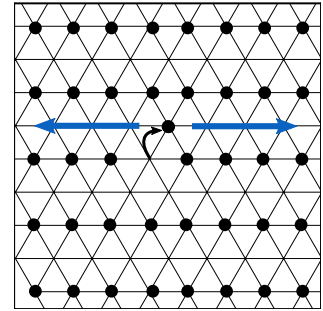


Figure 3.9: Creation of a defect (black arrow) in the stripe-ordered phase in the thermodynamic limit. The blue arrows indicate the directions in which the defect can move, thereby gaining kinetic energy.

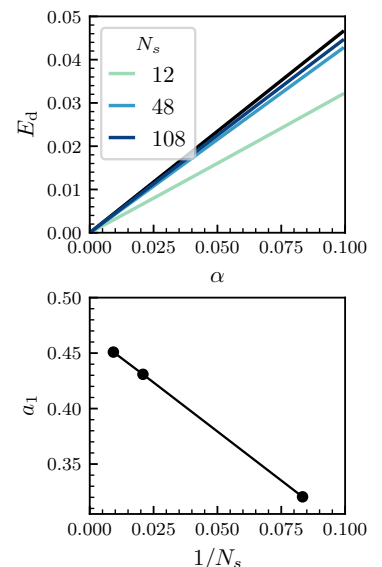


Figure 3.10: The defect creation energy, E_d , as a function of α for different system sizes with N_s sites (top panel). The black line indicates the asymptotic limit calculated through finite-size scaling (bottom panel).

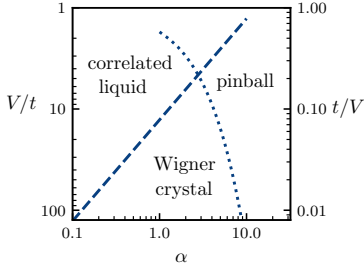


Figure 3.11: Preliminary estimate of the phase diagram in $(V/t, \alpha)$ space for our long-range interacting Hamiltonian constructed from estimates for the transitions from pinball to Wigner crystal (dotted) and from Wigner crystal to correlated metal (dashed).

tween the conventional Hubbard model which is used to strongly correlated lattice systems and the Pariser-Parr-Pople model which examines long-range interactions in quantum chemistry calculations [164]. We reproduce the Hamiltonian here for the convenience of the reader,

$$H = -t \sum_{\langle ij \rangle} (\hat{c}_i^\dagger \hat{c}_j + h.c.) + \frac{1}{2} \sum_{ij}^{N_s} V_{ee}(R_{ij}, \alpha) (\hat{n}_i - \bar{n})(\hat{n}_j - \bar{n}). \quad (3.13)$$

The two main parameters of interest to us are the range of the interactions, α , and the ratio of the interaction strength to the kinetic energy, V/t .

Arguably the most fundamental classification that we can make is to determine whether the system is an insulator or a metal with respect to these parameters. This task can be carried out by an analysis of a quantity known as the Drude weight, D , which represents the response of the system to a static electric field. Equivalently, D corresponds to the $\omega = 0$ limit of the optical conductivity [165]. The optical conductivity is a measure of the current-current correlation function and at $T = 0K$ has the form

$$\sigma(\omega) = D\delta(\omega) + \sigma_{\text{reg}}(\omega). \quad (3.14)$$

In the case of a metal, we expect a finite value of D whereas the Drude weight of an insulator will vanish [166]. With TBCs, the Drude weight can easily be computed as an average over a grid of flux points (as in Ref. [149]). At each flux point, we evaluate

$$\frac{D_\mu(\varphi)}{2\pi e^2} = \frac{1}{2N_s} \langle 0, \varphi | F_{\mu\mu} | 0, \varphi \rangle + \frac{1}{N_s} \sum_{n \neq 0} \frac{|\langle n, \varphi | J_\mu | 0, \varphi \rangle|^2}{E_0(\varphi) - E_n(\varphi)} \quad (3.15)$$

where

$$J_\mu = \frac{\partial H}{\partial \varphi_\mu} \quad \text{and} \quad F_{\mu\nu} = \frac{\partial^2 H}{\partial \varphi_\mu \partial \varphi_\nu}. \quad (3.16)$$

and μ, ν represent directions along the lattice. The notations $|0, \varphi\rangle$ and $|n, \varphi\rangle$ indicate the ground state and the n -th excited state, respectively, for a given flux, $\varphi = (\varphi_x, \varphi_y)$. As a reminder, TBCs only modify the hopping terms of the Hamiltonian which enables this particular expression of the Drude weight in terms of derivatives of the flux.

Based upon these calculations, we present a rudimentary phase diagram of the long-range interacting model (Eq. 3.13) as a function of the power-law exponent α and interaction strength, V/t , in Fig. 3.12. The color map represents the value of the ratio of the Drude weight to the non-interacting value, D/D_0 . This quantity enables us to quickly characterize areas of the phase diagram as metallic phases (blue regions) or insulating phases (light green regions). For Fig. 3.12, the Drude weight has been calculated in the \hat{x} direction of the rotationally symmetric $N_s = 12$ cluster on the triangular lattice. The classification in Fig. 3.12 roughly agrees so far with the general results that we established in the previous section: strong electronic interactions will drive

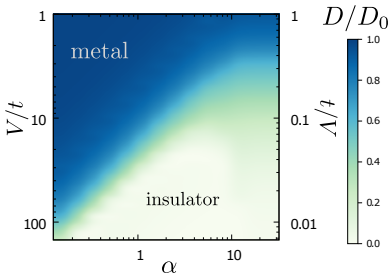


Figure 3.12: The color map is the Drude weight (697 grid points, $N_s=12$ sites, 400 TBCs).

the system towards an insulating state whereas quantum fluctuations promote the delocalization of electrons, resulting in a metallic state. We expect that the insulating phase will host a charge-ordered pattern, with threefold-order and stripe-order being equally likely in the limit of nearest neighbor interactions. We will examine this direction, along with other signatures of charge ordering, next.

With the primary characterization of the phase diagram by D/D_0 complete, we proceed to examine another observable to better define the different phases present—the charge correlation function evaluated in momentum space. This observable is defined as

$$C(\mathbf{q}) = \langle \psi_0 | \hat{\rho}_{\mathbf{q}} \hat{\rho}_{-\mathbf{q}} | \psi_0 \rangle, \quad (3.17)$$

where $|\psi_0\rangle$ is the ground state wave function and $\hat{\rho}_{\mathbf{q}}$ is the Fourier transform of the number operator

$$\hat{\rho}_{\mathbf{q}} = \frac{1}{\sqrt{N_s}} \sum_{i=1}^{N_s} e^{-i\mathbf{q}\cdot\mathbf{r}_i} \hat{n}_i.$$

This quantity allows us to determine the presence and structure of any charge ordering in the system. We begin by examining $C(\mathbf{q})$ for the nearest-neighbor type interactions ($\alpha \rightarrow \infty$) in the classical limit, $t/V = 0$. This corresponds to the lower right corner of Fig. 3.12. As mentioned in the previous section, there exist infinitely many classical configurations in which part of the particles are located on a superlattice with three-fold periodicity (wave vector $\mathbf{q} = K$) while the remaining charge density is distributed randomly throughout the remaining honeycomb sublattice [159, 160]. In other words, the threefold order corresponds to a peak in the charge correlation function at $\mathbf{q} = K$. The threefold-ordered particles on the superlattice are referred to as *pins* and the remaining particles are referred to as *balls*. These classically degenerate configurations all have the same Madelung (electrostatic) energy per site, $E_{\text{Mad}}/N_s = V/2$, as shown in Fig. 3.13.

As discussed in the previous section, finite quantum fluctuations ($t/V > 0$) will lift this degeneracy as the quantum fluctuations minimize the kinetic term for the balls (Fig. 3.14). This minimization yields a net energy gain $\propto t$ and leads to a unique ground state known as the pinball liquid [159]. The influence of the three-fold charge correlation remains from the classical limit (see Fig. 3.15) and this phase eventually evolves into a normal metal as the quantum fluctuations become the dominant energy scale ($t/V \rightarrow \infty$) [167]. As we are concerned primarily with the effect of long-range interactions, we will not spend more time discussing the pinball liquid, but the interested reader can find more information about this phase in Refs. [159, 167, 168]. Furthermore, as we are not interested in the pinball liquid, it is acceptable that one of our finite-size clusters with $N_s = 24$ sites does not respect three-fold symmetry as mentioned previously in Sec. 3.2.

We have already discussed how quantum fluctuations lift the macroscopic degeneracy of threefold-ordered ground state configurations in

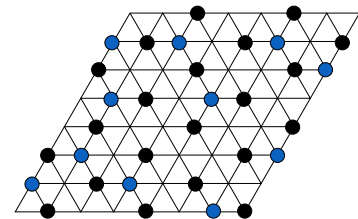


Figure 3.13: Example of three-fold order classical configuration with pins (black circles) and balls (blue circles).

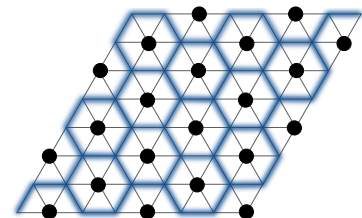


Figure 3.14: Illustration of pinball liquid where "pins" (black circles) are surrounded by the remaining charge density (blue) flowing over the hexagonal sublattice.

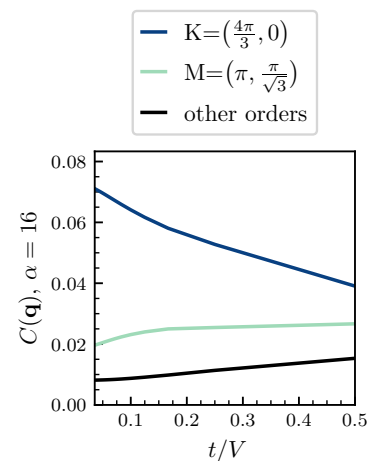


Figure 3.15: $C(\mathbf{q})$ as a function of t/V on the $N_s = 12$ site cluster (triangular lattice) for $\alpha = 16$. The threefold correlations ($\mathbf{q} = K$) remain high as the pinball liquid melts into a normal metallic state. The black line indicates $C(\mathbf{q})$ for all orders $\mathbf{q} \neq M, K$.

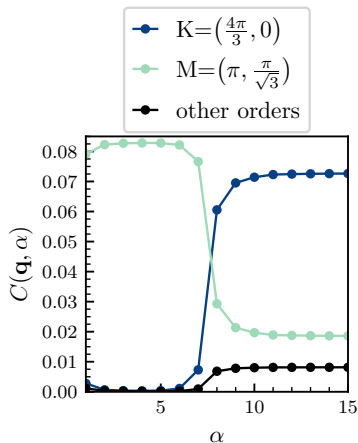


Figure 3.16: The evolution of the charge correlation function across the Wigner crystal-pinball liquid transition as a function of α . Results presented from the $N_s = 12$ site cluster at $V/t = 50$ with 16 points considered in the average over TBCs.

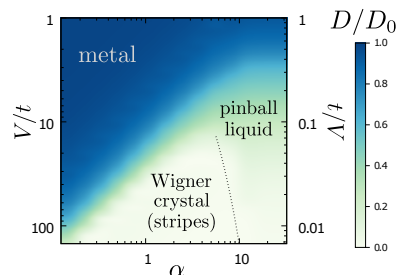


Figure 3.17: Updated phase diagram with the transition between the pinball liquid and Wigner crystal phase (dotted line).

this limit. This degeneracy can also be lifted with the inclusion of long-range interactions [110]. Therefore we next consider the effect of increasing the range of the interactions by decreasing the value of α in the electrostatic potential term. Let us assume that our starting point in the phase diagram is again the classical limit ($t/V = 0$) of a system with short-range interactions ($\alpha \rightarrow \infty$). As we reduce α , this corresponds to moving from the bottom right corner of Fig. 3.12 to the bottom left corner.

Increasing the range of interactions beyond that of nearest-neighbor interactions immediately lifts the degeneracy, leading to a charge-order insulator in which the charges form linear stripes with the ordering wave vector $\mathbf{q} = M$. This stripe-ordered phase is the lattice analogue of a Wigner crystal [162], and will remain insulating even in the presence of weak quantum fluctuations. This can be observed in a large region at the bottom of Fig. 3.17 where $D/D_0 \approx 0$ (light green in the colormap). Fig. 3.16 provides evidence for this transition by demonstrating the evolution of the momentum-resolved charge correlation function by varying α . We clearly observe a sharp transition for $\alpha_c \approx 7$ as the main contribution to $C(\mathbf{q})$ changes from $\mathbf{q} = M$ (stripe) to $\mathbf{q} = K$ (threefold). Note that for short-range interactions ($\alpha > \alpha_c$) the pinball order is not the uniquely dominant order present in the ground state, which can be seen by the fact that $C(\mathbf{q} = K)$ does not saturate at the maximum value $1/N_s \approx 0.083$. The predicted transition from this stripe-ordered insulating phase to the pinball liquid was previously discussed in Sec. 3.3 and we update our phase diagram to include this transition line (see Fig. 3.17, dotted line).

When the interactions are sufficiently long-ranged ($\alpha \leq 2$), the stability of the stripe-ordered insulator decreases with α , revealing a dome-like shape (see Fig 3.17). This instability is not surprising given the fragile nature of the Wigner crystal [116, 152]. This fragility manifests itself in the elusive nature of the Wigner crystal, which is difficult to detect and has only been observed in low-dimensional systems at very low temperatures [116, 169]. Recently, moiré bilayers in transition metal dichalcogenide heterostructures have been found to host Wigner crystals at a variety of fractional fillings [46, 120, 169]. Wigner crystals are typically described in terms of a dimensionless parameter, $r_s = r_0/a_B$, that describes the average distance between two electrons in units of the Bohr radius. Here r_0 represents the typical distance between two electrons and $a_B = \hbar^2/me^2$ represents the Bohr radius. The typical energy scales in a two-dimensional electron gas (with a pure Coulomb interaction) can be expressed in terms of this parameter as

$$E_{\text{Coul}} = \frac{e^2}{r_0} = \frac{2}{r_s} [\text{Ry}] \quad (3.18)$$

$$E_{\text{kin}} = \frac{E_F}{2} = \frac{\hbar^2}{2m_e r_0^2} = \frac{1}{r_s^2} [\text{Ry}] \quad (3.19)$$

where we have assumed that the kinetic energy follows from a parabolic

energy dispersion relation, $\varepsilon \propto k^2$, and E_F represents the Fermi energy [170]. The energies are reported in units of $1\text{Ry} = me^4/2\hbar^2 = 13.6\text{eV}$ and equating the two energies leads us to the estimated value $r_s = 1/2$. Wigner originally predicted the existence of the interaction-driven electron solid (Wigner crystal) in the low density limit ($r_s \gg 1$) where the Coulomb interaction dominates the kinetic energy [114]. Quantum Monte Carlo calculations have predicted that $r_s \simeq 31$ at the transition from crystal to liquid in the case of the two-dimensional electron gas [171]. This value is much larger than the rough estimate ($r_s = 1/2$) previously obtained, suggesting that quantum fluctuations play a key role in stabilizing the metallic phase. Furthermore, the large value of r_s implies that interaction effects should be strong at the transition and thus, we anticipate that the liquid phase obtained upon melting from the stripe-ordered phase will similarly display strong interaction effects. In particular, we expect that the stripe-ordered phase will melt due to low-lying, shear collective modes (as is the case in the classical electron solid [152]) and that the resulting metallic phase will exhibit short-range spatial correlations similar to those in the stripe-ordered crystal [172], giving rise to a large correlation energy.

In the previous section, we discussed the role of charge fluctuations in the melting transition as a function of α by examining the low-lying excitations, or defects, from the stripe-ordered phase. The quantum melting transition occurs when the gain in kinetic energy associated with the proliferation of these defects outweighs the cost to create a defect, $t \sim E_d$ [161–163]. We previously obtained a qualitative estimate for the melting transition and have updated the phase diagram with this estimate (dashed line) in Fig. 3.19. At this point, the stripe-ordered phase melts into a metallic state, driven by charge fluctuations that are favored by the long-ranged nature of the interactions. In the process, the metallic system inherits strong correlation effects, reminiscent of the melting of the Wigner crystal in the continuum.

As a reminder, the colormap in Fig. 3.20 indicates the value of the Drude weight with respect to the non-interacting value, D/D_0 , computed on a finite cluster of $N_s = 12$ sites and averaged over 400 TBCs. The metal-insulator transition occurs when this quantity vanishes which corresponds to the light green region of the colormap. The solid black dots in Fig. 3.19 indicate the position of the metal-insulator transition in terms of V/t and α as computed on a finite cluster of $N_s = 18$ sites. The values reported correspond to an average obtained over 121 TBCs. Despite the use of symmetries and shifted flux points, some spurious degeneracy effects were observed that led to the removal of a subset of points from the average. This removal was conducted by implementing a cutoff and discarding nonphysical values below the cutoff ($D/D_0 \leq -0.05$). For any given α and V/t , at most 30 points were discarded which still yields an accurate averaging over 91 flux points. The development of a more rigorous evaluation is currently underway that employs an alternative definition of D in

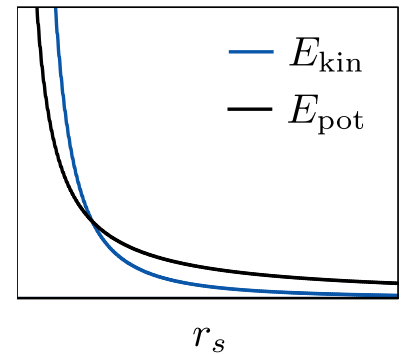


Figure 3.18: The Coulomb interaction (black) dominates the kinetic energy (blue) in the Wigner crystal limit.

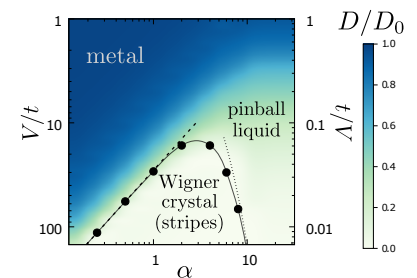


Figure 3.19: Updated phase diagram with the transition between the pinball liquid and Wigner crystal phase (dashed line), and the transition between the (correlated) metallic phase and the Wigner crystal phase.

Figure 3.20: Phase diagram of the triangular lattice model with long-range interactions. The line and the full symbols indicate the metal-insulator transition to a stripe-ordered Wigner crystal, signaled by the vanishing of the Drude weight D ($N_s=18$ sites, using 121 TBCs). The color map is the Drude weight (697 grid points, $N_s=12$ sites, 400 TBCs). The gray dashed line is the charge ordering transition as obtained from the random phase approximation (RPA), which ignores correlations and does not capture the extreme fragility of the Wigner crystal. The black dashed and dotted lines are strong-coupling estimates for the Wigner crystal melting.

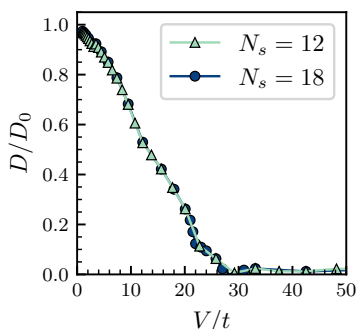
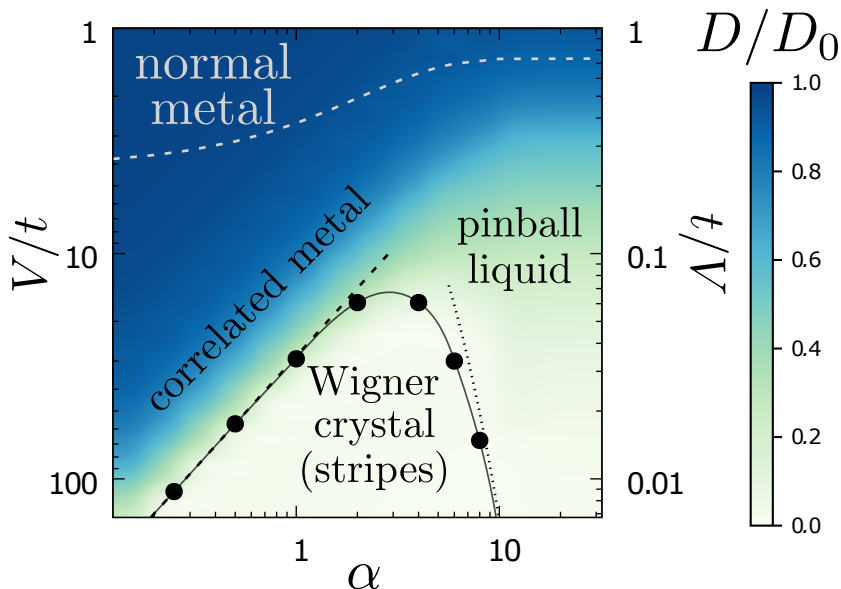


Figure 3.21: Finite size comparison of D/D_0 for clusters with $N_s = 12$ sites (green) and $N_s = 18$ sites (blue).

terms of the curvature of $E(\varphi)$.

We bring the reader's attention to the fact that the results agree remarkably well for different system sizes, which suggests that the finite size effects that can plague exact diagonalization calculations are controlled by the use of TBCs and the Ewald summation technique. The finite size agreement is also shown in Fig. 3.21 for the pure Coulomb case, $\alpha = 1$. Additionally, we would like to emphasize the impressive agreement between our transition estimates and the numerical results for the transitions.

At this point, we would like to complete the phase diagram by considering an estimate for the region in which electron-electron correlation effects are strong. This preliminary estimate is achieved by a comparison of our results for the metal-insulator transition with those predicted by the random phase approximation (gray dashed line, Fig. 3.20) [173]. The random phase approximation is a mean-field level approximation that is capable of correctly capturing the onset of local charge order. However, this technique predicts the metal-insulator transition to occur at much lower values of the interaction strength, V/t , than we observe in our exact diagonalization results. This oversight occurs because this mean-field treatment completely neglects the strong correlation effects inherited from the charge-ordered insulating phase at small α . These strong correlation effects will be discussed in more detail in the following sections.

We can conclude that the region between the long-range ordering line and the RPA line corresponds to a novel correlated metallic phase. At this point, we have identified four unique phases in the phase diagram as a function of V/t and α : normal metal, pinball liquid, stripe

ordered insulator (Wigner crystal), and correlated metal (see Fig 3.20). If we examine more closely the pure Coulomb case ($\alpha = 1$), we observe that it indeed qualifies as part of the small α region of the phase diagram where strong interaction effects are expected to play an important role on the metallic side of the metal-insulator transition. As reference, the critical interaction strength is $(V/t)_c \simeq 29$, which corresponds to $r_s = 7.2$. We bring the reader's attention to the fact that this is lower than the value expected in the continuum ($r_s = 31$). This reflects the fact that commensurability with the underlying lattice stabilizes the Wigner crystal [174, 175]. Furthermore, we understand that the long-range contribution to the creation of a defect is much lower than the local, short-range scale ($E_d^{\alpha=1} \ll V$). This suggests that there is a separation of energy scales between the local order ($E_{\text{local}} \sim V$) and the global, long-range order ($E_{\text{global}} \sim E_d^{\alpha=1}$) that is responsible for both collective behavior and the quantum melting transition. This separation of energy scales shall have significant consequences on the electronic properties of the metal as shall be discussed in the following sections.

In summary, we have established the phase diagram of our long-range interacting spinless model presented in Eq. (3.13) in terms of interaction strength, V/t , and range, α . The numerical results coincide remarkably well with analytical estimates obtained from the classical limit (discussed in detail in Sec. 3.3). Strikingly, the phase diagram in Fig. 3.20 qualitatively resembles that of the classical electron solid in $d = 3$ [152], assuming that one considers the quantum fluctuations, t , on the same footing as the thermal fluctuations, T . We produce here a rough comparison of the two phase diagrams in Fig. 3.22 to highlight this analogy. The classical phase space, described by the interaction range, α , and temperature, T , displays a Wigner crystal phase in a region that is roughly equivalent to that of the quantum version. The classical results also demonstrate the existence of a pseudogap phase that eventually melts into a normal metal beyond the RPA prediction (blue, dashed line). Indeed, the classical results foreshadow the significance of strong electronic correlations arising from the Wigner crystal phase which will be discussed in greater detail in the remainder of this chapter.

3.5 Correlated pseudogap metal

In this section, we will delve deeper into the presence of electronic correlations and their ensuing effects by focusing on the pure Coulomb case of repulsive interactions ($\alpha = 1$). We shall begin by providing evidence for correlation effects in the metallic state obtained upon the melting of the stripe-ordered insulator by quantum fluctuations. Furthermore, we will discuss how the correlation mechanism differs significantly from the conventional Mott-Hubbard mechanism and the generality of results in terms of lattice geometry. We argue that the fol-

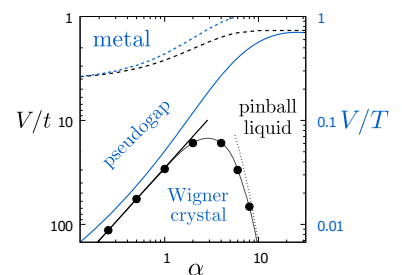


Figure 3.22: Comparison of the two-dimensional quantum phase diagram of our model (black) to the three-dimensional classical phase diagram of Ref. [152] (blue).

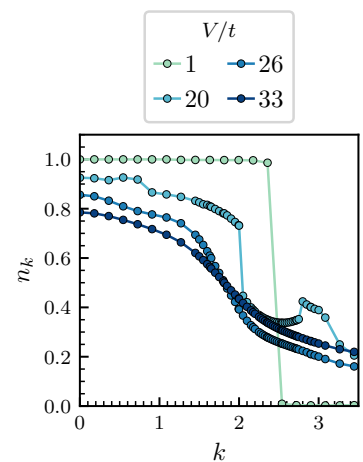


Figure 3.23: The occupation function, $n_{\mathbf{k}}$, as a function of the k_y component of \mathbf{k} . The transition from occupied ($n_{\mathbf{k}} = 1$) to unoccupied ($n_{\mathbf{k}} = 0$) is quite sharp for weak interactions. However, the discontinuity closes with increasing interaction strength, eventually disappearing as the system transitions from metal to insulator.

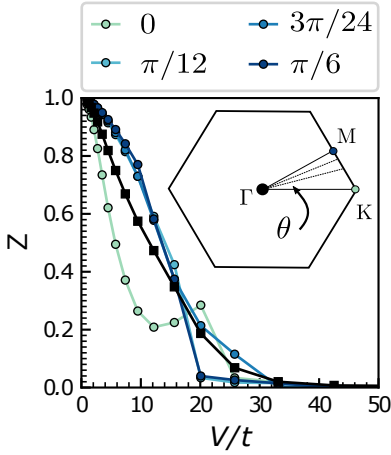


Figure 3.24: The quasiparticle weight Z computed over a path in momentum space dictated by the angle θ from the horizontal (shown in inset). The average over all paths is shown in the black line with square symbols.

lowing information clearly indicates that long-range interactions provide a novel method for correlated behavior in quantum materials.

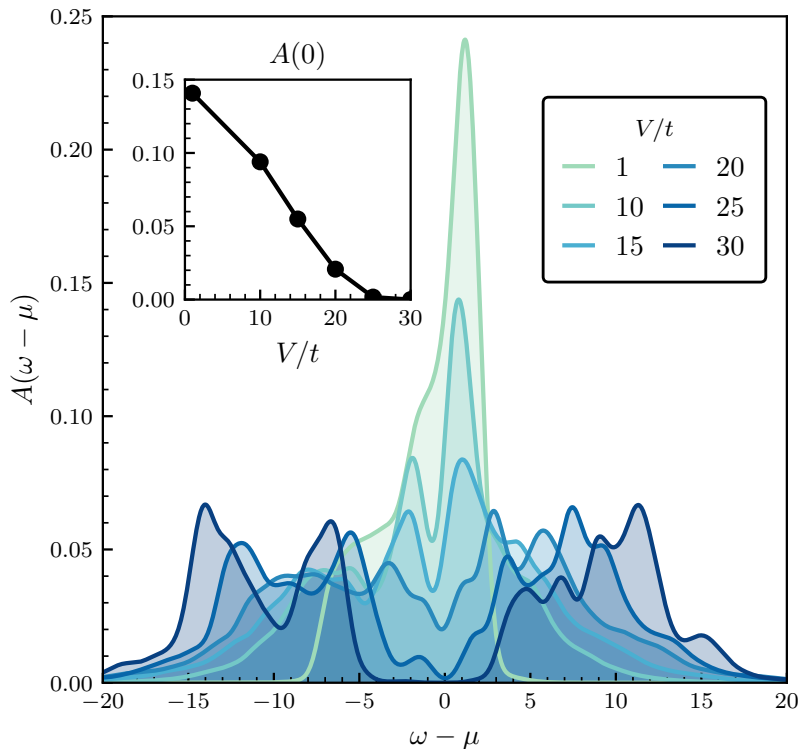
We begin with a discussion of the quasiparticle weight, Z , as it is a direct indicator of the correlated nature of a system. This quantity is calculated as the magnitude of the discontinuity of the occupation function, $\langle n_{\mathbf{k}} \rangle = \langle \psi_0 | \hat{n}_{\mathbf{k}} | \psi_0 \rangle$, where $\hat{n}_{\mathbf{k}} = \hat{c}_{\mathbf{k}}^\dagger \hat{c}_{\mathbf{k}}$ with $\hat{c}_{\mathbf{k}}$ ($\hat{c}_{\mathbf{k}}^\dagger$) the Fourier transform of the annihilation (creation) operator in real space, \hat{c}_i (\hat{c}_i^\dagger). TBCs enable us to compute this quantity along a finely discretized path in momentum space. For a given path, we begin by determining $\langle n_{\mathbf{k}} \rangle$ at $\mathbf{k} = 0$ (the Γ point). We then apply a flux such that \mathbf{k} is shifted by the pseudo-momentum associated to the boundary conditions [144]. The shift is controlled such that \mathbf{k} lies along the line in momentum space dictated by the given path. An example of the jump (discontinuity) in $\langle n_{\mathbf{k}} \rangle$ that closes upon approach of the metal-insulator transition, $(V/t)_c \approx 29$, is shown in Fig. 3.23. As can be seen in this figure, the reported values for $\langle n_{\mathbf{k}} \rangle$ display non-monotonic behavior for $V/t = 20$. Whether this non-monotonic behavior is a numerical artifact or a sign of Fermi surface distortion at the approach of the transition remains an open question.

Our results indicate some degree of anisotropy, stemming from an anisotropic quasiparticle renormalization. Therefore, we computed Z as an angular average over four different paths, shown in Fig. 3.24. The angle θ is measured from the line between Γ and the high symmetry point K located at the corner of the Brillouin zone (see Fig. 3.3). We note that Z goes to zero as V/t approaches its critical value, $(V/t)_c \approx 29$, signaling that the effective quasiparticle mass, $m_{\text{eff}} \sim 1/Z$, diverges at the approach of the melting transition and that the metallic phase becomes more correlated [176]. Indeed, the divergence of the quasiparticle mass can be described as a signature of strongly correlated systems. This quantity also diverges in the well-studied Mott metal-insulator transition, with its divergence arising from the zero frequency peak of the single-particle spectral function.

In order to understand if we have a similar mechanism driving the strongly correlated behavior in our model, we next consider the single-particle spectral function, $A(\omega)$. The spectral function, reported from calculations on the $N_s = 18$ site system, is evaluated as

$$A(\omega) = -\frac{1}{\pi} \text{Im} \sum_{i=1}^{N_s} \sum_{n \neq 0} \frac{|\langle \psi_n^{N+1} | \hat{c}_i^\dagger | \psi_0^N \rangle|^2}{\omega - (E_n^{N+1} - E_0^N) + i0^+} + \frac{|\langle \psi_n^{N-1} | \hat{c}_i | \psi_0^N \rangle|^2}{\omega - (E_0^N - E_n^{N-1}) + i0^+}, \quad (3.20)$$

where the summation over i indicates a sum over the discrete lattice sites in real space. The subscripts on the wave functions indicate the ground or n -th excited state, while the superscripts indicate the number of particles. As we are interested in the half-filled case in our spinless model, N corresponds to 9 particles on the 18 site cluster (similarly,



$N + 1 = 10$ and $N - 1 = 8$).

When we examine the evolution of $A(\omega)$ as a function of V/t leading up to the ordering transition (Fig. 3.25), we observe that a pseudogap opens at the Fermi energy ($\omega = \mu$). This pseudogap progressively deepens and widens as the single-particle excitations move toward higher energies, $\omega \sim V/t$. The density of states at the Fermi energy, $A(\omega = \mu)$, falls approximately linearly with V/t , then flattens deep in the pseudogap phase and eventually vanishes at the MIT at $(V/t)_c \simeq 29$ (inset of Fig. 3.25). Beyond the transition point, the pseudogap coalesces into a hard (insulating) gap in the stripe phase.

As the interaction strength increases, the development of a pseudogap combined with the divergence of the quasiparticle mass ($m_{\text{eff}} \sim 1/Z$) implies that the long-ranged interactions cause an ordering transition that is markedly different from the conventional Mott-Hubbard mechanism. In the Mott-Hubbard metal-insulator transition, the spectral function features a quasiparticle peak that remains pinned at the Fermi energy ($\omega = \mu$) and the narrowing of this peak with Z causes the divergence of the effective mass [20, 148]. However, our results find a divergence of the quasiparticle mass in the *absence* of a pinned peak. Instead, the value of the renormalized density of states at the Fermi energy, $A(\mu)$, falls continuously to 0, thereby controlling the quasiparticle renormalization (Fig. 3.25).

Before proceeding, we take a moment to discuss a few technical as-

Figure 3.25: Spectral function $A(\omega)$ at $\alpha = 1$ and $N_s = 18$ and averaged over 121 TBCs, illustrating the pseudogap phenomenon. All spectra are smoothed by a Gaussian broadening $\delta = 0.5t$. Inset shows how $A(\omega = \mu)$ decreases in a linear manner until vanishing at the transition.

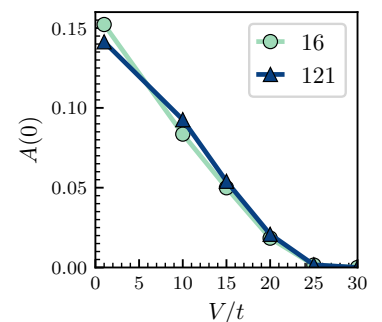


Figure 3.26: Using a grid of flux points with $N_\phi = 16$ (black) is already sufficient to track the behavior of $A(\omega = \mu)$ in the pseudogap phase. Increasing the number of flux points to $N_\phi = 121$ displays the same trend in $A(0)$.

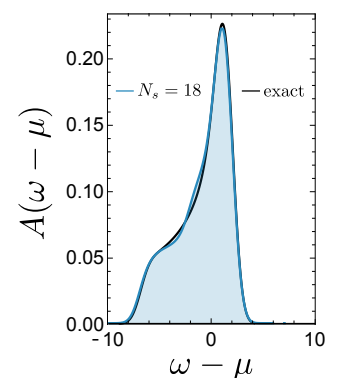


Figure 3.27: A comparison of the non-interacting spectral function on the triangular lattice in the thermodynamic limit (black) and averaged over 121 twisted boundary conditions for a calculation on the $N_s = 18$ site cluster (blue) with Gaussian broadening $\delta = 0.5t$.

Figure 3.28: The development of the pseudogap in the spectral function on the square lattice for $\alpha = 1$ as V/t is increased (gradient of green to blue lines; the corresponding values of V/t are indicated in the figure legend; Gaussian broadening $\delta = 0.7t$). The inset shows the value of $A(\omega - \mu)$ at $\omega = \mu$ which steadily decreases before a hard gap opens at $V/t \approx 8$. Values are reported for a finite cluster with $N_s = 18$ sites and averaging over $N_\varphi = 121$ flux points.

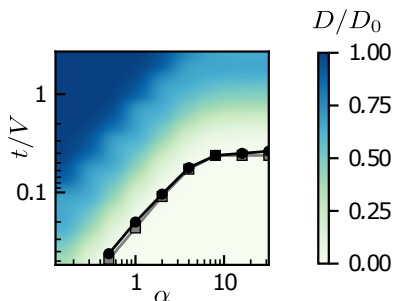
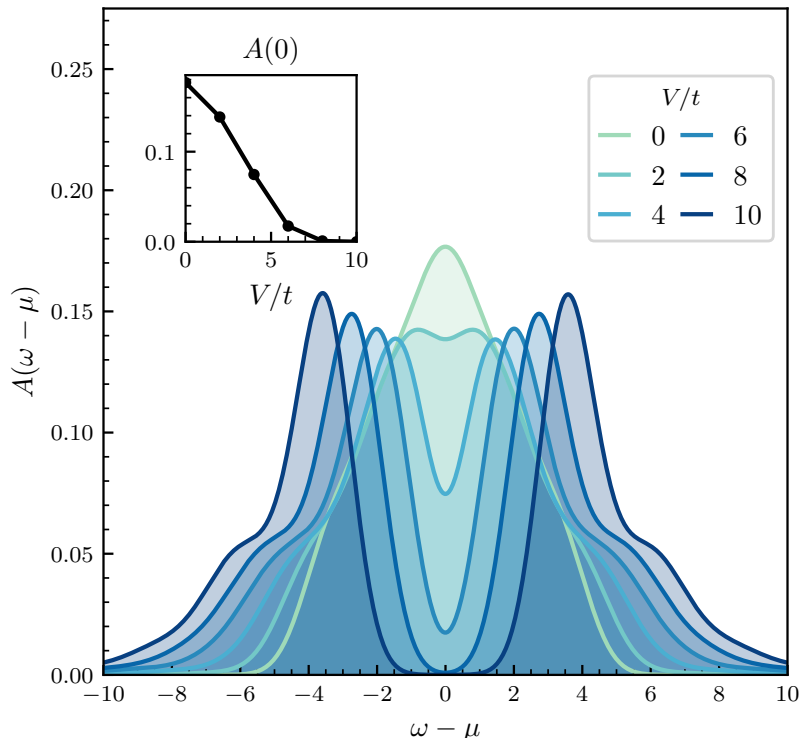


Figure 3.29: Phase diagram of the long-range interacting spinless model on the square lattice. As previously seen, colormap corresponds to the ratio of the Drude weight to the non-interacting value, D/D_0 . The metal-insulator transitions computed with $N_\varphi = 16$ points (gray squares) and $N_\varphi = 400$ points (black circles) are shown.

pects regarding the computation of the spectral function. The results presented in Fig. 3.25 were obtained by averaging over spectra evaluated at $N_\varphi = 121$ flux points (boundary conditions). However, Fig. 3.26 demonstrates that the spectral function was already well-converged for the 4×4 grid of flux points and increasing the size of the mesh to 11×11 did not qualitatively change the results. Furthermore, we demonstrate how averaging over TBCs, coupled with Gaussian filtering, enables us to reach the exact, thermodynamic result of $A(\omega)$ in the non-interacting case in Fig. 3.27.

One might argue that the existence of a correlated, pseudogap phase is model-specific and possibly linked to the frustrating lattice geometry in our model (triangular lattice). Indeed, charge frustration arising from the quarter-filling on the triangular lattice is suspected to give rise to the exotic phases observed in the $\theta - (\text{ET})_2\text{X}$ salts [59, 177, 178]. However, we show that the development of a pseudogap is a general effect that does not depend on the geometry of the lattice. Indeed, the collective behavior arising from long-range interactions necessarily involves the coordination of many sites, regardless of the local lattice geometry.

The spectral function for our long-range interacting model on the square lattice is shown in Fig. 3.28 and similarly displays a pseudogap that deepens and widens with V/t upon the approach to the ordering transition. However, for short-ranged interactions, the square lattice

will not give rise to a pinball liquid phase because the local coordination number does not frustrate the charge order at half-filling (one particle every two sites). The phase diagram for the square lattice computed for $N_s = 12$ is provided in Fig. 3.29. It is interesting to note that Refs. [152,162,179] have demonstrated frustration of charge order arising from long-range interactions in otherwise non-frustrated lattices (square, cubic) in the classical limit. In summary, the development of a strongly correlated pseudogap phase arising from long-range interactions is a general phenomenon and does not rely on the geometrical frustration of the lattice.

In this section we have focused on the pure Coulomb case ($\alpha = 1$) in order to investigate the correlated nature of the metallic state reached upon melting of the stripe-ordered (Wigner crystal) phase in the small α region of the phase diagram (Fig. 3.20). We have examined the quasiparticle weight, Z , as a measure of the strength of correlations and we have demonstrated that it is strongly reduced in the correlated metal phase, before eventually disappearing at the metal-insulator transition. This behavior indicates the divergence of the quasiparticle mass, which is usually associated with a narrowing peak at the Fermi level in the Mott-Hubbard picture.

However, our results for the single-particle spectral function clearly establish the absence of such a peak that drives the mass divergence. Indeed, we have demonstrated that the long-range interactions in our model act as a novel mechanism of strongly correlated behavior in giving rise to a pseudogap in the spectral function. This signature of strongly correlated behavior is *not* limited to conventionally frustrated systems, as shown by the presence of a pseudogap in the results on the square lattice. In the remainder of this chapter we shall investigate the general nature of this mechanism and draw parallels with classically disordered systems. These systems typically exhibit so-called Coulomb gaps in their density of states as a result of the long-range interactions, a phenomenon remarkably similar to what we have observed here.

3.6 *Self-induced disorder*

We have established that long-range interactions provide a general mechanism for strongly correlated behavior in quantum electrons at zero temperature. We now proceed to investigating the details of this mechanism. We begin by remarking that the presence of a pseudogap in the spectral function (see Figs. 3.25 and 3.28) is strongly reminiscent of the soft Coulomb gap characteristic of disordered insulators. In those systems, the long-range interactions of an interacting electron system with quenched disorder causes the density of states to vanish at the Fermi energy, creating a so-called Coulomb gap [180]. A similar Coulomb gap phenomenon has also been established in classical Coulomb liquids in the absence of disorder. In these clean liq-

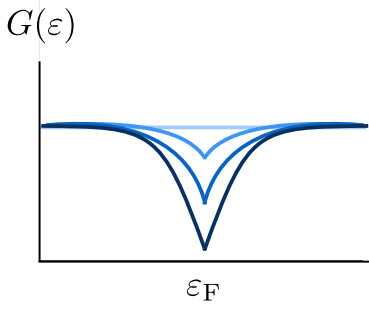


Figure 3.30: Sketch of the suppression of the density of states in the Coulomb gap with increasing interaction strength (gradient light to dark blue lines).

uids, the long-range interactions from electrons beyond the correlation length act as a source of self-generated disorder when considered collectively [110, 152, 179, 181, 182].

In 1975, Efros and Shklovskii proposed that long-range interactions would necessarily suppress the density of states of disordered systems, $G(\varepsilon)$, near the Fermi surface at $T = 0\text{K}$ such that $G(\varepsilon)$ would tend to zero as

$$G(\varepsilon) \lesssim |\varepsilon|^{d-1}, \quad (3.21)$$

where d is the dimensionality of the system [180] (see Fig. 3.30). The presence of such a Coulomb gap was confirmed with a classical Hamiltonian that included an external disordered potential term at finite temperature [180, 183]. In 1992, Efros further demonstrated that external disorder was not necessary to deplete the density of states at the Fermi level [181]. Instead, long-range Coulomb interactions act as a source of self-generated disorder that depletes the density-of-states, $G(\varepsilon)$, and the Efros-Shklovskii Coulomb gap phenomenon was speculated to occur as well in quantum electrons at $T = 0\text{K}$ [181]. We demonstrate its existence here.

To determine if the long-range interactions generate a source of disorder that drives the development of the pseudogap (Fig. 3.25), we examine the distribution of on-site energies, arising from the electrostatic interactions between electrons. Our interaction potential is defined with a summation over all pairs of sites, $\sum_{ij}^{N_s}$. From this complex interaction, it is not directly straightforward to disentangle the effects of one site from the rest. Thus, we rewrite the potential as

$$E_{\text{pot}} = \frac{1}{2} \sum_{ij}^{N_s} V(R_{ij}, \alpha) (\hat{n}_i - \bar{n})(\hat{n}_j - \bar{n}) \rightarrow \frac{1}{2} \sum_i^{N_s} (\hat{n}_i - \bar{n}) \underbrace{\sum_j^{N_s} V(R_{ij}, \alpha) (\hat{n}_j - \bar{n})}_{\phi_i} \quad (3.22)$$

where we identify the on-site potential as ϕ_i . This quantity is the electrostatic interaction that a particle feels when it is located at site i . The distribution of on-site potentials, $P(\phi_i)$, is then defined as

$$P(\phi_i) = \left\langle \psi_0 \left| \delta \left(\phi_i - \sum_{j \neq i} V(R_{ij}, \alpha) (\hat{n}_j - \bar{n}) \right) \right| \psi_0 \right\rangle, \quad (3.23)$$

where $|\psi_0\rangle$ is the ground state wave function and the average electronic density, \bar{n} , has been included in ϕ_i to ensure charge neutrality, thereby centering the results around $\phi_i = 0$. As the system is translationally invariant, we can consider the distribution of on-site potentials for a fixed reference site, $P(\phi) = P(\phi_i)$.

In the case of quantum electrons, $P(\phi)$ represents the fluctuating landscape where the electron motion takes place. Fig. 3.31 shows that a broad dip develops in $P(\phi)$ in a similar fashion to the pseudogap opening observed in the full electronic spectrum, $A(\omega)$. The inset of Fig. 3.31 illustrates the central value $P(0)$ vs V/t for clusters with

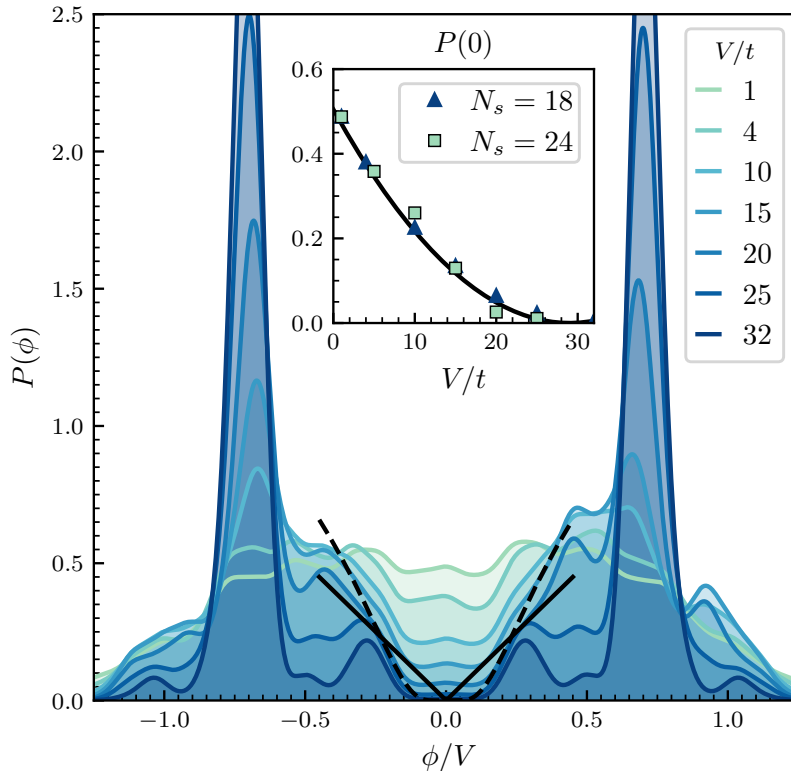


Figure 3.31: Distribution of the local electrostatic potentials, $P(\phi)$, showing the opening of the Coulomb gap. Also plotted are $P \sim e^{-V/\xi|\phi|}$ with $\xi = 2$ (dashed line) and $P = |\phi|$ (solid line). $P(\phi)$ was computed on a 4×4 grid of flux points for $N_s = 18$ and broadened with a Gaussian filter, $\delta = 0.05V$. The inset shows the central value $P(0)$ vs V/t for $N_s = 18$ (blue triangles) and 24 (green squares), and $P(0) \sim |V - V_c|^2$ (black line).

$N_s = 18$ and 24 sites, demonstrating that finite-size effects are under control. We would like to emphasize that this pseudogap behavior is unique to systems with long-range interactions. With decreasing range of interaction (increasing α), the spectrum of on-site electrostatic potentials loses its continuous nature. This can be understood intuitively from the nearest-neighbor limit, $\alpha \rightarrow \infty$. In a nearest-neighbor model, the only sources of interaction arise from neighboring sites that are occupied. Therefore, the total on-site electrostatic potential can only assume values that are integer multiples of V , where the maximum integer value corresponds to the coordination number of the lattice. The discrete nature of $P(\phi)$ for short-range interactions is shown in Fig. 3.32 for the case $\alpha = 8$. At weak values of interaction strength, we observe that multiple (discrete) values of ϕ are accessible. However, in the strong coupling limit, the system exists in a charge-ordered (stripe) phase where only two values, $+V$ and $-V$, are accessible.

When the system is in a charge-ordered state, the translational symmetry is spontaneously broken and we can expect a bimodal distribution to arise from the charge order. However, in the case of pure long-range interactions, shown in Fig. 3.31, we observe that a bimodal distribution develops in $P(\phi)$ far from the Wigner crystallization transition. The fact that this structure develops far from the transition indicates that the crystallization is truly a strong coupling phenomena

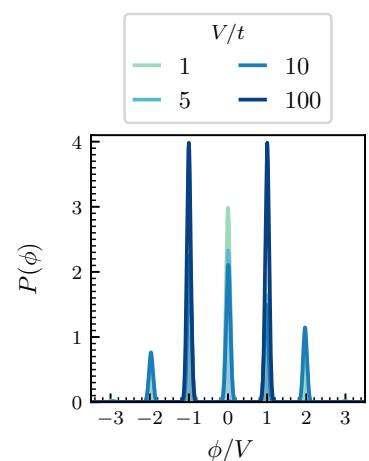
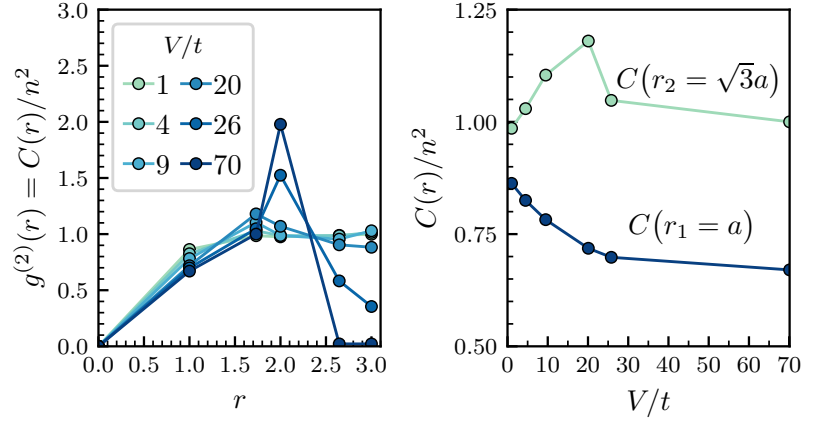


Figure 3.32: $P(\phi)$ for short-ranged interactions with $\alpha = 8$, averaged over a 4×4 grid of flux points.

Figure 3.33: The radial distribution function (left panel) as a function of distance r . The charge correlation function (right panel) evaluated at distances $r_1 = a$ (blue) and $r_2 = \sqrt{3}a$ (light green) that correspond to sites on the first and second shells, respectively, from a reference site.



and signals the presence of Coulomb polarons, analogous to what has been discovered boson-mediated charge ordering [184].

In addition to displaying a gap that falls with the pseudogap in $A(\omega)$, we would also like to comment on the fact that $P(\phi)$ near $\phi = 0$ is suppressed faster than the proposed upper bound, $|\phi|^{d-1} = |\phi|$ (solid black line in Fig. 3.31) [180, 185]. However, the shape of the soft gap in $P(\phi)$ at the transition is compatible with that caused by short-range charge correlations in self-generated Coulomb glasses, $P \sim e^{-V/\xi|\phi|}$ for $d = 2$ (dashed black line in Fig. 3.31) [179] where ξ is the correlation length. In these glassy systems, a correlation hole forms around the electrons in order to minimize their mutual repulsive interactions. This correlation hole was shown to deplete the classical DOS below the Efros-Shklovskii bound, $P_{ES} \sim |\phi|^{d/\alpha-1}$ in the general case of d dimensions and interaction exponent α [179]. This correlation hole, or electronic polaron, is a common feature of quantum electron liquids with unscreened Coulomb interactions [172].

To examine the behavior of short-range correlations in our system, we finally calculate the charge correlation function in real space,

$$C(r_i - r_j) = \sum_{i,j}^{N_s} \langle \psi_0 | \hat{n}_i \hat{n}_j | \psi_0 \rangle \quad (3.24)$$

where \hat{n}_i is the occupation number operator for site i in second quantization and $|\psi_0\rangle$ is the ground state. As the system is translation invariant, we can evaluate $C(r_i - r_j)$ at a reference site $r_j = 0$ and rewrite $C(r_i - r_j)$ as

$$C(r_i) = \sum_i^{N_s} \langle \psi_0 | \hat{n}_i \hat{n}_0 | \psi_0 \rangle. \quad (3.25)$$

This quantity is connected to the radial distribution function, shown in the left panel of Fig. 3.33, which details the electronic density modulation as a function of the distance away from the particle. We observe that the radial distribution function, $g^{(2)}(r) = C(r)/n^2$, steadily

decreases for the nearest-neighbor distance, $r = 1$ (in units of the lattice spacing a) as the interaction strength is increased. At the same time, $g^{(2)}(r)$ for the next-nearest-neighbor distance, $r = \sqrt{3}$, initially increases with V/t before becoming partially suppressed at the stripe-ordering transition (see right panel of Fig. 3.33). This quantity is only partially suppressed because some next-nearest-neighbor sites will necessarily be occupied in the stripe-order phase.

We are able to classify the sites $\{i\}$ into various shells surrounding the reference site (see Fig. 3.34). The first shell contains all of the nearest neighbors, $|r_i - r_0| = a$, while the second shell contains the next-nearest neighbors, $|r_i - r_0| = \sqrt{3}a$. In order to understand how the electronic correlation changes with increasing V/t , we compute the difference between the correlation with the second shell, C_2 , and that with the first shell, C_1 . The results are shown in Fig. 3.35 for calculations on the $N_s = 12$ and 18 site clusters. We observe that $C_2 - C_1$ increases leading up to the metal-insulator transition, $(V/t)_c \approx 29$. In other words, this signals the formation of a correlation hole around each charge carrier. This build-up of short-range correlation in the normal phase parallels the renormalization of the quasiparticle weight previously shown in Fig. 3.24, until it is eventually interrupted by the establishment of long-range stripe correlations at the metal-insulator transition.

In conclusion, the pseudogap observed in the single-particle spectral function evokes the concept of disorder-driven correlated behavior. In particular, we recall that long-range interactions act as a source of self-generated disorder in classical systems, leading to the development of the so-called Coulomb gap in the density of states. Here we have introduced a new observable, $P(\phi)$, that we refer to as the distribution of on-site electrostatic potentials. This quantity acts as the quantum version of the classical distribution of on-site energies and displays a soft gap that mirrors the pseudogap development in the spectral function.

Strikingly, the shape of the gap in $P(\phi)$ resembles that observed in Coulomb glasses which leads us to suspect that short-range correlations are responsible for the exponential form of the gap. We measure the build-up of these short-range correlations (the development of a correlation hole) by calculating the difference in correlation between a shell of next-nearest neighbor sites and a shell of nearest neighbor sites (with respect to a reference site). In summary, we conclude that long-range interactions act as a source of self-generated disorder beyond the correlation length, causing the suppression of the spectral function near the Fermi level. With this information in mind, we turn our attention to examining collective charge movement and excitations in the context of disordered electrostatic landscapes.

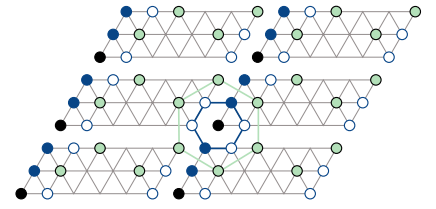


Figure 3.34: Assuming a diagonal stripe order for illustrative purposes, the first neighbors of a reference site (black) live on either an occupied stripe (full blue circles) or an unoccupied stripe (empty blue circles). The shell of second-nearest neighbors are shown in green.

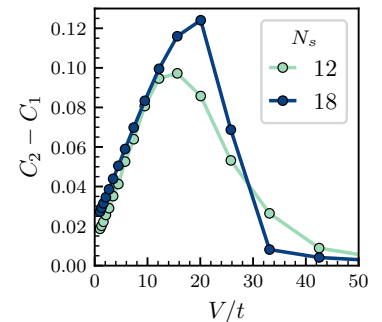


Figure 3.35: Difference of the charge-charge correlation function $C(r_i - r_j)$ computed on the second and on the first shell of neighbors, illustrating the buildup of the correlation hole.

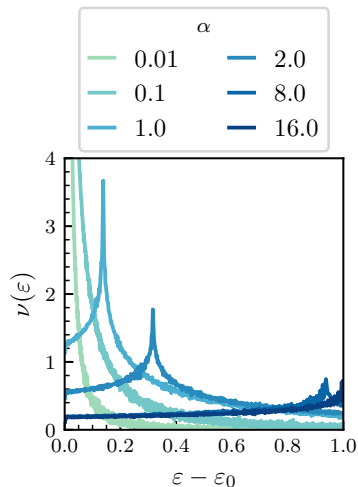


Figure 3.36: Classical spectral density of plasmon modes in $d = 2$ as a function of the excitation energy, $\varepsilon - \varepsilon_0$, and the interaction range, α .

3.7 Collective charge excitations

As discussed in the previous section, long-range interactions are capable of self-generating a disordered environment which leads to the existence of a strongly correlated, pseudogap phase on the metallic side of the metal-insulator transition. We emphasize that this is unrelated to the Mott-Hubbard mechanism for strongly correlated behavior which instead is controlled by a well-defined quasiparticle peak up to the transition. In this section, we turn our attention to understanding the nature of the low-lying charge excitations in the pseudogap phase with strong short-range correlations.

We begin by considering the classical limit, $t = 0$. In Sec. 3.4, we discussed the striking similarities in the phase diagrams of our quantum model with that of a classical system with long-range interactions [152]. In particular, we are interested in understanding the excitations in the correlated pseudogap phase leading up to the Wigner crystal ordering transition. In the classical case, where the fragility of the Wigner crystal is well-known, it has been shown that the Wigner crystal forms upon the freezing of the plasmon modes [152]. In other words, at the approach of the ordering transition, these collective density excitations slow down until they eventually freeze at the transition. As a function of the range of interactions, Fig. 3.36 shows the spectral density of these modes, defined as

$$\nu(\varepsilon) = \sum_k \delta(\varepsilon - V_k) \quad (3.26)$$

where V_k is the Fourier transform of the interaction potential. Specifically, we observe that increasing the range of interactions (decreasing α) results in a shift of the spectral peak (and the accompanying spectral weight) to lower values of the excitation energy, $\varepsilon - \varepsilon_0$. In other words, the Wigner crystal is more unstable to long-range interactions.

Naturally, we would like to apply these ideas to our quantum model in order to analyze the charge fluctuations present and their role in the observed strongly correlated behavior. As such, we examine the spectrum of collective charge fluctuations,

$$\mathcal{D}(\mathbf{q}, \omega) = \sum_n \left| \langle \psi_n | \hat{\rho}_{\mathbf{q}} | \psi_0 \rangle \right|^2 \delta(\omega - (E_n - E_0)) \quad (3.27)$$

where $\hat{\rho}_{\mathbf{q}}$ is the Fourier transform of the charge density (\hat{n}_i), and ψ_n and E_n are the n -th excited eigenstates and eigenenergies respectively. This quantity essentially measures collective fluctuations (excitations) corresponding to a particular charge order, as dictated by the wave vector \mathbf{q} . As we cross a charge-ordering transition from the disordered phase to the ordered phase, the corresponding mode ($\mathbf{q} = \mathbf{q}_{\text{order}}$) in the spectrum of charge fluctuations will go soft, $\omega_{\text{peak}} \rightarrow 0$. Therefore, we begin our discussion of the charge fluctuation spectrum from the metallic side of the metal-insulator transition and first consider the

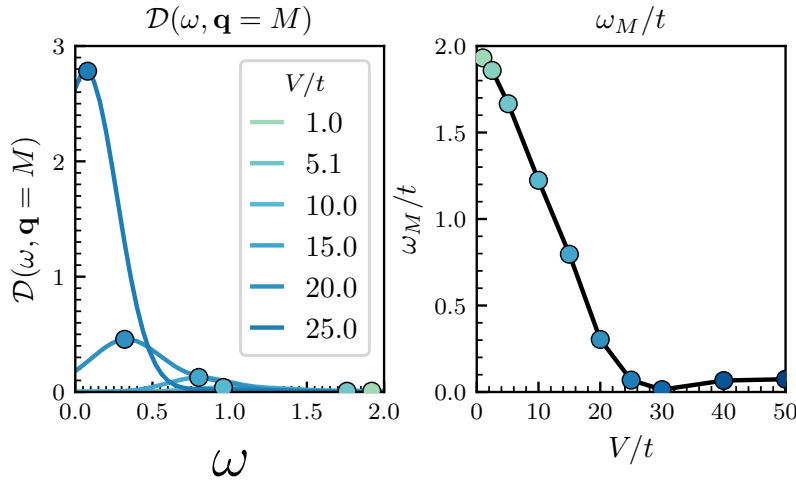


Figure 3.37: Left panel: $\mathcal{D}(\mathbf{q}, \omega)$ for $\mathbf{q} = M$, the stripe-order wave vector. A Gaussian broadening $\delta = 0.2t$ has been applied. The location of the critical mode is labeled with a circle. The values of V/t for both the lines and the markers corresponds to those in the legend. Right panel: The location of the peak as a function of V/t . Three additional values of V/t beyond $(V/t)_c$ are reported with the corresponding color in the legend.

wave vector corresponding to stripe order as this provides a straightforward, pedagogical introduction to the charge spectrum.

For our half-filled system on the triangular lattice, the stripe-ordered phase (wave vector $\mathbf{q} = M$) minimizes the repulsive interactions between the particles. Therefore, we track the evolution of $\mathcal{D}(\mathbf{q} = M, \omega)$ as a function of interaction strength leading up to the transition in Fig. 3.37. In the limit of weak interactions (small V/t), the spectrum is relatively flat with its maximum corresponding to a frequency $\omega \approx 2t$. However, as the interaction strength increases, this collective fluctuation mode strengthens into a peaked structure with the peak moving towards zero. The location of the peak is displayed as a function of V/t in the inset of Fig. 3.37. In other words, density fluctuations corresponding to the stripe order ($\mathbf{q} = M$) slow down and eventually freeze at the transition, $(V/t)_c \approx 29$.

We have seen that collective fluctuations related to the stripe-order wave vector are strong in the vicinity of the metal-insulator transition, $(V/t)_c \approx 29$. However, this is not the only relevant order in the charge spectral function going soft in the pseudogap phase upon the approach to the metal-insulator transition. In Fig. 3.38, we show $\mathcal{D}(\omega)$ averaged over all wave vectors \mathbf{q} (all orders). From the momentum-averaged charge spectral function shown in Fig. 3.38, we conclude that there are multiple, incipient charge orders competing with one another throughout the correlated pseudogap phase. This conclusion aligns well with that of Ref. [110] which demonstrated that long-range interactions in a similar classical system give rise to glassy behavior with a macroscopic degeneracy of metastable semi-ordered states. This can be seen in the diffuse signature of the charge correlation function, $C(\mathbf{q})$, around the Brillouin zone (see Fig. 3.39). This diffuse nature indicates that the system is susceptible to ordering along the entire edge of the Brillouin zone as many competing orders are frustrated by the long-range

Figure 3.38: Left panel: Spectral function, $\mathcal{D}(\omega)$, of the charge fluctuations averaged over the Brillouin zone (Gaussian broadening $\delta=0.2t$). Right panel: The frequency of the boson peak, controlling the timescale of the charge fluctuations. The peak frequency is compared for the averaged spectrum (blue) to the frequency obtained from $\mathbf{q} = M$ (black).

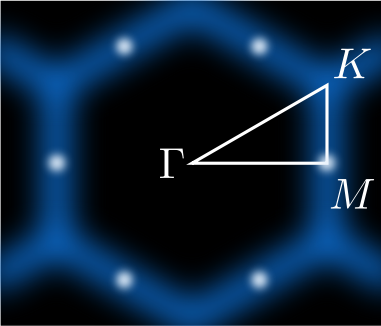
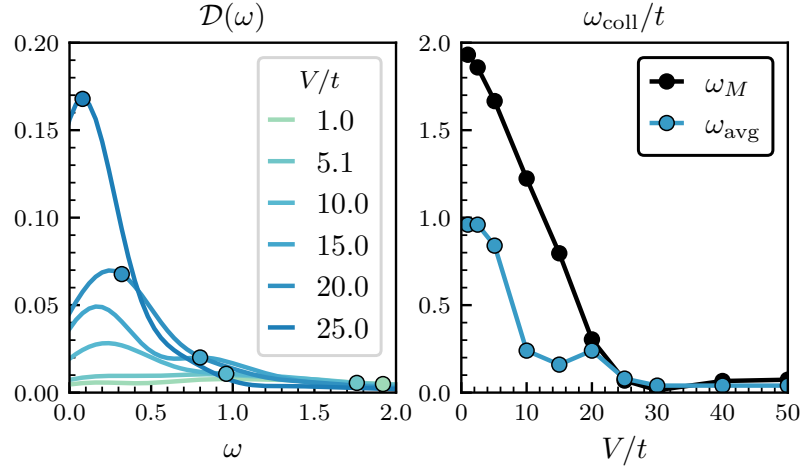


Figure 3.39: The intensity of the charge correlation function, $C(\mathbf{q})$, in the classical version of our model. Bright spots indicate well-defined Bragg peaks corresponding to stripe order, $\mathbf{q} = M$. Diffuse spots seen around the Brillouin zone indicate the presence of other competing orders. Adapted from Ref. [110].

interactions leading up to the transition [182]. In other words, the competition among many orders leads to the creation of a quasi-local order mediated by the charge fluctuations. Translated to real space, these zone-boundary features correspond to the buildup of a correlation hole, previously studied as $C_2 - C_1$.

Therefore, we conclude that the soft, collective mode seen in Fig. 3.38 arises from this diffuse region near the edges of the Brillouin zone. At weak values of the interaction strength, we see that the averaged mode occurs around $\omega_{\text{avg}} \sim t$, lower than the value corresponding to the stripe-order mode alone. As V/t increases, the system enters the pseudogap phase and $\omega_{\text{avg}} \sim 0.2t$, remaining lower than ω_M . Both modes soften at the approach of the transition, thereby indicating that the timescale of collective charge fluctuations is slowing down. Finally, as V/t approaches its critical value, the stripe order dominates and drives the system into the charge-ordered (Wigner crystal) phase.

Furthermore, we surmise that the long-range interactions produce a separation of timescales between individual and global charge motion. This separation is highlighted upon comparison of the bosonic frequency throughout the pseudogap phase ($\omega_{\text{avg}} \sim 0.2t$) to the bandwidth of the free electron model ($W = 9t$). The movement of individual electrons in nearest-neighbor hopping processes should occur rapidly. However, the long-range interactions create an energetic landscape with short-range correlations and longer-ranged disorder. These effects constrain the movement of the global charge background to a much longer timescale as a result.

In other words, changing from one disordered electrostatic configuration to another necessarily requires the coordination and movement of all of the charge carriers, but the mutual interactions of these carriers causes a collective jamming. This interaction-driven jamming essentially signifies that the charge fluctuations background is almost

frozen [182,186–188] because electrons now effectively move in a quasi-static disordered landscape, which in turn enables the Efros-Shklovskii phenomenon discussed earlier. The separation between the rapid movement of individual electrons in nearest-neighbor hopping processes and the much slower charge rearrangements on a global scale ought to have a profound impact on the transport properties of such systems. Indeed, this topic will be the discussion of the following chapter as we examine the possibility that long-range interactions act as a general mechanism for bad metallic transport in correlated systems.

3.8 Conclusions and summary

In summary, we have examined a spinless model of electrons with power-law repulsive interactions at zero temperature where the range of interactions is controlled by a continuous parameter, α . We have established the phase diagram in terms of interaction range and strength and classified the four distinct phases present: normal metal, pinball liquid, stripe-ordered insulator (Wigner crystal), and a novel correlated metallic phase [153]. This last phase exists for sufficiently long-ranged interactions, $\alpha \lesssim 2$. It is characterized by a suppression of quasiparticle weight Z and the development of a pseudogap in the spectral function $A(\omega)$ arising from the onset of charge order in the metal-insulator transition. This manifestation of electronic correlation is inherently different from that observed in conventional Mott-Hubbard physics where the divergence of the quasiparticle mass is instead driven by the narrowing width of the peak pinned at $\omega = \mu$.

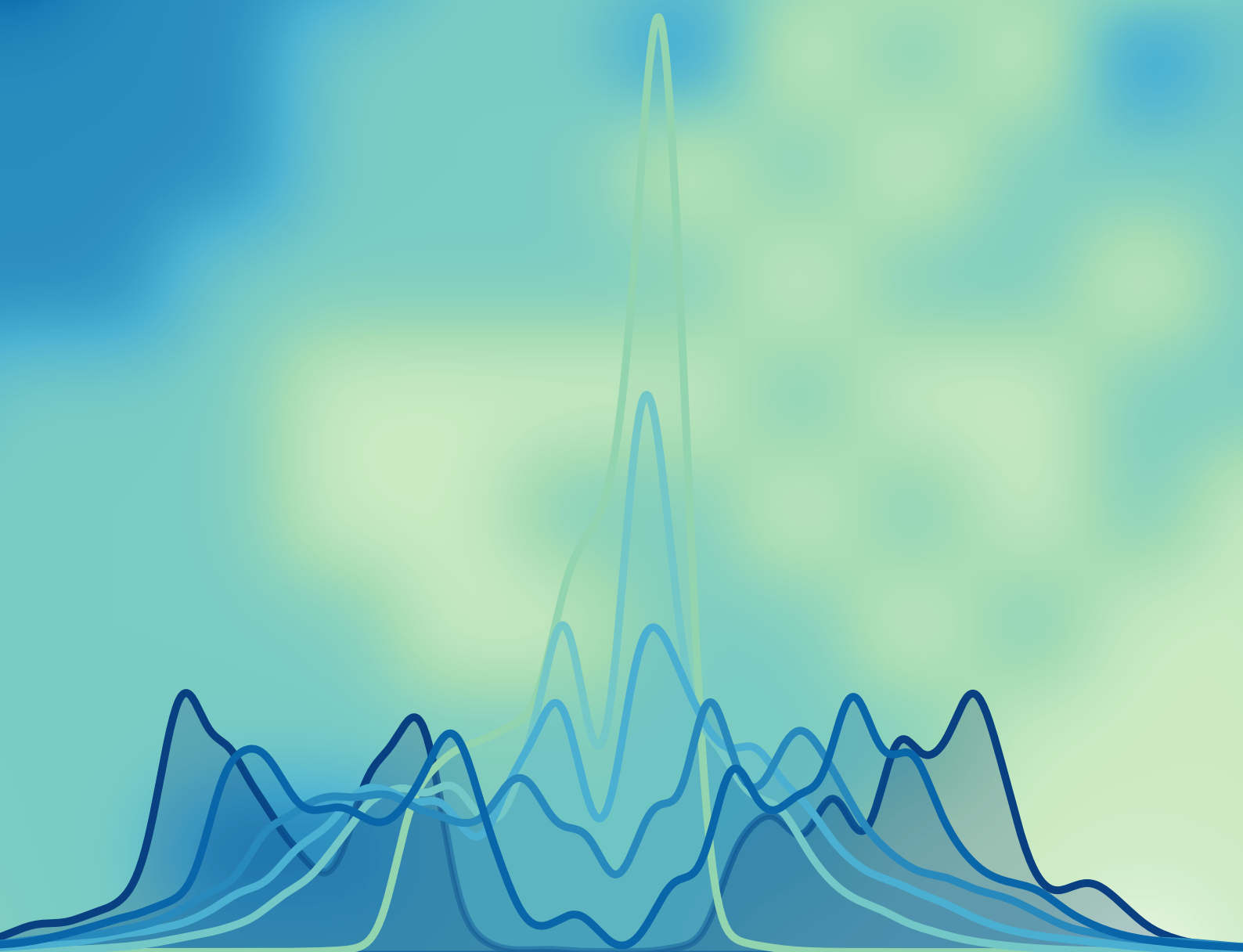
Furthermore, we have demonstrated that this correlated behavior driven by long-range interactions is a general phenomenon and is not restricted to frustrated lattice geometries. As our model is spinless, we evidently cannot examine the role of spin fluctuations in the metal-insulator transition and we instead focus on understanding the charge fluctuations. We identify the connection between the pseudogap in $A(\omega)$ and the Efros-Shklovskii Coulomb gap, which is demonstrated here in a quantum system for the first time since its prediction in 1975. The Coulomb gap indicates the presence of Coulomb polarons as it sets in far from the charge-ordering side of the metal-insulator transition. These polarons are most likely associated with the disordered nature of the charge landscapes and evokes the idea of boson-mediated charge ordering [184]. Interestingly, the shape of the Coulomb gap observed in our system resembles that of Coulomb glasses [179] as the build-up of local correlations suppresses the gap below the universal Efros-Shklovskii bound. We conclude that long-range interactions act as a source of self-generated disorder that gives rise to slow, collective charge excitations. The momentum-resolved spectrum of these charge fluctuations indicates that multiple orders compete with one another throughout the correlated metallic phase, similar to the competition unearthed in studies of classical Coulomb glasses [110] in the context

of the quarter-filled organic salts, θ -(BEDT-TTF)₂X, mentioned at the beginning of this chapter. These materials show precursors of glassiness despite the lack of structural disorder [189,190], and display frustrated metastable orders that compete with the stripe-ordering [190].

The slow nature of the collective charge excitations also indicates a separation of timescales between individual electron motion and global charge rearrangements, which could explain anomalous transport trends observed in a number of materials. Additionally, this could explain the success of the classical Monte Carlo approach used in Ref. [110] to describe quantum systems with anomalous charge states, such as the θ -ET₂X salts. In particular, these materials display strange metallic behavior [59,191] that is compatible with strong scattering by low-energy bosonic modes. Their optical conductivity spectra also contain signatures of localization, indicating that self-generated randomness could also be playing a key role in the charge transport mechanism [192,193]. Furthermore, the separation of timescales suggests that classical methods (or at least partially classical) could be used to treat the problem, as we proceed to do in the following chapter. The benefit of using such classical methods is that larger system sizes are more accessible, thereby reducing finite size effects.

Due to the general nature of the effects revealed here, it is interesting to investigate their relevance in other quantum materials exhibiting bad metallic behavior [70,74], especially those near integer fillings. These systems typically host Mott insulators at integer fillings, but the reduced screening ability of electrons at the onset of the Mott transition implies that long-range interactions could potentially play a significant role [121,182,187]. Furthermore, this begs the question of how the interplay between spin and charge degrees of freedom impacts the ability of long-range interactions to produce correlated, or anomalous, behavior. This topic will be explored in greater detail in the following chapter.

Chapter 4: Anomalous transport and interplay with Mott physics

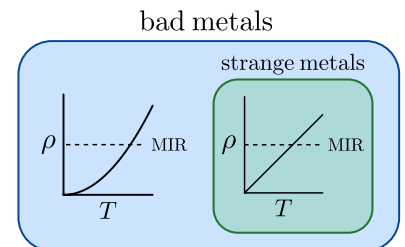


Anomalous transport and interplay with Mott physics

4.1 Introduction

Numerous experiments throughout the past few decades have revealed anomalous transport properties in several strongly correlated electronic systems, which have collectively been classified as bad metallic systems [61, 76]. As a reminder, in this manuscript we define a *bad metal* to be a metal whose resistivity surpasses the Mott-Ioffe-Regel limit derived from semi-classical Boltzmann theory. For reference, we define *strange metals* to be a subgroup of bad metals whose resistivity depends linearly on temperature for a wide range of temperature. Our main focus will be on understanding bad metallic transport in general, as opposed to analyzing sources of anomalous power law trends observed in strange metallic transport.

Bad metallic systems include the high-temperature cuprate superconductors [51], pnictides [52–54], fullerenes [55], vanadium dioxide [56], ruthenates [57], layered organic salts [58, 59], and nickelates [60]. The fact that such a broad range of materials displays similarly anomalous transport properties and can even have similar scattering rates hints at the existence of one (or a few) general, material-independent mechanism(s) driving this behavior [74]. Understanding the microscopic mechanism(s) underlying bad metallic transport remains at the forefront of open challenges facing the condensed matter physics community today despite the immense experimental and theoretical progress made in the past half-century in understanding strongly correlated systems. This challenge is relatively young given the fact that resistivity saturation in conventional metals was only partly understood as recently as the late 1970s [64, 76] and more recent developments suggest that full saturation never happens [194].



Recently, it was observed that a universal Planckian timescale exists that might explain the bad metallic behavior observed in a variety of materials, each with different underlying microscopic mechanisms [74]. This Planckian timescale prompted the proposal of a universal diffusion bound [73] governing the anomalous transport. This idea arises from the description of bad metallic systems as incoherent metals whose electric and thermal transport can be described by simple diffusion relations [73]. These ideas condense the complicated mess of potential mechanisms underlying bad metallic transport to only the most essential elements, thereby establishing a general, unified theoretical description of anomalous transport across many classes of strongly correlated materials.

A microscopic theoretical model without external parameters was introduced in Ref. [195] to examine the proposed universal behavior. This work investigated the thermal and electrical transport properties of a classical Hubbard model that was modified to include a screened Coulomb interaction. Their results accurately predicted linear-in- T resistivity and demonstrated that the strong electronic interactions create a disordered landscape of on-site potentials. As this work was conducted in the strong coupling limit, $t \ll U, V$, this assumed that the timescale of individual electronic motion (controlled by t) is well-separated from that of global charge motion, or rearrangement. This hierarchical scheme is consistent with our discovery of a collective charge excitation in the long-range model of Chapter 3 with frequency $\omega_{\text{coll}} \sim 0.2t$, well below the non-interacting bandwidth value, $\omega_{\text{BW}} \sim 9t$.

In this chapter, we examine how this separation of timescales gives rise to a novel type of transport at finite temperature. We choose to work with a variation of our long-ranged model, introduced in Chapter 3, because the continuous parameter α enables us to understand the role of the range of interactions. The variation of our long-range model that we work with includes local, on-site interactions (the U term from the Hubbard model). This additionally allows us to examine the interplay between local and non-local interactions and to determine how the local interactions quench charge fluctuations at various doping levels and temperatures.

The typically low frequency of collective charge fluctuations arising from strong, long-range interactions implies a long timescale for global charge rearrangements, which therefore justifies the use of a classical numerical method—Monte Carlo. A technical introduction to classical Monte Carlo methods is provided for the interested reader in Appendix C. Although the global charge arrangements can be treated classically, the rapid, individual electronic motion should be treated quantum mechanically. As such, we develop a mixed quantum-classical method to provide a proof-of-principle study of the impact of quantum corrections beyond a semi-classical treatment. This approach is similar in spirit to the extended dynamic mean field theory study

As a reminder to the reader, the Hamiltonian of the long-range model examined in Chapter 3 is of the form:

$$H = -t \sum_{\langle ij \rangle}^{N_s} (\hat{c}_i^\dagger \hat{c}_j + h.c.) + \frac{1}{2} \sum_{ij}^{N_s} V_{ee}(R_{ij}, \alpha) (\hat{n}_i - \bar{n})(\hat{n}_j - \bar{n})$$

of Ref. [152]. However, our approach includes both the spatial correlations of the collective background and the quantum interference effects of the electrons within such a background.

We begin with a brief discussion of the model under consideration. This model shares many features with that of the previous chapter and serves as a preliminary extension of our zero-temperature work to finite temperature. After introducing the model, we will provide evidence for anomalous, incoherent transport arising from long-range interactions, in qualitative agreement with the linear-in- T resistivity results in Ref. [195]. Following our analysis of the driving factors behind the bad-metallic resistivity, we discuss the self-generated disordered landscape that is responsible for slow collective charge fluctuations. We provide an estimate for a region in parameter space where these collective excitations can be treated classically, although individual motion should still be treated quantum mechanically. Finally, we determine how including quantum corrections beyond a semiclassical level leads to a novel form of anomalous transport in metals, *transient localization*, which was originally discovered in organic semiconductors [78].

4.2 Hubbard-Wigner Model

We consider a two-dimensional square lattice Hamiltonian with both on-site and long-range interactions of the form

$$\begin{aligned}
 H = & -t \sum_{\langle ij \rangle, \sigma} (\hat{c}_{i\sigma}^\dagger \hat{c}_{j\sigma} + h.c.) + U \sum_i \hat{n}_{i\uparrow} \hat{n}_{i\downarrow} \\
 & + \frac{1}{2} \sum_{ij} V(R_{ij}) (\hat{n}_i - \bar{n}) (\hat{n}_j - \bar{n})
 \end{aligned}
 \tag{4.1}$$

where t is the nearest-neighbor hopping matrix element, $\hat{n}_i = \sum_{\sigma} \hat{c}_{i\sigma}^\dagger \hat{c}_{i\sigma}$ is the standard number operator with i indexing the lattice sites and σ indexing the spins, $\sigma = (\uparrow, \downarrow)$. U is the strength of the on-site potential which is activated when a site is doubly occupied. The last term, $V(R_{ij}) = V/R_{ij}^\alpha$, describes the repulsive electron-electron interactions as a function of the inverse distance between sites i and j with the strength controlled by V , the value of the potential at one lattice spacing, a . An illustration of the interactions involved in this model is provided in Fig. 4.1.

As in Chapter 3, the parameter α controls the range of interactions, with $\alpha = 1$ corresponding to the pure Coulomb interaction and $\alpha \rightarrow \infty$ the nearest neighbor interaction. The values of the potential are computed via the Ewald summation technique, which ensures that the electrostatic (Madelung) energy of periodic configurations is exactly recovered in the classical limit, $t/V \rightarrow 0$. The last term also includes a background charge compensation \bar{n} to ensure charge neutrality. Further details on the computation of the interaction potential can be found in Appendix B.

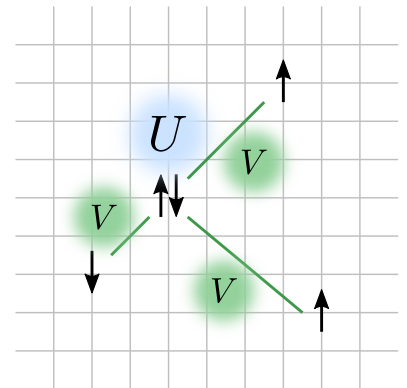


Figure 4.1: Illustration of the interacting portion of the Hubbard-Wigner model.

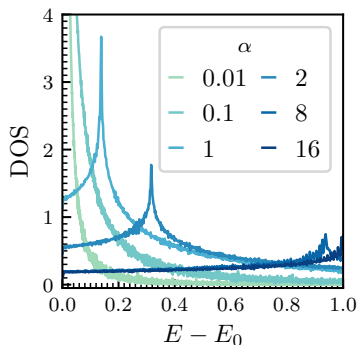


Figure 4.2: A reminder of the collective charge modes that grow softer with increasing range of interaction.

We are interested in a regime, where strong electronic interactions are responsible for *almost frozen* charges. As such we study Eq. 4.1 in the weak-hopping limit, $t \ll U, T, V$. In this regime, that can for example be reached by melting from the Wigner crystal phase, the low-lying excitations are collective modes that correspond to slow, self-generated disorder. These slow, collective modes arise from the long-range Coulomb interaction and should, in principle, be found in systems with poor screening [152]. The typical degeneracy in this weak-hopping limit is lifted by the interaction term, V , enabling us to investigate this system with classical Monte Carlo simulations [195].

As discussed in Appendix C, the nature of the observable in question determines which statistical mechanical ensemble (canonical or grand-canonical) is used for calculations. In the following sections, we proceed to present our results on anomalous transport and the competition between local and non-local interactions in three distinct regimes: quarter-filled ($n = 0.5$), lightly doped insulators ($n = 0.9$), and half-filled insulator ($n = 1.0$). We fix the on-site potential $U = 1$ and report all values in units of this energy scale: T/U , V/U , etc. Unless explicitly stated otherwise, all results presented are on a square lattice with $L = 12$ sites along one side (total number of sites, $N_s = 144$). Unlike exact diagonalization, classical Monte Carlo calculations are not limited by the exponential growth of the Hilbert space which enables us to access much larger system sizes where finite size effects do not typically bias results and we can safely conclude that our results reflect the thermodynamic limit.

In this chapter, we are interested in studying bad metallic transport arising from long-range interactions. By definition, this transport regime fails to be described by conventional Boltzmann theory. As such, we will study electron transport by means of the Nernst-Einstein relation which is an extremely general theoretical description of transport in terms of the diffusion of charges. Unfortunately, we cannot directly compute the diffusion constant of individual particles in our Monte Carlo calculations. Therefore, we will extract this quantity in a two-step process. First, we will compute the semi-classical expression for the optical conductivity to second-order in small- t perturbation theory where t is the strength of the hopping integral. This provides us with access to the semi-classical resistivity which can be analyzed in terms of contributions from the Drude weight and transport lifetime.

The second step consists of incorporating the resistivity in the Nernst-Einstein diffusion relation to obtain an expression for the diffusion constant which cannot be computed directly as it is a proportionality constant. This formulation will relate the diffusion constant to the resistivity and the charge compressibility. This second quantity is directly accessible via the use of grand canonical Monte Carlo calculations. Finally, we can compare the contributions of the compressibility and the diffusion constant to understand factors responsible for bad metallic transport in this diffusion-based framework.

4.3 Incoherent high- T transport

In order to compute the resistivity, we first compute the semi-classical optical conductivity by evaluating the Kubo formula with small t perturbation theory, as in Ref. [195]. The formal definition of the semi-classical optical conductivity is given as

$$\sigma_{\text{sc}}(\omega) = Af(\omega) \sum_s \frac{e^{-\beta E_s}}{\mathcal{Z}} \sum_{i,\sigma} \Delta_{i\sigma}(\omega) \quad (4.2)$$

where $A = \pi a^2 / (\hbar^2 \text{vol})$ is a system-dependent prefactor, $f(\omega) = (1 - e^{-\beta \hbar \omega}) / \hbar \omega$, and \sum_s indicates a thermal summation over states s with a fixed number of particles, N , for a given volume, vol . As a reminder, all of our calculations are performed on the square lattice so the volume is simply given as $\text{vol} = L^2$ where L is the length along one side. The lattice spacing a is set to unity in all calculations. The Boltzmann weight, $e^{-\beta E_s}$, depends on the inverse temperature $\beta = 1/k_B T$ and the energy of each N -particle state, E_s .

The final part of Eq. (4.2) describes the spectral weight of all excitations, or electron hops between neighboring sites,

$$\Delta_{i\sigma}(\omega) = \Delta_{i\sigma}^+(\omega) + \Delta_{i\sigma}^-(\omega) \quad (4.3)$$

in a fixed spin sector σ . The terms $\Delta_{i\sigma}^+(\omega)$ and $\Delta_{i\sigma}^-(\omega)$ are respectively defined as

$$\Delta_{i\sigma}^+(\omega) = \delta(\omega + \Delta E_{+i\vec{u}} / \hbar) \hat{n}_{i\sigma} (1 - \hat{n}_{i-\vec{u},\sigma}) \quad (4.4)$$

$$\Delta_{i\sigma}^-(\omega) = \delta(\omega - \Delta E_{-i\vec{u}} / \hbar) \hat{n}_{i-\vec{u},\sigma} (1 - \hat{n}_{i,\sigma}) \quad (4.5)$$

and account for all possible hops (both forward and backward in direction \vec{u}) between site i and its neighboring site $i - \vec{u}$ (Fig. 4.3). The variable $\Delta E_{\pm i\vec{u}}$ represents the difference in energy between the two configurations considered in each hopping process. Overall, the semi-classical optical conductivity, $\sigma_{\text{sc}}(\omega)$, is numerically implemented as a sampling of the excitation spectrum at each Monte Carlo time step. As we are interested in understanding the transport properties at fixed fillings, we compute this quantity via canonical Monte Carlo simulations (fixed N, V, T).

Selected results are presented in Fig. 4.5. Only the $\omega \geq 0$ halves are plotted as the spectra are symmetric. In the classical Hubbard model, which corresponds to $V/U = 0$ in our model, the semi-classical optical conductivity consists of three delta functions: the Drude peak at $\omega/U = 0$, and the upper and lower Hubbard peaks at $\omega/U = \pm 1$. This occurs because the only possibility for a finite-frequency ($\omega \neq 0$) excitation via a hopping process occurs when a particle hops to/from a site with another particle, thereby inducing an energy change $\Delta = \pm U$ due to the change in double occupation of the sites in question. These processes are illustrated in Fig. 4.4.

When non-local interactions are turned on ($V/U \neq 0$), we observe that the classical delta functions broaden into a Drude peak (centered

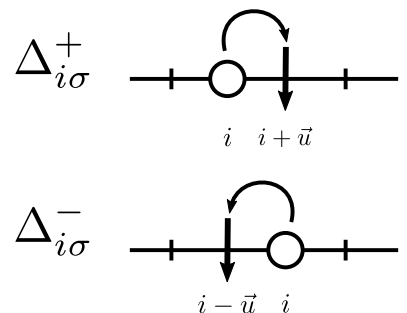


Figure 4.3: Hopping processes under consideration in the classical optical conductivity for the $\vec{u} = +\hat{x}$ unit direction.

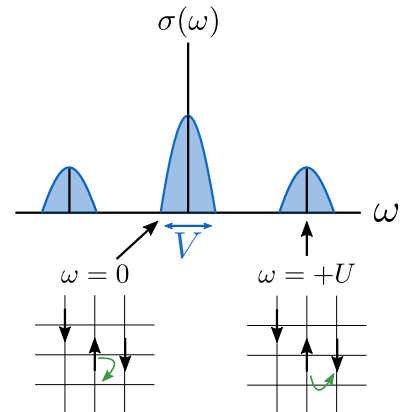
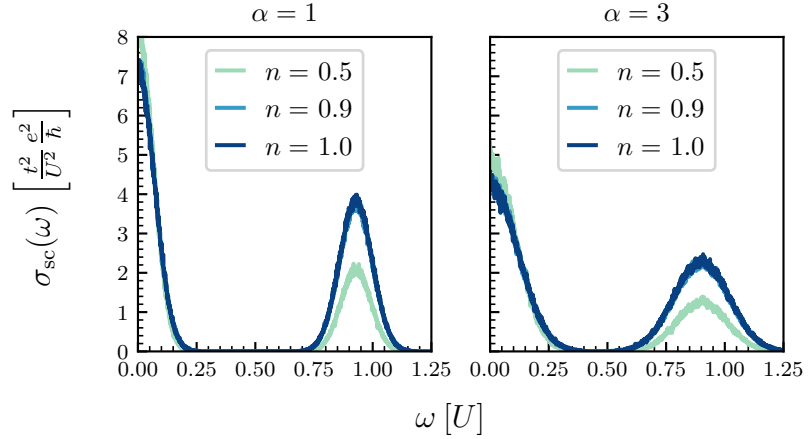


Figure 4.4: Illustration of the different hopping processes contributing to the current in the classical Hubbard model. The delta peaks are shown in black, while the broadening with V is illustrated in blue. The process corresponding to $\omega = -U$ is not shown as it is the opposite of that for $\omega = +U$.

Figure 4.5: Semi-classical optical conductivity, $\sigma_{\text{sc}}(\omega)$, for the cases $\alpha = 1, 3$ for $V/U = 0.2$ and $T/U = 1.2$ fixed. Both cases have a large Drude peak for the quarter-filled case, $n = 0.5$ (green), and essentially identical curves for the lightly doped (light blue) and half-filling (purple) case.



around $\omega/U = 0$), and upper and lower Hubbard-like peaks (Fig. 4.5). In other words, long-range interactions are responsible for a finite transport lifetime, even in the classical limit. In the pure Hubbard model, one would instead find an infinite transport lifetime for the (local) electronic states. As we will see next, this interaction-driven broadening of the Drude peak will necessarily dictate the high-temperature trends of the resistivity. In later sections, we will take a closer look at the precise mechanism by which these long-range interactions produce signatures of anomalous transport.

As Fig. 4.5 shows, the quarter-filled case (light green curves) presents a slightly higher Drude peak for both pure long-range ($\alpha = 1$) and dipolar interactions ($\alpha = 3$) with respect to the lightly doped ($n = 0.9$) and half-filled ($n = 1.0$) cases. Furthermore, the lightly doped case ($n = 0.9$) essentially mirrors that of the half-filled case for both cases. A general comparison of the size of the peaks shows that increasing the range of interactions (decreasing α) corresponds to a narrowing of peak width and an increase in peak height. The increased peak height for longer-ranged interactions will correspond to lower resistivity values as we will see next. Finally, we remark that the Drude peaks have Gaussian shapes, suggesting that the energy excitations contained in the spectrum are essentially random [195].

From the semi-classical optical conductivity, we can compute the semi-classical resistivity, ρ_{sc} , as in Ref. [195] by fitting the low-frequency peak of $\sigma_{\text{sc}}(\omega)$ to a Gaussian,

$$\sigma_{\text{sc}}(\omega) = \mathcal{D}\tau e^{-\pi(\tau\omega)^2} \quad (4.6)$$

where \mathcal{D} is the Drude weight and τ is the transport lifetime. The semi-classical resistivity is then defined as

$$\rho_{\text{sc}}(T) = \frac{1}{\mathcal{D}\tau} \quad (4.7)$$

and is shown in Fig. 4.6 for the pure long-range case ($\alpha = 1$, full circles)

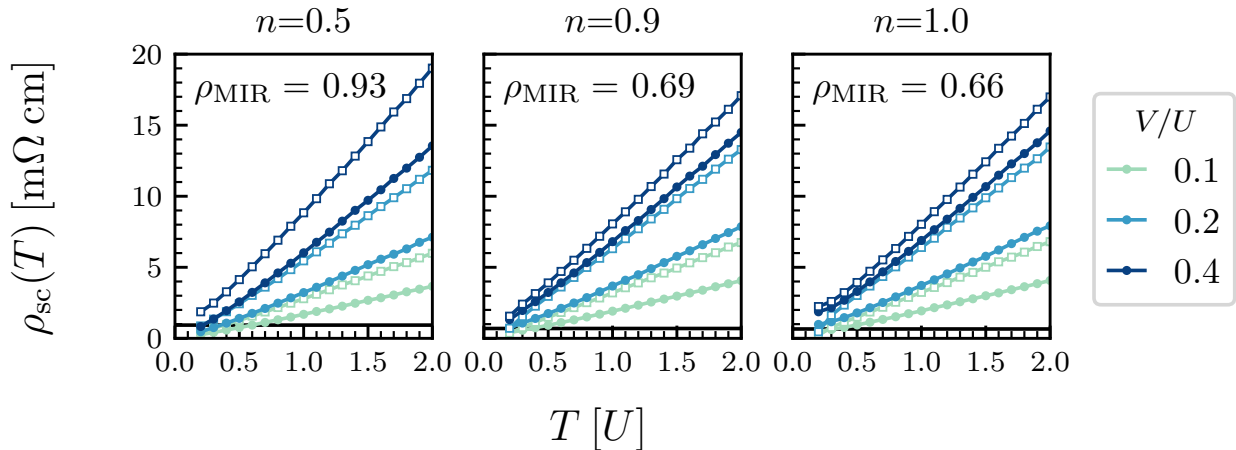


Figure 4.6: Semi-classical resistivity, ρ_{sc} . Values are reported for $\alpha = 1$ (full circles) and $\alpha = 3$ (open squares). The Mott-Ioffe-Regel limits (black lines) computed for $\text{La}_{2-x}\text{Sr}_x\text{CuO}_4$ are $\rho_{\text{MIR}} = 0.93$ ($n = 0.5$), $\rho_{\text{MIR}} = 0.69$ ($n = 0.9$), and $\rho_{\text{MIR}} = 0.66$ ($n = 1.0$) in units of $\text{m}\Omega \text{ cm}$.

and a shorter-ranged case ($\alpha = 3$, open squares) for different values of V/U .

As a reminder, the Mott-Ioffe-Regel limit is the value of the resistivity from Boltzmann theory when the scattering length is equal to one lattice spacing, $\ell = a$. Beyond this value ρ_{MIR} , conventional Bloch-Boltzmann theory is no longer valid to describe electron transport as the electrons can no longer be described as Bloch waves. The black lines in Fig. 4.6 indicate estimates for the Mott-Ioffe-Regel limit computed for a representative member of the high- T_c cuprate superconductor family, $\text{La}_{2-x}\text{Sr}_x\text{CuO}_4$. Details on the calculation can be found in Appendix D. The semi-classical resistivity from our Hubbard-Wigner model evidently exceeds the predicted Mott-Ioffe-Regel limit for this characteristic strongly correlated system which is often modeled by the conventional Hubbard model (i.e. without non-local interactions) on the square lattice. Furthermore, the bad metallic resistivity trends linearly with temperature and the magnitude of the slope increases with V/U and α , consistent with the relative sizes of the zero-frequency conductivity peaks in Fig. 4.5.

Results for $T/U < 0.2$ are not shown due to convergence issues associated with jamming at low temperatures. At low temperatures we would expect the resistivity to diverge for the half-filled case, as in Refs. [72, 195]. However, this is hardly relevant as we are more interested in understanding the high temperature behavior and because we can not expect this classical Monte Carlo treatment to be accurate at low temperature. For the other fillings, the vanishing resistivity as the temperature decreases is in qualitative agreement with the results presented in Ref. [195], suggesting that our model correctly captures the relevant physics due to long-range interactions and functions as a paradigmatic model that is capable of producing transport properties resembling those of bad metallic systems.

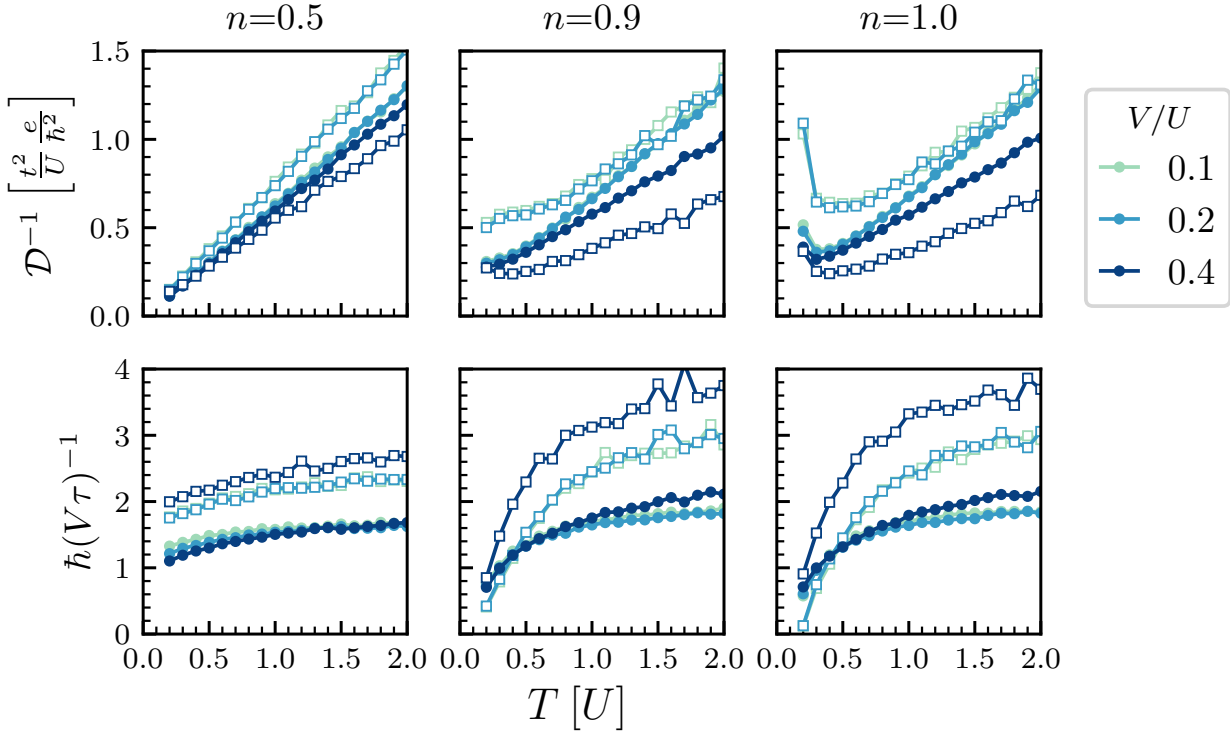


Figure 4.7: Inverse Drude weight (top row) and inverse transport lifetime (bottom row) as a function of temperature, filling, interaction strength and range. The closed circles correspond to $\alpha = 1$ and the open squares to $\alpha = 3$.

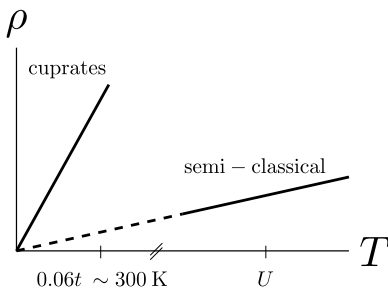


Figure 4.8: Illustration of the comparison of resistivity slopes between the cuprates at room temperature and our system at ultra high temperatures.

In order to further compare our results with experiments, we examine the slope of our resistivity curve with experimental values. With band structure estimates for LSCO from Ref. [196], we set $t = 0.43\text{eV}$ and with an approximate ratio $U = 8t$, we arrive at $U \approx 40,000\text{K}$. This temperature is obviously much higher than the standard room temperature (300K) at which transport in the cuprates is routinely studied. However, we argue that it is not unreasonable to compare the orders of magnitude of the slopes which should not change much provided there are no crossover events between room-temperature and our high-temperature limit [69]. From Ref. [90], we determine that the slope for $\text{Bi}_2\text{Sr}_{2-z}\text{La}_z\text{CuO}_{6+\delta}$ with about 10% doping is $0.003 \text{ m}\Omega \text{ cmK}^{-1}$, whereas our results with similar doping yields $0.000105 \text{ m}\Omega \text{ cmK}^{-1}$. This corresponds to approximately a thirty-fold difference between the magnitudes and hints at the fact that our classical treatment must be missing some of the relevant physics to explain the anomalous behavior in these systems. However, before exploring possible directions to account for this, we will analyze the individual contributions to the semi-classical resistivity in order to extract as much information as possible at this stage.

We next turn our attention to understanding the two components that contribute to the semi-classical resistivity—the Drude weight and the transport lifetime. We seek to determine if one, or both, is responsible for the linear growth of the resistivity with respect to the tem-

perature. These two observables are plotted in Fig. 4.7 for both $\alpha = 1$ (full circles) and $\alpha = 3$ (open squares). Across all fillings in the high temperature limit, the inverse Drude weight displays a linear behavior with increasing temperature, similar to that of the resistivity. We also observe a divergence at low temperatures for the half-filled case as the system freezes into the insulating ground state expected at $T = 0K$. While the inverse Drude weight does not diverge for the lightly doped case ($n = 0.9$), its rate of reduction slows down as the temperature decreases and its low-temperature behavior should be studied more carefully with a method that is better adapted to account for quantum effects.

Elucidating the effect of the non-local interaction strength and the range of interactions on the inverse Drude weight appears to be complicated. For a fixed range, weaker values of interaction strength, V/U , result in larger values of the inverse Drude weight across all fillings at high temperatures. Interestingly, the two weakest values reported ($V/U = 0.1, 0.2$) agree well for a given value of α , while the largest interaction strength ($V/U = 0.4$) reduces the value of the inverse Drude weight, an effect which is stronger closest to half-filling. This suggests that non-local interactions play an increasingly important role as the system approaches the insulating state, and aligns with early views of Wigner and Mott that strongly correlated systems display an incipient breakdown of screening at the approach of the Mott-metal insulator transition.

The inverse transport lifetime, on the other hand, remains essentially constant at high temperature, $T > U$. This allows us to conclude that the T -linear behavior of the semi-classical resistivity is controlled by the Drude weight in this region. In other words, as the temperature increases, the spectral weight in the low-frequency peak of the optical conductivity is shifted to the higher frequency peaks such that the height of the low-frequency peak (the Drude weight) drops as $\sim T$ while the width (transport lifetime) remains constant (Fig. 4.9). The inverse transport lifetime also shows a similar marked separation between weaker and stronger interaction strengths for the case with reduced interaction range ($\alpha = 3$, open squares). This separation in terms of interaction strength parallels the separation observed in the inverse Drude weight, suggesting that the effect of non-local interactions increases as the filling approaches $n = 1.0$. Overall, the transport lifetime, or current relaxation rate, displays a weak temperature dependence, which is in qualitative agreement with the results obtained in Ref. [195].

However, as the system approaches half-filling, the transport lifetime displays a stronger response with temperature, potentially even counterbalancing the divergence in the Drude weight to lead to an overall linear-in- T behavior that extends all the way down to extremely low temperatures. It is possible that there is a range of temperatures over which the divergent behaviors of the Drude weight and the trans-

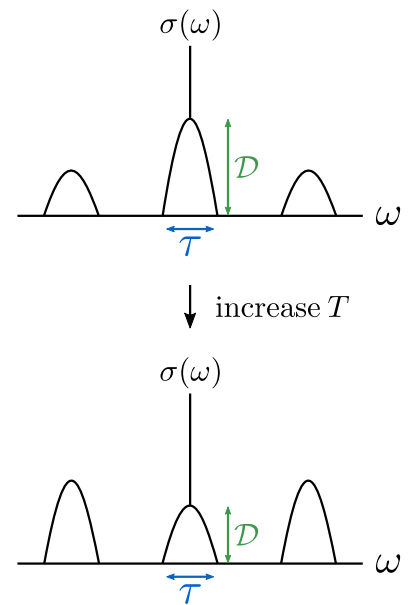
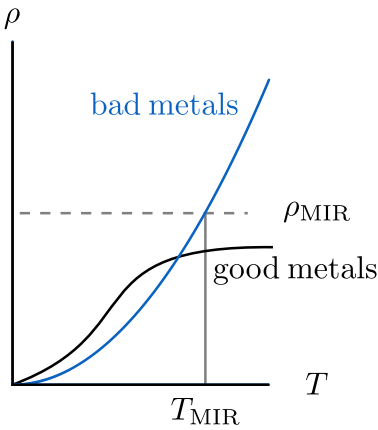


Figure 4.9: Illustration of the spectral shift from the low-frequency peak to the upper peaks as the temperature increases.

port lifetime essentially cancel each other out, resulting in a resistivity that continues to change linearly with decreasing temperature. In other words, there exist two distinct regimes where the T -linear behavior of the resistivity arises from different combinations of contributions, confirming the result found in Ref. [195].

Thus far we have demonstrated that our flexible long-range model is capable of producing bad metallic transport in the form of T -linear resistivities in qualitative agreement with Ref. [195]. In the framework of this particular semi-classical analysis, the Drude weight and the transport lifetime combine to produce the semi-classical resistivity and our results thus far suggest that the T -linear behavior in the resistivity is driven by the linear change of the Drude weight with temperature as the transport lifetime remains essentially constant at high temperatures ($T > U$). Our results also suggest that two distinct regions of bad metallic transport exist, in agreement with the conclusion reached separately in Ref. [195]. Furthermore, the fact that our resistivity results vastly exceed the Mott-Ioffe-Regel limit for a typical strongly correlated system suggests that a semi-classical picture of transport is no longer valid and that we should revisit the theoretical description of electronic transport in solids.

4.3.1 Nernst-Einstein description of transport



Semi-classical Bloch-Boltzmann theory typically describes electronic transport in solids and predicts that the resistivity should grow linearly with respect to the temperature at high temperatures. As the temperature increases, solids typically either melt or the resistivity saturates at a temperature $T \leq T_{\text{MIR}}$. This limiting temperature, T_{MIR} , corresponds to the Mott-Ioffe-Regel limit where Bloch-Boltzmann transport would predict that the typical scattering length is of the order of the lattice spacing, $\ell \approx a$. However, this resistivity saturation is absent in bad metallic systems where the resistivity continues to grow past T_{MIR} , into the region where the description of electrons in terms of Bloch waves is no longer valid as it would predict that $\ell < a$.

This breakdown of Bloch-Boltzmann theory (and most likely the loss of coherent quasiparticle-based transport) past the Mott-Ioffe-Regel limit invites us to revisit the theoretical description of transport. As such, we turn to a more general theoretical description for incoherent transport and we consider particle diffusion via Fick's law,

$$\mathbf{j}_m(\mathbf{r}) = -D_{\text{NE}}(T) \nabla n(\mathbf{r}) \quad (4.8)$$

where $\mathbf{j}_m(\mathbf{r})$ is the mass current, $D_{\text{NE}}(T)$ the temperature-dependent diffusion constant, and $n(\mathbf{r})$ the local concentration of particles [197, 198]. We note that we shall refer to the Nernst-Einstein diffusion constant as D_{NE} to avoid confusion with the notation for the Drude weight, D . We can further relate the mass current, $\mathbf{j}_m(\mathbf{r})$, to the electri-

Adolf Fick was a physiologist who originally trained as a mathematician and physicist. In physics, his main contribution is his description of the diffusive nature of particle transport. In cardiology, he adapted this idea to define cardiac output which describes the amount of blood pumped by the heart in a minute [199].

cal current upon inclusion of a factor of the electric charge,

$$\mathbf{j}_e(\mathbf{r}) = e \mathbf{j}_m(\mathbf{r}) = -e D_{\text{NE}}(T) \nabla n(\mathbf{r}) \quad (4.9)$$

and turn our attention to understanding the change in particle number, $\nabla n(\mathbf{r})$. From thermodynamics, we know that this quantity is directly connected to the chemical potential, $\mu(\mathbf{r})$, or the energy required to add or remove a particle. We can write the chemical potential for the general case as

$$\mu(\mathbf{r}) = \mu_0 + e \phi(\mathbf{r}) \quad (4.10)$$

where μ_0 is the chemical potential in the absence of an external field and $\phi(\mathbf{r})$ is the electric potential. As the derivative in Eq. (4.8) will only impact the $e \phi(\mathbf{r})$ term, we can rewrite the expression for the electric current, Eq. (4.9), as

$$\mathbf{j}_e(\mathbf{r}) = -e D_{\text{NE}}(T) \left. \frac{\partial n}{\partial \mu} \right|_T \nabla (e \phi(\mathbf{r})). \quad (4.11)$$

We immediately recognize that we can use Poisson's equation, $\mathbf{E}(\mathbf{r}) = -\nabla \phi(\mathbf{r})$, to express the electric current in terms of the electric field,

$$\mathbf{j}_e(\mathbf{r}) = e^2 D_{\text{NE}}(T) \left. \frac{\partial n}{\partial \mu} \right|_T \mathbf{E}(\mathbf{r}) \quad (4.12)$$

and further use Ohm's law to arrive at our final expression for the conductivity,

$$\sigma(T) = e^2 D_{\text{NE}}(T) \left. \frac{\partial n}{\partial \mu} \right|_T \quad (4.13)$$

which is known as the Nernst-Einstein relation [72]. If we compare this with the Drude formulation of optical conductivity, we see that only the charge carriers close to the Fermi surface contribute by means of their individual diffusivity to the electron transport in Eq. (4.13) [200, 201]. In the following sections, we will analyze each term from this general transport equation in the context of our long-range interacting model in order to shed more light on the origin of bad metallic behavior. Via Monte Carlo calculations, we have direct access to the charge compressibility, but not to the diffusion constant, which is a fundamental transport property of each particle. In order to compute D_{NE} , we will combine the conductivity computed in the previous section with our charge compressibility results and examine the role of each contribution to the resistivity.

We begin by examining the temperature dependence of the charge compressibility,

$$\kappa = \left. \frac{\partial n}{\partial \mu} \right|_T. \quad (4.14)$$

In the classical limit of the Hubbard model, we expect this quantity to scale as $\kappa = \mu/T$ with temperature. Because μ is proportional to a static potential (Eq. 4.10), we can consider the compressibility as the

Ohm's law states that the optical conductivity is the constant of proportionality between the electric current and the electric field, $\mathbf{j}_e(\mathbf{r}) = \sigma \mathbf{E}(\mathbf{r})$.

Figure 4.10: The average doping away from half-filling, $\delta(\mu, T) = |\langle n \rangle - 1.0|$, defined as a function of chemical potential, μ , and temperature, T/U . Values are reported for the case with pure, long-range interactions ($\alpha = 1$) and $V/U = 0.2$ with v_{uc} the unit cell volume. Select values of doping are shown as contours: $\delta = 0.05$ (solid), 0.1 (dashed), 0.25 (dash-dotted), and 0.5 (dotted).

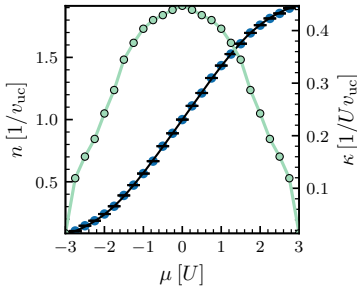
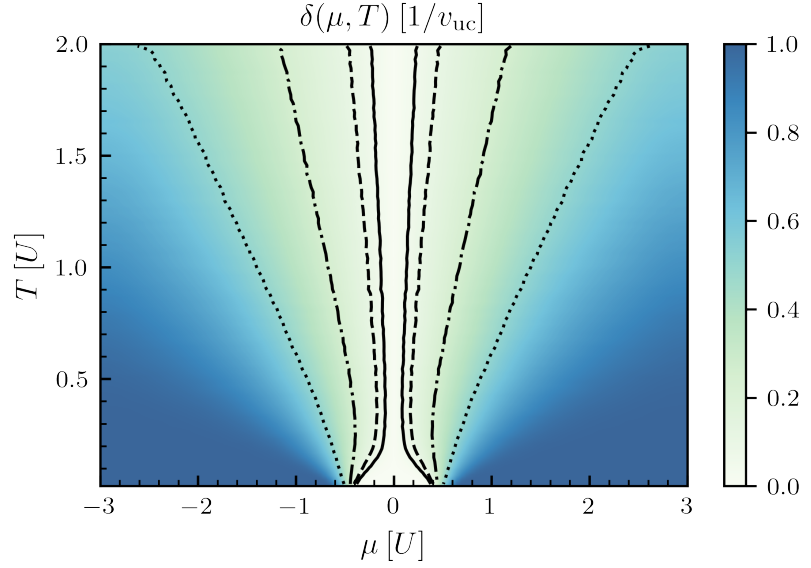


Figure 4.11: Representative plot of $n(\mu)$ for $T = 0.78U$ with raw data points shown in blue with black errorbars. The black line corresponds to the interpolated function of n . The green line corresponds to κ with the respective values given by the axis on the right.

redistribution of charge density in the presence of an external electric potential [72]. As this observable requires knowledge of variable particle number, we compute it via grand canonical Monte Carlo simulations (fixed μ, V, T). The average density $\langle n \rangle$ is calculated on a fine grid in (μ, T) space and filtered with a temperature-dependent Gaussian filter. Following this step, we construct an interpolated function $n(\mu, T)$ that we can use to establish a phase diagram in (μ, T) space (see Fig. 4.11). Error bars were not carried through the interpolation, but Fig. 4.11 demonstrates that the error on the raw data of n is already extremely small. The doping away from half-filling is shown in Fig. 4.10 as a function of chemical potential and temperature. The insulating, half-filled case is always centered around $\mu = 0$ for all temperatures due to our definition of the compensating charge background, \bar{n} , and we observe that a plateau develops as the temperature decreases (pale green region at the bottom of Fig. 4.10). This behavior is in agreement with that of the classical Hubbard model which corresponds to $V/U = 0$ in our model.

Examining Eq. (4.13) above, we see that the conductivity is directly related to the compressibility, which therefore implies that the resistivity is directly related to the inverse compressibility,

$$\rho = e^2 D_{NE}^{-1} \kappa^{-1} \quad (4.15)$$

As we are interested in discerning the cause of linear T behavior in the resistivity, we shall focus on understanding how κ^{-1} behaves with respect to the various parameters present. The aforementioned plateau in the number density at half-filling signals a divergence in the inverse compressibility which is computed as the inverse of the derivative of our interpolated $n(\mu, T)$ function (Fig. 4.12).

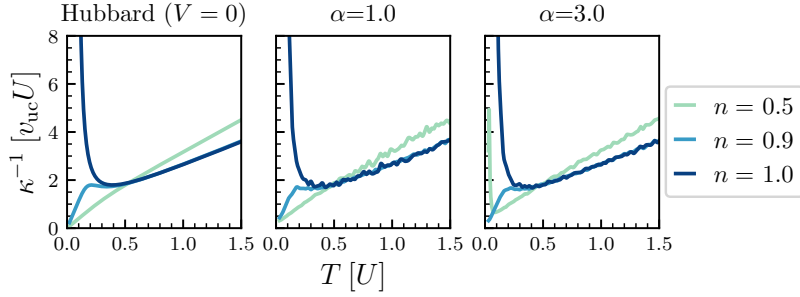


Figure 4.12: Inverse compressibility as a function of temperature, T/U , for the classical Hubbard model (left), and our Mott-Wigner model with $\alpha = 1$ (center) and $\alpha = 3$ (right) for a fixed ratio of non-local to local interactions $V/U = 0.2$. The volume of the unit cell is indicated by v_{uc} .

The inclusion of non-local interactions does not distort the high-temperature trends of the inverse charge compressibility, $\kappa^{-1} \sim T$. This can be seen upon comparison of the classical Hubbard model (left panel of Fig. 4.12) to our results for $\alpha = 1, 3$ (center, right panels of Fig. 4.12). The non-local interactions appear to have a negligible impact at high temperatures and indeed, the only deviations from the classical results occur at extremely low temperatures (Fig. 4.13) at the approach of charge-ordering.

These deviations first appear for strong values of non-local interactions in the case $\alpha = 3$ (Fig. 4.13) and correspond to the development of charge-ordering at low temperatures. It is well-known that the addition of short-range interactions favors checkerboard charge-order (see inset of Fig. 4.14) on the square lattice at quarter-filling [202,203]. This ordering transition manifests itself in the development of a plateau at quarter-filling (symmetrically at three-quarters filling) in the occupation function, as shown for a representative case in Fig. 4.14. As shown in Fig. 4.13, weaker non-local interactions (smaller V/U) push the ordering transition to lower temperatures where the thermal fluctuations finally give way, around the order of $T \sim V/2$.

Furthermore, the ordering transition is dependent on α and we do not yet observe the charge-ordering transition for $\alpha = 1$ down to the lowest temperatures computed ($T/V = 0.05$). This fact is not surprising as an increased range of interaction (smaller α) reduces the tendency to long-range order, while leaving the short-range correlations intact. Wigner crystals are well-known to be fragile, especially to collective excitations that grow increasingly soft with increasing range of interaction [152]. This idea of a delayed transition that is dependent on α was also seen in the phase diagram presented in the previous chapter, where the stripe-ordering transition occur at higher values of interaction strength as the range was decreased (see Fig. 3.20 in Chapter 3).

Overall, our results qualitatively agree with those reported in Refs. [72, 195]. First, our long-ranged model displays a linear growth of κ^{-1} with temperature across all fillings, as also seen in Refs. [72, 195]. As shown in Ref. [72], we observe a divergence of the inverse charge compress-

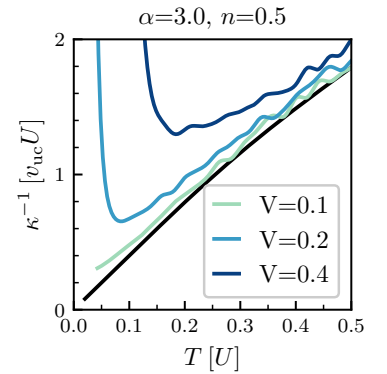


Figure 4.13: Low temperature examination of κ^{-1} for the quarter-filled case with $\alpha = 3$. The onset of charge-ordering causes a divergence of κ^{-1} and occurs when $T \sim V/2$. Black indicates the classical Hubbard result.

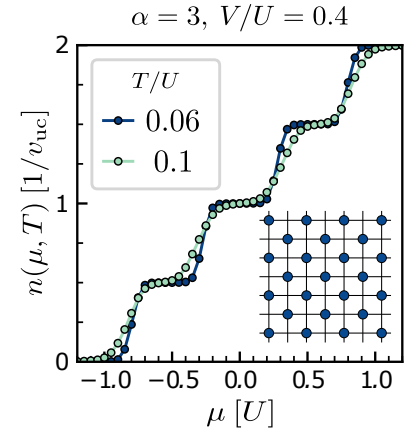


Figure 4.14: Low temperature examination of n for the quarter-filled case with $\alpha = 3$. For $T = 0.1U$ (green), the occupation function displays ramps at $n = 0.5, 1.0$, and 1.5 , signaling the onset of ordering. These ramps will transform into plateaus as the temperature decreases further (blue, $T = 0.06U$).

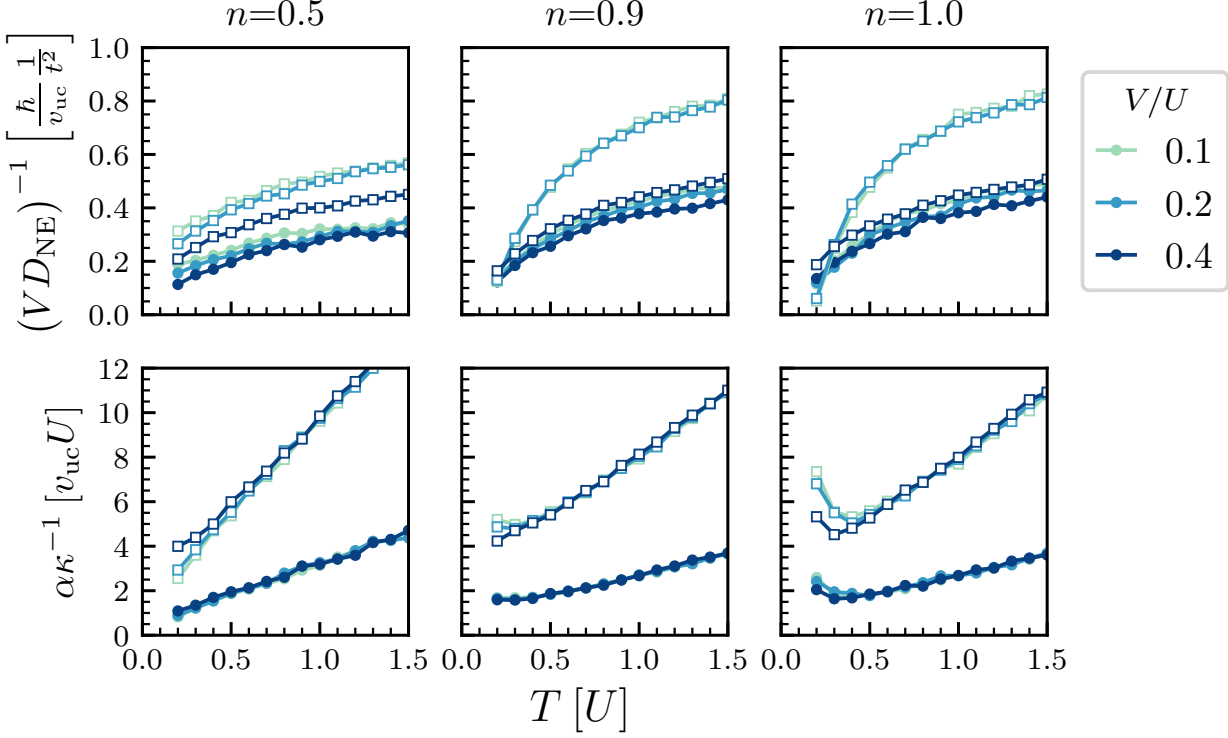


Figure 4.15: The inverse Nernst-Einstein diffusion constant (top row) and the inverse compressibility (bottom row) as functions of temperature. Results are shown for different values of interaction strength, V/U , (color guide in legend), and interaction range, ($\alpha = 1$, closed circles, and $\alpha = 3$, open squares). The inverse compressibility is scaled by α for greater legibility.

ibility for the half-filled case as the temperature decreases and Mott insulator behavior sets in. Furthermore, the lightly-doped case ($n = 0.9$) presented here also exhibits a slight increase towards half-filled values at low temperature before decreasing towards a finite value. This trend was also observed with the inclusion of long-range interactions in Ref. [195]. The qualitative difference between our results and previous works is that we have presented detailed results demonstrating that our model captures charge-ordering behavior for decreasing interaction range in the quarter-filled case. However, we are generally uninterested in exploring this behavior as we are instead interested in the high-temperature non-saturating behavior of bad metallic systems. We have merely discussed the low-temperature behavior at length here for the sake of completeness. Overall, we find that the inverse compressibility, κ^{-1} , grows in a linear fashion with increasing temperature, which suggests that this is the driving contribution to the linear behavior of the semi-classical resistivity with temperature. We next turn our attention to computing the Nernst-Einstein diffusion constant from Eq. (4.13).

We remind the reader that the original motivation for these calculations was to study the relationship between the diffusion constant and the compressibility in the Nernst-Einstein relation (see Eq. (4.13)),

$$\sigma(T) \sim \rho_{\text{sc}}^{-1}(T) = e^2 D_{\text{NE}} \kappa \quad \longrightarrow \quad \rho_{\text{sc}} = (e^2 D_{\text{NE}} \kappa)^{-1}, \quad (4.16)$$

which we have rewritten in terms of the semi-classical resistivity, $\rho_{\text{sc}}(T)$. Combining our results for the semi-classical resistivity and the compressibility, we arrive at an understanding of the inverse diffusion constant, $D_{\text{NE}}^{-1} = \kappa\rho/e^2$ (see Fig. 4.15). Similar to the transport lifetime in the semi-classical analysis previously discussed, the inverse diffusion constant displays weak temperature dependence in the high temperature regime and eventually diverges in the lightly-doped case and insulating case as the temperature decreases. Therefore, analyzing the resistivity in this diffusion-compressibility decomposition enables us to conclude that the inverse charge compressibility drives the linear growth of the resistivity with respect to temperature (see Fig. 4.15). Intuitively speaking, one would expect the rate of diffusion to increase with temperature as the larger thermal fluctuations should increase the motion of the charge carriers. However, the weak temperature dependence of the diffusion constant suggests that some underlying mechanism must be limiting the diffusive nature of the charge carriers. One such mechanism is the self-generated disorder arising from long-ranged interactions which we will examine in more detail in the following section.

In this section we have studied semi-classical electron transport in terms of the Nernst-Einstein diffusion relation. As we did not have access to the diffusion constant directly in our Monte Carlo calculations, we first computed the optical conductivity by means of small- t perturbation theory. The resistivity obtained from this computation displays markedly bad metallic behavior, by increasing well beyond the Mott-Ioffe-Regel limit and displaying a linear growth with temperature. The Mott-Ioffe-Regel limit was calculated for a representative strongly correlated system ($\text{La}_{2-x}\text{Sr}_x\text{CuO}_4$). Further analysis of the semi-classical resistivity suggests that the Drude weight controls the high temperature growth beyond $T = U$ in this framework and that two distinct regimes of bad metallic transport exist, as first proposed in Ref. [195].

Once we have established that the resistivity exceeds the Mott-Ioffe-Regel limit, we proceeded to analyze the electron transport in the context of charge diffusion in the Nernst-Einstein framework. This requires knowledge of the charge compressibility and the diffusion constant, which is not directly accessible but can be derived in combination with our results for the semi-classical resistivity. We have compared the contributions of the diffusion and the compressibility and have determined that the inverse compressibility controls the high temperature growth of the resistivity as the inverse diffusion remains constant. As the diffusive nature of the charge carriers does not increase with temperature, we will next consider whether the self-generated disorder from the long-range interactions impacts the diffusion.

$$\begin{array}{c}
 \sigma_{\text{sc}}(T) \\
 \downarrow \\
 \rho_{\text{sc}}(T) \begin{array}{l} \nearrow \mathcal{D} \\ \searrow \tau \end{array} \\
 \downarrow \\
 \rho_{\text{sc}}(T) = \frac{1}{e^2 \kappa D_{\text{NE}}}
 \end{array}$$

4.3.2 Self-generated disorder

In the previous section we have examined electron transport in systems with long-range interactions from a diffusive standpoint. We have determined that the diffusion is limited by the presence of long-range interactions. In the present section we delve more deeply into how the long-range interactions generate a disordered landscape that corresponds to slow, collective charge fluctuations. We argue that these fluctuations are sufficiently slow that a classical treatment of them is justified above a given temperature ($T \gtrsim 0.2U$). Finally, we conclude that although the timescale to change the global charge arrangements is long, accurate descriptions of electron transport should still treat individual hopping processes in a quantum mechanical fashion. This topic will be explored in the following section.

Similar to our zero-temperature study in Chapter 3, we argue that the long-range nature of the electronic interactions gives rise to an emergent disorder which limits the diffusive nature of the charge carriers. Furthermore, we demonstrate that this phenomenon survives even in the presence of local interactions of the Hubbard type. As such, we first focus on the distribution of on-site electrostatic potentials, $P(\phi)$. This quantity is computed at fixed filling via canonical Monte Carlo calculations (fixed N, V, T). We shall refer to ϕ as the on-site electrostatic potential in this chapter to avoid confusion with the on-site (local U) potential already present in our model. We define the on-site electrostatic potential for a site i to be

As a reminder, the distribution of on-site potentials, $P(\phi_i)$, in the quantum case was defined as:

$$\left\langle \psi_0 \left| \delta \left(\phi_i - \sum_{j \neq i} V(R_{ij}, \alpha) (\hat{n}_j - \bar{n}) \right) \right| \psi_0 \right\rangle$$

$$\tilde{\phi}_i = \frac{\phi_i}{V} = \sum_{j \neq i} (\hat{n}_j - \bar{n}) R_{ij}^{-\alpha} \quad (4.17)$$

and the distribution $P(\tilde{\phi})$ at finite temperature to be

$$P(\tilde{\phi}) = \left\langle \delta \left(\tilde{\phi}_i - \sum_{j \neq i} (\hat{n}_j - \bar{n}) R_{ij}^{-\alpha} \right) \right\rangle_{\beta} \quad (4.18)$$

where $\langle \cdot \rangle_{\beta}$ now indicates a thermal average at a fixed temperature, $\beta = 1/k_B T$.

Selected results, presented in Fig. 4.16, illustrate typical configurations and their associated on-site electrostatic potentials (left and central panels, respectively). At the chosen temperature ($T/U = 0.14$), the difference in landscapes between $\alpha = 1$ (long-range) and $\alpha = 3$ (dipolar) is striking. The $\alpha = 3$ clearly indicates short-range charge correlations that lead to polaronic signatures in the $P(\phi)$, as evidenced in the snapshots of the site-wise occupation and the on-site electrostatic potentials (top left and center panels, respectively). The overall distribution (top right panel) exhibits the onset of a bimodal structure, which will eventually settle into a hard gap with two peaks as the system freezes into its charge-ordered ground state.

On the other hand, the pure long-range case ($\alpha = 1$) presents a more disordered landscape, as can be seen from the snapshots of the representative configuration and its on-site electrostatic potentials (bottom

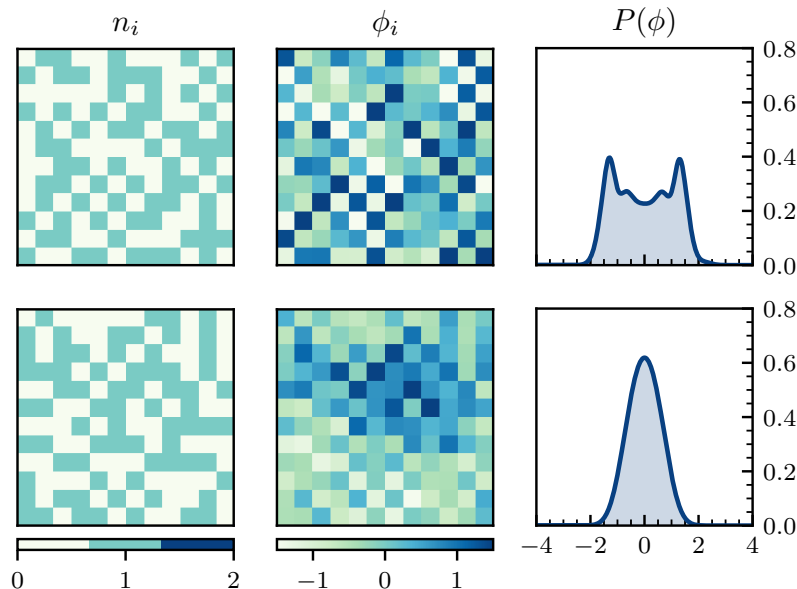


Figure 4.16: *Left panels*: The site-wise occupation of a representative configuration, n_i . *Center panels*: The on-site electrostatic potentials of the representative configuration, ϕ_i . *Right panels*: The distribution of on-site potentials, $P(\phi)$. Results for $\alpha = 3$ are shown in the top row and for $\alpha = 1$ in the bottom row. All other parameter values ($V/U = 0.4$, $n = 0.5$ and $T/U = 0.14$) are the same for both rows.

left and center panels of Fig. 4.16, respectively). This disordered landscape ultimately leads to a Gaussian distribution of on-site electrostatic potentials (bottom right panel of Fig. 4.16). As the temperature rises and thermal fluctuations increase, we can expect that the shorter-ranged system ($\alpha = 3$) will also move away from the charge-ordering transition and explore a more uniform distribution of on-site electrostatic potentials. However, each individual snapshot will continue to look disordered, as in the case of the pure long-range interactions (bottom center panel of Fig. 4.16).

We would like to take a moment to emphasize the fact that this disordered landscape of on-site electrostatic potentials is unique to long-range interactions. If we consider the nearest-neighbor limit of our model ($\alpha \rightarrow \infty$), then we observe that the spectrum of $\tilde{\phi}$ values is no longer continuous. The necessarily discrete nature is shown in Fig. 4.17 for a representative case with $\alpha = 32$. This range-driven discrete nature of this spectrum impacts other observables, such as the semi-classical optical conductivity (see Fig. 4.19). In stark contrast to the continuous conductivity spectra shown earlier in Fig. 4.5 for $\alpha = 1, 3$, these spectra for $\alpha = 32$ display discrete peaks located at integer multiples of $0.1U$. In other words, the only excitation frequencies accessible can be easily enumerated based upon the lattice coordination number ($z = 4$ for the square lattice). With increasing range of interactions, on the other hand, the one-electron hopping processes explore on average an increasingly continuous spectrum of on-site electrostatic energies (Fig. 4.16), resulting directly in continuous conductivity spectra (Fig. 4.5).

To further explore the effects of the long-range interactions on the

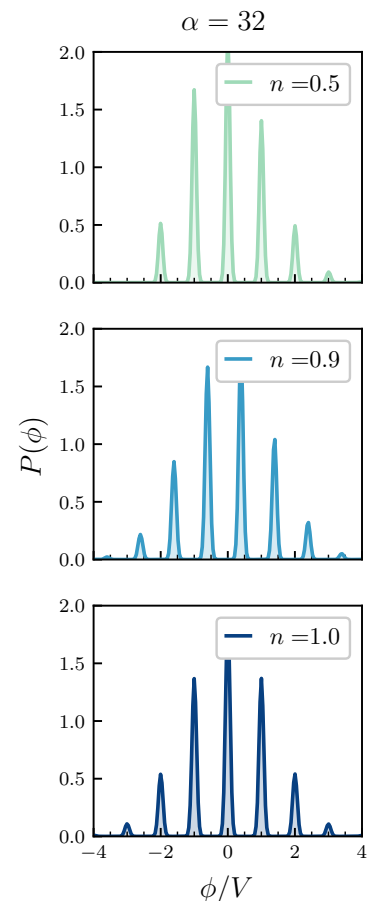


Figure 4.17: Distribution of on-site electrostatic potentials for the short-range interacting limit, $\alpha = 32$. All results are shown for $V/U = 0.1$ and $T/U = 1.2$.

Figure 4.18: Fluctuations of the on-site electrostatic potentials, $\delta\phi$, as a function of T/U . Results are shown for the long-range case ($\alpha = 1$, solid lines) and a shorter-ranged case ($\alpha = 3$, dashed lines). The cutoff line (gray) indicates when the charge fluctuations are reduced to the order of half the bandwidth and provides an estimate for the crossover between the classical and quantum behavior of the collective charge fluctuations.

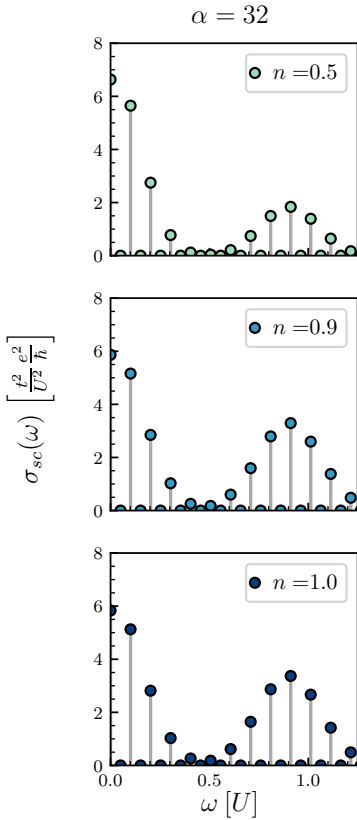
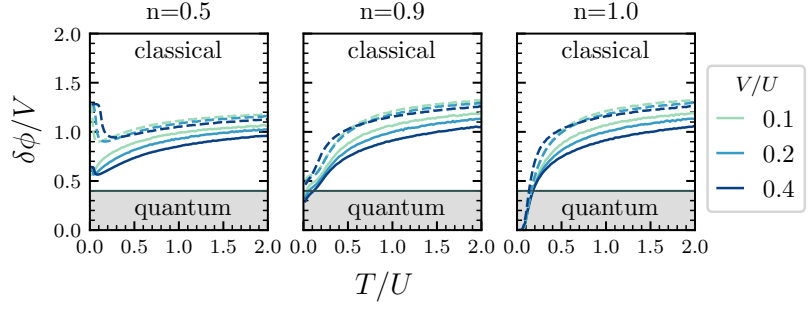


Figure 4.19: Semi-classical optical conductivity for the short-range interacting limit, $\alpha = 32$. All results are shown for $V/U = 0.1$ and $T/U = 1.2$.

The nearest-neighbor limit for $\delta\phi/V$ is straightforward to determine in the charge-ordered phase for $n = 0.5$. This phase displays a checkerboard order, with every other site occupied by an electron. This leads to $\langle\phi_i\rangle = 2V$, $\langle\phi_i^2\rangle = 8V^2$ and $\delta\phi/V = 2$.

system, we compute the fluctuation of the on-site electrostatic potentials, $\delta\phi_i = \sqrt{\langle\phi_i^2\rangle - \langle\phi_i\rangle^2}$. This provides a qualitative measure of the self-generated electrostatic disorder. All results in Fig. 4.18 are compared with a cutoff value (gray line) that provides an estimate for the crossover between classical and quantum behavior for the collective charge fluctuations. The cutoff line (gray) indicates when the charge fluctuations become comparable with half the bandwidth

$$\delta\phi/V \sim W/2 = 4t \quad (4.19)$$

for a representative choice of quantum fluctuations, $t = 0.1U$, and representative bandwidth, $W = 8t$. In other words, this cutoff provides us with an estimate of the region in parameter space where all electronic states become incoherent, enabling a classical treatment. From this approximation, we can reasonably assume that in the lightly-doped and half-filled cases we can treat the charge fluctuations classically for temperatures $T \gtrsim 0.2$, which corresponds to the high-temperature regime where the resistivity continues to climb well past expected Mott-Ioffe-Regel limits (see Fig. 4.6). We argue that the classical treatment of collective motion should be appropriate at all temperatures in the quarter-filled case, a question which was left open in a previous study of Coulomb glasses [110].

As shown in Fig. 4.18, the choice of interaction type also has a profound impact on the fluctuations of the on-site electrostatic potential for much of the temperature range. If we first consider the quarter-filled case ($n = 0.5$), we observe the charge-ordering transition as $\delta\phi$ suddenly increases at low temperatures, for both the pure long-range ($\alpha = 1$, full lines) and the dipolar ($\alpha = 3$, dashed lines) cases. The strength of the non-local interaction plays a role in this transition as higher values of V/U correspond to transitions at higher temperatures, as to be expected from the previous signatures of charge-ordering observed in the charge compressibility (Fig. 4.13). The transition also occurs at higher values of T/U for $\alpha = 3$ than for $\alpha = 1$, in agreement with the fact that systems with short-ranged interactions are more susceptible to charge-ordering. In other words, long-range interactions reduce the energy scale, and thereby the temperature, for

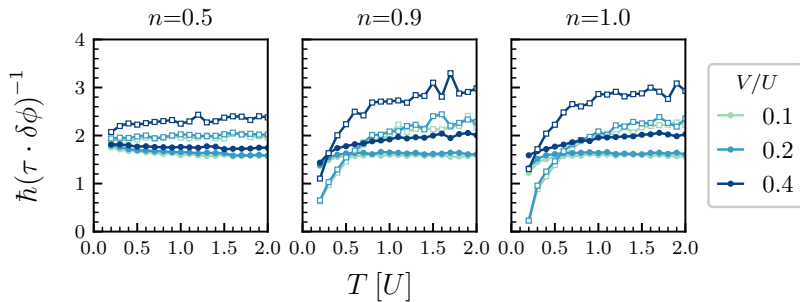


Figure 4.20: The inverse transport lifetime scaled with the electrostatic charge fluctuations for $\alpha = 1$ (full circles) and $\alpha = 3$ (open squares). Although charge fluctuations are quenched by U in all panels, the low temperature behavior is clearly dependent on the filling.

charge-ordering transitions as previously discussed.

If we next consider the lightly-doped case ($n = 0.9$), we again observe that the values of $\delta\phi$ remain segregated by values of α across much of the temperature range. As the temperature decreases, the values appear to converge to a finite value, which is most likely due to the effect of the on-site potential term, U , quenching charge fluctuations. Determining the value of $\delta\phi/V$ at convergence requires more intensive studies at low temperatures, which would rapidly become prohibitive using classical Monte Carlo calculations due to exponentially long sampling times. Finally, in the half-filled case ($n = 1.0$), the interaction range again plays a role in the values of $\delta\phi/V$ across most temperatures before all charge fluctuations are eventually quenched at low temperature as the system approaches its insulating ground state. This quenching occurs regardless of interaction range and signals that the Mott physics dominates in this low-temperature region. However, the role of non-local interactions remains relevant for temperatures $T \gtrsim 0.2U$. Overall, our results have shown that long-range interactions give rise to self-generated disorder at finite temperature, even in the presence of a local potential.

We can utilize the fluctuation of the on-site electrostatic potentials to characterize how the previously computed contributions to the semiclassical resistivity depend on the charge fluctuations. In fact, the inverse transport lifetime scales with $\delta\phi/V$ across most of the temperature range, as shown in Fig. 4.20. In particular, in the quarter-filled case, the ratio $\tau^{-1}/\delta\phi$ is almost universal, suggesting the relevance of the interplay between U and V . It is important to remark that the universal behavior appears for small values of α . Similarly, the inverse diffusion constant calculated from the Nernst-Einstein relation scales with $\delta\phi/V$ (see Fig. 4.21), suggesting that the relatively constant charge fluctuations control the limited behavior of the diffusion constant (i.e. its constant nature) across the range of temperatures explored. With these observables constant, then the other contributions are unchecked and dictate the growth of the observed bad metallic resistivity.

Overall, we have demonstrated that long-range interactions give rise to a disordered landscape of on-site electrostatic potentials. We have

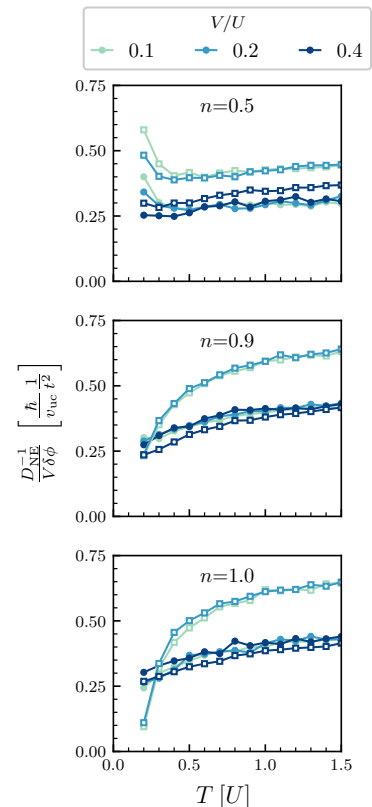


Figure 4.21: The inverse diffusion constant scaled with the electrostatic charge fluctuations for $\alpha = 1$ (full circles) and $\alpha = 3$ (open squares).

computed the average fluctuation of these potentials and used this quantity to estimate a region in our parameter space where global charge fluctuations can be treated as classical objects. In order to understand how the disordered landscape impacts electron transport, we have explored how the transport lifetime and diffusion constant scale with the fluctuation of the on-site electrostatic potentials. We have discovered that these quantities scale in a constant manner with the fluctuation at high temperatures, thereby suggesting that this quantity is responsible for limiting the diffusion of charges. In the next section, we will examine transport in a framework that goes beyond semi-classical treatment revealing the importance of localization processes in the emergent disordered potential of the electrons.

4.4 Anomalous quantum transport: transient localization

At this point we have established that our long-range interacting model provides a microscopic description of bad-metallic resistivity. In particular, we have shown that the long-range interactions generate disordered landscapes of electrostatic on-site potentials, leading to large values of the resistivity. The fluctuations of these potentials constrain the behavior of the charge diffusion at high temperature where their energy scale is much larger than that of a typical bandwidth, suggesting that the fluctuations in local field (or global charge rearrangements) can be treated classically across much of the temperature range accessible in classical Monte Carlo. We would now like to address the question of how corrections beyond a semi-classical treatment impact the observed bad metallic transport, thereby connecting our high-temperature study with our zero-temperature exact diagonalization results.

Going beyond a semi-classical treatment of the individual electron motion will enable us to determine if the long-range interactions are capable of driving localization processes, which could potentially resolve the mismatch of resistivity slopes as discussed earlier. Furthermore, disorder-driven localization processes have been proposed as a mechanism responsible for the observation of so-called *displaced Drude peaks*. This phenomenon has been observed in several bad metallic systems, including the ruthenates [204, 205], cobaltates [206, 207], cuprates [208–212], vanadates [213, 214], manganates [215, 216], nickelates [60], and organic conductors [217]. However, most theoretical attempts to understand bad metallic systems have failed to reproduce this behavior as these approaches relied on the conventional Hubbard model [72, 80, 218]. This model only accounts for local electronic interactions which are incapable of generating continuously disordered electrostatic landscapes. In an attempt to answer this important open question, we provide here an analysis of the origin of displaced Drude peaks, and bad metallic transport in general, in the context of disorder-driven localization caused by long-range interactions.

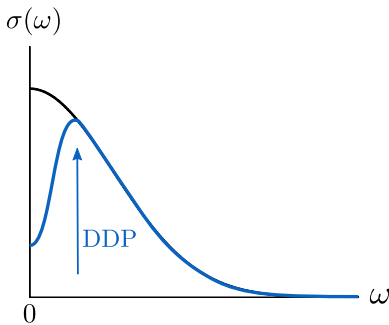


Figure 4.22: Illustration of displaced Drude peak occurring because of reduced diffusion of the carriers.

4.4.1 Mixed quantum-classical treatment

Monte Carlo calculations are devised for numerical studies of classical systems, which is suitable for the treatment of the slow, global charge rearrangements. However, we must develop a workaround to include the effects of quantum corrections beyond a semi-classical level in our calculations. As such, we work in a basis of single-particle (one-electron) states, $\{ |i\sigma\rangle \}$, where i represents the site of the particle and σ its spin sector. We construct a Hamiltonian in this basis that details the possible kinetic processes and interparticle interactions, $H_{\text{body}} = H_{\text{kin}} + H_{\text{int}}$. The kinetic processes for a state in a fixed spin sector are described by the kinetic Hamiltonian,

$$H_{\text{kin}} = -t \sum_{i,\sigma} \sum_{\langle j \rangle} (\hat{c}_{i\sigma}^\dagger \hat{c}_{j\sigma} + h.c.) \quad (4.20)$$

where t represents the magnitude of the hopping integral, or the quantum fluctuations, and the summation over $\langle j \rangle$ indicates a summation over the nearest neighbors of site i . The interacting portion of the Hamiltonian is constructed from the on-site (local) and on-site electrostatic (non-local) potentials of the configuration under consideration in each Monte Carlo time step,

$$H_{\text{int}} = U \sum_{i,\sigma} \left((\hat{n}_{i\sigma} - 0.5) + \phi_i \right), \quad (4.21)$$

where $\phi_i = \sum_j V_{ij} \hat{n}_j$. The one-body Hamiltonian is diagonalized exactly to obtain the corresponding single-particle energies, $\{\varepsilon_i\}$, which are then used (in conjunction with the density of the configuration) to determine the chemical potential according to the Fermi-Dirac distribution,

$$n = \sum_i \frac{1}{e^{\beta(\varepsilon_i - \mu)} + 1}. \quad (4.22)$$

Finally with the chemical potential, the quantum optical conductivity can be computed as

$$\sigma_{\text{q}}(\omega) = \pi \sum_{ij} f(\varepsilon_i) (1 - f(\varepsilon_j)) \frac{1 - e^{-\beta\Delta_{ij}}}{\Delta_{ij}} \left| \langle j | J_x | i \rangle \right|^2 \delta(\omega - \Delta_{ij}) \quad (4.23)$$

where $f(\varepsilon_i) = 1 / (e^{\beta(\varepsilon_i - \mu)} + 1)$ is the Fermi-Dirac distribution of eigenenergy ε_i , $\Delta_{ij} = \varepsilon_j - \varepsilon_i$ is the energy difference between the two configurations involved in the hopping process, and J_x is the current matrix that describes nearest-neighbor hopping processes in the \hat{x} direction. It is important to remark that the single-particle Hamiltonian, whose terms are described in Eq. 4.20 and 4.21, are only used to compute the optical conductivity and are not implemented in the acceptance criterion underlying the classical Monte Carlo scheme.

Selected results are presented in Fig. 4.23. We choose two values of the quantum fluctuations, t/U , with $t/U = 0.1$ chosen as the representative ratio for strongly correlated materials and $t/U = 0.01$ chosen

Figure 4.23: Quantum optical conductivity results for $\alpha = 1$ at $T/U = 1.2$ and two different values of quantum fluctuations, $t/U = 0.01, 0.1$. The classical results (green) are plotted for comparison. A Gaussian filtering of $\delta = 0.002\omega$ has been applied. The top row shows the entire spectrum ($\omega > 0$) while the bottom row focuses on the low-frequency region, illustrating how the addition of quantum fluctuations suppresses the weight around $\omega = 0$ and pushes it to higher values.

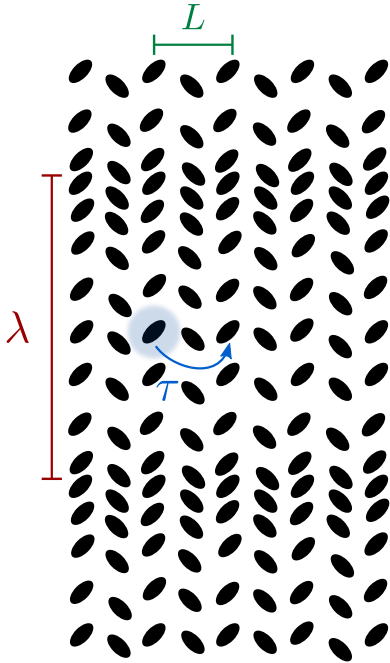
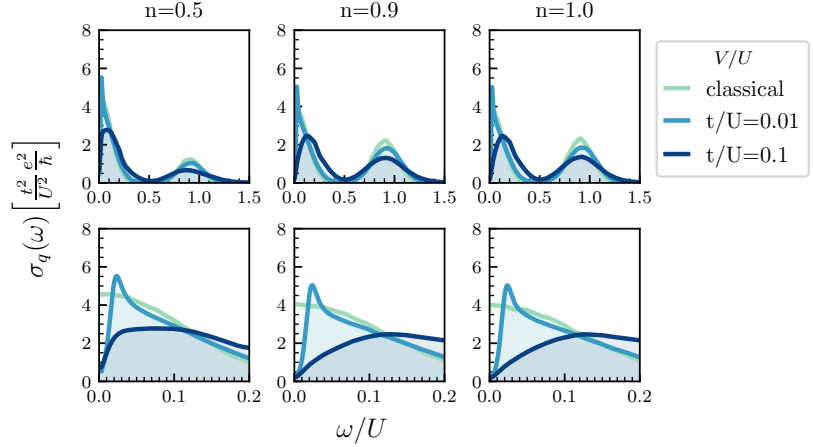


Figure 4.24: Illustration of transient localization. The carriers travel through a disordered landscape created by lattice vibrations and localize within each landscape on a timescale τ (blue). With a timescale $t \sim \omega_0$, the landscape changes and the build-up of quantum correlations leading to localization repeats. The localization length is denoted by L (green).

to understand how the classical result is approached in the limit $t \rightarrow 0$. Due to the increased computational cost of exactly diagonalizing a matrix of dimensions $2L^2 \times 2L^2$ at each Monte Carlo time step, the results presented correspond to a square lattice with side length $L = 6$. At the time of writing, preliminary calculations performed on systems with $L = 12$ suggest that the results do not suffer greatly from finite size effects. The confirmation of this point is still an open matter that requires a proper finite-size study. We observe that the inclusion of quantum corrections broadens the finite frequency peaks previously seen in the classical optical conductivity spectra (Fig. 4.5), but does not shift them to different values of ω/U . The classical results are also plotted in Fig. 4.5 for comparison. Most importantly, we notice a decrease in the zero-frequency weight of σ_q , with the spectral weight being shifted to the vicinity of small, finite frequency. In other words, the inclusion of quantum fluctuations suppresses the zero-frequency peak, leading to the development of a displaced Drude peak. As discussed in the introduction of this section, this phenomenon has been observed in several bad metallic systems, but has escaped general theoretical understanding thus far. In the following part, we examine how transient localization can act as a mechanism for these displaced Drude peaks.

4.4.2 Displaced Drude peaks

Recently, it was proposed that this displaced Drude peak phenomenon arises from a transient localization scheme where a source of disorder induces localization in the charge carriers, thereby causing a larger resistivity than predicted by semi-classical Boltzmann theory [77]. This transient localization theory was originally developed in the context of organic semi-conductors. These systems are comprised of molecules with a large molecular weight, leading to very slow lattice vibrations, $\omega_0 \sim \sqrt{K/M}$, which act as strong electron scatterers. Within the

framework of Boltzmann theory, these strong scatterers would give rise to a mean free path that is of the order of (or even shorter than) the intermolecular spacing, $\ell = a$, which corresponds to the Mott-Ioffe-Regel limit where Bloch-Boltzmann theory is no longer valid [78].

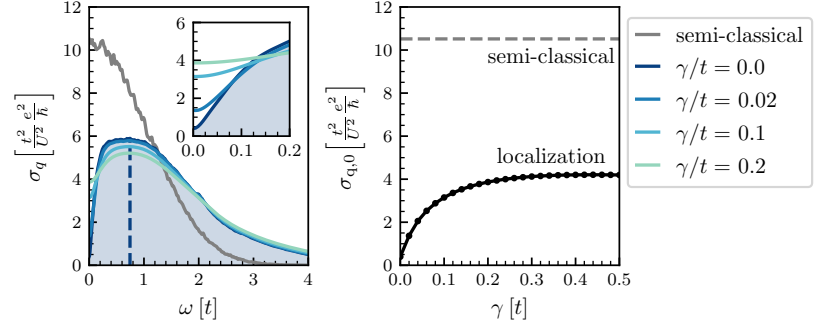
As shown in Ref. [78], the transient localization of the charge carriers occurs on a timescale smaller than that of the disorder, $t_{\text{loc}} < \omega_0^{-1}$. In other words, on the timescale of disorder (lattice vibrations in the case of organic semi-conductors) the electrons explore a disordered landscape and their quantum correlations enable Anderson localization. However, upon the fluctuation of disorder, the disordered potential landscape changes and the localization from the previous landscape is destroyed as the destructive interference pattern from the previous disordered potential no longer exists [219]. The average distance, or spread, that a carrier can travel before becoming localized is characterized by a localization length, L . This concept of fluctuating disorder leading to localization is illustrated in Fig. 4.24. This transient localization description of organic semi-conductors was later incorporated into unifying theoretical framework that smoothly connects the localization (strong disorder) limit with the semi-classical (weak disorder) limit [79].

Following the establishment of this consolidated framework, this theory was applied to a many-body electronic lattice model at half-filling with generic electron-boson interactions [77]. In this setting, the slow bosonic fluctuations caused a displaced Drude peak by reducing the carrier diffusion, a localization effect that was only properly accounted for by a quantum treatment of the electronic correlation. The appearance of transient localization in this low-dimensional metallic model encourages us to consider whether the self-generated landscape from long-range interactions can act as a source of disorder that reduces carrier diffusion, thereby leading to anomalous transport as quantum correlations build up.

4.4.3 Beyond semi-classical transport

Indeed, the suppression of the zero-frequency weight of $\sigma_q(\omega)$ (previously shown in the bottom row of Fig. 4.23) suggests that long-range interactions can reduce carrier diffusion in the absence of external sources of disorder, thereby creating a displaced Drude peak. However, our hybrid quantum-classical approach completely suppresses the zero-frequency value. This occurs because the electronic problem is solved in an effectively static random background which means that all states are localized and the conductivity vanishes identically. We can only restore a finite value of $\sigma_{q,0}$ if we reestablish the energy scale of the slow fluctuations [193, 220, 221]. This can be achieved by applying a Lorentzian broadening to our conductivity spectra in order to obtain a finite value $\sigma_{q,0}$ that can be used to define the quantum resistivity, $\rho_q = 1/\sigma_{q,0}$. We perform a convolution of the optical con-

Figure 4.25: *Left*: Plot of $\sigma_q(\omega/t)$ (main panel) demonstrating the suppression near $\omega/t = 0$ with the inclusion of quantum effects. A Gaussian filter of $\delta = 0.05t$ was applied to the semi-classical (gray) and quantum (dark blue) curves. Inset shows how the Lorentzian convolution changes with the broadening, γ/t , in the low-frequency regime. *Right*: Comparison of the zero-frequency values of the semi-classical ($\sigma_{sc,0}$) and quantum ($\sigma_{q,0}$) conductivities as a function of γ/t . Parameter values ($\alpha = 1$, $t/U = 0.1$, $V/U = 0.2$, $n = 0.5$ and $T/U = 0.6$) are the same for both panels.



ductivity with a Lorentzian function, $\mathcal{L}(\omega - x, \gamma)$, as

$$\sigma(\omega) = \int_{-\infty}^{+\infty} dx \sigma_q(x) \mathcal{L}(x - \omega, \gamma) \quad (4.24)$$

where γ is the broadening and is of the order of the energy scale of the relevant source of disorder in the system. This broadening approach provides estimates very similar to those obtained from the relaxation time approximation developed in the original theory of transient localization, but originates from a different physical motivation [193].

The effect of this broadening approach to yield a finite value of $\sigma_{q,0}$ is shown in Fig. 4.25. The left panel compares the low frequency region between the semi-classical conductivity (gray) and the quantum version for various degrees of broadening, γ . The inset demonstrates that as the broadening, γ , increases, the suppressed zero-frequency weight rises toward the semi-classical values. The right panel shows in more detail how the zero-frequency value, $\sigma_{q,0}$, increases with the broadening. This value never fully saturates to that predicted by the semi-classical treatment of the optical conductivity and instead saturates for $\gamma \sim 0.3t$, which is still above the estimated value of the frequency of the slow charge fluctuation, $\omega \sim 0.2t$, as estimated from the results in the previous chapter. It is important to note that this broadening procedure is not valid when γ exceeds the energy scale of the slow disorder, which is labeled by the dashed blue line in Fig. 4.25.

For the values of the quantum resistivity reported in Fig. 4.26, we selected a broadening of $\gamma = 0.2t$ as this corresponds to the frequency of the peak of collective charge excitations observed in the spinless, zero temperature version of our model ($\omega_{\text{coll}} \sim 0.2t$, see Chapter 3), thereby providing a reasonable order-of-magnitude estimate. At low temperatures, we observe that the resistivity stops decreasing with decreasing temperature for the half-filled case, but we attribute this behavior to the onset of jamming. As shown in Fig. 4.26, our quantum-classical hybrid approach predicts even more anomalous transport representative of bad metallic systems. In fact, the reduction of diffusion of the charge carriers by the presence of almost static, self-generated disorder further drives the quantum resistivity past the Mott-Ioffe-Regel limit,

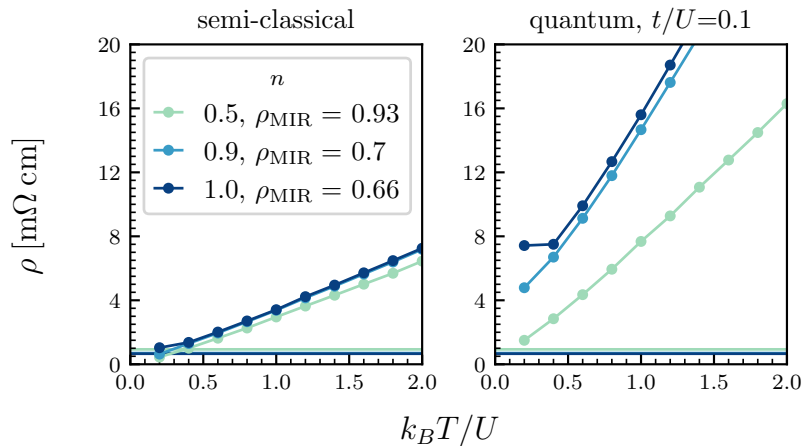


Figure 4.26: Quantum resistivity, ρ_q , compared with the semi-classical resistivity, ρ_c , for $\alpha = 1$ and $V/U = 0.1$ on the 6×6 square lattice. Results (solid lines with full circles) are plotted for different values of the filling. The estimates for the Mott-Ioffe-Regel limit of each filling are provided (solid lines, right legend). The color scheme for the estimates is the same as for the resistivity curves (left legend).

the estimates of which are given in solid lines in Fig. 4.26.

Furthermore, this approach provides us with a mechanism to understand the displaced Drude peaks observed in many bad metallic systems. We turn our attention to understanding the scaling behavior of the displaced Drude peaks, shown in Fig. 4.28. The top row demonstrates how the peak location evolves as a function of temperature and typical energy scales. The open squares correspond to the limiting classical case, ($t/U = 0.01$, open squares), and we see immediately from the top row of Fig. 4.28 that the displaced Drude peak saturates at $2t$, as predicted in Ref. [77,222]. On the other hand, the frequency of the displaced Drude peak representative of typical strongly correlated systems ($t/U = 0.1$, full circles) displays a growth with the temperature towards this maximum value, $\omega_{\text{peak}} = 2t$.

Ref. [77] additionally predicted that the peak should scale universally with the amount of disorder associated to the bosonic modes (see Fig. 4.27). In our particular model, this quantity is represented by the fluctuation of the on-site electrostatic potentials, $\delta\phi$, introduced in the previous section. We therefore anticipate that the displaced Drude peak will demonstrate a universal scaling behavior with $\delta\phi$. Indeed, the scaling of ω_{peak} shown in the bottom row of Fig. 4.28 strikingly resembles that observed in Ref. [77], despite the fact that the models in question are very different in nature. In other words, the long-range interactions cause a disordered landscape of on-site electrostatic potentials with the amount of disorder quantified by $\delta\phi$. This disorder triggers a response in the electronic behavior such that ω_{peak} reflects the strength of the localization effects induced by this source of disorder. This method of disorder-induced localization therefore provides a long-sought-after universal mechanism for bad metallic behavior.

We observe differences in scaling as a function of the filling in the bottom row of Fig. 4.28, which indicates that the local (Hubbard U) potentials also contribute to the disorder. This contribution is not con-

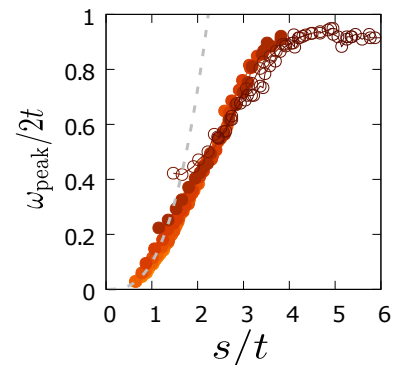


Figure 4.27: The frequency of the displaced Drude peak as a function of bosonic disorder, s , in the Holstein model (generic electron-boson interactions). Adapted from Ref. [77].

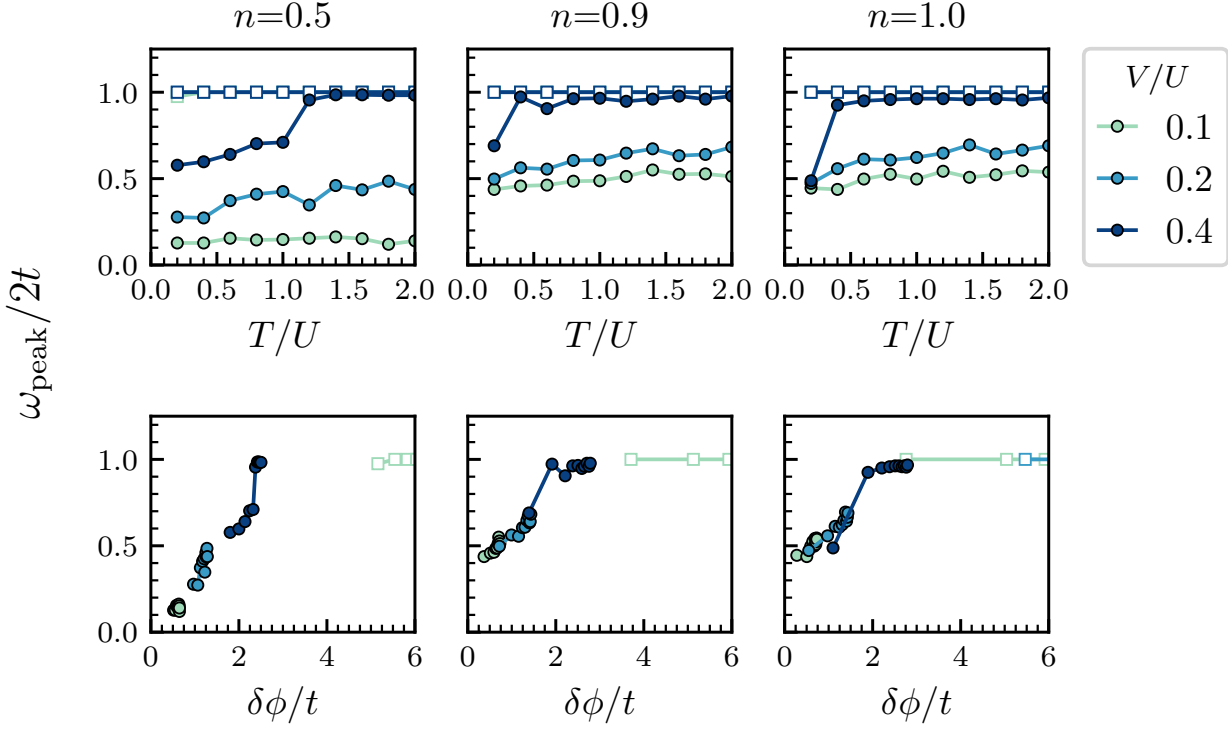


Figure 4.28: The frequency of the displaced Drude peak for $\alpha = 1$ as a function of temperature (top row) and fluctuations of on-site electrostatic potentials (bottom row). Open squares correspond to the limiting case $t/U = 0.01$ while full circles correspond to the strongly correlated case $t/U = 0.1$.

tained in our fluctuation of disorder, $\delta\phi$, and we predict that the frequency should scale on a universal curve if plotted as a function of the fluctuation of *all* potentials,

$$\delta\Phi^2 = \delta\phi^2 + \delta\phi_U^2 \quad (4.25)$$

where $\delta\phi_U^2 = U^2(\langle n_{i\sigma}^2 \rangle - \langle n_{i\sigma} \rangle^2)$. However, confirmation would require sampling of this last quantity, $\delta\phi_U^2$, which has not been performed yet. Overall, our results provide preliminary evidence for a universal mechanism of bad metallic behavior arising from long-range interactions. This will need to be confirmed by a fully quantum treatment such as the finite temperature Lanczos method. This point is under active consideration and will be addressed in more detail in Chapter 5.

Finally we should stress that this procedure is not self-consistent because the quantum corrections are not included directly in the Monte Carlo sampling of the phase space. Their inclusion is not straightforward as the solution to the one-body Hamiltonian with external disorder $P(\phi)$ already assumes that the system is at thermodynamic equilibrium. Therefore, these single-particle energies cannot be used in the acceptance term that governs how the Markov chain samples through phase space. The appropriate formulation is still under active consideration.

4.5 *Conclusions and summary*

In this chapter, we have analyzed the role of long-range interactions in the context of anomalous electrical transport. With classical Monte Carlo calculations, we have examined a spinful model with long-range interactions and details on this numerical technique can be found in Appendix C. Initially, we investigated incoherent transport in the high temperature limit and demonstrated that the electrical resistivity of our long-range model grows linearly with temperature and greatly exceeds the predicted Mott-Ioffe-Regel limit for a representative strongly correlated system. Furthermore, a large difference upon comparison of the experimental value of the resistivity-temperature slope to that computed from our model implied that we revisit the theoretical understanding of metallic transport in these systems. Following this comparison, we studied charge transport in the Nernst-Einstein diffusion framework and determined that charge diffusion is limited by the fluctuations of the on-site electrostatic potentials. This last step was made possible by incorporating our knowledge on collective charge fluctuations obtained in Chapter 3.

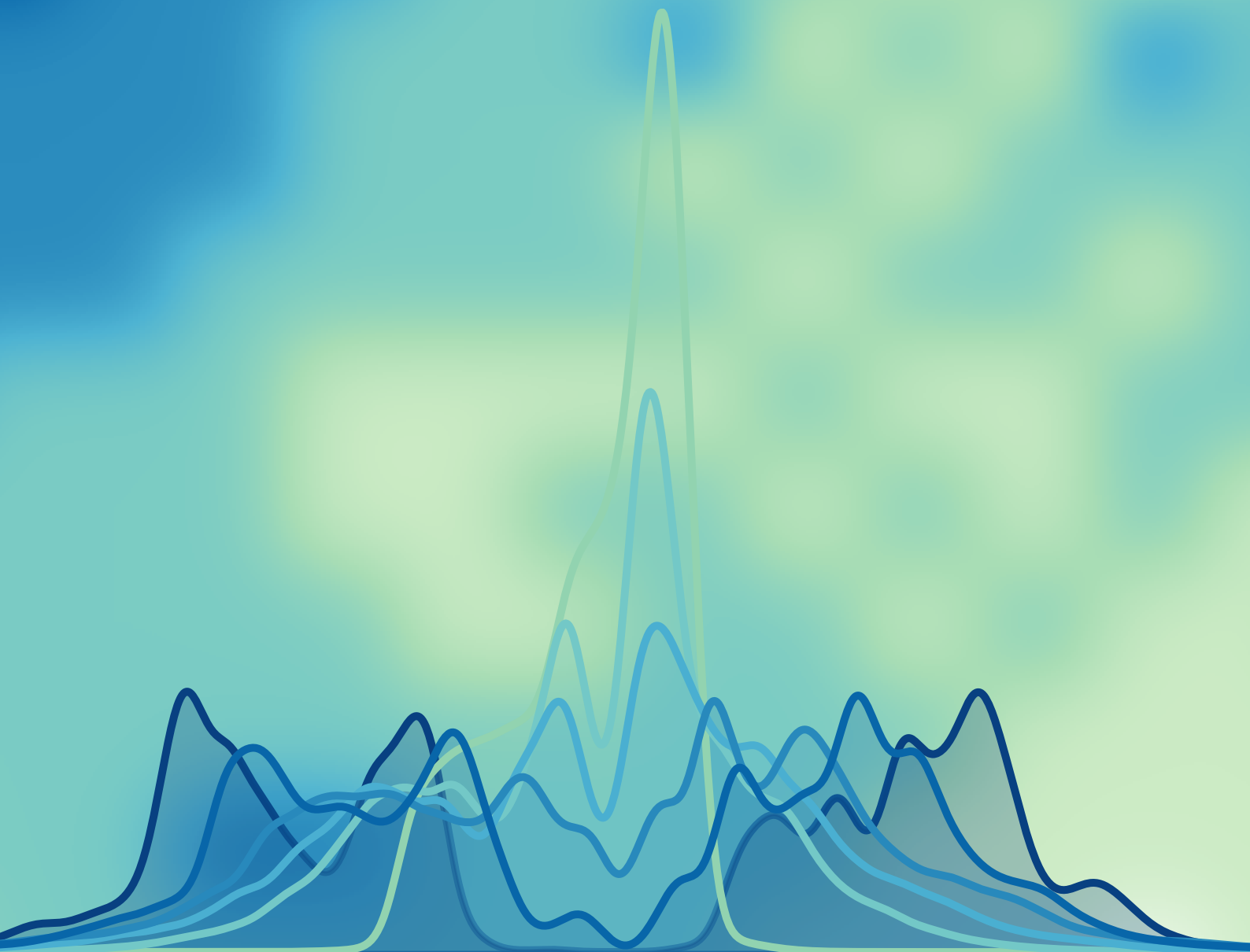
Motivated by the idea that a separation of timescales exists between rapid, individual electron motion and slow, collective fluctuations, we examined how quantum corrections beyond a semi-classical treatment impacted the transport properties of our system. By treating the individual electron motion quantum mechanically, we were able to demonstrate that the disorder generated from the long-range interactions causes transient localization of the charge carriers, a phenomenon also found in organic semi-conductors [78]. The key concept underlying the anomalous behavior observed in both of these systems is that a proper theoretical description can treat the sources of disorder as classical objects, while the individual carrier motion should be treated quantum mechanically.

The decreased diffusion of charge carriers gave rise to resistivity results that were even more anomalous than those previously computed in the semi-classical framework. Furthermore, we showed that long-range interactions also act as a microscopic mechanism for the development of displaced Drude peaks, another signature of bad metallic behavior in certain systems, and we provided preliminary evidence suggesting that the frequency of the peak obeys a universal scaling law with respect to the strength of the disorder present in the system, as previously shown for a generic electron-boson interaction model in Ref. [79].

We emphasize that these effects are missed completely by models that reduce electronic interactions to only on-site or nearest-neighbor contributions. They are also missed in treatments such as DMFT that completely neglect localization (vertex) corrections in the evaluation of the current-current correlation function. Overall, the work presented in this chapter has served as a first step towards extending our zero

temperature work to include thermal effects and in doing so, we have discovered that long-range interactions act as a microscopic mechanism for anomalous transport at finite temperatures. In summary, these results pave the way for a novel theoretical understanding of anomalous transport in materials with weak screening.

Chapter 5: Conclusions



Conclusions

This dissertation has examined the impact of long-range interactions in lattice models of low-dimensional strongly correlated systems and firmly establishes this subject as an exciting avenue of research with many questions to be explored in the future. Over the past several decades, effective fermionic lattice models have commonly been employed in investigations of strongly correlated electronic behavior. These models typically begin from the assumption that the long-range Coulomb interaction between electrons can be reduced to an effective, short-range interaction due to efficient screening processes. In particular, the archetypal Hubbard model, which functions as the minimal model of electronic correlation with only local (on-site) interactions, has proven very successful in explaining strongly correlated phenomena such as the Mott metal-insulator transition [16, 18].

There are only a few analytical solutions to this simple model [19, 20], which has triggered a massive development in numerical methods capable of studying strongly correlated systems in the past several decades. Despite the immense progress made in this direction, the existence of several phenomena that escape general theoretical description hints at the fact that we might be reaching the limit of information accessible from the Hubbard model and other conventional lattice models. Notably, an explanation for the anomalous transport properties observed across a broad range of materials represents one of the most important open questions in modern condensed matter physics. These properties include the growth of the electrical resistivity beyond the Mott-Ioffe-Regel limit where the Bloch-Boltzmann picture breaks down, anomalous scaling laws of the resistivity around this region, and the development of displaced Drude peaks in some cases. Studies of the Hubbard model are unable to fully explain this anomalous, or bad-metallic, behavior which suggests that a crucial element must be missing from the model.

The fact that these bad-metallic signatures are seen in a variety of

strongly correlated materials further suggests that this missing element must have a general nature. In this thesis, we have focused our efforts on understanding the effects of one proposed mechanism in particular—long-range electronic interactions. Indeed, several experimental and theoretical works have hinted at the potential relevance of this mechanism in a number of systems. For example, although the cuprate family of superconductors is arguably the best studied group of strongly correlated materials, the Hubbard model remains unable to accurately characterize its stripe order. Ref. [88] proposed that this failure was due to the lack of long-range interactions and even provided evidence that the expected contribution of the long-range interactions would be of the order of the energy scales seen in the competing ground states. Another example of systems with important long-range contributions would be the family of transition metal dichalcogenide heterostructures, which recently were shown to host Wigner crystal phases at several fractional filling values [45, 46, 120]. These clean materials form Moiré superlattices with narrow bandwidths which render them an ideal experimental platform in which to analyze the physics of strong, long-range interactions.

Motivated by these examples (and several others), we set out to examine the impact of long-range interactions by means of a spinless model at zero temperature. The analysis of this model is the focus of Chapter 3 of this thesis and it has been studied with exact diagonalization calculations. This powerful numerical technique grants us with complete control over the microscopic degrees of freedom including the form of interactions. Chapter 2 provides a technical introduction to this methodology. In particular, this chapter focuses on strategies that we employ in order to overcome the main limitation of this technique which is finite size effects that arise from being restricted to studying small system sizes due to the exponential growth of the Hilbert space. These strategies include the use of twisted boundary conditions to minimize finite size effects in the kinetic portion of the Hamiltonian and the use of the Ewald summation technique to compute electrostatic potentials representative of the thermodynamic limit.

With these techniques implemented, we proceed to inspect the novel correlated behavior arising from our long-range interacting spinless model in Chapter 3. Before presenting the phase diagram in terms of the interaction range, α , and strength, V/t , we predict the existence of the phases contained within and their respective transitions based upon results from the classical limit ($V/t \rightarrow \infty$) and the limit of nearest-neighbor interactions, $\alpha \rightarrow \infty$. The numerical results obtained for the phase diagram agree remarkably well with these analytical estimates and additionally provide evidence that the finite size effects are well under control. The phase diagram is reproduced here in Fig. 5.1 and contains a novel correlated metal phase in the long-range (small α) region. We focus on the case of $\alpha = 1$, corresponding to the pure Coulomb interaction and measure the presence of strong

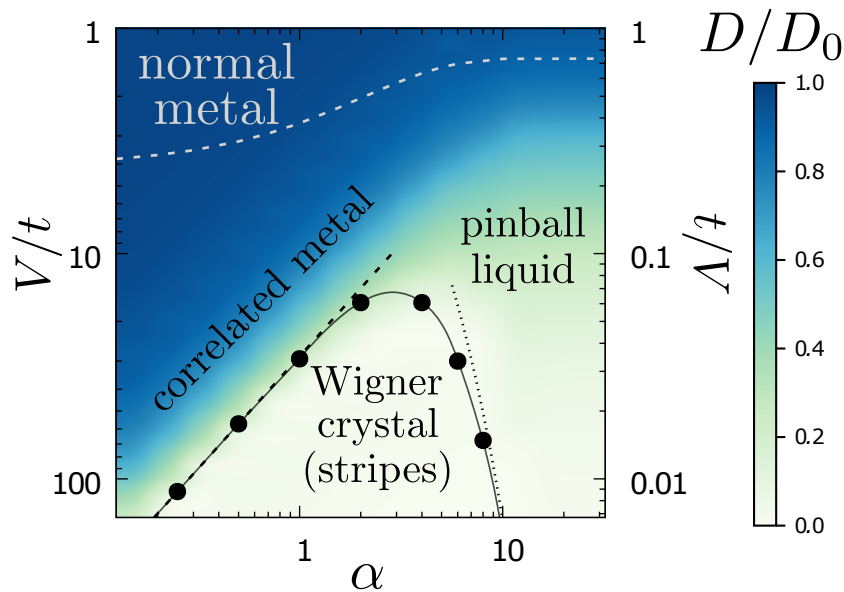
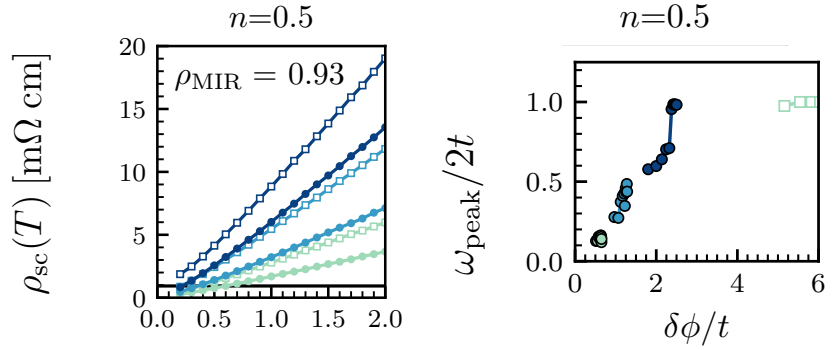


Figure 5.1: Phase diagram of the long-range spinless model studied in Chapter 3.

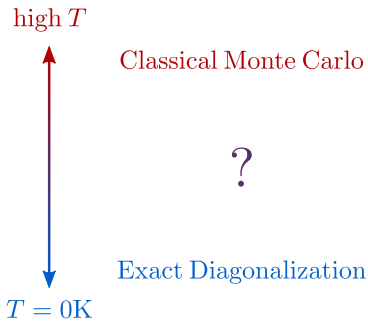
electronic correlations throughout the metallic phase by means of the quasiparticle weight, Z . We further demonstrate that a pseudogap develops in the single-particle spectral function upon the approach to the metal-insulator transition, behavior that is completely unrelated to the conventional Mott-Hubbard metal-insulator transition. We emphasize that this correlated pseudogap phase arises directly from the disorder of electrostatic potentials which is self-generated by the long-range interactions. Furthermore, we draw a parallel between the observed pseudogap and the Coulomb gaps seen in disordered classical systems. Finally we examine the nature of the collective charge fluctuations, discovering frustration due to competition among several competing charge orders at the approach of the metal-insulator transition. We conclude that the long-range interactions generate disordered landscapes that lead to slow charge fluctuations that we anticipate will have a profound impact on electrical transport at finite temperatures.

The analysis of the role of long-range interactions in anomalous transport constitutes the topic of Chapter 4. In this chapter, we study a spinful model with long-range interactions by means of classical Monte Carlo calculations. Details on this numerical technique can be found in Appendix C. We initially study incoherent transport in the limit of high temperature where we observe that our resistivity results grow linearly with temperature and exceed the expected Mott-Ioffe-Regel limit for a representative strongly correlated system (see left panel of Fig. 5.2). Additionally, we study charge transport in the Nernst-Einstein diffusion framework and incorporating ideas from Chapter 3, we determine that charge diffusion is limited by the fluctuations of the on-site electrostatic potentials.

Figure 5.2: Examples of the resistivity violating the Mott-Ioffe-Regel limit for a representative strongly correlated system (left panel). Scaling of the displaced Drude peak with the strength of disorder from the long-range interactions (right panel).



Motivated by comparison with experimental values and the idea that a separation of timescales exists between rapid, individual electron motion and slow, collective fluctuations, we proceed to address the question of how corrections beyond a semi-classical treatment impact the observed bad metallic transport. This serves as a first step towards connecting our zero temperature work with our discovery that long-range interactions act as a microscopic mechanism for anomalous transport at finite temperatures. By treating the individual electron motion quantum mechanically, we are able to demonstrate that the disorder generated from the long-range interactions leads to a phenomenon known as transient localization. This causes a reduction in the motion of the charge carriers, leading to even more anomalous behavior than previously observed. Furthermore, we demonstrate that long-range interactions also act as a microscopic mechanism for the development of displaced Drude peaks and provide preliminary evidence suggesting that the frequency of the peak obeys a universal scaling law with respect to the strength of the disorder present in the system, as shown for a generic electron-boson interaction model in Ref. [79]. An example of this scaling with the disorder (as measured by the fluctuations) is shown in Fig. 5.2.



Overall, the work presented in this thesis opens the door for many new, exciting avenues of research to be explored in the future. We have conducted a thorough study of the physics of long-range interacting electrons at zero temperature via exact diagonalization, discussed in Ch. 3. In addition, we have investigated the high temperature behavior of long-range interactions in conjunction with local, on-site interactions via our classical Monte Carlo work presented in Ch. 4. This work in particular has attempted to draw connections with physical systems where appropriate. However, we recognize that this classical method is inherently limited and that there is still a gaping need to understand transport properties at intermediate temperatures.

As discussed in Ch. 4, proper treatment of quantum fluctuations plays an important role in determining the mechanisms underlying electronic transport in strongly interacting systems. Therefore, extending the zero-temperature exact diagonalization machinery to finite temperature would be a logical first step towards bridging the gap between our two main works as it would allow for investigation of finite-temperature transport properties with exact quantum treatment. This extension is conceptually straightforward and consists of defining observables in terms of thermal averages,

$$\langle A \rangle_\beta = \frac{1}{\mathcal{Z}} \sum_n^{N_{\mathcal{H}}} \langle \psi_n | \hat{A} | \psi_n \rangle e^{-\beta E_n} \quad (5.1)$$


where the summation is now performed over *all* many-body states $|\psi_n\rangle$ for a given inverse temperature, $\beta = 1/k_{\text{B}}T$, as opposed to simply the ground state $|\psi_0\rangle$. Unfortunately, the computational cost of this summation is already prohibitive for spinless systems, whose Hilbert spaces grow as 2^N where N is the number of sites.

Additionally, meaningful connection with real, physical systems would necessitate that one properly account for the presence of spin in calculations at both zero and finite temperature. Moreover, our results from Chapter 4 indicate that the interplay between local and non-local interactions plays an important, and currently unexplained, role in the transient localization mechanism that drives the observed anomalous transport. Unfortunately, the inclusion of the spin degree of freedom would render the diagonalization and summations even more prohibitively expensive as the Hilbert space of spinful systems grows as 4^N , as discussed in Chapter 2.


One attempt to circumvent this finite-size limitation that the group has already begun to implement is the use of a projector-based method. This approach essentially projects out states from the Hilbert space that are not anticipated to contribute much to the thermal averages based upon high energetic costs associated with the spin degrees of freedom. In more formal terms, the Hamiltonian is written using Gutzwiller projector operators that enforce the single-occupancy constraints, or in other words, the $U = \infty$ limit [223, 224]. While this projector-based method would certainly reduce the size of the Hilbert space under consideration, computing a thermal summation over all states in the Hilbert space still remains a daunting—and computationally expensive—task.

Therefore, the best approach moving forward would be to implement the finite-temperature Lanczos technique. This technique employs Lanczos diagonalization to diagonalize the Hamiltonian matrix and then implements a cutoff in terms of states involved in the thermal summation. One single summation over M states where $M \ll N_{\mathcal{H}}$ cannot possibly be expected to yield an accurate estimate of a thermal average, except perhaps in the limiting case where $T \rightarrow 0$ and only a few states contribute to the ground state. Therefore, a sampling

$$\hat{\mathcal{P}} = \prod_i \hat{\mathcal{P}}_i = \prod_i g_i^{\hat{D}_i}$$

no double occupation 

$$\hat{\mathcal{P}} | \uparrow, \uparrow, \uparrow, \uparrow \rangle = | \uparrow, \uparrow, \uparrow, \uparrow \rangle$$

double occupation 

$$\hat{\mathcal{P}} | \uparrow, 0, \uparrow\downarrow, \uparrow \rangle = 0$$

Figure 5.3: Illustration of the projector method. Setting $g_i = 0$ (projector weight), states with double occupation ($\hat{D}_i = 1$) on any site i are automatically projected out of the Hilbert space.

over starting vectors, $|r\rangle$, for the Lanczos diagonalization routine is implemented. This sampling is similar to the statistical sampling of the classical Monte Carlo method and results in thermal averages of observables being computed as

$$\langle A \rangle = \frac{1}{\mathcal{Z}} \frac{N_{\mathcal{H}}}{R} \sum_{r=1}^R \sum_{m=1}^M e^{-\beta E_m} |\langle r | \psi_m^r \rangle|^2 A_m^r \quad (5.2)$$

where \mathcal{Z} is the partition function, $N_{\mathcal{H}}$ is the total number of states in the Hilbert space and R is the number of samples over random initial states [139]. Moreover, it has been shown that increasing the temperature strongly suppresses finite-size effects, and consequently the exact thermodynamic limit can be reached for all $T \gtrsim 0.5t$ already for the currently accessible system sizes [139].

This numerical technique, in conjunction with twisted boundary conditions, would be another tool with which to study how long-range interactions act as a universal mechanism for bad-metallic transport. In particular, this method would be ideal for rigorous studies disentangling the interplay between local, Hubbard-type potentials and non-local, Coulomb-type potentials as a function of filling. Indeed, it would be particularly use to determine for which sets of parameters the effects of long-range interactions can safely be neglected and in which regions they cannot be neglected in spinful systems. Furthermore, clean, tunable experimental systems, such as the transition metal dichalcogenide heterostructures and cold atomic platforms discussed in Chapter 1, could provide valuable sources of experimental evidence for these ideas.

In addition to understanding transport properties at lower temperatures, another interesting research direction would be investigating the competition between external disorder and self-generated disorder arising from poor screening. For instance, it could be interesting to understand many-body localization in the context of two very different sources of disorder. A comprehensive understanding and a large body of literature already accompanies this phenomenon of many-body localization in condensed-matter systems [225]. However, an understanding of many-body localization in the context of long-range interactions is still a topic of much recent debate and is being investigated via the use of cold atomic systems [226, 227].

Furthermore, a concrete problem that could be addressed in the next few years would be to develop a theoretical framework to describe how systems can be tuned between saturated Efros-Shklovskii gaps and exponentially soft gaps in their distributions of on-site potential. Most of the arguments and studies investigating Efros-Shklovskii disorder phenomena have focused on general arguments or mean-field type approaches. However, the few studies that have gone beyond mean field, including our work in Chapter 3 and Ref. [179], have hinted at the importance of the build-up of short-range correlations which rely on long-range interactions.

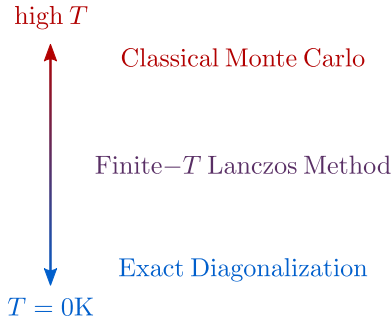


Figure 5.4: Schematic of method applicability.

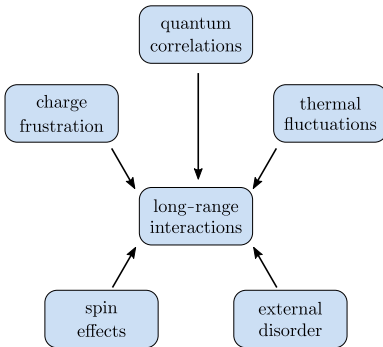
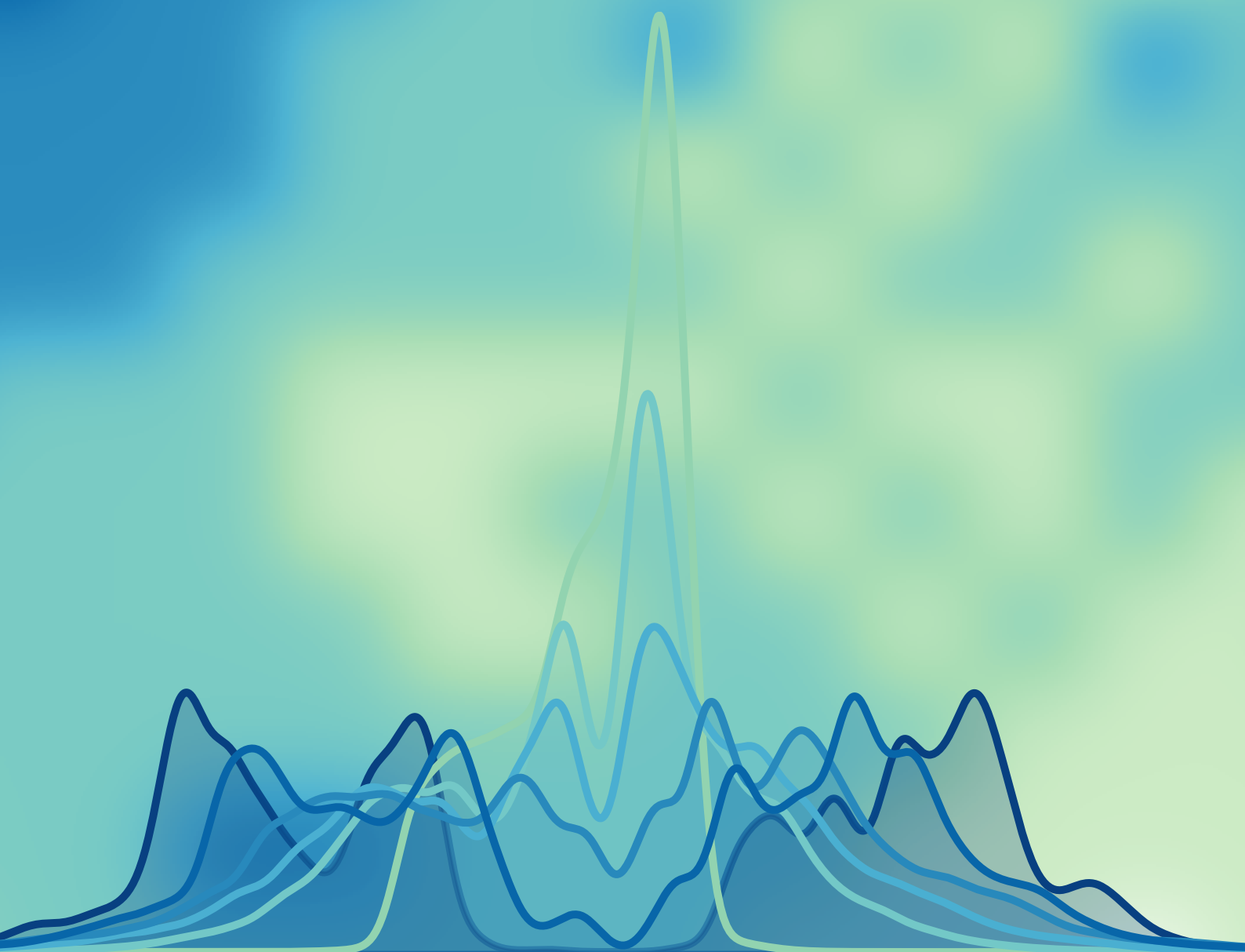


Figure 5.5: Infographic summarizing the numerous intertwining effects in strongly correlated materials.

Overall, this thesis clearly demonstrates the power of long-range interactions in giving rise to novel forms of strongly correlated behavior. We have shown that long-range interactions lead to multiple signatures of bad-metallic transport when treated in a framework beyond semiclassical theory. Moreover, we have argued that they could constitute a universal mechanism for the anomalous transport seen in a broad variety of materials. In summary, the work presented here invites us to examine strong electronic correlations from a new perspective, one which has many possible future directions as the interplay between the self-generated disorder of long-range interactions and other factors, such as external disorder and thermal fluctuations, is disentangled.

Appendices



Exact Diagonalization

This appendix contains technical details related to exact diagonalization that were not covered in Chapter 2. In particular, we discuss the fermionic sign convention implemented to account for the antisymmetric nature of the wave function in our calculations. We additionally cover the Gram-Schmidt orthogonalization procedure that we utilize during our Lanczos diagonalization runs in order to reduce numerical instabilities. Finally we conclude with a discussion of the mixing matrix used with a symmetrized basis of states and a computation of the phase factor for the kinetic hopping processes that arises from the use of twisted boundary conditions.

A.1 Fermionic sign convention

Typically, when we study fermionic models, there will be a hopping term which accounts for the kinetic energy generated by electrons moving along the lattice. Due to fermionic statistics (antisymmetric nature of the wave function), we must keep track of minus signs when encoding this term. Thankfully, the bookkeeping of this sign can be easily accounted for with a well-chosen convention for the representation of the basis states. In one dimension with open boundary conditions, we do not need to worry about the fermionic signs because the electrons cannot pass around each. However, this is not the case in higher dimensions and in one dimension with periodic boundary conditions. For simplicity, let us now consider a system of spinless fermions that move via nearest-neighbor hoppings. In other words, an electron on site i can hop to any of its nearest-neighbor sites, provided that it is unoccupied. Let us consider a square lattice with $N = 16$ sites, shown in Fig. A.1.

We choose to define our states as a bit string, where the i -th bit (going from left to right) corresponds to the occupation state (0 or 1) on the i -th site in the lattice. Let us consider the state

$$|\phi\rangle = 1110010010101010$$

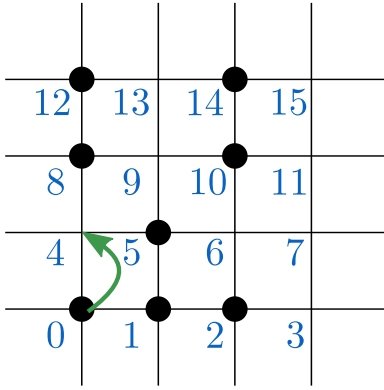


Figure A.1: Illustration of hopping process from site 0 to site 4.

where sites 0, 1, 2, 5, 8, 10, 12, and 14 are occupied (see Fig. A.1). Let us now consider that the matrix element that describes the hopping process that involves moving the electron on site 0 to its neighboring site 4 (green arrow in the figure). This process will yield a new state, $|\phi'\rangle$, which will be multiplied by a factor $(-1)^{\Delta n}$, where Δn is equal to the number of electrons in between sites 0 and 4 (not included). By choice of our numbering convention, we can easily count that there are 2 electrons on sites 1 – 3 and include this in the appropriate matrix element.

The computation of the fermionic signs can be generalized rather straightforwardly to the spinful case as the hopping terms conserve the spin. In other words, if we choose to label our spinful states as a pair of bit strings and we compute the hopping element of a particular spin from a site i to j , then we can easily count the number of spins in a given sector between sites (indices) i and j on the appropriate bit string.

A.2 Gram-Schmidt Orthogonalization

The Gram-Schmidt process ensures the orthogonalization of a set of vectors which is a necessary property for our Krylov basis as discussed in Chapter 2. The use of this technique helps to suppress numerical instabilities that can arise during the creation and normalization of new Krylov vectors. The method utilizes a series of projections on the basis of Krylov vectors, \mathcal{K} . We briefly describe the algorithm here in this section and refer to Ref. [228] for more information on the process and its applications in linear algebra.

We assume that at iteration n in our Lanczos diagonalization routine we have our set of Krylov vectors, $\{|x_i\rangle, i = 1, \dots, n\}$. From this set, we can construct an orthogonal Krylov basis of vectors, $\mathcal{K} = \{|v_i\rangle, i = 1, \dots, n\}$ via the following steps:

1. $|v_i\rangle = |x_i\rangle$
2. $|v_n\rangle = |x_n\rangle - \sum_{i=1}^{n-1} \frac{\langle x_n | v_i \rangle}{\|v_i\|^2} |v_i\rangle.$

This orthogonalization process is straightforward and inexpensive in terms of computational resources. In our diagonalization codes, we perform this procedure at every iteration in our Lanczos runs in order to prevent any numerical instabilities from growing out of control.

A.3 Orthonormalization of symmetry basis

As discussed in Chapter 2, we can utilize the discrete translation and point group symmetries of our lattice to transform our Hamiltonian matrix into block diagonal form. Each block diagonal matrix corresponds to a certain symmetry sector, ℓ , and has dimensions much

smaller than that of the original matrix ($N_\ell < N_{\mathcal{H}}$). A general state within a symmetry sector can be expressed as a linear combination of the parents,

$$|l\rangle = \sum_{i=1}^{N_\ell} \alpha_i |r_i\rangle. \quad (\text{A.1})$$

Here we restrict the summation to only the relevant parents, N_ℓ , as discussed in Chapter 2. These general states must be properly symmetrized as

$$|\tilde{l}\rangle = \frac{1}{\sqrt{N_s}} \sum_{s=1}^{N_s} \hat{s} \left(\sum_{j=1}^{N_\ell} \mu_{ij}^\ell |r_j\rangle \right), \quad (\text{A.2})$$

in order to be used as the basis of states for the block diagonal matrix of the symmetry sector. The first summation is carried out over all of the discrete symmetries, \hat{s} , and the second summation is carried out over all of the relevant parents. Here, the linear weights, α_i , have now been replaced by μ_{ij}^ℓ which we refer to as the *mixing matrix*. This is responsible for enforcing the orthonormality condition among these symmetrized states, $\{|\tilde{l}\rangle\}$. For the remainder of this section, we shall assume that we are working with an orthonormal basis of parents, $\langle r_i | r_j \rangle = \delta_{ij}$, and we shall determine the exact form of μ_{ij}^ℓ .

Unfortunately, the orthogonality of the parents is not sufficient to ensure the orthonormality of the properly symmetrized states, $\{|\tilde{l}\rangle\}$. We note that the mixing matrix depends on the symmetry sector, ℓ . We begin by stating our requirement that two symmetrized states are orthonormal to each other,

$$\delta_{lm} = \langle \tilde{l} | \tilde{m} \rangle = \sum_{s=1}^{N_s} \sum_{i,j=1}^{N_\ell} \mu_{ji}^{\ell*} \mu_{mi}^\ell \langle r_j | \hat{s} | r_i \rangle \quad (\text{A.3})$$

where we assume that the normalization factors of $\frac{1}{\sqrt{N_s}}$ are contained in the mixing matrix. We have combined the double summation over symmetry operations into one summation due to the group theoretic properties of the symmetry group. We proceed to write the orthonormality requirement as

$$\langle \tilde{l} | \tilde{m} \rangle = \sum_{s=1}^{N_s} \sum_{i,j=1}^{N_\ell} \mu_{ji}^{\ell*} \mu_{mi}^\ell \langle r_j | \chi_s | \hat{s}(r_i) \rangle \quad (\text{A.4})$$

which can be further expressed as

$$\langle \tilde{l} | \tilde{m} \rangle = \sum_{i,j=1}^{N_\ell} \mu_{ji}^{\ell*} \mu_{mi}^\ell \left[\sum_{s \in \epsilon_i} \langle r_j | \chi_s | r_i \rangle + \sum_{s \notin \epsilon_i} \langle r_j | \chi_s | \hat{s}(r_i) \rangle \right] \quad (\text{A.5})$$

where ϵ_i is the group of symmetry operations that leaves $|r_i\rangle$ unchanged, $\epsilon_i = \{s | \hat{s}(r_i) = r_i\}$. By use of the orthogonality of the parents, we immediately see that the second term will not contribute because \hat{s} will transform $|r_i\rangle$ into a child configuration which cannot be $|r_j\rangle$ by construction of the parent-children sets. Therefore, we are

We shall denote symmetrized states with a tilde, $|\tilde{l}\rangle$, and unsymmetrized states without a tilde, $|l\rangle$.

left with

$$\langle \vec{l} | \vec{m} \rangle = \sum_{i,j=1}^{N_\ell} \mu_{jl}^{\ell*} \mu_{mi}^\ell \left\langle r_j \left| \sum_{s \in \epsilon_i} \chi_s \right| r_i \right\rangle \quad (\text{A.6})$$

which simplifies to

$$\langle \vec{l} | \vec{m} \rangle = \sum_{i,j=1}^{N_\ell} \mu_{jl}^{\ell*} \mu_{mi}^\ell \text{deg}(r_i) \delta_{ij} \quad (\text{A.7})$$

when we use the definition for the degeneracy of a parent configuration,

$$\text{deg}(r_i) = \sum_{s \in \epsilon_i} \chi_s. \quad (\text{A.8})$$

From Eq. (A.7), we can easily deduce that the mixing matrix elements are of the form

$$\mu_{ij}^\ell = \frac{\delta_{ij}}{\sqrt{\text{deg}(r_i)}}, \quad (\text{A.9})$$

where the degeneracy is independent of the symmetry sector ℓ and coincides with the number of symmetries that leave the parent invariant, $|\epsilon_i|$. This simple expression for the mixing matrix elements is readily implemented in calculations of observables, as discussed in Chapter 2. For the case of a non-orthogonal basis of parents, we invite the reader to refer to Ref. [140].

A.4 Twisted boundary condition phase factor

As discussed in Chapter 2, twisted boundary conditions (TBCs) amount to a modification of the hopping terms in the Hamiltonian of interest by a Peierls phase,

$$\hat{c}_i^\dagger \hat{c}_j \rightarrow e^{i\theta}. \quad (\text{A.10})$$

In this section, we provide an example calculation of the phase factor for a finite-size cluster on the isotropic triangular lattice. The computation of the phase for any other lattice geometry should follow straightforwardly from this example. We consider a finite-size cluster with translation vectors defined as

$$\vec{T}_1 = \ell \hat{u}_1 + \ell \hat{u}_2 \quad (\text{A.11})$$

$$\vec{T}_2 = -\ell \hat{u}_1 + 2\ell \hat{u}_2, \quad (\text{A.12})$$

as illustrated in Fig. A.2 for $\ell = 2$, $\hat{u}_1 = (1, 0)$, and $\hat{u}_2 = (1/2, \sqrt{3}/2)$ (isotropic triangular lattice unit vectors).

We write the Peierls phase as

$$\theta = \frac{q}{\hbar c} \int_i^f \vec{A} \cdot d\vec{l} = \frac{2\pi}{\phi_0} \int_i^f \vec{A} \cdot d\vec{l} \quad (\text{A.13})$$

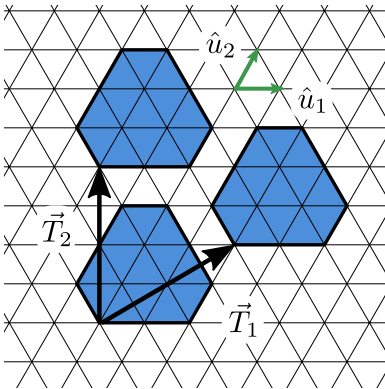


Figure A.2: Illustration of finite cluster (blue) on triangular lattice. The cluster translation vectors are shown in black, and triangular lattice unit vectors in green.

where $\phi_0 = hc/q$. We define the unit translation vectors of the finite-size cluster as

$$\begin{aligned}\hat{\alpha}_1 &= \frac{\vec{T}_1}{|\vec{T}_1|} = \frac{\ell\hat{u}_1 + \ell\hat{u}_2}{\ell\sqrt{3}} = \frac{1}{\sqrt{3}}(\hat{u}_1 + \hat{u}_2) \\ \hat{\alpha}_2 &= \frac{\vec{T}_2}{|\vec{T}_2|} = \frac{-\ell\hat{u}_1 + 2\ell\hat{u}_2}{\sqrt{3}} = \frac{1}{\sqrt{3}}(-\hat{u}_1 + 2\hat{u}_2).\end{aligned}$$

We wish to identify the components of the vector potential, \vec{A} ,

$$\vec{A} = A_1\hat{\alpha}_1 + A_2\hat{\alpha}_2, \quad (\text{A.15})$$

required as the cluster is wrapped according to the translation vectors \vec{T}_1 and \vec{T}_2 to achieve a total twist,

$$\begin{aligned}\theta_{T_1} &= 2\pi\xi_1 = \frac{2\pi}{\phi_0} \oint (A_1\hat{\alpha}_1 + A_2\hat{\alpha}_2) \cdot d\vec{l} & (\text{A.16}) \\ &= \frac{2\pi}{\phi_0} (A_1\hat{\alpha}_1 + A_2\hat{\alpha}_2) \cdot \vec{T}_1 \\ &= \frac{2\pi}{\phi_0} (A_1\hat{\alpha}_1 + A_2\hat{\alpha}_2) \cdot \ell\sqrt{3}\hat{\alpha}_1 \\ &= \frac{\pi\ell\sqrt{3}}{\phi_0} (2A_1 + A_2)\end{aligned}$$

$$\begin{aligned}\theta_{T_2} &= 2\pi\xi_2 = \frac{2\pi}{\phi_0} \oint (A_1\hat{\alpha}_1 + A_2\hat{\alpha}_2) \cdot d\vec{l} & (\text{A.17}) \\ &= \frac{2\pi}{\phi_0} (A_1\hat{\alpha}_1 + A_2\hat{\alpha}_2) \cdot \vec{T}_2 \\ &= \frac{2\pi}{\phi_0} (A_1\hat{\alpha}_1 + A_2\hat{\alpha}_2) \cdot \ell\sqrt{3}\hat{\alpha}_2 \\ &= \frac{\pi\ell\sqrt{3}}{\phi_0} (A_1 + 2A_2) = 2\pi\xi_2.\end{aligned}$$

In other words, θ_{T_i} corresponds to the total phase acquired along the path from a site to its replica located \vec{T}_i away. From the last line for each phase above we can determine expressions for A_1 and A_2 as

$$A_1 = \frac{2}{3}(2\xi_1 - \xi_2) \frac{\phi_0}{\ell\sqrt{3}} \quad (\text{A.18})$$

$$A_2 = \frac{2}{3}(-\xi_1 + 2\xi_2) \frac{\phi_0}{\ell\sqrt{3}}. \quad (\text{A.19})$$

These can be used to define the phase acquired when an electron hops from a site i to its nearest neighbor on site j along any of the 6 bonds

These prefactors arise from the expression of the Lorentz force in c.g.s. units

$$\mathbf{F} = q\left(\mathbf{E} + \frac{\mathbf{v}}{c} \times \mathbf{B}\right) \quad (\text{A.14})$$

where q is the charge of the particle, c is the speed of light, \mathbf{v} is the speed of the particle, and \mathbf{E} and \mathbf{B} are the electric and magnetic fields, respectively.

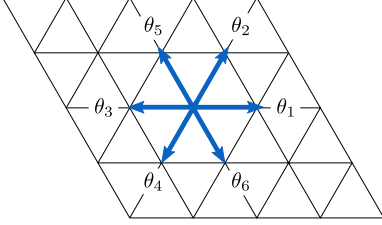


Figure A.3: Definitions of the bond directions on the triangular lattice.

of the triangular lattice,

$$\theta_1 = \frac{2\pi}{\phi_0} \vec{A} \cdot \hat{u}_1 = \frac{2\pi}{3\ell} (2\xi_1 - \xi_2) \quad (\text{A.20})$$

$$\theta_2 = \frac{2\pi}{\phi_0} \vec{A} \cdot \hat{u}_2 = \frac{2\pi}{3\ell} (\xi_1 + \xi_2) \quad (\text{A.21})$$

$$\theta_3 = \frac{2\pi}{\phi_0} \vec{A} \cdot -\hat{u}_1 = \frac{2\pi}{3\ell} (-2\xi_1 + \xi_2) \quad (\text{A.22})$$

$$\theta_4 = \frac{2\pi}{\phi_0} \vec{A} \cdot -\hat{u}_2 = \frac{2\pi}{3\ell} (-\xi_1 - \xi_2) \quad (\text{A.23})$$

$$\theta_5 = \frac{2\pi}{\phi_0} \vec{A} \cdot \hat{u}_2 = \frac{2\pi}{3\ell} (-\xi_1 + 2\xi_2) \quad (\text{A.24})$$

$$\theta_6 = \frac{2\pi}{\phi_0} \vec{A} \cdot \hat{u}_2 = \frac{2\pi}{3\ell} (\xi_1 - 2\xi_2). \quad (\text{A.25})$$

The definitions of the bond directions are shown in Fig. A.3. These phases are incorporated accordingly into any matrix elements involving kinetic (hopping) processes, including the computation of the kinetic energy and the Drude weight, as discussed in Chapter 2 and Chapter 3.

Ewald Summation

B.1 Derivation of the Ewald Summation

This thesis examines the effects of long-range (Coulomb type) interactions in quantum lattice models. This form of interaction is computed by considering a finite-size cluster with several surrounding replicas to mimic the thermodynamic limit. In order to compute the total potential energy of a given configuration of charges, we must compute the contribution from a pair of sites (i and j) in the finite cluster, as well as the contributions from the mirror images of site j . Numerically speaking, this boils down to solving the following type of infinite summations over finite clusters in the thermodynamic limit,

$$U_\alpha = \frac{1}{2} \sum_{\mathbf{R}}' \sum_{ij} \frac{V(\hat{n}_i - \bar{n})(\hat{n}_j - \bar{n})}{|\mathbf{r}_{ij} + \mathbf{R}|^\alpha} \quad (\text{B.1})$$

where \sum_{ij} is a summation over pairs of sites (i and j , $i \neq j$) in the finite cluster with a factor of $1/2$ in the front to avoid double counting. In the numerator, \hat{n}_i is the occupation number operator in second quantization for site i , \bar{n} is the neutralizing charge background and V is the interaction strength. Throughout the remainder of the discussion, we shall write the numerator as V_{ij} for the sake of simplicity, $V_{ij} = V(\hat{n}_i - \bar{n})(\hat{n}_j - \bar{n})$. The distance between the two sites is provided as \mathbf{r}_{ij} and the translation vector of the finite-size cluster is \mathbf{R} (see Fig. B.1). The range of the interaction is given as α , with $\alpha = 1$ corresponding to the pure Coulomb interaction. The prime on the first summation (over translation vectors) indicates that the sum does not include terms where $\mathbf{R} + \mathbf{r}_{ij} = 0$. The vector \mathbf{R} is defined as a multiple of the translation vectors of the cluster,

$$\mathbf{R} = n_1 \hat{T}_1 + n_2 \hat{T}_2 + n_3 \hat{T}_3 \quad n_i \in \mathbb{Z}. \quad (\text{B.2})$$

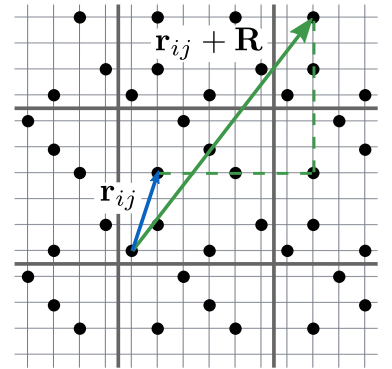


Figure B.1: We are interested in calculating the inverse distance between two sites, \mathbf{r}_{ij} (blue), and the contribution from the mirror images to the potential, $\mathbf{r}_{ij} + \mathbf{R}$ (red). The thick gray lines indicate the edges of the finite-size cluster.

We define the volume of the finite cluster, vol , as

$$\text{vol} = \hat{T}_1 \cdot (\hat{T}_2 \times \hat{T}_3). \quad (\text{B.3})$$

The reciprocal unit cell vectors are defined as

$$\hat{K}_i = 2\pi \cdot \frac{\hat{T}_j \times \hat{T}_k}{\text{vol}} \quad (\text{B.4})$$

and the reciprocal unit cell volume as

$$\Omega = \hat{K}_1 \cdot (\hat{K}_2 \times \hat{K}_3) = \frac{(2\pi)^d}{\text{vol}}. \quad (\text{B.5})$$

These quantities are defined for the general, three-dimensional case but can easily be generalized to cases of lower dimension. For example, the two-dimensional case can be reached by setting $\hat{T}_3 = (0, 0, 1)$.

Solving the kind of lattice summations present in Eq. (B.1) via a direct method typically does not converge well and requires large amounts of computational time and resources. However, in Ref. [229], Ewald established a technique to circumvent this problem that rests on the following definition of the gamma function:

$$\Gamma(\alpha) = \lambda^\alpha \int_0^\infty dx x^{\alpha-1} e^{-\lambda x}. \quad (\text{B.6})$$

We make the substitution $\lambda = |\mathbf{r}|^2$,

$$\frac{1}{|\mathbf{r}|^{2\alpha}} = \frac{1}{\Gamma(\alpha)} \int_0^\infty dx x^{\alpha-1} e^{-|\mathbf{r}|^2 x}. \quad (\text{B.7})$$

If we redefine $2\alpha \rightarrow \alpha$, then we arrive at the following expression:

$$\frac{1}{|\mathbf{r}|^\alpha} = \frac{1}{\Gamma(\alpha/2)} \int_0^\infty dx x^{\frac{\alpha}{2}-1} e^{-|\mathbf{r}|^2 x}. \quad (\text{B.8})$$

This expression can be split into two parts as

$$\frac{1}{|\mathbf{r}|^\alpha} = \frac{1}{\Gamma(\alpha/2)} \int_0^{\varepsilon^2} dx x^{\frac{\alpha}{2}-1} e^{-|\mathbf{r}|^2 x} + \frac{1}{\Gamma(\alpha/2)} \int_{\varepsilon^2}^\infty dx x^{\frac{\alpha}{2}-1} e^{-|\mathbf{r}|^2 x} \quad (\text{B.9})$$

$$= I_A + I_B \quad (\text{B.10})$$

where the cutoff parameter ε is typically chosen to be $\sim \frac{2\pi}{L}$ where L is a typical length of the finite size cluster in real space. This split allows us to partition our energy expression (Eq. (B.1)) into two parts

$$U_\alpha = \frac{1}{2} \sum_{\mathbf{R}}' \sum_{ij} I_A + \frac{1}{2} \sum_{\mathbf{R}}' \sum_{ij} I_B \quad (\text{B.11})$$

$$= \phi_A + \phi_B \quad (\text{B.12})$$

where we now write $V_{ij} = 1$ for the sake of simplicity. As a reminder, V_{ij} contains the interaction strength V and the factors of $n_i - \bar{n}$. The idea of the Ewald summation technique is that these two terms will be solved separately, one in real space and one in reciprocal space, because the overall summation will converge exponentially fast this way.

We begin by examining ϕ_B first. Written out completely we have

$$\phi_B = \frac{1}{2\Gamma(\alpha/2)} \sum_{\mathbf{R}}' \sum_{ij} \int_{\varepsilon^2}^{\infty} dx x^{\frac{\alpha}{2}-1} e^{-|\mathbf{r}_{ij}+\mathbf{R}|^2 x}. \quad (\text{B.13})$$

We substitute $u = |\mathbf{r}_{ij} + \mathbf{R}|^2 x$ which implies that $du = |\mathbf{r}_{ij} + \mathbf{R}|^2 dx$. We update the limits of integration accordingly to

$$\begin{aligned} \varepsilon^2 &\rightarrow |\mathbf{r}_{ij} + \mathbf{R}|^2 \varepsilon^2 \\ \infty &\rightarrow \infty. \end{aligned}$$

Incorporating all of these elements of the substitution, we obtain

$$\phi_B = \frac{1}{2\Gamma(\alpha/2)} \sum_{\mathbf{R}}' \sum_{ij} \int_{\varepsilon^2 |\mathbf{r}_{ij}+\mathbf{R}|^2}^{\infty} du |\mathbf{r}_{ij} + \mathbf{R}|^{-2} \left(u |\mathbf{r}_{ij} + \mathbf{R}|^{-2} \right)^{\frac{\alpha}{2}-1} e^{-u} \quad (\text{B.14})$$

$$= \frac{1}{2\Gamma(\alpha/2)} \sum_{\mathbf{R}}' \sum_{ij} \int_{\varepsilon^2 |\mathbf{r}_{ij}+\mathbf{R}|^2}^{\infty} du |\mathbf{r}_{ij} + \mathbf{R}|^{-2} \cdot |\mathbf{r}_{ij} + \mathbf{R}|^{2-\alpha} \cdot u^{\frac{\alpha}{2}-1} \cdot e^{-u} \quad (\text{B.15})$$

$$= \frac{1}{2\Gamma(\alpha/2)} \sum_{\mathbf{R}}' \sum_{ij} |\mathbf{r}_{ij} + \mathbf{R}|^{-\alpha} \int_{\varepsilon^2 |\mathbf{r}_{ij}+\mathbf{R}|^2}^{\infty} du u^{\frac{\alpha}{2}-1} e^{-u} \quad (\text{B.16})$$

We can further simplify this expression by use of the incomplete gamma function,

$$\Gamma(a, x) = \int_x^{\infty} dt t^{a-1} e^{-t}, \quad (\text{B.17})$$

where we identify $t = u$, $a = \alpha/2$, and $x = \varepsilon^2 |\mathbf{r}_{ij} + \mathbf{R}|^2$. This simplifies our expression for ϕ_B to

$$\phi_B = \frac{1}{2\Gamma(\alpha/2)} \sum_{\mathbf{R}}' \sum_{ij} |\mathbf{r}_{ij} + \mathbf{R}|^{-\alpha} \Gamma\left(\alpha/2, \varepsilon^2 |\mathbf{r}_{ij} + \mathbf{R}|^2\right). \quad (\text{B.18})$$

This is our final expression for ϕ_B and we see that it amounts to a sum in real space of the inverse distance multiplied by the incomplete gamma function.

We now proceed to examine ϕ_A which is given as

$$\phi_A = \frac{1}{2\Gamma(\alpha/2)} \sum_{\mathbf{R}}' \sum_{ij} \int_0^{\varepsilon^2} dx x^{\frac{\alpha}{2}-1} e^{-|\mathbf{r}_{ij}+\mathbf{R}|^2 x}. \quad (\text{B.19})$$

This time we will substitute $x = u^2$ which yields $dx = 2u du$ and sends the limits of integration to

$$0 \rightarrow 0 \quad (\text{B.20})$$

$$\varepsilon^2 \rightarrow \varepsilon. \quad (\text{B.21})$$

With this substitution, we now have

$$\phi_A = \frac{1}{2\Gamma(\alpha/2)} \sum'_{\mathbf{R}} \sum'_{ij} \int_0^\varepsilon du 2u \cdot (u^2)^{\frac{\alpha}{2}-1} e^{-|\mathbf{r}_{ij}+\mathbf{R}|^2 u^2} \quad (\text{B.22})$$

which we can express in simpler terms as

$$\phi_A = \frac{1}{\Gamma(\alpha/2)} \sum'_{\mathbf{R}} \sum'_{ij} \int_0^\varepsilon du u^{\alpha-1} e^{-|\mathbf{r}_{ij}+\mathbf{R}|^2 u^2} \quad (\text{B.23})$$

We recognize the last part of this integral as a Gaussian which can be expanded using the d -dimensional Fourier integral expression:

$$e^{-a^2|\mathbf{t}|^2} = \frac{1}{(2\pi)^{d/2}} \left(\frac{1}{\sqrt{2a}} \right)^d \int_{-\infty}^{\infty} d^d \mathbf{v} e^{-|\mathbf{v}|^2/4a^2} e^{-i\mathbf{v}\cdot\mathbf{t}} \quad (\text{B.24})$$

where we identify $a = u$ and $\mathbf{t} = |\mathbf{r}_{ij} + \mathbf{R}|$. Implementing this in our expression for ϕ_A (Eq. (B.23)), we have

$$\phi_A = \frac{1}{\Gamma(\alpha/2)} \sum'_{\mathbf{R}} \sum'_{ij} \int_0^\varepsilon du u^{\alpha-1} \cdot \frac{1}{(2\pi)^{d/2}} \left(\frac{1}{\sqrt{2u}} \right)^d \int_{-\infty}^{\infty} d^d \mathbf{v} e^{-|\mathbf{v}|^2/4u^2} e^{-i\mathbf{v}\cdot|\mathbf{r}_{ij}+\mathbf{R}|} \quad (\text{B.25})$$

$$= \frac{\pi^{-d/2}}{2^d \Gamma(\alpha/2)} \sum'_{\mathbf{R}} \sum'_{ij} \int_0^\varepsilon du u^{\alpha-1-d} \int_{-\infty}^{\infty} d^d \mathbf{v} e^{-|\mathbf{v}|^2/4u^2} e^{-i\mathbf{v}\cdot|\mathbf{r}_{ij}+\mathbf{R}|}. \quad (\text{B.26})$$

We reverse the order of integration,

$$\phi_A = \frac{\pi^{-d/2}}{2^d \Gamma(\alpha/2)} \sum'_{\mathbf{R}} \sum'_{ij} \int_{-\infty}^{\infty} d^d \mathbf{v} e^{-i\mathbf{v}\cdot|\mathbf{r}_{ij}+\mathbf{R}|} \int_0^\varepsilon du u^{\alpha-1-d} e^{-|\mathbf{v}|^2/4u^2}, \quad (\text{B.27})$$

and perform the substitution $s = |\mathbf{v}|^2/4u^2$, which implies that

$$u^2 = \frac{|\mathbf{v}|^2}{4s} \rightarrow u = \frac{|\mathbf{v}|}{2} s^{-1/2}$$

Subsequently, we also have

$$u^{\alpha-1-d} = \left(\frac{|\mathbf{v}|}{2s^{1/2}} \right)^{\alpha-1-d}$$

and the integration variables are updated as

$$du = -\frac{1}{2} \frac{|\mathbf{v}|}{2} s^{-3/2} ds$$

$$0 \rightarrow \infty$$

$$\varepsilon \rightarrow \frac{|\mathbf{v}|^2}{4\varepsilon^2}$$

We incorporate all of these substitutions into Eq. (B.27) and arrive at the following expression:

$$\phi_A = \frac{\pi^{-d/2}}{2^d \Gamma(\alpha/2)} \sum'_{\mathbf{R}} \sum_{ij} \int_{-\infty}^{\infty} d^d \mathbf{v} e^{-i\mathbf{v} \cdot |\mathbf{r}_{ij} + \mathbf{R}|} \int_{\frac{|\mathbf{v}|^2/4\epsilon^2}^{\infty}} ds \left(-\frac{|\mathbf{v}|}{4} s^{-3/2} \right) \left(\frac{|\mathbf{v}|}{2} s^{-1/2} \right)^{\alpha-1-d} e^{-s}, \quad (\text{B.28})$$

$$= \frac{\pi^{-d/2}}{2^d \Gamma(\alpha/2)} \sum'_{\mathbf{R}} \sum_{ij} \int_{-\infty}^{\infty} d^d \mathbf{v} e^{-i\mathbf{v} \cdot |\mathbf{r}_{ij} + \mathbf{R}|} \int_{\frac{|\mathbf{v}|^2/4\epsilon^2}^{\infty}} ds \left(\frac{|\mathbf{v}|}{4} s^{-3/2} \right) \left(\frac{|\mathbf{v}|}{2} s^{-1/2} \right)^{\alpha-1-d} e^{-s}, \quad (\text{B.29})$$

$$= \frac{\pi^{-d/2}}{2^d \Gamma(\alpha/2)} \sum'_{\mathbf{R}} \sum_{ij} \int_{-\infty}^{\infty} d^d \mathbf{v} e^{-i\mathbf{v} \cdot |\mathbf{r}_{ij} + \mathbf{R}|} \int_{\frac{|\mathbf{v}|^2/4\epsilon^2}^{\infty}} ds \frac{|\mathbf{v}|^{\alpha-d}}{2^{\alpha-d+1}} s^{\frac{d-\alpha}{2}-1} e^{-s}, \quad (\text{B.30})$$

$$= \frac{\pi^{-d/2}}{2^{d+1} \Gamma(\alpha/2)} \sum'_{\mathbf{R}} \sum_{ij} \int_{-\infty}^{\infty} d^d \mathbf{v} e^{-i\mathbf{v} \cdot |\mathbf{r}_{ij} + \mathbf{R}|} \left(\frac{|\mathbf{v}|}{2} \right)^{\alpha-d} \int_{\frac{|\mathbf{v}|^2/4\epsilon^2}^{\infty}} ds s^{\frac{d-\alpha}{2}-1} e^{-s} \quad (\text{B.31})$$

Next, we want to write

$$\int_{\frac{|\mathbf{v}|^2/4\epsilon^2}^{\infty}} ds s^{\frac{d-\alpha}{2}-1} e^{-s}$$

in terms of an incomplete gamma function

$$\Gamma(a, x) = \int_x^{\infty} dt t^{a-1} e^{-t}.$$

We can immediately identify that $t = s$, $x = |\mathbf{v}|^2/4\epsilon^2$, and $a = \frac{d-\alpha}{2}$, which allows us to write the following incomplete gamma function:

$$\Gamma\left(\frac{d-\alpha}{2}, \frac{|\mathbf{v}|^2}{4\epsilon^2}\right) = \int_{\frac{|\mathbf{v}|^2/4\epsilon^2}^{\infty}} ds s^{\frac{d-\alpha}{2}-1} e^{-s}. \quad (\text{B.32})$$

This finally allows us to write ϕ_A as

$$\phi_A = \frac{\pi^{-d/2}}{2^{d+1} \Gamma(\alpha/2)} \sum'_{\mathbf{R}} \sum_{ij} \int_{-\infty}^{\infty} d^d \mathbf{v} e^{-i\mathbf{v} \cdot |\mathbf{r}_{ij} + \mathbf{R}|} \left(\frac{|\mathbf{v}|}{2} \right)^{\alpha-d} \Gamma\left(\frac{d-\alpha}{2}, \frac{|\mathbf{v}|^2}{4\epsilon^2}\right). \quad (\text{B.33})$$

Now we transform the integral over all reciprocal space, $\int_{-\infty}^{\infty} d^d \mathbf{v}$, to a sum over all reciprocal lattice vectors, \mathbf{k} , of the integral over the reciprocal unit cell (U^*),

$$\phi_A = \frac{\pi^{-d/2}}{2^{d+1} \Gamma(\alpha/2)} \sum'_{\mathbf{R}} \sum_{ij} \sum_{\mathbf{k} \in U^*} \int d^d \mathbf{v} e^{-i(\mathbf{v} + \mathbf{k}) \cdot (\mathbf{r}_{ij} + \mathbf{R})} \left(\frac{|\mathbf{v} + \mathbf{k}|}{2} \right)^{\alpha-d} \Gamma\left(\frac{d-\alpha}{2}, \frac{|\mathbf{v} + \mathbf{k}|^2}{4\epsilon^2}\right). \quad (\text{B.34})$$

The $\mathbf{k} \cdot \mathbf{R}$ term will be neglected because it will just give $e^{i \cdot 2\pi m}$, $m \in \mathbb{Z}$. Therefore, our expression simplifies to

$$\phi_A = \frac{\pi^{-d/2}}{2^{d+1} \Gamma(\alpha/2)} \sum'_{\mathbf{R}} \sum_{ij} \sum_{\mathbf{k} \in U^*} \int d^d \mathbf{v} e^{-i(\mathbf{v} + \mathbf{k}) \cdot \mathbf{r}_{ij}} e^{-i\mathbf{v} \cdot \mathbf{R}} \left(\frac{|\mathbf{v} + \mathbf{k}|}{2} \right)^{\alpha-d} \Gamma\left(\frac{d-\alpha}{2}, \frac{|\mathbf{v} + \mathbf{k}|^2}{4\epsilon^2}\right). \quad (\text{B.35})$$

We further simplify this by $\sum_{\mathbf{R}'} \rightarrow \sum_{\mathbf{R}}$ so that we now include the $\mathbf{r}_{ij} + \mathbf{R} = 0$ terms. This will be corrected for later in the derivation. At this point we now have

$$\phi_A = \frac{\pi^{-d/2}}{2^{d+1}\Gamma(\alpha/2)} \sum_{\mathbf{R}} \sum_{ij} \sum_{\mathbf{k}} \int_{U^*} d^d \mathbf{v} e^{-i(\mathbf{v}+\mathbf{k})\cdot\mathbf{r}_{ij}} e^{-i\mathbf{v}\cdot\mathbf{R}} \left(\frac{|\mathbf{v}+\mathbf{k}|}{2} \right)^{\alpha-d} \Gamma\left(\frac{d-\alpha}{2}, \frac{|\mathbf{v}+\mathbf{k}|^2}{4\epsilon^2} \right). \quad (\text{B.36})$$

We will perform the summation over real space vectors, \mathbf{R} , first so that the integrand makes a series expansion of the reciprocal space function of the general form:

$$\frac{(2\pi)^d}{\text{vol}} f(\mathbf{k}) = \sum_{\mathbf{R}} e^{i\mathbf{k}\cdot\mathbf{R}} \int_{U^*} d^d \mathbf{v} f(\mathbf{v}+\mathbf{k}) e^{-i\mathbf{v}\cdot\mathbf{R}}. \quad (\text{B.37})$$

This leads us to

$$\phi_A = \frac{\pi^{-d/2}}{2^{d+1}2^{\alpha-d}\Gamma(\alpha/2)} \sum_{ij} \sum_{\mathbf{k}} \sum_{\mathbf{R}} \int_{U^*} d^d \mathbf{v} \underbrace{|\mathbf{v}+\mathbf{k}|^{\alpha-d} e^{-i(\mathbf{v}+\mathbf{k})\cdot\mathbf{r}_{ij}} \Gamma\left(\frac{d-\alpha}{2}, \frac{|\mathbf{v}+\mathbf{k}|^2}{4\epsilon^2} \right)}_{f(\mathbf{v}+\mathbf{k})} e^{-i\mathbf{v}\cdot\mathbf{R}} \quad (\text{B.38})$$

This now gives us

$$\phi_A = \frac{\pi^{-d/2}}{2^{\alpha+1}\Gamma(\alpha/2)} \sum_{\mathbf{k}} \sum_{ij} \frac{(2\pi)^d}{\text{vol}} f(\mathbf{k}) \quad (\text{B.39})$$

$$= \frac{\pi^{d/2}\text{vol}^{-1}}{2^{\alpha-d+1}\Gamma(\alpha/2)} \sum_{\mathbf{k}} \sum_{ij} |\mathbf{k}|^{\alpha-d} e^{-i\mathbf{k}\cdot\mathbf{r}_{ij}} \Gamma\left(\frac{d-\alpha}{2}, \frac{|\mathbf{k}|^2}{4\epsilon^2} \right) \quad (\text{B.40})$$

$$= \frac{\pi^{d/2}\text{vol}^{-1}}{2^{\alpha-d+1}\Gamma(\alpha/2)} \sum_{\mathbf{k}} \sum_{ij} |\mathbf{k}|^{\alpha-d} \Gamma\left(\frac{d-\alpha}{2}, \frac{|\mathbf{k}|^2}{4\epsilon^2} \right) (\cos(\mathbf{k}\cdot\mathbf{r}_{ij}) - i \sin(\mathbf{k}\cdot\mathbf{r}_{ij})) \quad (\text{B.41})$$

$$= \frac{\pi^{d/2}\text{vol}^{-1}}{2^{\alpha-d+1}\Gamma(\alpha/2)} \sum_{\mathbf{k} \neq 0} \sum_{ij} |\mathbf{k}|^{\alpha-d} \Gamma\left(\frac{d-\alpha}{2}, \frac{|\mathbf{k}|^2}{4\epsilon^2} \right) \cos(\mathbf{k}\cdot\mathbf{r}_{ij}) \quad (\text{B.42})$$

where the $\sin(\mathbf{k}\cdot\mathbf{r}_{ij})$ term in the second-to-last line drops out because it is an odd function evaluated over the whole interval of reciprocal lattice vectors. In the last line, we only keep the $\mathbf{k} \neq 0$ terms and will need to account for the prior inclusion of the $\mathbf{k} = 0$ term next. This term is evaluated as

$$\phi_A(\mathbf{k} = 0) = \frac{\pi^{d/2}\text{vol}^{-1}}{2^{\alpha-d+1}\Gamma(\alpha/2)} \lim_{\mathbf{k} \rightarrow 0} |\mathbf{k}|^{\alpha-d} \Gamma\left(\frac{d-\alpha}{2}, \frac{|\mathbf{k}|^2}{4\epsilon^2} \right) \sum_{ij} \cos(\mathbf{k}\cdot\mathbf{r}_{ij}) \quad (\text{B.43})$$

We focus on the term

$$\lim_{\mathbf{k} \rightarrow 0} \frac{\Gamma\left(\frac{d-\alpha}{2}, \frac{|\mathbf{k}|^2}{4\epsilon^2} \right)}{|\mathbf{k}|^{\alpha-d}} = \frac{\infty}{0} \quad (\text{B.44})$$

and neglect the $\cos(\mathbf{k}\cdot\mathbf{r}_{ij})$ because it will evaluate to 1 for $\mathbf{k} = 0$. The values of the numerator and denominator obviously depend on d and α and can in general give rise to values that render this limit impossible to take. For example, $\Gamma\left(\frac{d-\alpha}{2}, \frac{|\mathbf{k}|^2}{4\epsilon^2} \right) = \infty$ for $d = 2$ and $\alpha = 2$. Therefore, we will employ

L'Hôpital's rule to compute the derivative in the general case, which means that we need to compute the derivatives of the numerator and denominator in Eq. (B.44).

$$\frac{\partial}{\partial k} (k^{d-\alpha}) = (d-\alpha)k^{d-\alpha-1} \quad (\text{B.45})$$

$$\frac{\partial}{\partial k} \Gamma\left(\frac{d-\alpha}{2}, \frac{|\mathbf{k}|^2}{4\varepsilon^2}\right) = -\left(\frac{|\mathbf{k}|^2}{4\varepsilon^2}\right)^{\frac{d-\alpha}{2}-1} e^{-|\mathbf{k}|^2/4\varepsilon^2} \frac{2|\mathbf{k}|}{4\varepsilon^2} \quad (\text{B.46})$$

$$= -\left(\frac{|\mathbf{k}|}{2}\right)^{d-\alpha-1} \varepsilon^{\alpha-d} e^{-|\mathbf{k}|^2/4\varepsilon^2} \quad (\text{B.47})$$

Now with these derivatives, we can apply L'Hôpital's rule and arrive at

$$\lim_{\mathbf{k} \rightarrow 0} = -\frac{\left(\frac{|\mathbf{k}|}{2}\right)^{d-\alpha-1} \cdot \varepsilon^{\alpha-d} \cdot e^{-|\mathbf{k}|^2/4\varepsilon^2}}{(d-\alpha) |\mathbf{k}|^{d-\alpha-1}} = \frac{\varepsilon^{\alpha-d}}{2^{d-\alpha-1}(\alpha-d)} \quad (\text{B.48})$$

which means that $\phi_A(\mathbf{k} = 0)$ is given as

$$\phi_A(\mathbf{k} = 0) = \frac{\pi^{d/2} \text{vol}^{-1}}{2^{\alpha-d+1} \Gamma(\alpha/2)} \frac{\varepsilon^{\alpha-d}}{2^{d-\alpha-1}(\alpha-d)} \sum_{ij} V_{ij} \quad (\text{B.49})$$

$$= \frac{\pi^{d/2} \text{vol}^{-1}}{\Gamma(\alpha/2)} \frac{\varepsilon^{\alpha-d}}{(\alpha-d)} \sum_{ij} V_{ij} \quad (\text{B.50})$$

where we have included again the pairwise interaction term $V_{ij} = V(\hat{n}_i - \bar{n})(\hat{n}_j - \bar{n})$ as a reminder to the reader that this term is still contained in our expression. However, this $\mathbf{k} = 0$ term can be neglected when working with a charge-neutral system [230].

Previously we changed the summation over real space lattice vectors to include terms where $\mathbf{r}_{ij} + \mathbf{R} = 0$. We now correct for this by subtracting this term from the total energy,

$$U_\alpha = \frac{1}{2} \sum_{\mathbf{R}}' \sum_{ij} \frac{V_{ij}}{|\mathbf{r}_{ij} + \mathbf{R}|^\alpha} = \frac{1}{2} \sum_{\mathbf{R}}' \sum_{ij} I_A + \frac{1}{2} \sum_{\mathbf{R}}' \sum_{ij} I_B. \quad (\text{B.51})$$

The pairwise sum can be split into two components, $\sum_{ij} = \sum_{i \neq j} + \sum_{i=j}$. We are only interested in the $i = j$ term because this represents the self-energy that we artificially added in I_A by extending $\sum_{\mathbf{R}}'$ to $\sum_{\mathbf{R}}$,

$$\frac{1}{2} \sum_i \frac{V_{ii}}{|\mathbf{r}_{ii}|^\alpha} = \sum_i I_A + \sum_i \frac{V_{ii}}{|\mathbf{r}_{ii}|^\alpha} \Gamma(\alpha/2, \varepsilon^2 |\mathbf{r}_{ii}|^2). \quad (\text{B.52})$$

We define the self-energy correction term as

$$\phi_0 = \lim_{r \rightarrow 0} \frac{1}{2} \sum_i I_A \quad (\text{B.53})$$

$$= \lim_{r \rightarrow 0} \sum_i \frac{V_{ii} \left(1 - \Gamma(\alpha/2, \varepsilon^2 |\mathbf{r}_{ii}|^2)\right)}{|\mathbf{r}_{ii}|^\alpha} \quad (\text{B.54})$$

$$= \frac{0}{0}. \quad (\text{B.55})$$

Again we must apply L'Hôpital's rule

$$\phi_0 = \lim_{r \rightarrow 0} \frac{1}{2} \sum_i \frac{\frac{\partial}{\partial r} V_{ii} \cdot \left(1 - \Gamma(\alpha/2, \varepsilon^2 |\mathbf{r}|^2)\right)}{\frac{\partial}{\partial r} \left(|\mathbf{r}|^\alpha\right)} \quad (\text{B.56})$$

$$= \lim_{r \rightarrow 0} \frac{1}{2} \sum_i \frac{V_{ii} \cdot \left(\varepsilon^2 |\mathbf{r}|^2\right)^{\frac{\alpha}{2}-1} e^{-\varepsilon^2 |\mathbf{r}|^2} 2\varepsilon^2 |\mathbf{r}|}{\alpha |\mathbf{r}|^{\alpha-1}} \quad (\text{B.57})$$

$$= \lim_{r \rightarrow 0} \frac{1}{2} \sum_i \frac{V_{ii} \varepsilon^{\alpha-2} |\mathbf{r}|^{\alpha-2} \cdot 2\varepsilon^2 |\mathbf{r}| e^{-\varepsilon^2 |\mathbf{r}|^2}}{\alpha |\mathbf{r}|^{\alpha-1}} \quad (\text{B.58})$$

$$= \sum_i \frac{V_{ii} \varepsilon^\alpha}{\alpha}. \quad (\text{B.59})$$

This self-energy correction is the last component that we need in order to write a complete expression for the energy. To do so, we combine Eqs. (B.18), (B.42), (B.50), and (B.59) to obtain our final expression for U_α :

$$U_\alpha = \phi_B + \phi_A(\mathbf{k} \neq 0) + \phi_A(\mathbf{k} = 0) - \phi_0 \quad (\text{B.60})$$

$$\begin{aligned} U_\alpha &= \frac{1}{2\Gamma(\alpha/2)} \sum_{\mathbf{R}}' \sum_{ij} \frac{V_{ij}}{|\mathbf{r}_{ij} + \mathbf{R}|^\alpha} \Gamma\left(\alpha/2, \varepsilon^2 |\mathbf{r}_{ij} + \mathbf{R}|^2\right) \\ &+ \frac{\pi^{d/2} \text{vol}^{-1}}{2^{\alpha-d+1} \Gamma(\alpha/2)} \sum_{\mathbf{k} \neq 0} \sum_{ij} |\mathbf{k}|^{\alpha-d} \Gamma\left(\frac{d-\alpha}{2}, \frac{|\mathbf{k}|^2}{4\varepsilon^2}\right) \cos(\mathbf{k} \cdot \mathbf{r}_{ij}) \\ &+ \frac{\pi^{d/2} \text{vol}^{-1}}{\Gamma(\alpha/2)} \frac{\varepsilon^{\alpha-d}}{(\alpha-d)} \sum_{ij} V_{ij} - \sum_i \frac{V_{ii} \varepsilon^\alpha}{\alpha}. \end{aligned}$$

This term typically converges with a ~ 5 replicas of a finite-size cluster. For more information on the Ewald summation technique, we invite the interested reader to refer to Refs. [151, 152, 230–232].

Classical Monte Carlo

C.1 Classical Monte Carlo

In Chapter 4, we studied the high temperature behavior of two-dimensional systems with long-range interactions. In order to carry out numerical investigations of such systems, we employ the classical Monte Carlo method, a well-known technique in statistical physics. The main goal of this technique is to compute high-dimensional integrals and as such it has enjoyed a wide variety of applications, ranging from nuclear physics to astrophysics. In this appendix, we discuss the general motivation and implementation of Monte Carlo schemes.

In statistical physics, the high-dimensional integral in question is most often related to the partition function,

$$\mathcal{Z} = \int_{\text{PS}} [d\mathbf{r}^d] e^{-\beta H(\mathbf{r})}, \quad (\text{C.1})$$

which is an integral over phase space (PS) of the Boltzmann weight, $e^{-\beta H(\mathbf{r})}$, with the inverse temperature defined as $\beta = 1/k_B T$. The differential, $[d\mathbf{r}^d]$, and the Hamiltonian, $H(\mathbf{r})$, are defined in terms of the spatial coordinates of a general N -particle system in d dimensions. The simple notation above is chosen to avoid cluttering our discussion with cumbersome and unnecessary details. For a many-particle system, the dimension of the phase space corresponding to the Hamiltonian, H , and the partition function, \mathcal{Z} , scales with the number of particles, $\sim N$, and any attempt at efficient integration can appear helpless. However, we will see that all is not lost with the use of Monte Carlo calculations.

Let us momentarily forget the complicated details of statistical physics

In nuclear physics, for example, Monte Carlo has been applied to compute integrals of actions in lattice gauge theories [233]. In astrophysics, Monte Carlo methods have been employed to examine the size and geometrical structure of galaxies [234].

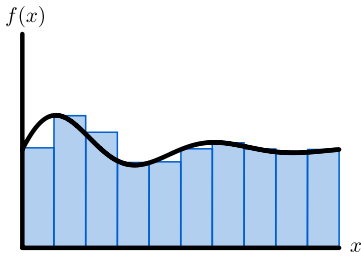


Figure C.1: The function $f(x)$ divided in M evenly spaced bins.

The bin width, $\delta x = x_{i+1} - x_i$, will be equivalent for all bins assuming they are evenly spaced in the interval $[a, b]$.

Simpson's rule (or Simpson's 1/3 rule) approximates the interval in Eq. C.2 as $I \approx \frac{b-a}{6} [f(a) + 4f(\frac{a+b}{2}) + f(b)]$. This estimation can be improved by applying Simpson's rule to subintervals in $[a, b]$.

For example, the convergence using Simpson's rule will scale as $M^{-4/d}$ where d is the dimensionality of the integral under question.

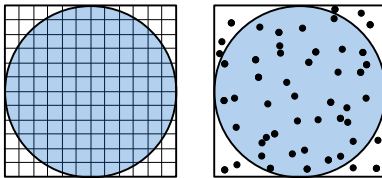


Figure C.2: The unit circle divided in $M \times M$ evenly spaced bins (left). Random points sampled in the square bordering the unit circle (right).

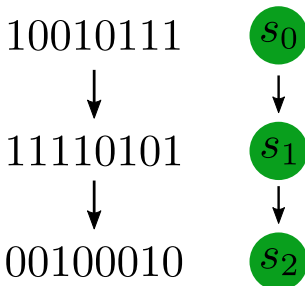


Figure C.3: Random walk that generates new state completely uncorrelated from the previous state.

and instead focus on the efficient integration of a general, one-dimensional function,

$$I = \int_a^b dx f(x). \tag{C.2}$$

We can divide the region $x \in [a, b]$ into M evenly spaced bins and approximate I by performing a discrete summation over the values of $f(x)$ at the midpoint of each bin,

$$I \approx \sum_{i=0}^{M-1} \delta x \times f\left(\frac{x_{i+1} - x_i}{2}\right). \tag{C.3}$$

This is the midpoint rule approximation and as the number of bins increases, this estimate will converge to the true value of I as M^{-1} . Other sophisticated discretization schemes can improve the convergence; for example, Simpson's rule improves the convergence to M^{-4} . These approaches work well and are straightforward to implement for simple, low-dimensional integrals. However, they converge extremely slowly for high-dimensional integrals as each variable, or dimension, requires discretization [235].

In order to overcome this slow convergence, one might naively try a simple sampling Monte Carlo approach. An example of this technique would be to compute π from a simple sampling of the area of the unit circle. We can imagine that the unit circle is bounded by a square such that the coordinates of any point are bounded by $x \in [-1, 1]$ and $y \in [-1, 1]$. We can sample over M random points, $p_i = (x_i, y_i)$, to determine an estimate for the area of the unit circle, $A \approx n_{\text{hits}}/M$, where n_{hits} is the number of random points that lie within the unit circle. From this, the estimate of π directly follows as $\pi \approx A/r^2$ where r is the radius of the unit circle.

The benefits of simple sampling are that the samples are independent and that the method is straightforward to implement. For our example estimating the value of π , we simply need to generate two coordinates, x and y , which can be done using a pseudorandom number generator that operates based on a uniform distribution. Instead of generating a random point, $p = (x, y)$, let us consider sampling in the phase space of many-body states to measure a given quantity, such as the energy. At each step in the simple sampling scheme, we would generate a brand new configuration by generating a random value for each degree of freedom. If our states are represented by bitstrings as in Chapter 2, then we would generate bit strings filled with randomly placed zeros and ones (Fig. C.3).

However, fully generating a random configuration at each step can be numerically costly. To reduce the computational overhead and improve efficiency, we can instead work with a kind of random walk known as a Markov chain where a state at a given time step depends upon the state at the previous time step. In other words, for a system with L sites, we do not need to generate L new random values at each step. Instead, we can choose to modify the value at one of the L sites at

random, resulting in a new configuration (Fig. C.4). While this method of sampling through phase space is less costly for large systems, each new state retains a memory of the previous state which can lead to correlation effects that one should treat carefully.

At this point, we have established that we can approximate high-dimensional integrals by using Markov chains, which sample the phase space of many-body states in a manner that strategically reduces the computational effort. However, we still need to ensure that the "path" through phase space along which we are sampling is actually relevant to the computation at hand. For example, let us suppose that we are interested in computing the average height of the Eiffel tower (example adapted from Ref. [236]) and that this is done with a function $f_{\text{Eiffel}}(x, y)$ that returns the height of the Eiffel tower at a point (x, y) . If the point falls outside the area of the structure, then the function returns zero. We can design a Markov chain process such that we generate new geographical coordinates (points) by adding random displacements within a window $\delta x, \delta y \in [-w, +w]$ to the point from the previous step. By doing this, we could perform a random walk all over Paris (see Fig. C.5) and obtain an estimate for the average depth. However, most of the points would not be relevant and would only add zero to our running average.

If we instead modify our Markov chain process to sample places that are likely visited by tourists, then we will be able to more efficiently obtain an accurate estimate for the average height of the tower (see Fig. C.6). This practice of selecting relevant points is known as importance sampling. The formal motivation for this technique is directly related to the variance of the function f in the integrand, $I = \int_a^b dx f(x)$. The error from estimating this integral is given as

$$\delta I = \sqrt{\frac{\text{Var}(f)}{M-1}} \quad \text{where } \text{Var}(f) = \langle f^2 \rangle - \langle f \rangle^2 \quad (\text{C.4})$$

for the one-dimensional case (generalization to higher dimensions is straightforward) and scales with the variance of $f(x)$. When we implement importance sampling, we sample random numbers (or configurations) according to a distribution, $p(x)$, that should be close to $f(x)$ [235]. We can rewrite the integral as

$$I = \langle f \rangle = \langle f/p \rangle_p = \int_a^b \frac{f(x)}{p(x)} p(x) dx \approx \frac{1}{M} \sum_i \frac{f(y_i)}{p(y_i)} \quad (\text{C.5})$$

where the randomly generated y_i are generated with distribution $p(x)$. Now the error depends on $\text{Var}(f/p)$ and with $p \sim f$ this quantity should be much smaller than $\text{Var}(f)$. A visual depiction of the benefits of importance sampling is shown again in Fig. C.7.

If we leave our simple examples behind and return to statistical many-body physics, we recall that we are interested in computing the

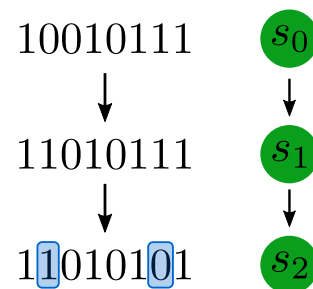


Figure C.4: Random walk that slightly modifies previous state to generate a new one.

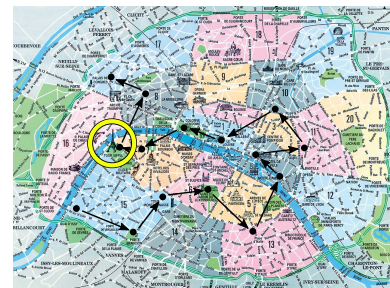


Figure C.5: Random walk around Paris with the Eiffel tower circled in yellow [237].

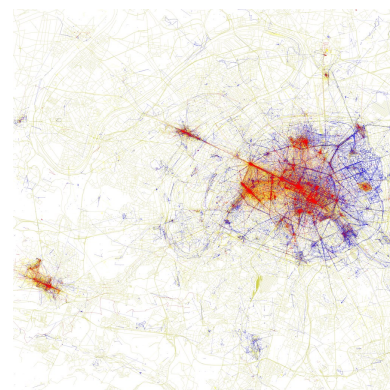


Figure C.6: Map representing the distribution of tourists (red) in Paris [238].

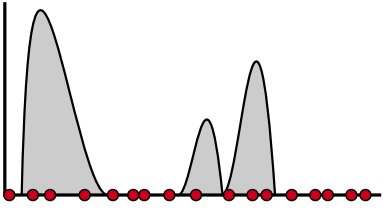
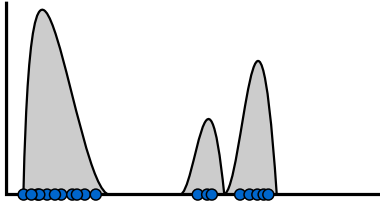


Figure C.7: Another illustration showing how importance sampling (blue dots) is much more efficient than sampling from a uniform distribution (red dots).

average values of observables, \mathcal{O} , of the form

$$\langle \mathcal{O} \rangle = \frac{1}{\mathcal{Z}} \int_{\text{PS}} [d\mathbf{r}^d] \mathcal{O}(\mathbf{r}) e^{-\beta H(\mathbf{r})}. \quad (\text{C.6})$$

This integral expression can be approximated as

$$\langle \mathcal{O} \rangle \approx \frac{1}{\mathcal{Z}} \frac{1}{M} \sum_{i=1}^M \mathcal{O}(\mathbf{r}_i) e^{-\beta H(\mathbf{r}_i)} \quad (\text{C.7})$$

where \mathbf{r}_i represents a configuration of real-space coordinates corresponding to the sampled many-body state in phase space (PS).

However, if we apply importance sampling with a distribution $\mathcal{P}(\mathbf{r})$, then our integral expression for the average should be rewritten as

$$\langle \mathcal{O} \rangle = \int_{\text{PS}} [d\mathbf{r}^d] \mathcal{P}(\mathbf{r}) \frac{\mathcal{O}(\mathbf{r}) e^{-\beta H(\mathbf{r})}}{\mathcal{P}(\mathbf{r}) \mathcal{Z}}. \quad (\text{C.8})$$

where the prime on the summation indicates that the states are sampled according to $\mathcal{P}(\mathbf{r})$. The estimate of the integral expression is then updated as

$$\langle \mathcal{O} \rangle \approx \frac{1}{M} \sum_{i=1}^M \frac{\mathcal{O}(\mathbf{r}_i) e^{-\beta H(\mathbf{r}_i)}}{\mathcal{P}(\mathbf{r}_i) \mathcal{Z}}. \quad (\text{C.9})$$

We choose to sample the states according to the equilibrium Boltzmann distribution, $\mathcal{P}(\mathbf{r}) = e^{-\beta H(\mathbf{r})} / \mathcal{Z}$ [239], such that the final expression for the average value is simplified to

$$\langle \mathcal{O} \rangle \approx \frac{1}{M} \sum_{i=1}^M \frac{\mathcal{O}(\mathbf{r}_i)}{e^{-\beta H(\mathbf{r}_i)}} \mathcal{Z} \frac{e^{-\beta H(\mathbf{r}_i)}}{\mathcal{Z}} \quad (\text{C.10})$$

$$\approx \frac{1}{M} \sum_{i=1}^M \mathcal{O}(\mathbf{r}_i). \quad (\text{C.11})$$

In order to implement this task numerically, we make use of the Metropolis-Hastings algorithm which allows us to sample from the distribution of our choice [240, 241]. In our case, we will choose to work with either the Boltzmann distribution or the Gibbs distribution, as will be discussed later on.

Each Monte Carlo calculation begins from a random initial configuration, s_i , chosen such that it best represents the physical system under consideration. Once this configuration has been initialized, we must determine the transition probability for it to change into any other state in phase space, $\mathcal{T}(s_i \rightarrow s_f)$. We assume that the Monte Carlo simulations are run for a sufficiently long period of time such that an equilibrium distribution of states, $\mathcal{P}_{eq}(s)$, is reached. Furthermore, we impose a condition called detailed balance which states that the number of moves from s_i to a new state s_f must be equal to the number of moves from s_f to s_i . This can be written more formally as

$$\mathcal{T}(s_i \rightarrow s_f) \mathcal{P}(s_i) = \mathcal{T}(s_f \rightarrow s_i) \mathcal{P}(s_f) \quad (\text{C.12})$$

where $\mathcal{T}(s_i \rightarrow s_f)$ represents the transition probability between the two states and $\mathcal{P}(s)$ the probability of the occurrence of the state at a given time step during the routine (illustrated in Fig. C.8).

Many different choices exist for the form of $\mathcal{T}(s_i \rightarrow s_f)$ but we choose to work with the Metropolis algorithm as it is the most straightforward [240]. The transition probability has two components,

$$\mathcal{T}(s_i \rightarrow s_f) = \alpha(s_i \rightarrow s_f) \text{acc}(s_i \rightarrow s_f) \quad (\text{C.13})$$

where $\alpha(s_i \rightarrow s_f)$ describes the probability of performing a trial move that generates s_f from s_i and $\text{acc}(s_i \rightarrow s_f)$ is the probability that s_f is accepted. At each step in our algorithm we must attempt a trial move in which we alter the configuration by a pre-determined rule. For a configuration defined by a list of particle positions, a trial move might consist of adding a small displacement δr to a randomly chosen particle. For a configuration defined by occupation numbers on lattice sites, the trial move might instead consist of changing the occupation (or spin flavor) at a randomly chosen site. These rules determine the nature of the α matrix and are typically chosen to be symmetric as in the original Metropolis scheme [240]. We work with a symmetric α matrix and therefore the transition probability in our calculations reduces trivially to

$$\mathcal{T}(s_i \rightarrow s_f) = \text{acc}(s_i \rightarrow s_f). \quad (\text{C.14})$$

Inserting this into Eq. C.12 and rearranging yields

$$\frac{\text{acc}(s_i \rightarrow s_f)}{\text{acc}(s_f \rightarrow s_i)} = \frac{\mathcal{P}(s_f)}{\mathcal{P}(s_i)}. \quad (\text{C.15})$$

If we insert the equilibrium Boltzmann distribution on the right-hand side, then we obtain

$$\frac{\text{acc}(s_i \rightarrow s_f)}{\text{acc}(s_f \rightarrow s_i)} = e^{-\beta(H(s_f) - H(s_i))}. \quad (\text{C.16})$$

Again, there are many possible options for the definition of $\text{acc}(s_i \rightarrow s_f)$, but the most common is that of Metropolis [240]:

$$\text{acc}(s_i \rightarrow s_f) = \begin{cases} e^{-\beta(H(s_f) - H(s_i))} & \text{if } e^{-\beta H(s_f)} < e^{-\beta H(s_i)} \\ 1 & \text{if } e^{-\beta H(s_f)} \geq e^{-\beta H(s_i)} \end{cases} \quad (\text{C.17})$$

because it is both straightforward to implement and remarkably efficient. In a nutshell, the Metropolis rule always accepts new configurations that lower the energy ($H(s_f) \leq H(s_i)$) and accepts configurations that raise the energy by a probability equal to the ratio of their Boltzmann weights, $e^{-\beta H(s_f)} / e^{-\beta H(s_i)}$.

With the Metropolis rule, we are now able to sample the relevant states in phase space according to the distribution of our choice. The code listing in Fig. C.10 outlines a general structure for a Monte Carlo

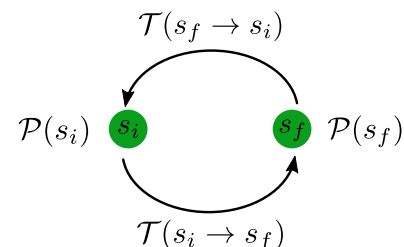


Figure C.8: Transition from s_i to s_f .

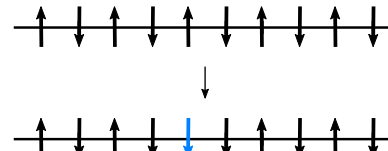
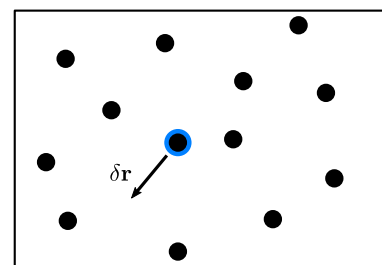


Figure C.9: Example trial moves for different systems.

Figure C.10: Pseudocode for Monte Carlo simulation.

```

1 import numpy as np
2
3 # initialization
4 Si = Initialization( N, vol )
5 Ei = Hamiltonian( Si )
6
7 for i in range( MCSteps ) :
8     # generate new state
9     Sf = TrialMove( si )
10    Ef = Hamiltonian( Sf )
11
12    # Metropolis: accept/reject
13    weight = np.exp( -Beta*(Ef-Ei) )
14    r = np.random.random()
15    if( r<weight or weight>=1. ):
16        Si = Sf
17        Ei = Ef
18    else :
19        pass
20
21    # compute any observables
22    Observables( Si )

```

algorithm. Up until this point, we have only mentioned the Boltzmann distribution which corresponds to Monte Carlo simulations in the canonical ensemble in which the number of particles, volume, and temperature are fixed. In our case, the calculation of certain observables requires access to a variable number of particles which entails the use of the grand canonical ensemble. In this ensemble, the chemical potential, volume and temperature are held fixed. The distribution used to generate states reflects this change, $e^{-\beta H(s)} \rightarrow e^{-\beta[H(s)+\mu N(s)]}$.

This concludes our introduction to classical Monte Carlo techniques. The interested reader may find more information on the theory, technical details and applications in Refs. [235, 236, 239]. Unless explicitly stated otherwise, our Monte Carlo calculations were thermalized for $10L^2$ time steps where L is the length of one side of the square lattice. Furthermore, all quantities were averaged over 15,000 measurements with 100 time steps between each measurement.

Mott-Ioffe-Regel Limit

D.1 Mott-Ioffe-Regel limit

Here we provide details on the computation of the Mott-Ioffe-Regel limit estimate for a representative member of the high- T_c family of cuprate superconductors. Through our Monte Carlo calculations, we compute the (in-plane) resistivity of a system of interacting electrons on the square lattice and we wish to compare our results to those obtained from a representative strongly correlated material, which we choose to be $\text{La}_{2-x}\text{Sr}_x\text{CuO}_4$. The crystal structure of the cuprate family consists of quasi-two-dimensional layers of copper and oxygen atoms, intercalated with layers of charge reservoirs. These materials are typically studied by effective Hamiltonians, in particular the Hubbard model, on the square lattice [88, 89]. However, these models typically fall short in capturing the exotic phenomena present across the phase diagram of the cuprates, including signatures of bad metallic transport. Therefore, we seek to determine if the resistivity obtained from our long-range interacting model corresponds to the bad metallic regime for the cuprates. This regime is dictated by the Mott-Ioffe-Regel limit where conventional Boltzmann theory falls as the electron scattering length reaches the size of the lattice spacing, $\ell \approx a$.

In order to compare the results of our two-dimensional model to experimental values, we must convert our results to a resistivity that corresponds to a layered system by including the length scale of the interlayer spacing. As in Ref. [76], we assume that the out-of-plane contribution to the resistivity will be negligible and set the Fermi surface of this layered structure to be a cylinder with height $2\pi/c$ and radius k_F . To solve for the Fermi wave vector, k_F , in terms of a general filling, n , we integrate the occupation function, $\theta(k - k_F)$, which fills

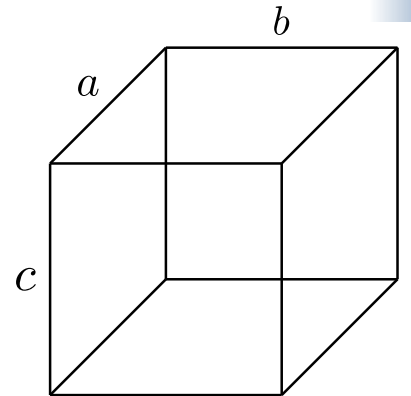


Figure D.1: Illustration of the cubic lattice structure in real space which roughly corresponds to the structure of the cuprates. The in-plane interatomic spacings are labeled by a and b . The interlayer spacing is labeled by c .

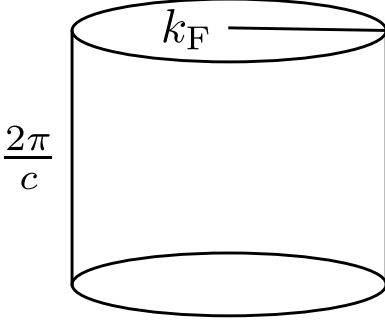


Figure D.2: Illustration of the cylindrical Fermi surface for the layered system.

the states with momenta $k < k_F$. We obtain

$$n = \frac{N}{V} = 2 \int_{-\frac{\pi}{c}}^{\frac{\pi}{c}} \frac{dk_z}{2\pi} \int_0^{k_F} \frac{k dk}{2\pi} \int_0^{2\pi} \frac{d\phi}{2\pi} \theta(k - k_F) \quad (\text{D.1})$$

$$= 2 \left[\frac{1}{2\pi} k \Big|_{-\frac{\pi}{c}}^{\frac{\pi}{c}} \right] \left[\frac{1}{2\pi} \frac{k^2}{2} \Big|_0^{k_F} \right] \left[\frac{1}{2\pi} \phi \Big|_0^{2\pi} \right] \quad (\text{D.2})$$

$$= \frac{k_F^2}{2\pi c} \quad (\text{D.3})$$

which can be rearranged to yield $k_F = \sqrt{2\pi c n}$. This expression can be inserted into the Drude expression for optical conductivity,

$$\sigma = \frac{ne^2\tau}{m^*} = \frac{ne^2\tau v_F}{\hbar k_F} \quad (\text{D.4})$$

where σ is the conductivity, e the charge of the electron, τ the mean free time between scattering events, and m^* the effective particle mass. We invert this to obtain the final expression for the resistivity in a layered system [74],

$$\rho = \frac{2\pi c \hbar}{k_F e^2 \ell}. \quad (\text{D.5})$$

where c is the interlayer spacing (see Fig. D.1) and ℓ is the mean free path traveled by a particle in between collisions.

To compute the Mott-Ioffe-Regel limit for the material of our choice, we simply need to set the scattering length, ℓ , equal to the lattice spacing, a . We illustrate this computation for half-filling, $n = 1/(a^2 c)$, where we assume $a = b$ for simplicity. This leads to $k_F = \sqrt{2\pi}/a$. Inserting this into Eq. (D.5) we arrive at the expression for the Mott-Ioffe-Regel limit,

$$\rho_{\text{MIR}} = \sqrt{2\pi} c \frac{\hbar}{e^2}, \quad (\text{D.6})$$

which evaluates to $\rho_{\text{MIR}} = 0.66 \text{ m}\Omega \text{ cm}$ upon insertion of the interlayer spacing of $\text{La}_{2-x}\text{Sr}_x\text{CuO}_4$ ($c = 6.4 \text{ \AA}$) [76]. The Mott-Ioffe-Regel limit values for the other densities studied in Chapter 4 ($n = 0.5, 0.9$) are given as $\rho_{\text{MIR}} = 0.93 \text{ m}\Omega \text{ cm}$ and $0.69 \text{ m}\Omega \text{ cm}$, respectively.

In order to compare with our two-dimensional results, we need to include a factor of the interlayer spacing,

$$\rho_{\text{sc}}^{2D} = \rho_0 \left[\frac{U^2}{t^2} \frac{\hbar}{e^2} \right] \rightarrow \rho_{\text{sc}}^{\text{layered}} = \rho_{\text{sc}}^{2D} \cdot c = 6.4 \rho_0 \left[\frac{U^2}{t^2} \frac{\hbar}{e^2} \right]. \quad (\text{D.7})$$

We choose a reasonable factor of the band-structure parameters, $U = 8t$, to describe $\text{La}_{2-x}\text{Sr}_x\text{CuO}_4$ [242], arriving at a final expression for our two-dimensional results for a representative layered system,

$$\rho_{\text{sc}}^{\text{layered}} = 16.8 \rho_0 [\text{m}\Omega \text{ cm}]. \quad (\text{D.8})$$

This factor and the Mott-Ioffe-Regel limits previously discussed were incorporated into our results in Chapter 4 in order to demonstrate that our long-range interacting model gives rise to bad-metallic behavior as the resistivity climbs well beyond the Mott-Ioffe-Regel limit expected for a typical strongly correlated system.

Bibliography

- [1] P. Drude. Zur Elektronentheorie der Metalle. *Annalen der Physik*, [306, 566–613](#), 1900.
- [2] P. Drude. Zur Elektronentheorie der Metalle; II. Teil. Galvanomagnetische und thermomagnetische Effecte. *Annalen der Physik*, [308, 369–402](#), 1900.
- [3] R. Franz and G. Wiedemann. Ueber die Wärme-Leitungsfähigkeit der Metalle. *Annalen der Physik*, [165, 497–531](#), 1853.
- [4] W. Pauli. Über den Zusammenhang des Abschlusses der Elektronengruppen im Atom mit der Komplexstruktur der Spektren. *Zeitschrift für Physik*, [31, 765–783](#), Feb. 1925.
- [5] W. Pauli. The Connection Between Spin and Statistics. *Physical Review*, [58, 716–722](#), Oct. 1940. Publisher: American Physical Society.
- [6] A. Sommerfeld. Zur Elektronentheorie der Metalle auf Grund der Fermischen Statistik. *Zeitschrift für Physik*, [47, 1–32](#), Jan. 1928.
- [7] Felix Bloch. Über die Quantenmechanik der Elektronen in Kristallgittern. *Zeitschrift für Physik*, [52, 555–600](#), Jul. 1929.
- [8] Gerald D. Mahan. *Condensed Matter in a Nutshell* (Princeton University Press 2010). Publication Title: Condensed Matter in a Nutshell.
- [9] J. H. de Boer and E. J. W. Verwey. Semi-conductors with partially and with completely filled 3d-lattice bands. [49, 59–71](#), Aug. 1937. Publisher: IOP Publishing.
- [10] N. F. Mott and R. Peierls. Discussion of the paper by de Boer and Verwey. [49, 72–73](#), Aug. 1937. Publisher: IOP Publishing.
- [11] N. F. Mott. The Basis of the Electron Theory of Metals, with Special Reference to the Transition Metals. [62, 416–422](#), Jul. 1949. Publisher: IOP Publishing.
- [12] Gabriel Kotliar and Dieter Vollhardt. Strongly Correlated Materials: Insights From Dynamical Mean-Field Theory. *Physics Today*, [57, 53–59](#), Mar. 2004. Publisher: American Institute of Physics.

- [13] Elbio Dagotto. Complexity in Strongly Correlated Electronic Systems. *Science*, **309**, 257–262, Jul. 2005. Publisher: American Association for the Advancement of Science.
- [14] H. v. Löhneysen. Strongly Correlated Electron Systems. Franco Bassani, Gerald L. Liedl, and Peter Wyder (Eds.), *Encyclopedia of Condensed Matter Physics*, pp. 46–54 (Elsevier, Oxford2005).
- [15] J. Hubbard and Brian Hilton Flowers. Electron correlations in narrow energy bands. *Proceedings of the Royal Society of London. Series A. Mathematical and Physical Sciences*, **276**, 238–257, Nov. 1963. Publisher: Royal Society.
- [16] J. Hubbard and Brian Hilton Flowers. Electron correlations in narrow energy bands. II. The degenerate band case. *Proceedings of the Royal Society of London. Series A. Mathematical and Physical Sciences*, **277**, 237–259, Jan. 1964. Publisher: Royal Society.
- [17] Hubbard J. and Flowers Brian Hilton. Electron correlations in narrow energy bands III. An improved solution. *Proceedings of the Royal Society of London. Series A. Mathematical and Physical Sciences*, **281**, 401–419, Sep. 1964.
- [18] N. Mott. *Metal-Insulator Transitions* (Taylor & Francis1990).
- [19] Elliott H. Lieb and F. Y. Wu. Absence of Mott Transition in an Exact Solution of the Short-Range, One-Band Model in One Dimension. *Physical Review Letters*, **20**, 1445–1448, Jun. 1968. Publisher: American Physical Society.
- [20] Antoine Georges, Gabriel Kotliar, Werner Krauth, and Marcelo J. Rozenberg. Dynamical mean-field theory of strongly correlated fermion systems and the limit of infinite dimensions. *Reviews of Modern Physics*, **68**, 13–125, Jan. 1996. Publisher: American Physical Society.
- [21] Fabian H. L. Essler, Holger Frahm, Frank Göhmann, *et al.* *The One-Dimensional Hubbard Model* (Cambridge University Press, Cambridge2005).
- [22] T. Deguchi, F. H. L. Essler, F. Göhmann, *et al.* Thermodynamics and excitations of the one-dimensional Hubbard model. *Physics Reports*, **331**, 197–281, Jul. 2000.
- [23] Luke Shulenburger, Michele Casula, Gaetano Senatore, and Richard M. Martin. Correlation effects in quasi-one-dimensional quantum wires. *Physical Review B*, **78**, 165303, Oct. 2008. Publisher: American Physical Society.
- [24] T. Giamarchi. Theoretical Framework for Quasi-One Dimensional Systems. *Chemical Reviews*, **104**, 5037–5056, 2004. Publisher: Chemical Reviews.
- [25] Steven R. White. Density matrix formulation for quantum renormalization groups. *Physical Review Letters*, **69**, 2863–2866, Nov. 1992. Publisher: American Physical Society.
- [26] Steven R. White. Density-matrix algorithms for quantum renormalization groups. *Physical Review B*, **48**, 10345–10356, Oct. 1993. Publisher: American Physical Society.
- [27] Steven R. White. Spin Gaps in a Frustrated Heisenberg Model for CaV_4O_9 . *Phys. Rev. Lett.*, **77**, 3633–3636, Oct. 1996. Publisher: American Physical Society.

- [28] E.M. Stoudenmire and Steven R. White. Studying Two-Dimensional Systems with the Density Matrix Renormalization Group. *Annual Review of Condensed Matter Physics*, **3**, 111–128, 2012.
- [29] W. M. C. Foulkes, L. Mitas, R. J. Needs, and G. Rajagopal. Quantum Monte Carlo simulations of solids. *Reviews of Modern Physics*, **73**, 33–83, Jan. 2001. Publisher: American Physical Society.
- [30] Paulo H. Acioli. Review of quantum Monte Carlo methods and their applications. *Journal of Molecular Structure: THEOCHEM*, **394**, 75–85, May 1997.
- [31] Brian M. Austin, Dmitry Yu Zubarev, and William A. Jr Lester. Quantum Monte Carlo and related approaches. *Chemical reviews*, **112**, 263–288, Jan. 2012. Place: United States.
- [32] H. Q. Lin. Exact diagonalization of quantum-spin models. *Physical Review B*, **42**, 6561–6567, Oct. 1990. Publisher: American Physical Society.
- [33] Elbio Dagotto. Correlated electrons in high-temperature superconductors. *Reviews of Modern Physics*, **66**, 763–840, Jul. 1994. Publisher: American Physical Society.
- [34] N. V. Prokof'ev, B. V. Svistunov, and I. S. Tupitsyn. Exact, complete, and universal continuous-time worldline Monte Carlo approach to the statistics of discrete quantum systems. *Journal of Experimental and Theoretical Physics*, **87**, 310–321, Aug. 1998.
- [35] Nikolai V. Prokof'ev and Boris V. Svistunov. Polaron Problem by Diagrammatic Quantum Monte Carlo. *Physical Review Letters*, **81**, 2514–2517, Sep. 1998. Publisher: American Physical Society.
- [36] Kris Van Houcke, Evgeny Kozik, N. Prokof'ev, and B. Svistunov. Diagrammatic Monte Carlo. *Physics Procedia*, **6**, 95–105, Jan. 2010.
- [37] Christina V. Kraus, Norbert Schuch, Frank Verstraete, and J. Ignacio Cirac. Fermionic projected entangled pair states. *Physical Review A*, **81**, 052338, May 2010. Publisher: American Physical Society.
- [38] A. Kshetrimayum, M. Rizzi, J. Eisert, and R. Orús. Tensor Network Annealing Algorithm for Two-Dimensional Thermal States. *Physical Review Letters*, **122**, 070502, Feb. 2019. Publisher: American Physical Society.
- [39] Benedikt Kloss, David Reichman, and Yevgeny Bar Lev. Studying dynamics in two-dimensional quantum lattices using tree tensor network states. *SciPost Physics*, **9**, 070, Nov. 2020.
- [40] Yusuke Nomura, Andrew S. Darmawan, Youhei Yamaji, and Masatoshi Imada. Restricted Boltzmann machine learning for solving strongly correlated quantum systems. *Physical Review B*, **96**, 205152, Nov. 2017. Publisher: American Physical Society.
- [41] Kelvin Ch'ng, Juan Carrasquilla, Roger G. Melko, and Ehsan Khatami. Machine Learning Phases of Strongly Correlated Fermions. *Physical Review X*, **7**, 031038, Aug. 2017. Publisher: American Physical Society.
- [42] Annabelle Bohrdt, Christie S. Chiu, Geoffrey Ji, *et al.* Classifying snapshots of the doped Hubbard model with machine learning. *Nature Physics*, **15**, 921–924, Sep. 2019.

- [43] Simons Collaboration on the Many-Electron Problem, J. P. F. LeBlanc, Andrey E. Antipov, *et al.* Solutions of the Two-Dimensional Hubbard Model: Benchmarks and Results from a Wide Range of Numerical Algorithms. *Physical Review X*, **5**, 041041, Dec. 2015. Publisher: American Physical Society.
- [44] Adolfo Avella and Ferdinando Mancini (Eds.). *Strongly Correlated Systems: Experimental Techniques*, vol. 180 of *Springer Series in Solid-State Sciences* (Springer, Berlin, Heidelberg2015), 1 ed.
- [45] Yang Xu, Song Liu, Daniel A. Rhodes, *et al.* Correlated insulating states at fractional fillings of moiré superlattices. *Nature*, **587**, 214–218, Nov. 2020.
- [46] Emma C. Regan, Danqing Wang, Chenhao Jin, *et al.* Mott and generalized Wigner crystal states in WSe₂/WS₂ moiré superlattices. *Nature*, **579**, 359–363, Mar. 2020.
- [47] Nicolò Defenu, Tobias Donner, Tommaso Macrì, *et al.* Long-range interacting quantum systems. Sep. 2021.
- [48] B. Keimer, S. A. Kivelson, M. R. Norman, *et al.* From quantum matter to high-temperature superconductivity in copper oxides. *Nature*, **518**, 179–186, Feb. 2015. Number: 7538 Publisher: Nature Publishing Group.
- [49] Adolfo Avella and Ferdinando Mancini (Eds.). *Strongly Correlated Systems: Theoretical Methods*, vol. 171 of *Springer Series in Solid-State Sciences* (Springer, Berlin, Heidelberg2012), 1 ed.
- [50] Adolfo Avella and Ferdinando Mancini (Eds.). *Strongly Correlated Systems: Numerical Methods*. Springer Series in Solid-State Sciences (Springer-Verlag, Berlin Heidelberg2013).
- [51] M. Gurvitch and A. T. Fiory. Resistivity of La_{1.825}Sr_{0.175}CuO₄ and YBa₂Cu₃O₇ to 1100 K: Absence of saturation and its implications. *Physical Review Letters*, **59**, 1337–1340, Sep. 1987. Publisher: American Physical Society.
- [52] R. H. Liu, G. Wu, T. Wu, *et al.* Anomalous Transport Properties and Phase Diagram of the FeAs-Based SmFeAsO_{1-x}F_x Superconductors. *Physical Review Letters*, **101**, 087001, Aug. 2008. Publisher: American Physical Society.
- [53] Nicolas Doiron-Leyraud, Pascale Auban-Senzier, Samuel René de Cotret, *et al.* Correlation between linear resistivity and T_c in the Bechgaard salts and the pnictide superconductor Ba(Fe_{1-x}Co_x)₂As₂. *Physical Review B*, **80**, 214531, Dec. 2009. Publisher: American Physical Society.
- [54] J. J. Ying, X. F. Wang, T. Wu, *et al.* Measurements of the Anisotropic In-Plane Resistivity of Underdoped FeAs-Based Pnictide Superconductors. *Physical Review Letters*, **107**, 067001, Aug. 2011. Publisher: American Physical Society.
- [55] O. Gunnarsson and J. E. Han. The mean free path for electron conduction in metallic fullerenes. *Nature*, **405**, 1027–1030, Jun. 2000.
- [56] M. M. Qazilbash, K. S. Burch, D. Whisler, *et al.* Correlated metallic state of vanadium dioxide. *Physical Review B*, **74**, 205118, Nov. 2006. Publisher: American Physical Society.

- [57] A. W. Tyler, A. P. Mackenzie, S. NishiZaki, and Y. Maeno. High-temperature resistivity of Sr_2RuO_4 : Bad metallic transport in a good metal. *Physical Review B*, [58, R10107–R10110](#), Oct. 1998. Publisher: American Physical Society.
- [58] B. J. Powell and Ross H. McKenzie. Quantum frustration in organic Mott insulators: from spin liquids to unconventional superconductors. *Reports on Progress in Physics*, [74, 056501](#), Apr. 2011. Publisher: IOP Publishing.
- [59] T. Sato, K. Kitai, K. Miyagawa, *et al.* Strange metal from a frustration-driven charge order instability. *Nature Materials*, [18, 229–233](#), Mar. 2019.
- [60] R. Jaramillo, Sieu D. Ha, D. M. Silevitch, and Shriram Ramanathan. Origins of bad-metal conductivity and the insulator–metal transition in the rare-earth nickelates. *Nature Physics*, [10, 304–307](#), Apr. 2014.
- [61] N. E. Hussey, K. Takenaka, and H. Takagi. Universality of the Mott–Ioffe–Regel limit in metals. *Philosophical Magazine*, [84, 2847–2864](#), Sep. 2004.
- [62] AF Ioffe and AR Regel. Non-crystalline, amorphous, and liquid electronic semiconductors. *Progress in Semiconductors*, vol. 4 (Heywood and co., London1960).
- [63] N. F. Mott. Conduction in non-crystalline systems IX. the minimum metallic conductivity. *The Philosophical Magazine: A Journal of Theoretical Experimental and Applied Physics*, [26, 1015–1026](#), Oct. 1972.
- [64] H. Wiesmann, M. Gurvitch, H. Lutz, *et al.* Simple Model for Characterizing the Electrical Resistivity in A – 15 Superconductors. *Physical Review Letters*, [38, 782–785](#), Apr. 1977. Publisher: American Physical Society.
- [65] P. B. Allen. Theory of Resistivity Saturation. H Suhl and M. B. Maple (Eds.), *Superconductivity in d- and f-band metals (Third Rochester Conference, San Diego)*, pp. 291–304 (Academic Press, New York1980).
- [66] H. Takagi, B. Batlogg, H. L. Kao, *et al.* Systematic evolution of temperature-dependent resistivity in $\text{La}_{2-x}\text{Sr}_x\text{CuO}_4$. *Physical Review Letters*, [69, 2975–2978](#), Nov. 1992. Publisher: American Physical Society.
- [67] A. F. Hebard, T. T. M. Palstra, R. C. Haddon, and R. M. Fleming. Absence of saturation in the normal-state resistivity of thin films of K_3C_{60} and Rb_3C_{60} . *Physical Review B*, [48, 9945–9948](#), Oct. 1993. Publisher: American Physical Society.
- [68] V. J. Emery and S. A. Kivelson. Superconductivity in Bad Metals. *Physical Review Letters*, [74, 3253–3256](#), Apr. 1995. Publisher: American Physical Society.
- [69] Debanjan Chowdhury, Antoine Georges, Olivier Parcollet, and Subir Sachdev. Sachdev-Ye-Kitaev Models and Beyond: A Window into Non-Fermi Liquids, 2021.
- [70] Luca Delacrétaz, Blaise Goutéraux, Sean Hartnoll, and Anna Karlsson. Bad Metals from Fluctuating Density Waves. *SciPost Physics*, [3, 025](#), Sep. 2017.

- [71] Xiaoyu Deng, Jernej Mravlje, Rok Žitko, *et al.* How Bad Metals Turn Good: Spectroscopic Signatures of Resilient Quasiparticles. *Physical Review Letters*, **110**, 086401, Feb. 2013. Publisher: American Physical Society.
- [72] Jure Kokalj. Bad-metallic behavior of doped Mott insulators. *Physical Review B*, **95**, 041110, Jan. 2017. Publisher: American Physical Society.
- [73] Sean A. Hartnoll. Theory of universal incoherent metallic transport. *Nature Physics*, **11**, 54–61, Jan. 2015.
- [74] J. a. N. Bruin, H. Sakai, R. S. Perry, and A. P. Mackenzie. Similarity of Scattering Rates in Metals Showing T-Linear Resistivity. *Science*, **339**, 804–807, Feb. 2013. Publisher: American Association for the Advancement of Science Section: Report.
- [75] Andrej Pustogow, Yohei Saito, Anja Löhle, *et al.* Rise and fall of Landau’s quasiparticles while approaching the Mott transition. *Nature Communications*, **12**, 1571, Mar. 2021.
- [76] O. Gunnarsson, M. Calandra, and J. E. Han. Colloquium: Saturation of electrical resistivity. *Reviews of Modern Physics*, **75**, 1085–1099, Oct. 2003. Publisher: American Physical Society.
- [77] Simone Fratini and Sergio Ciuchi. Displaced Drude peak and bad metal from the interaction with slow fluctuations. *SciPost Physics*, **11**, 039, Aug. 2021.
- [78] S. Ciuchi, S. Fratini, and D. Mayou. Transient localization in crystalline organic semiconductors. *Physical Review B*, **83**, 081202, Feb. 2011. Publisher: American Physical Society.
- [79] S. Fratini and S. Ciuchi. Dynamical localization corrections to band transport. *Physical Review Research*, **2**, 013001, Jan. 2020. Publisher: American Physical Society.
- [80] Edwin W. Huang, Ryan Sheppard, Brian Moritz, and Thomas P. Devereaux. Strange metallicity in the doped Hubbard model. *Science*, **366**, 987–990, Nov. 2019. Publisher: American Association for the Advancement of Science.
- [81] Yoshinori Tokura. Correlated-Electron Physics in Transition-Metal Oxides. *Physics Today*, **56**, 50–55, Jul. 2003. Publisher: American Institute of Physics.
- [82] C. N. R. Rao. Transition Metal Oxides. *Annual Review of Physical Chemistry*, **40**, 291–326, Oct. 1989. Publisher: Annual Reviews.
- [83] J. G. Bednorz and K. A. Müller. Possible high- T_c superconductivity in the Ba-La-Cu-O system. *Zeitschrift für Physik B Condensed Matter*, **64**, 189–193, Jun. 1986.
- [84] Shin-ichi Uchida, Hidenori Takagi, Koichi Kitazawa, and Shoji Tanaka. High T_c Superconductivity of La-Ba-Cu Oxides. *Japanese Journal of Applied Physics*, **26**, L1, Jan. 1987. Publisher: IOP Publishing.
- [85] M. K. Wu, J. R. Ashburn, C. J. Torng, *et al.* Superconductivity at 93 K in a new mixed-phase Y-Ba-Cu-O compound system at ambient pressure. *Physical Review Letters*, **58**, 908–910, Mar. 1987. Publisher: American Physical Society.

- [86] Cyril Proust and Louis Taillefer. The Remarkable Underlying Ground States of Cuprate Superconductors. *Annual Review of Condensed Matter Physics*, **10**, 409–429, Mar. 2019. Publisher: Annual Reviews.
- [87] Wolfram Brenig. Aspects of electron correlations in the cuprate superconductors. *Physics Reports*, **251**, 153–266, Jan. 1995.
- [88] Bo-Xiao Zheng, Chia-Min Chung, Philippe Corboz, *et al.* Stripe order in the underdoped region of the two-dimensional Hubbard model. *Science*, **358**, 1155–1160, Dec. 2017. Publisher: American Association for the Advancement of Science Section: Research Article.
- [89] Edwin W. Huang, Christian B. Mendl, Hong-Chen Jiang, *et al.* Stripe order from the perspective of the Hubbard model. *npj Quantum Materials*, **3**, 1–6, Apr. 2018.
- [90] Yoichi Ando, Seiki Komiya, Kouji Segawa, *et al.* Electronic Phase Diagram of High- T_c Cuprate Superconductors from a Mapping of the In-Plane Resistivity Curvature. *Physical Review Letters*, **93**, 267001, Dec. 2004. Publisher: American Physical Society.
- [91] J. M. Tranquada, B. J. Sternlieb, J. D. Axe, *et al.* Evidence for stripe correlations of spins and holes in copper oxide superconductors. *Nature*, **375**, 561–563, Jun. 1995.
- [92] W. A. Little. Possibility of Synthesizing an Organic Superconductor. *Physical Review*, **134**, A1416–A1424, Jun. 1964. Publisher: American Physical Society.
- [93] J. Wosnitzer. Quasi-Two-Dimensional Organic Superconductors. *Journal of Low Temperature Physics*, **146**, 641–667, Mar. 2007.
- [94] Denis Jérôme. Organic Conductors: From Charge Density Wave TTF-TCNQ to Superconducting (TMTSF)₂PF₆. *Chemical Reviews*, **104**, 5565–5592, Nov. 2004. Publisher: American Chemical Society.
- [95] Hitoshi Seo, Chisa Hotta, and Hidetoshi Fukuyama. Toward Systematic Understanding of Diversity of Electronic Properties in Low-Dimensional Molecular Solids. *Chemical Reviews*, **104**, 5005–5036, Nov. 2004. Publisher: American Chemical Society.
- [96] Chisa Hotta. Theories on Frustrated Electrons in Two-Dimensional Organic Solids. *Crystals*, **2**, 1155–1200, Sep. 2012. Number: 3 Publisher: Molecular Diversity Preservation International.
- [97] Qiang Wang, Matteo Zecchini, John D. Wallis, *et al.* A family of unsymmetrical hydroxyl-substituted BEDT-TTF donors: syntheses, structures and preliminary thin film studies. *RSC Advances*, **5**, 40205–40218, Apr. 2015. Publisher: The Royal Society of Chemistry.
- [98] Hatsumi Mori. Materials Viewpoint of Organic Superconductors. *Journal of the Physical Society of Japan*, **75**, 051003, May 2006. Publisher: The Physical Society of Japan.
- [99] Hitoshi Seo, Jaime Merino, Hideo Yoshioka, and Masao Ogata. Theoretical Aspects of Charge Ordering in Molecular Conductors. *Journal of the Physical Society of Japan*, **75**, 051009, May 2006. Publisher: The Physical Society of Japan.

- [100] L. Ducasse, A. Fritsch, and F. Castet. A Valence-Bond/Hartree-Fock method to determine the extended Hubbard parameters in organic conductors. *Synthetic Metals*, **85**, 1627–1628, Mar. 1997.
- [101] Yutaka Imamura, Seiichiro Ten-no, Kenji Yonemitsu, and Yoshitaka Tanimura. Structures and electronic phases of the bis(ethylenedithio)tetrathiafulvalene (BEDT-TTF) clusters and κ -(BEDT-TTF) salts: A theoretical study based on ab initio molecular orbital methods. *The Journal of Chemical Physics*, **111**, 5986–5994, Oct. 1999. Publisher: American Institute of Physics.
- [102] Takehiko Mori. Estimation of Off-Site Coulomb Integrals and Phase Diagrams of Charge Ordered States in the θ -Phase Organic Conductors. *Bulletin of the Chemical Society of Japan*, **73**, 2243–2253, Oct. 2000. Publisher: The Chemical Society of Japan.
- [103] Takehiko Mori. Structural Genealogy of BEDT-TTF-Based Organic Conductors I. Parallel Molecules: β and β' Phases. *Bulletin of the Chemical Society of Japan*, **71**, 2509–2526, Nov. 1998. Publisher: The Chemical Society of Japan.
- [104] Takehiko Mori, Hatsumi Mori, and Shoji Tanaka. Structural Genealogy of BEDT-TTF-Based Organic Conductors II. Inclined Molecules: θ , α , and κ Phases. *Bulletin of the Chemical Society of Japan*, **72**, 179–197, Feb. 1999. Publisher: The Chemical Society of Japan.
- [105] Takehiko Mori. Structural Genealogy of BEDT-TTF-Based Organic Conductors III. Twisted Molecules: δ and α' Phases. *Bulletin of the Chemical Society of Japan*, **72**, 2011–2027, Sep. 1999. Publisher: The Chemical Society of Japan.
- [106] Kaoru Yamamoto, Kyuya Yakushi, Kazuya Miyagawa, *et al.* Charge ordering in θ -(BEDT – TTF)₂RbZn(SCN)₄ studied by vibrational spectroscopy. *Physical Review B*, **65**, 085110, Feb. 2002. Publisher: American Physical Society.
- [107] Hiori Kino and Hidetoshi Fukuyama. On the Phase Transition of α -(ET)₂I₃. *Journal of the Physical Society of Japan*, **64**, 1877–1880, Jun. 1995. Publisher: The Physical Society of Japan.
- [108] Hitoshi Seo and Hidetoshi Fukuyama. Frustrated Spin System in θ -(BEDT-TTF)₂RbZn(SCN)₄. *Journal of the Physical Society of Japan*, **67**, 1848–1851, Jun. 1998. Publisher: The Physical Society of Japan.
- [109] Hitoshi Seo. Charge Ordering in Organic ET Compounds. *Journal of the Physical Society of Japan*, **69**, 805–820, Mar. 2000. Publisher: The Physical Society of Japan.
- [110] Samiyeh Mahmoudian, Louk Rademaker, Arnaud Ralko, *et al.* Glassy Dynamics in Geometrically Frustrated Coulomb Liquids without Disorder. *Physical Review Letters*, **115**, 025701, Jul. 2015.
- [111] Yuan Cao, Valla Fatemi, Shiang Fang, *et al.* Unconventional superconductivity in magic-angle graphene superlattices. *Nature*, **556**, 43–50, Apr. 2018.
- [112] Wonbong Choi, Nitin Choudhary, Gang Hee Han, *et al.* Recent development of two-dimensional transition metal dichalcogenides and their applications. *Materials Today*, **20**, 116–130, Apr. 2017.
- [113] Lynn Bonsall and A. A. Maradudin. Some static and dynamical properties of a two-dimensional Wigner crystal. *Physical Review B*, **15**, 1959–1973, Feb. 1977. Publisher: American Physical Society.

- [114] E. Wigner. On the Interaction of Electrons in Metals. *Physical Review*, **46**, 1002–1011, Dec. 1934. Publisher: American Physical Society.
- [115] C. C. Grimes and G. Adams. Evidence for a Liquid-to-Crystal Phase Transition in a Classical, Two-Dimensional Sheet of Electrons. *Physical Review Letters*, **42**, 795–798, Mar. 1979. Publisher: American Physical Society.
- [116] Yu. P. Monarkha and V. E. Syvokon. A two-dimensional Wigner crystal (Review Article). *Low Temperature Physics*, **38**, 1067–1095, Dec. 2012. Publisher: American Institute of Physics.
- [117] E. Y. Andrei, G. Deville, D. C. Glattli, *et al.* Observation of a Magnetically Induced Wigner Solid. *Physical Review Letters*, **60**, 2765–2768, Jun. 1988. Publisher: American Physical Society.
- [118] V. T. Dolgoplov. Quantum melting of a two-dimensional Wigner crystal. *Physics-Uspokhi*, **60**, 731, Oct. 2017. Publisher: IOP Publishing.
- [119] H. Deng, L. N. Pfeiffer, K. W. West, *et al.* Probing the Melting of a Two-Dimensional Quantum Wigner Crystal via its Screening Efficiency. *Physical Review Letters*, **122**, 116601, Mar. 2019. Publisher: American Physical Society.
- [120] Xiong Huang, Tianmeng Wang, Shengnan Miao, *et al.* Correlated insulating states at fractional fillings of the WS_2/WSe_2 moiré lattice. *Nature Physics*, **17**, 715–719, Jun. 2021.
- [121] Bikash Padhi, Chandan Setty, and Philip W. Phillips. Doped Twisted Bilayer Graphene near Magic Angles: Proximity to Wigner Crystallization, Not Mott Insulation. *Nano Letters*, **18**, 6175–6180, Oct. 2018. Publisher: American Chemical Society.
- [122] Bikash Padhi and Philip W. Phillips. Pressure-induced metal-insulator transition in twisted bilayer graphene. *Physical Review B*, **99**, 205141, May 2019. Publisher: American Physical Society.
- [123] M. H. Anderson, J. R. Ensher, M. R. Matthews, *et al.* Observation of Bose-Einstein Condensation in a Dilute Atomic Vapor. *Science*, **269**, 198–201, Jul. 1995. Publisher: American Association for the Advancement of Science.
- [124] Maciej Lewenstein, Anna Sanpera, Veronica Ahufinger, *et al.* Ultracold atomic gases in optical lattices: mimicking condensed matter physics and beyond. *Advances in Physics*, **56**, 243–379, Mar. 2007.
- [125] C. Monroe, W. C. Campbell, L.-M. Duan, *et al.* Programmable quantum simulations of spin systems with trapped ions. *Reviews of Modern Physics*, **93**, 025001, Apr. 2021. Publisher: American Physical Society.
- [126] Markus Greiner, Olaf Mandel, Tilman Esslinger, *et al.* Quantum phase transition from a superfluid to a Mott insulator in a gas of ultracold atoms. *Nature*, **415**, 39–44, Jan. 2002.
- [127] Peter T. Brown, Debayan Mitra, Elmer Guardado-Sanchez, *et al.* Bad metallic transport in a cold atom Fermi-Hubbard system. *Science*, **363**, 379–382, Jan. 2019. Publisher: American Association for the Advancement of Science.

- [128] Rhys Anderson, Fudong Wang, Peihang Xu, *et al.* Conductivity Spectrum of Ultracold Atoms in an Optical Lattice. *Physical Review Letters*, **122**, 153602, Apr. 2019. Publisher: American Physical Society.
- [129] W. Xu, W. R. McGehee, W. N. Morong, and B. DeMarco. Bad-metal relaxation dynamics in a Fermi lattice gas. *Nature Communications*, **10**, 1588, Apr. 2019.
- [130] Renate Landig, Lorenz Hruby, Nishant Dogra, *et al.* Quantum phases from competing short- and long-range interactions in an optical lattice. *Nature*, **532**, 476–479, Apr. 2016.
- [131] Immanuel Bloch, Jean Dalibard, and Wilhelm Zwerger. Many-body physics with ultracold gases. *Reviews of Modern Physics*, **80**, 885–964, Jul. 2008. Publisher: American Physical Society.
- [132] Jill C. Bonner and Michael E. Fisher. Linear Magnetic Chains with Anisotropic Coupling. *Physical Review*, **135**, A640–A658, Aug. 1964. Publisher: American Physical Society.
- [133] Roger G. Melko. Stochastic Series Expansion Quantum Monte Carlo. Adolfo Avella and Ferdinando Mancini (Eds.), *Strongly Correlated Systems: Numerical Methods*, Springer Series in Solid-State Sciences, pp. 185–206 (Springer, Berlin, Heidelberg 2013).
- [134] Åke Björck. *Numerical Methods in Matrix Computations*. Texts in Applied Mathematics (Springer International Publishing 2015).
- [135] Angelika Bunse-Gerstner, Volker Mehrmann, and Ralph Byers. A chart of numerical methods for structured eigenvalue problems. Gene H. Golub and Paul Van Dooren (Eds.), *Numerical Linear Algebra, Digital Signal Processing and Parallel Algorithms*, NATO ASI Series, pp. 547–547 (Springer, Berlin, Heidelberg 1991).
- [136] C. Lanczos. An iteration method for the solution of the eigenvalue problem of linear differential and integral operators. *Journal of Research of the National Bureau of Standards*, **45**, 255, Oct. 1950.
- [137] Wolfgang von der Linden. Numerical Approaches to Coupled Quantum Systems. *AIP Conference Proceedings*, **846**, 162–217, Jul. 2006. Publisher: American Institute of Physics.
- [138] Erik Koch. *The LDA+DMFT approach to strongly correlated materials: Autumn school organized by the DFG Research Unit 1346 Dynamical Mean-Field Approach with Predictive Power for Strongly Correlated Materials at Forschungszentrum Jülich, 4-7 October 2011 ; Lecture notes*. No. 1 in Schriften des Forschungszentrums Jülich Reihe Modeling and Simulation (Forschungszentrum Jülich, Jülich 2011). OCLC: 838915041.
- [139] P. Prelovšek and J. Bonča. Ground State and Finite Temperature Lanczos Methods. Adolfo Avella and Ferdinando Mancini (Eds.), *Strongly Correlated Systems: Numerical Methods*, Springer Series in Solid-State Sciences, pp. 1–30 (Springer, Berlin, Heidelberg 2013).
- [140] Matthieu Mambrini. *Etude des excitations de basse énergie dans des systèmes magnétiques frustrés de basse dimensionnalité: gap de spin et singulets de basse énergie*. Theses, Université Paul Sabatier - Toulouse III, Jul. 2000.

- [141] Sylvain Capponi. *Etude théorique du rôle des processus interchaînes dans des liquides de Luttinger couplés*. phdthesis, Université Paul Sabatier - Toulouse III, Oct. 1999.
- [142] Nicolas Laflorencie and Didier Poilblanc. Simulations of pure and doped low-dimensional spin- $1/2$ gapped systems. Ulrich Schollwöck, Johannes Richter, Damian J. J. Farnell, and Raymod F. Bishop (Eds.), *Quantum Magnetism*, Lecture Notes in Physics, pp. 227–252 (Springer, Berlin, Heidelberg2004).
- [143] Mildred S. Dresselhaus, Gene Dresselhaus, and Ado Jorio. *Group Theory: Application to the Physics of Condensed Matter* (Springer-Verlag, Berlin Heidelberg2008).
- [144] Didier Poilblanc. Twisted boundary conditions in cluster calculations of the optical conductivity in two-dimensional lattice models. *Physical Review B*, [44](#), [9562–9581](#), Nov. 1991.
- [145] Claudius Gros. The boundary condition integration technique: results for the Hubbard model in 1D and 2D. *Zeitschrift fur Physik B Condensed Matter*, [86](#), [359–365](#), Oct. 1992.
- [146] W. Ehrenberg and R. E. Siday. The Refractive Index in Electron Optics and the Principles of Dynamics. *Proceedings of the Physical Society. Section B*, [62](#), [8–21](#), Jan. 1949. Publisher: IOP Publishing.
- [147] J. Kokalj and P. Prelovšek. Luttinger sum rule for finite systems of correlated electrons. *Physical Review B*, [75](#), [045111](#), Jan. 2007.
- [148] Masatoshi Imada, Atsushi Fujimori, and Yoshinori Tokura. Metal-insulator transitions. *Reviews of Modern Physics*, [70](#), [1039–1263](#), Oct. 1998. Publisher: American Physical Society.
- [149] Takashi Koretsune, Yukitoshi Motome, and Akira Furusaki. Exact Diagonalization Study of Mott Transition in the Hubbard Model on an Anisotropic Triangular Lattice. *Journal of the Physical Society of Japan*, [76](#), [074719](#), Jul. 2007.
- [150] J. Jaklič and P. Prelovšek. Lanczos method for the calculation of finite-temperature quantities in correlated systems. *Physical Review B*, [49](#), [5065–5068](#), Feb. 1994. Publisher: American Physical Society.
- [151] Paul Gibbon and Godehard Sutmann. Long-Range Interactions in Many-Particle Simulation, Quantum Simulations of Complex Many-Body Systems: From Theory to Algorithms. *Lecture Notes*, J. Grotendorst, D. Marx, A. Muramatsu (Eds.), *John von Neumann Institute for Computing, Jülich, NIC Series*, pp. 467–506 (2002).
- [152] Y. Pramudya, H. Terletska, S. Pankov, *et al.* Nearly frozen Coulomb liquids. *Physical Review B*, [84](#), [125120](#), Sep. 2011.
- [153] K. Driscoll, A. Ralko, and S. Fratini. Pseudogap metal induced by long-range Coulomb interactions. *Physical Review B*, [103](#), [L201106](#), May 2021. Publisher: American Physical Society.
- [154] Y. Zhang and J. Callaway. Extended Hubbard model in two dimensions. *Physical Review B*, [39](#), [9397–9404](#), May 1989. Publisher: American Physical Society.

- [155] Boris Spivak and Steven A. Kivelson. Phases intermediate between a two-dimensional electron liquid and Wigner crystal. *Physical Review B*, **70**, 155114, Oct. 2004. Publisher: American Physical Society.
- [156] M. A. Baranov, M. Dalmonte, G. Pupillo, and P. Zoller. Condensed Matter Theory of Dipolar Quantum Gases. *Chemical Reviews*, **112**, 5012–5061, Sep. 2012. Publisher: American Chemical Society.
- [157] B. Valenzuela, S. Fratini, and D. Baeriswyl. Charge and spin order in one-dimensional electron systems with long-range Coulomb interactions. *Physical Review B*, **68**, 045112, Jul. 2003. Publisher: American Physical Society.
- [158] S. Fratini, B. Valenzuela, and D. Baeriswyl. Incipient quantum melting of the one-dimensional Wigner lattice. *Synthetic Metals*, **141**, 193–196, Mar. 2004.
- [159] Chisa Hotta and Nobuo Furukawa. Strong coupling theory of the spinless charges on triangular lattices: Possible formation of a gapless charge-ordered liquid. *Physical Review B*, **74**, 193107, Nov. 2006.
- [160] Chisa Hotta and Nobuo Furukawa. Filling dependence of a new type of charge ordered liquid on a triangular lattice system. **19**, 145242, Mar. 2007. Publisher: IOP Publishing.
- [161] Aleksandr F. Andreev and I. M. Lifshitz. Quantum Theory of Defects in Crystals. **13**, 670–670, May 1971. Publisher: IOP Publishing.
- [162] S. Fratini and J. Merino. Unconventional metallic conduction in two-dimensional Hubbard-Wigner lattices. *Physical Review B*, **80**, 165110, Oct. 2009.
- [163] E. V. Tsiper and A. L. Efros. Structural and insulator-metal quantum phase transitions on a lattice. *Physical Review B*, **57**, 6949–6956, Mar. 1998. Publisher: American Physical Society.
- [164] L. Z. Stolarczyk. On the hierarchy of pi-electron models. *Polish Journal of Chemistry*, 1998.
- [165] Douglas J. Scalapino, Steven R. White, and Shoucheng Zhang. Insulator, metal, or superconductor: The criteria. *Physical Review B*, **47**, 7995–8007, Apr. 1993. Publisher: American Physical Society.
- [166] Walter Kohn. Theory of the Insulating State. *Physical Review*, **133**, A171–A181, Jan. 1964. Publisher: American Physical Society.
- [167] Mitake Miyazaki, Chisa Hotta, Shin Miyahara, *et al.* Variational Monte Carlo Study of a Spinless Fermion t - V Model on a Triangular Lattice: Formation of a Pinball Liquid. *Journal of the Physical Society of Japan*, **78**, 014707, Jan. 2009. Publisher: The Physical Society of Japan.
- [168] Arnaud Ralko, Jaime Merino, and Simone Fratini. Pinball liquid phase from Hund's coupling in frustrated transition-metal oxides. *Physical Review B*, **91**, 165139, Apr. 2015. Publisher: American Physical Society.
- [169] Hongyuan Li, Shaowei Li, Emma C. Regan, *et al.* Imaging two-dimensional generalized Wigner crystals. *Nature*, **597**, 650–654, Sep. 2021.

- [170] Yuriy Monarkha and Kimitoshi Kono. Wigner Solid. I. Dynamics on Rigid and Soft Interfaces. Yuriy Monarkha and Kimitoshi Kono (Eds.), *Two-Dimensional Coulomb Liquids and Solids*, Springer Series in Solid-State Sciences, pp. 237–292 (Springer, Berlin, Heidelberg 2004).
- [171] N. D. Drummond and R. J. Needs. Phase Diagram of the Low-Density Two-Dimensional Homogeneous Electron Gas. *Physical Review Letters*, [102](#), [126402](#), Mar. 2009. Publisher: American Physical Society.
- [172] Gerald D. Mahan. *Many-Particle Physics*. Physics of Solids and Liquids (Springer US 2000), 3 ed.
- [173] L. Cano-Cortés, J. Merino, and S. Fratini. Quantum Critical Behavior of Electrons at the Edge of Charge Order. *Physical Review Letters*, [105](#), [036405](#), Jul. 2010.
- [174] D. Baeriswyl and S. Fratini. Fate of the Wigner crystal on the square lattice. *Journal de Physique IV (Proceedings)*, [131](#), [247–250](#), Dec. 2005. Publisher: EDP Sciences.
- [175] Yohei Noda and Masatoshi Imada. Quantum Phase Transitions to Charge-Ordered and Wigner-Crystal States under the Interplay of Lattice Commensurability and Long-Range Coulomb Interactions. *Physical Review Letters*, [89](#), [176803](#), Oct. 2002. Publisher: American Physical Society.
- [176] M. M. Qazilbash, J. J. Hamlin, R. E. Baumbach, *et al.* Electronic correlations in the iron pnictides. *Nature Physics*, [5](#), [647–650](#), Sep. 2009.
- [177] T. Sato, K. Miyagawa, and K. Kanoda. Electronic crystal growth. *Science*, [357](#), [1378–1381](#), Sep. 2017.
- [178] Fumitaka Kagawa and Hiroshi Oike. Quenching of Charge and Spin Degrees of Freedom in Condensed Matter. *Advanced Materials*, [29](#), [1601979](#), 2017.
- [179] Louk Rademaker, Zohar Nussinov, Leon Balents, and Vladimir Dobrosavljević. Suppressed density of states in self-generated Coulomb glasses. *New Journal of Physics*, [20](#), [043026](#), Apr. 2018. Publisher: IOP Publishing.
- [180] A. L. Efros and B. I. Shklovskii. Coulomb gap and low temperature conductivity of disordered systems. *Journal of Physics C: Solid State Physics*, [8](#), [L49–L51](#), Feb. 1975. Publisher: IOP Publishing.
- [181] A. L. Efros. Coulomb gap and transport in classical electron liquid. *Physical Review Letters*, [68](#), [2208–2211](#), Apr. 1992. Publisher: American Physical Society.
- [182] Jörg Schmalian and Peter G. Wolynes. Stripe Glasses: Self-Generated Randomness in a Uniformly Frustrated System. *Physical Review Letters*, [85](#), [836–839](#), Jul. 2000. Publisher: American Physical Society.
- [183] A. L. Efros and M. Pollak. *Electron-Electron Interactions in Disordered Systems* (Elsevier 2012). Google-Books-ID: XFj74hRLpWIC.
- [184] S. Ciuchi and F. de Pasquale. Charge-ordered state from weak to strong coupling. *Phys. Rev. B*, [59](#), [5431–5440](#), Feb 1999.

- [185] A. L. Efros. Coulomb gap in disordered systems. [9, 2021–2030](#), Jun. 1976. Publisher: IOP Publishing.
- [186] A F Andreev and Yu A Kosevich. Kinetic phenomena in semiquantum liquids, 1979.
- [187] V. J. Emery and S. A. Kivelson. Frustrated electronic phase separation and high-temperature superconductors. *Physica C: Superconductivity*, [209, 597–621](#), May 1993.
- [188] B. Spivak. Properties of the strongly correlated two-dimensional electron gas in Si MOSFET's. *Physical Review B*, [64, 085317](#), Aug. 2001. Publisher: American Physical Society.
- [189] F. Nad, P. Monceau, and H. M. Yamamoto. Effect of cooling rate on charge ordering in $\theta - (\text{BEDT} - \text{TTF})_2\text{RbZn}(\text{SCN})_4$. *Physical Review B*, [76, 205101](#), Nov. 2007. Publisher: American Physical Society.
- [190] F. Kagawa, T. Sato, K. Miyagawa, *et al.* Charge-cluster glass in an organic conductor. *Nature Physics*, [9, 419–422](#), Jul. 2013.
- [191] K. Takenaka, M. Tamura, N. Tajima, *et al.* Collapse of Coherent Quasiparticle States in $\theta - (\text{BEDT} - \text{TTF})_2\text{I}_3$ Observed by Optical Spectroscopy. *Physical Review Letters*, [95, 227801](#), Nov. 2005. Publisher: American Physical Society.
- [192] M Kaveh and N F Mott. Universal dependences of the conductivity of metallic disordered systems on temperature, magnetic field and frequency. *Journal of Physics C: Solid State Physics*, [15, L707–L716](#), 1982. Publisher: IOP.
- [193] Simone Fratini, Didier Mayou, and Sergio Ciuchi. The Transient Localization Scenario for Charge Transport in Crystalline Organic Materials. *Advanced Functional Materials*, [26, 2292–2315](#), 2016.
- [194] A. J. Millis, Jun Hu, and S. Das Sarma. Resistivity Saturation Revisited: Results from a Dynamical Mean Field Theory. *Physical Review Letters*, [82, 2354–2357](#), Mar. 1999. Publisher: American Physical Society.
- [195] Connie H. Mousatov, Ilya Esterlis, and Sean A. Hartnoll. Bad Metallic Transport in a Modified Hubbard Model. *Physical Review Letters*, [122, 186601](#), May 2019. Publisher: American Physical Society.
- [196] R. S. Markiewicz, S. Sahrakorpi, M. Lindroos, *et al.* One-band tight-binding model parametrization of the high- T_c cuprates including the effect of k_z dispersion. *Physical Review B*, [72, 054519](#), Aug. 2005. Publisher: American Physical Society.
- [197] Nandan Pakhira and Ross H. McKenzie. Absence of a quantum limit to charge diffusion in bad metals. *Physical Review B*, [91, 075124](#), Feb. 2015. Publisher: American Physical Society.
- [198] Adolf Fick. Ueber Diffusion. *Annalen der Physik*, [170, 59–86](#), 1855.
- [199] Max Planck Institute for the History of Science. Fick, Adolf Eugen.

- [200] S. Ciuchi and S. Fratini. Electronic transport and quantum localization effects in organic semiconductors. *Physical Review B*, **86**, 245201, Dec. 2012. Publisher: American Physical Society.
- [201] Ryogo Kubo. Statistical-Mechanical Theory of Irreversible Processes. I. General Theory and Simple Applications to Magnetic and Conduction Problems. *Journal of the Physical Society of Japan*, **12**, 570–586, Jun. 1957. Publisher: The Physical Society of Japan.
- [202] M. Calandra, J. Merino, and Ross H. McKenzie. Metal-insulator transition and charge ordering in the extended Hubbard model at one-quarter filling. *Physical Review B*, **66**, 195102, Nov. 2002. Publisher: American Physical Society.
- [203] A. Amaricci, A. Camjayi, K. Haule, *et al.* Extended Hubbard model: Charge ordering and Wigner-Mott transition. *Physical Review B*, **82**, 155102, Oct. 2010. Publisher: American Physical Society.
- [204] P. Kostic, Y. Okada, N. C. Collins, *et al.* Non-Fermi-Liquid Behavior of SrRuO₃: Evidence from Infrared Conductivity. *Physical Review Letters*, **81**, 2498–2501, Sep. 1998. Publisher: American Physical Society.
- [205] Y. S. Lee, Jaejun Yu, J. S. Lee, *et al.* Non-Fermi liquid behavior and scaling of the low-frequency suppression in the optical conductivity spectra of CaRuO₃. *Physical Review B*, **66**, 041104, Jul. 2002. Publisher: American Physical Society.
- [206] N. L. Wang, P. Zheng, D. Wu, *et al.* Infrared Probe of the Electronic Structure and Charge Dynamics of Na_{0.7}CoO₂. *Physical Review Letters*, **93**, 237007, Dec. 2004. Publisher: American Physical Society.
- [207] C. Bernhard, A. V. Boris, N. N. Kovaleva, *et al.* Charge Ordering and Magnetopolarons in Na_{0.82}CoO₂. *Physical Review Letters*, **93**, 167003, Oct. 2004. Publisher: American Physical Society.
- [208] A. A. Tsvetkov, J. Schützmann, J. I. Gorina, *et al.* In-plane optical response of Bi₂Sr₂CuO₆. *Physical Review B*, **55**, 14152–14155, Jun. 1997. Publisher: American Physical Society.
- [209] J. Hwang, T. Timusk, and G. D. Gu. Doping dependent optical properties of Bi₂Sr₂CaCu₂O_{8+δ}. **19**, 125208, Mar. 2007. Publisher: IOP Publishing.
- [210] K. Takenaka, J. Nohara, R. Shiozaki, and S. Sugai. Incoherent charge dynamics of La_{2-x}Sr_xCuO₄: Dynamical localization and resistivity saturation. *Physical Review B*, **68**, 134501, Oct. 2003. Publisher: American Physical Society.
- [211] A.V. Puchkov, T. Timusk, S. Doyle, and A.M. Hermann. *ab*-plane optical properties of Tl₂Ba₂CuO_{6+δ}. *Physical Review B*, **51**, 3312–3315, Feb. 1995. Publisher: American Physical Society.
- [212] T. Osafune, N. Motoyama, H. Eisaki, *et al.* Pseudogap and Collective Mode in the Optical Conductivity Spectra of Hole-Doped Ladders in Sr_{14-x}Ca_xCu₂₄O₄₁. *Physical Review Letters*, **82**, 1313–1316, Feb. 1999. Publisher: American Physical Society.
- [213] M. J. Rozenberg, G. Kotliar, H. Kajueter, *et al.* Optical Conductivity in Mott-Hubbard Systems. *Physical Review Letters*, **75**, 105–108, Jul. 1995. Publisher: American Physical Society.

- [214] P. E. Jönsson, K. Takenaka, S. Niitaka, *et al.* Correlation-Driven Heavy-Fermion Formation in LiV_2O_4 . *Physical Review Letters*, **99**, 167402, Oct. 2007. Publisher: American Physical Society.
- [215] K. Takenaka, Y. Sawaki, and S. Sugai. Incoherent-to-coherent crossover of optical spectra in $\text{La}_{0.825}\text{Sr}_{0.175}\text{MnO}_3$: Temperature-dependent reflectivity spectra measured on cleaved surfaces. *Physical Review B*, **60**, 13011–13015, Nov. 1999. Publisher: American Physical Society.
- [216] K. Takenaka, R. Shiozaki, and S. Sugai. Charge dynamics of a double-exchange ferromagnet $\text{La}_{1-x}\text{Sr}_x\text{MnO}_3$. *Physical Review B*, **65**, 184436, May 2002. Publisher: American Physical Society.
- [217] J. Dong, J. L. Musfeldt, J. A. Schlueter, *et al.* Optical properties of $\beta'' - (\text{ET})_2\text{SF}_5\text{CH}_2\text{CF}_2\text{SO}_3$: A layered molecular superconductor with large discrete counterions. *Physical Review B*, **60**, 4342–4350, Aug. 1999. Publisher: American Physical Society.
- [218] J. Vučičević, J. Kokalj, R. Žitko, *et al.* Conductivity in the Square Lattice Hubbard Model at High Temperatures: Importance of Vertex Corrections. *Physical Review Letters*, **123**, 036601, Jul. 2019. Publisher: American Physical Society.
- [219] Patrick A. Lee and T. V. Ramakrishnan. Disordered electronic systems. *Rev. Mod. Phys.*, **57**, 287–337, Apr 1985.
- [220] V. Cataudella, G. De Filippis, and C. A. Perroni. Transport properties and optical conductivity of the adiabatic Su-Schrieffer-Heeger model: A showcase study for rubrene-based field effect transistors. *Physical Review B*, **83**, 165203, Apr. 2011. Publisher: American Physical Society.
- [221] Ian E. Jacobs, Gabriele D’Avino, Vincent Lemaure, *et al.* Structural and dynamic disorder, not ionic trapping, controls charge transport in highly doped conducting polymers. Jan. 2021.
- [222] G. Schubert, G. Wellein, A. Weisse, *et al.* Optical absorption and activated transport in polaronic systems. *Phys. Rev. B*, **72**, 104304, Sep 2005.
- [223] Martin Indergand, Carsten Honerkamp, Andreas Läuchli, *et al.* Plaquette bond order wave in the quarter-filled extended Hubbard model on the checkerboard lattice. *Physical Review B*, **75**, 045105, Jan. 2007. Publisher: American Physical Society.
- [224] Arnaud Ralko, Fabien Trouselet, and Didier Poilblanc. Quantum Melting of Valence-Bond Crystal Insulators and Novel Supersolid Phase at Commensurate Density. *Physical Review Letters*, **104**, 127203, Mar. 2010. Publisher: American Physical Society.
- [225] Fabien Alet and Nicolas Laflorencie. Many-body localization: An introduction and selected topics. *Comptes Rendus Physique*, **19**, 498–525, 2018.
- [226] Rahul M. Nandkishore and S. L. Sondhi. Many-Body Localization with Long-Range Interactions. *Phys. Rev. X*, **7**, 041021, Oct 2017.
- [227] Piotr Sierant, Krzysztof Biedroń, Giovanna Morigi, and Jakub Zakrzewski. Many-body localization in presence of cavity mediated long-range interactions. *SciPost Phys.*, **7**, 8, 2019.

- [228] E. W. (Elliott Ward) Cheney. *Linear algebra : theory and applications / Ward Cheney, David Kincaid*. Jones & Bartlett Learning series in mathematics (Jones & Bartlett Learning, Sudbury, MA2012), second edition. ed. Publication Title: Linear algebra : theory and applications.
- [229] P. P. Ewald. Die Berechnung optischer und elektrostatischer Gitterpotentiale. *Annalen der Physik*, [369](#), [253–287](#), 1921. Publisher: Annalen der Physik.
- [230] Brad A. Wells and Alan L. Chaffee. Ewald Summation for Molecular Simulations. *Journal of Chemical Theory and Computation*, [11](#), [3684–3695](#), Aug. 2015. Publisher: American Chemical Society.
- [231] E. R. Smith and John Shipley Rowlinson. Electrostatic energy in ionic crystals. *Proceedings of the Royal Society of London. A. Mathematical and Physical Sciences*, [375](#), [475–505](#), Apr. 1981. Publisher: Royal Society.
- [232] Ulrich Essmann, Lalith Perera, Max L. Berkowitz, *et al.* A smooth particle mesh Ewald method. *The Journal of Chemical Physics*, [103](#), [8577–8593](#), Nov. 1995.
- [233] Heinz J. Rothe. *Lattice Gauge Theories: An Introduction*, vol. 82 of *World Scientific Lecture Notes in Physics* (World Scientific Publishing Co. Pte. Ltd.2012), 4th ed.
- [234] H. T. MacGillivray and R. J. Dodd. Monte-Carlo simulations of galaxy systems. *Astrophysics and Space Science*, [86](#), [419–435](#), Sep. 1982.
- [235] Helmut G. Katzgraber. Introduction to Monte Carlo Methods. *arXiv:0905.1629 [cond-mat, physics:physics]*, May 2011. ArXiv: 0905.1629.
- [236] Daan Frenkel. *Computational soft matter: from synthetic polymers to proteins. lect:Lecture notes*, vol. 23 of *NIC Series* (NIC, Jülich2004).
- [237] Martin Gautron. Paris Time Maps.
- [238] Eric Fischer. Locals and Tourists #4 (GTWA #3): Paris.
- [239] Kari Rummukainen. Monte Carlo simulations in physics.
- [240] Nicholas Metropolis, Arianna W. Rosenbluth, Marshall N. Rosenbluth, *et al.* Equation of State Calculations by Fast Computing Machines. *The Journal of Chemical Physics*, [21](#), [1087–1092](#), Jun. 1953. Publisher: American Institute of Physics.
- [241] W. K. Hastings. Monte Carlo sampling methods using Markov chains and their applications. *Biometrika*, [57](#), [97–109](#), Apr. 1970.
- [242] Pietro M. Bonetti, Johannes Mitscherling, Demetrio Vilardi, and Walter Metzner. Charge carrier drop at the onset of pseudogap behavior in the two-dimensional Hubbard model. *Physical Review B*, [101](#), [165142](#), Apr. 2020. Publisher: American Physical Society.